Investigation of Reaction and Transport Phenomena during Flame-Wall Interaction Using Laser Diagnostics

Vom Fachbereich Maschinenbau
der Technischen Universität Darmstadt

zur Erlangung des Grades eines
Doktors der Ingenieurwissenschaften (Dr.-Ing.)
genehmigte

Dissertation

von

Florian Maximilian Zentgraf, M.Sc.

aus Aschaffenburg

Berichterstatter:	Prof. Dr. rer. nat. A. Dreizler
Mitberichterstatter:	Prof. Dr. rer. nat. C. Schulz
Tag der Einreichung:	24.01.2022
Tag der mündlichen Prüfung:	23.03.2022

Darmstadt 2022

D17

It doesn't matter how beautiful your theory is, it doesn't matter how smart you are. If it doesn't agree with experiment, it's wrong.

Richard P. Feynman

Danksagung

Mit Fertigstellung dieser Dissertationsschrift blicke ich auf nunmehr 9 Jahre spannende und vielseitige Forschungstätigkeit am Institut für Reaktive Strömungen und Messtechnik (RSM) an der Technischen Universität Darmstadt zurück, die ich seit 2013 als Student und ab 2016 als wissenschaftlicher Mitarbeiter erfüllen durfte. Insbesondere die gute und kollegiale Zusammenarbeit am RSM, sowie mit verschiedenen Einrichtungen auf nationaler und internationaler Ebene, waren dabei ein wesentlicher Bestandteil. Auch wenn diese Dissertationsschrift als eigenständige wissenschaftliche Arbeit entstanden ist, haben mich und die präsentierte Arbeit viele Kolleg*innen über die Jahre hinweg maßgeblich geprägt und unterstützt. Dafür möchte ich mich im Folgenden bedanken.

Besonderer Dank gilt meinem geschätzten Doktorvater Prof. Dr. rer. nat. Andreas Dreizler. Zum einen für die schönen und zielführenden wissenschaftlichen Diskussionen, die wir in den vergangenen Jahren geführt haben und für die du dir stets Zeit genommen hast. Zum anderen für deine nie abreißende Begeisterung für unsere Forschung, dein Vertrauen und all die Freiheiten die du mir bei der Umsetzung stets gegeben hast. Deine gute Betreuung hat maßgeblich zu den erzielten Resultaten meiner Forschungsarbeit beigetragen.

Prof. Dr. rer. nat. Christof Schulz, Leiter des Instituts für Verbrennung und Gasdynamik (IVG) – Reaktive Fluide an der Universität Duisburg-Essen, möchte ich herzlich für die Übernahme des Korreferates danken, sowie für die gute Zusammenarbeit und Unterstützung bei der Organisation von Gordon Research Conference/Seminar 2017 bis 2019.

Ganz besonderer Dank gilt meinen Kollegen Pascal Johe und Dr. Max Greifenstein, für die großartige Unterstützung im Labor, all die guten fachlichen Diskussionen und auch privaten Gespräche. Meinem Vorgänger Dr. Hidemasa Kosaka danke ich für die thematische Einführung, sowie meinem Kollegen Matthias Steinhausen für die Bereitstellung ergänzender numerischer Simulationen. Auch möchte ich mich bei meinen beiden langjährigen Studenten Jonas Bargon und Sven Franek bedanken, die als studentische Hilfskräfte eine Vielzahl an Arbeiten im Labor übernahmen. Prof. Dr. Andrew D. Cutler von der George Washington University danke ich für die Bereitstellung seines Fitting Codes für CARS Spektren, sowie Dr. Robert Barlow, der mir als Mercator Fellow im TRR 150 stets mit wissenschaftlichem Rat zur Seite stand. Dr. Brian Peterson und Alexander Nicolas von der University of Edinburgh danke ich für die stetige Diskussion zu Geschwindigkeitsmessungen. Insbesondere Brian und auch Dr. Benjamin Böhm waren mir seit 2013 kontinuierliche Weggefährten und standen mir als Mentoren stets mit Rat und Tat zur Seite. Dafür danke ich euch beiden sehr.

Darüber hinaus hatte ich in den Jahren am RSM das Vergnügen mit vielen Kolleg*innen an einer Vielzahl von kleineren und größeren Vorhaben zu arbeiten. Dazu zählen Dr. Elias Baum, Dr. Johannes Bode, Dr. Carl-Philipp Ding, Dr. Johannes Emmert, Dr. Christian Fach, Christopher Geschwindner, Dr. Jens Hermann, Dr. Ayane Johchi, Dr. Jan Köser, Wibke Leudesdorff, Dr. Tao Li, Yujuan Luo, Dr. David Escofet-Martin, Dr. Henrik Nicolai, Dr. Jhon Pareja, Dr. Andreas Preusche, Marius Schmidt, Dr. Michael Stephan und Johannes Trabold. Euch allen möchte ich an dieser Stelle herzlich danken, für die fachliche Interaktion und natürlich auch die schönen privaten Momente neben dem Arbeitsalltag.

II

Darmstadt, Januar 2022   Florian Maximilian Zentgraf

Abstract

In this dissertation, flame-wall interaction (FWI) is investigated experimentally with respect to near-wall reaction and transport effects. In technical combustion, FWI processes are crucial, as they involve negative aspects like lowered efficiency or promoted pollutant formation. FWI is a highly complex interaction between surface, reaction and flow, where the most relevant processes occur a few hundred microns above the surface. So far, it is not yet fully understood. As near-wall reaction chemistry is fuel-dependent, FWI of novel alternative fuels thus requires investigation, like for the partially oxygenated dimethyl ether used here. A generic side-wall quenching (SWQ) burner for premixed atmospheric operation is used, with well-defined boundary conditions and good accessibility for experimental and numerical studies. Comprehensive measurements during FWI are performed by means of various laser diagnostics implemented simultaneously.

Near-wall flame and flow dynamics are assessed simultaneously by spatially and temporally highly resolved fields of velocity (by particle image velocimetry) and flame front distribution (by laser-induced fluorescence (LIF) of OH). In turbulent operation, SWQ-like and head-on quenching (HOQ)-like events alternate randomly. Turbulent boundary layers are resolved down to $y^+ = 1.5$. During flame quenching, the inner structure ($y^+ \leq 5$) remains unaffected while scaling laws are no longer valid farther from the wall. The results suggest that near-wall vortex structures promote exhaust gas recirculation (EGR) in SWQ-like events, while they push the reaction zone towards the wall in HOQ-like cases.

Near-wall thermochemistry is studied by quantitatively and simultaneously measuring gas temperature and mole fractions of CO_2 (by dual-pump coherent anti-Stokes Raman spectroscopy) as well as CO (by CO-LIF) along with qualitative OH-LIF. This is the first reported application of this three-parameter thermochemistry diagnostics in FWI environments. A validation of the approach yields good accuracy and precision for application during FWI. CO_2 proves to be less affected by the non-adiabatic conditions during FWI than CO. Under laminar conditions, the importance of differential diffusion effects in near-wall thermochemistry is demonstrated by comparison to numerical simulation. Investigation of turbulent FWI suggests the presence of further transport mechanisms compared to the laminar case, different for SWQ- and HOQ-like events. Through coupling with the findings on vortex structures, the hypothesis on near-wall EGR is supported, as CO_2 is evident upstream the quenching point. Overall, additionally measuring CO_2 proves highly suitable to describe FWI and enables the identification of novel insights and phenomena. A feasibility study on partially premixed FWI reveals that both near-wall flame structure and thermochemistry change significantly compared to the fully premixed case.

The presented results provide novel insights into FWI that extend beyond the state of research and yield outstanding validation data for numerical simulation.

Kurzfassung

In dieser Dissertation wird Flammen-Wand-Interaktion (FWI) im Hinblick auf wandnahe Reaktions- und Transporteffekte experimentell untersucht. Bei technischer Verbrennung sind FWI-Prozesse von entscheidender Bedeutung, da sie negative Aspekte wie einen verringerten Wirkungsgrad oder verstärkte Schadstoffbildung mit sich bringen. FWI ist eine hochkomplexe Wechselwirkung zwischen Oberfläche, Reaktion und Strömung, wobei die wichtigsten Prozesse einige hundert Mikrometer über der Oberfläche stattfinden. Bislang ist sie noch nicht vollständig verstanden. Da wandnahe Reaktionschemie brennstoffabhängig ist, muss FWI neuartiger alternativer Brennstoffe untersucht werden, wie beim hier verwendeten partiell oxygenierten Dimethylether. Es wird ein generischer Side-Wall-Quenching (SWQ)-Brenner für vorgemischten, atmosphärischen Betrieb verwendet, der gut definierte Randbedingungen aufweist und für experimentelle und numerische Studien gut zugänglich ist. Umfangreiche Messungen in FWI werden mit verschiedenen, gleichzeitig angewendeten Lasermesstechniken durchgeführt.

Die wandnahe Flammen- und Strömungsdynamik wird durch räumlich und zeitlich hochaufgelöste Felder der Geschwindigkeit (mittels Particle Image Velocimetry) und der Flammenfrontverteilung (mittels Laser-induzierter Fluoreszenz (LIF) von OH) simultan bewertet. Im turbulenten Betrieb wechseln sich SWQ-artige und Head-on Quenching (HOQ)-artige Zustände zufällig ab. Turbulente Grenzschichten werden bis zu $y^+ = 1{,}5$ aufgelöst. Beim Verlöschen bleibt die innere Struktur ($y^+ \leq 5$) unverändert, während Skalierungsgesetze weiter von der Wand entfernt keine Gültigkeit mehr haben. Die Ergebnisse legen nahe, dass wandnahe Wirbelstrukturen bei SWQ-artigen Fällen Abgasrückführung (AGR) fördern, während sie in HOQ-artigen Fällen die Reaktionszone zur Wand drücken.

Die Thermochemie in Wandnähe wird durch quantitative und gleichzeitige Messung der Gastemperatur und der Molanteile von CO_2 (dual-pump kohärente anti-Stokes Raman Spektroskopie) sowie von CO (CO-LIF) zusammen mit qualitativer OH-LIF untersucht. Dies ist die erste berichtete Anwendung dieser Drei-Parameter-Thermochemie-Diagnostik in FWI-Umgebungen. Eine Validierung des Ansatzes ergibt eine gute Genauigkeit und Präzision für die Anwendung bei FWI. CO_2 erweist sich bei FWI als weniger betroffen von den nicht-adiabaten Bedingungen als CO. Unter laminaren Bedingungen wird die Bedeutung von differentiellen Diffusionseffekten in der wandnahen Thermochemie durch den Vergleich mit numerischen Simulationen aufgezeigt. Die Untersuchung von turbulenter FWI deutet auf das Vorhandensein weiterer Transportmechanismen im Vergleich zum laminaren Fall hin, die sich für SWQ- und HOQ-artige Fälle unterscheiden. Durch die Kopplung mit den Erkenntnissen zu Wirbelstrukturen wird die These zur wandnahen AGR gestützt, da CO_2 stromauf des Verlöschungspunkts nachweisbar ist. Insgesamt erweist sich die zusätzliche Messung von CO_2 als sehr geeignet, um FWI zu beschreiben und ermöglicht die Identifizierung neuer Erkenntnisse und Phänomene. Eine Machbarkeitsstudie zur teilweise vorgemischten FWI zeigt, dass sich sowohl die wandnahe Flammenstruktur als auch die Thermochemie signifikant verändern, verglichen zum vollständig vorgemischten Fall.

Die vorgestellten Ergebnisse liefern neue Einblicke in FWI, die über den Stand der Forschung hinausgehen sowie hervorragende Validierungsdaten für die numerische Simulation.

Contents

List of Tables

List of Figures

Nomenclature

Lower-case Latin letters		Unit
b_{ij}	anisotropy tensor	—
f	focal length	m
f_{Sr}	vortex shedding frequency	s^{-1}
h_i	observed frequency of category i	—
i	sample number	—
k_{F}, k_{P}, k_{Q}	rate of fluorescence, pre-dissociation, collision quenching	s^{-1}
l_{F}	laminar flame thickness	m
l_{Q}	quenching distance	m
n	exponent **or** number of iterations	—
r	single-shot residuum	a.u.
r_{n}	distance between atomic nuclei	m
t	time	s
t_{R}	relaxation time	s
$\mathbf{u}'$	velocity fluctuation field (vector)	$\mathrm{m\,s}^{-1}$
u^+	dimensionless velocity	—
u_{F}	laminar flame speed	$\mathrm{m\,s}^{-1}$
u_τ	friction velocity	$\mathrm{m\,s}^{-1}$
u_i'	velocity fluctuation in i-th direction	$\mathrm{m\,s}^{-1}$
$u_{i,\,\mathrm{RMS}}'$	root mean square of velocity fluctuation in i-th direction	$\mathrm{m\,s}^{-1}$
v, v', v''	vibrational energy levels	—
$\vec{x}$	spatial coordinate vector	m
x	out of plane coordinate	m
x_i	spatial coordinate in i-th direction	m
y	wall-normal coordinate	m
y^+	dimensionless wall distance, wall unit	—
z	streamwise coordinate	m
z_{abs}	streamwise coordinate referred to burner nozzle exit	m

Upper-case Latin letters   Unit

A	area **or** cross-section	m^2
B	constant offset in log law	$-$
CV	coefficient of variation	$-$
Da	Damköhler number	$-$
E	energy	J
G	quadratic gradient magnitude	
I	intensity (laser **or** image)	$J\,m^{-2}$, counts
I_1, I_2, I_3	invariants of the anisotropy tensor	$-$
J, J', J''	rotational energy levels	$-$
Ka	Karlovitz number	$-$
L	length **or** characteristic length	m
L_{ii}	integral length scale	m
$L_{yy,+y}$	integral length scale of y-velocity in positive y-direction	m
$L_{zz,+z}$	integral length scale of z-velocity in positive z-direction	m
Le_k	Lewis number	$-$
Ma	Mach number	$-$
N	number of total samples **or** number density (in laser diag. context)	$-$
$\dot{Q}_{\mathrm{w}}$	wall heat flux	$W\,m^{-2}$
Q	values of Q-criterion	s^{-2}
R^2	coefficient of determination	$-$
R_{ij}	two-point correlation of velocity	$m^2\,s^{-2}$
Re	Reynolds number	$-$
Sr	Strouhal number	$-$
S_n	n-th singlet state	
T	gas phase temperature	K
$T_{\mathrm{wall}}^{(\mathrm{nom})}$	nominal wall temperature	K
$T_{\mathrm{wall}}^{(\mathrm{TC})}$	wall temperature from thermocouples	K
$T_{\mathrm{wall}}^{(\mathrm{TPT})}$	wall temperature from TPT	K
T_n	n-th triplet state	
$\langle U_i \rangle$	ensemble-averaged velocity in i-th direction	$m\,s^{-1}$
$\mathbf{U}$	instantaneous velocity field (vector)	$m\,s^{-1}$
U_∞	bulk flow velocity	$m\,s^{-1}$
U_i	instantaneous velocity in i-th direction	$m\,s^{-1}$
$U_{i,\mathrm{rel}}$	relative velocity in i-th direction	$m\,s^{-1}$

W	geometric correction function CO-LIF	$-$
X_i	mole fraction of species i	$-$

Lower-case Greek letters | | Unit

$\alpha,\ \beta$	angle	a.u.
δ_{ij}	Kronecker delta	$-$
δ_{99}	boundary layer thickness (at 99% bulk velocity)	m
ϵ	shape parameter	$-$
κ	von Kármán constant log law	$-$
λ	wavelength	m
μ	dynamic viscosity	$\mathrm{kg\,m^{-1}\,s^{-1}}$
ν	kinematic viscosity (in flow context)	$\mathrm{m^2\,s^{-1}}$
ν	frequency (in laser diagnostic context)	$\mathrm{s^{-1}}$
$\tilde{\nu}$	wavenumber	$\mathrm{m^{-1}}$
ξ	anisotropy coordinate	$-$
π_i	probability of category i	$-$
ρ	density	$\mathrm{kg\,m^{-3}}$
σ	standard deviation	a.u.
σ_{ion}	ionization cross-section	
σ_{A}	absorption cross-section	
τ	decay time	s
τ_{w}	wall shear stress	$\mathrm{kg\,m^{-1}\,s^{-2}}$
ϕ_{F}	fluorescence quantum yield	$-$
$\chi^{(n)}$	susceptibility tensor	
χ^2	chi-squared value	$-$
ω	wavenumber (in laser diagnostic context)	$\mathrm{m^{-1}}$
ω_i	vorticity along i-th axis (in flow context)	$\mathrm{s^{-1}}$

Upper-case Greek letters | | Unit

Δt	time separation	s
Θ	orientation parameter	$-$
Φ	fuel equivalence ratio	$-$

Indices

i, j, k	indices for index notation
x, y, z	in x-, y-, z-coordinate direction
0	initial value **or** ambient value
∞	value far from wall **or** bulk value
BG	background
BL	baseline
exp	experiment
L	laser
P1, P2	pump laser 1, pump laser 2
S, aS	Stokes, anti-Stokes
sim	simulation
w	wall

Operators and Mathematical symbols

$\Delta...$	difference in value **or** increment of value
$\langle ... \rangle$	ensemble-average
$\|...\|$	absolute value, Euclidean norm
$\mu(...)$	mean value
$\sigma(...)$	standard deviation value
$\vec{...}$	three-dimensional vector

Physical constants

		Value
c	speed of light	$3 \times 10^8 \, \mathrm{m \, s^{-1}}$
h	Planck's constant	$6.63 \times 10^{-34} \, \mathrm{J \, s}$
k	Boltzmann's constant	$1.38 \times 10^{-23} \, \mathrm{J \, K^{-1}}$

Abbreviations

1D	one-dimensional
2D	two-dimensional
2D2C	two-dimensional, two-component
3D	three-dimensional
AOI	angle of incidence
BG	background
CARS	coherent anti-Stokes Raman spectroscopy
CCD	charge coupled device
CCW	counterclockwise
CFD	computational fluid dynamics
CMOS	complementary metal-oxide semiconductor
CV	coefficient of variation
DC	detailed chemistry
DME	dimethyl ether
DNS	direct numerical simulation
DP-CARS	dual-pump CARS
EGR	exhaust gas recirculation
FFT	fast Fourier transform
FGM	flamelet-generated manifold
FOV	field of view
FWHM	full width at half maximum
FWI	flame-wall interaction
HOQ	head-on quenching
HS	high speed
IRO	intensified relay optics
IRW	interrogation window
LES	large eddy simulation
LIF	laser-induced fluorescence
MixAvg	mixture-averaged transport modeling
OME	oxymethylene ether
OP	operation point
PAH	polycyclic aromatic hydrocarbons

PDF	probability density function
PIV	particle image velocimetry
PLIF	planar laser-induced fluorescence
PMT	photomultiplier tube
PTV	particle tracking velocimetry
QFM	quenching flamelet-generated manifold
REDIM	reaction-diffusion manifold
RMS	root mean square
ROI	region of interest
RSM	Reaktive Strömungen und Messtechnik (TU Darmstadt)
SWQ	side-wall quenching
TC	thermochemistry
TGP	thermographic phosphor
TPT	thermographic phosphor thermometry
UV	ultraviolet
VIS	visible
VUV	vacuum ultraviolet
WIDECARS	width-increased dual-pump enhanced CARS
YAG	yttrium-aluminum-garnet

Chapter 1

Introduction

There is no doubt that tackling the global climate crisis and its consequences is one of the major challenges that our modern society has to face in the 21st century. It is well-accepted that global warming was and is influenced through human activities [112]. Fortunately, these circumstances are increasingly recognized in society, economy and politics around the world, and activity to address them is continuously growing. This is demonstrated most recently by climate related conferences (e.g., the recently held 26th *UN Climate Change Conference of the Parties*, COP26) or comprehensive scientific reports published by the *Intergovernmental Panel on Climate Change* (IPCC) [112] or *International Energy Agency* (IEA) [78], to only name a few.

Due to the advancing effects of climate change, a rethinking is required with regard to many energy-related technologies but also with respect to our consumption behavior. In any case, a reduction of carbonaceous pollutants is needed. A potential but desirable scenario to achieve is *net zero emission* by 2050 (NZE, with respect to CO_2) that could reach the proposed 1.5 °C global warming aim with 50% chance [78, p. 110]. An implementation of the NZE scenario relies on far-reaching changes regarding both energy production and consumption, demanding electrification, energy efficient technology and change in the individual behavior [78, p. 111]. On the one hand, some present technologies may substitute the use of fossil, carbonaceous fuels by electricity, like passenger cars for individual transport for examples. On the other hand, it is evident that an electrification is not possible in all technology and thus gaseous, liquid and solid fuels will remain important as energy carriers in future [78, p. 213]. For 2030, the NZE scenario for example expects the oil consumption in passenger cars to decrease by about 40%, while the aviation sector will require an increased demand by 30% [78, p. 212]. Following the recent World Energy Outlook 2021 [78, p. 211] the use of so-called *low emission fuels* (like biofuels or hydrogen-based fuels) is expected to continuously increase till 2050, regardless of proposed scenarios. The application of such fuels is primarily seen in sectors of heavy trucks, aviation and shipping [78, p. 223 f.]. For example, the NZE scenario expects aviation's total fuel demand covered by $\approx$ 40% biojet fuel and $\approx$ 30% through synthetic kerosene by 2050 [78, p. 224 f.]. Semelsberger et al. [149] reviewed the potential of dimethyl ether (DME, CH_3-O-CH_3) to substitute petroleum-based fuels and emphasized its capability to be implemented in current technologies, especially diesel engines, and to use existing infrastructure for gas. They further pointed out its reduced emission characteristics, less well-to-wheel emissions of greenhouse gases during production and reduced global warming potential compared to

other alternatives. For diesel engines, both DME or larger-chain size oxymethylene ethers (OMEs, CH_3-O-$[CH_2$-O$]_n$-CH_3) can be synthesized CO_2-neutral in an economical manner (e.g., via methanol), and latter OMEs are considered promising additives in real diesel engine application [72, 105]. Additionally, these fuels possess the potential to strongly reduce nitric oxide emission [105] as well as reduced formation of soot precursors and related emission (due to missing C-C bonds) [72, 105]. In this context, it becomes clear that fuels as chemical energy carriers remain essential and consequently energy conversion by means of combustion will continue to play an important role in the future, however, with a stronger focus on new chemical energy sources, i.e., novel low emission fuels. As such fuel surrogates and additives are novel for practical application, their increasing demand in future is strongly accompanied with a fundamental research interest. For successful implementation, one needs to understand their combustion characteristics as well as pollutant formation behavior.

Combustion systems for power generation or energy conversion, like internal combustion engines or gas turbines, are always accompanied by the phenomenon of *flame-wall interaction* (FWI), as these applications occur in enclosed chambers or vessels where the progressing reaction may interact with cold solid surfaces [128, p. 327]. In practical applications, FWI implicates negative impacts on efficiency and thermal management (wall heat loss), formation of pollutants due to incomplete combustion and durability of the devices [128, p. 327] [49]. As the temperature close to a solid surface is typically low, the chemical reaction is extinguished in the vicinity of the wall, termed *quenching* [128, p. 327]. FWI results in a very complex mutual interaction between wall, flame and turbulence (i.e., flow) and for this reason is highly complex to study and understand [128, p. 327 f.]. In internal combustion engines for example, surface heat fluxes can peak up to 10 MW/m^2 during operation with extremely high temporal dynamic [25], while a significant amount of engine-out hydrocarbon emission involves quenching phenomena (5% from single-wall quenching and 38% from crevices in fully warmed engine) [6]. Thus, FWI is considered a very important topic in combustion technologies as well as for environmental protection, especially, as it is not yet fully explored nor sufficiently understood [128, p. 327]. This motivates the pressing needs for research on FWI.

1.1 State of Research on Flame-Wall Interaction

Flame-wall interaction has been investigated in the past with regard to various aspects. Review articles were recently presented by Dreizler and Böhm [49] in the context of laser diagnostics application as well as by Luo and Liu [107] with respect to pollutant formation. The following section provides a literature review on the current state of research and attempts to provide an overview on the most relevant previous work in the context of this thesis. Further literature may be found in the work cited below. The remainder of this section distinguishes experimental as well as numerical studies, points out FWI studies using DME fuel, and finally summarizes open scientific questions. Parts of the content of section 1.1 were published in Zentgraf et al. [E8, E11] and are reused with permission (see appendix B), in a modified wording and partially extended by further technical and scientific details to fit the structure of this thesis.

Experimental Studies   As pointed out by Poinsot and Veynante [128, p. 327], experimental investigations of FWI are extremely challenging, as the most relevant phenomena happen very close to the surface. Under turbulent flow conditions, investigation of FWI phenomena is increasingly complicated by the small spatial and temporal scales of turbulence superimposed. For this reason, the method of choice for detailed FWI experiments is the application of laser diagnostics, as they provide high resolution in both space and time at good accuracy as well as precision and probe the system non-intrusively without disturbing local flow and reaction [107]. As practical combustion devices are very complex, generic configurations with simplified geometries are typically studied, where individual phenomena like *side-wall quenching* (SWQ, flame propagates parallel to wall) or *head-on quenching* (HOQ, flame propagates normal to wall) can be accessed [49]. Further details on these cases can be found later in section 2.2.3. Such studies can explore quenching from different points of view regarding thermal aspects (like quenching distances or wall heat fluxes), fluid mechanics, flame topology or thermochemistry [49]. From the experimental literature review in Dreizler and Böhm [49] it appears that the first points are studied more frequently, while the latter point on near-wall thermochemistry, which denotes the coupling of temperature or heat with chemical reaction, is only studied occasionally.

With respect to the thermal management, quenching distances (l_Q) and wall heat fluxes ($\dot{Q}_W$) were evaluated at varying pressure in a constant-volume chamber for both SWQ- and HOQ-phenomena by Bellenoue et al. [14] for different wall materials and by Boust et al. [26] with respect to the mixture's equivalence ratio. These studies used chemiluminescence imaging to derive l_Q and either estimated $\dot{Q}_W$ from these results [14] or measured it separately by a thermocouple-based heat flux meter embedded in the wall [26]. Kosaka et al. [E2] assessed the parameter sensitivity of wall temperature and different fuels (CH_4 and DME) on both l_Q and $\dot{Q}_W$ in an atmospheric SWQ burner. Quantities in their work were derived from gas phase and wall temperatures measured by coherent anti-Stokes Raman spectroscopy (CARS) and thermographic phosphor thermometry (TPT). Likewise, l_Q and $\dot{Q}_W$ were also evaluated in atmospheric, laminar HOQ [110] and SWQ [82], and l_Q for turbulent HOQ [137]. Kosaka et al. [E3] visualized local heat release rate in the FWI zone during premixed atmospheric SWQ by planar laser-induced fluorescence (PLIF) of CH_2O and OH. Recently, studies on thermal management during FWI applied further advanced diagnostics. Bohlin et at. [22] demonstrated a hybrid femto-/picosecond CARS setup to instantaneously measure one-dimensional wall-normal temperature profiles in an atmospheric HOQ burner. Both Escofet-Martin et al. [55] and Ojo et al. [120] evaluated the thermal boundary layer evolution and wall heat loss characteristics in a fixed-volume chamber that simulates compression and expansion at engine-relevant time scales to observe SWQ phenomena. They also applied a hybrid femto-/picosecond CARS approach (gas phase temperatures), however, along with TPT (wall temperatures) and imaging of CH* (flame front position). Typically, peak wall-heat fluxes in such generic experiments reported above reached values up to 1 MW/m².

The interaction of flame quenching with the near-wall local flow field was studied early by Foucher et al. [59], who investigated laminar HOQ in an atmospheric pressure vessel to mimic engine-like geometrical boundaries. By using high-speed particle image velocimetry (PIV) to trace unburnt flow velocities (interrogation window (IRW) 1.6×1.6 mm²), they

focused on flame front wrinkling and stretch in dependency of the fuel's (CH_4) equivalence ratio and finally demonstrated the disturbance of the flame front when approaching the wall. Please note that data cannot be closer to the wall than half the IRW size. Further details on such flame-wall-flow interaction in atmospheric, transient HOQ were given by Rißmann et al. [137] for turbulent flow conditions. They used high-speed stereoscopic PIV (IRW 580×580 μm^2) in combination with OH-PLIF for flame front tracking to study numerous characteristics with their dependency on two different fuels (CH_4 and C_2H_4). They found flow laminarization when approaching the wall and pointed out the relevance of Lewis number effects on flame wrinkling between different fuels. Jainski et al. [83] conducted detailed experiments in atmospheric, turbulent SWQ (CH_4, focus $\Phi = 1.00$) using comparable diagnostics (IRW 800×800 μm^2) and focused on the impact of reaction on the boundary layer as well as related near-wall turbulence characteristics. Amongst other results, they found that flow streamlines and thus the boundary layers are contracting towards the SWQ-event and expand downstream, while production of turbulent kinetic energy features a sink approaching the reaction. This provided valuable insight in near-wall flow-flame-wall interaction. However, drawbacks were their simplified boundary layer definition (isoline at 95% non-reacting bulk flow that was straightforward transferred to the reacting cases) and the resolution of the velocimetry insufficient to resolve the viscous sublayer. Their first velocity information was available 400 µm from the quenching wall. As will be shown later in this thesis, this approximately equals the end of the viscous sublayer at $y^+ = 5$ in the studied SWQ-configuration. Recently, Ding et al. [47] investigated the near-wall flow field on response of approaching flames in an optical accessible spark ignition engine by combined high-speed particle tracking velocimetry (PTV) and SO_2-PLIF for flame front visualization. With this setting, they realized extremely high resolution with the first velocity vectors 25 µm from their wall (piston surface). They demonstrated the mutual relationship between near-wall flow and approaching reaction as well as that the flow acceleration by approaching reaction zones causes rapidly growing gradients in the turbulent boundary layer that become highly transient. However, their investigation was limited to velocimetry in the unburnt pre-quenching areas with an approaching flame front in close vicinity. Such high resolution would be desirable to cover the quenching and post-quenching areas, however, to the author's best knowledge this has not yet been reported in experimental literature.

Thermochemistry in FWI was already studied by Clendening et al. [36] in the early 1980s in an atmospheric SWQ device using laminar premixed propane/air flames. They measured spatially resolved profiles of gas phase temperature and relative hydrocarbon number densities and mole fractions close to the quenching wall by application of a spontaneous Raman-scattering setup (Gaussian beam diameter ≈ 80 μm) and demonstrated impact of the wall on combustion. Saffman [144] applied a similar setup and procedure for temperature an hydrocarbon concentration measurements, and conducted a parametric study on the effect of varying equivalence ratio, fuel and wall condition on the quenching layer structure in atmospheric premixed SWQ. However, both studies did not measure temperature and species concentrations simultaneously. In 1999, Mokhov et al. [115] presented numerical and experimental examinations of a laminar boundary layer in the combustion products of a propane/air flame at different equivalence ratios and wall temperatures. Their studied sidewall was positioned fully in the exhaust gas of a burner

and rather equaled an *exhaust gas-wall interaction* than FWI. They measured near-wall profiles of velocity (by laser Doppler anemometry, LDA; resolution 180 μm), gas phase temperatures (by a line reversal method; resolution $\leq$ 200 μm), OH (by absorption spectroscopy and LIF; resolution $\approx$ 250 μm) as well as CO number densities (by two-photon LIF; resolution 70 μm). It was not evident whether or not the data were measured simultaneously. More recently, Fuyuto et al. [61] investigated the capabilities of near-wall LIF diagnostics in an atmospheric SWQ device operated at laminar conditions with premixed CH_4/air (Φ = 0.9). They applied a comprehensive set of diagnostics and assessed two-dimensional distributions of gas phase temperature (by multi-line NO-PLIF thermometry), OH and CH_2O (by PLIF), and CO (by two-photon PLIF) as close as 200 μm to the wall's surface. In their study, temperature and species information were not measured simultaneously, and species distributions were only evaluated qualitatively or semi-quantitatively. However, to study the instantaneous near-wall thermochemistry, e.g., under turbulent conditions, simultaneous measurements are indispensable. Recently, gas phase temperature T (by CARS) and the CO mole fraction X_{CO} (by two-photon LIF) were quantified simultaneously at the same location in both stagnation-stabilized [110,151] and transient HOQ [110] as well as for SWQ configurations [82, E2]. This approach enabled a shot-to-shot correlation of T to the corresponding X_{CO} values, termed (CO,T) in the following, up to 100 μm close to the wall surface. These listed studies covered comprehensive parametric sensitivity analysis (Re, turbulence intensity, Φ, fuel, wall temperature) and provided valuable findings on near-wall thermochemistry during FWI. The mutual turbulence-thermochemistry relationship, which is extremely important for closer-to-reality interpretation, always appeared to be rather a side aspect than main topic. Turbulent near-wall thermochemistry was assessed by Mann et al. [110] (for HOQ, only in stationary stagnation-stabilized case) and Kosaka et al. [E2] (for SWQ). Both observed the presence of intermediate thermochemical states and pointed out an impact on CO oxidation. However, they primarily focused on laminar cases in their investigations. Consequently, the experimental evaluation of thermochemical states during FWI for turbulent flow conditions remains almost an unchartered field. Furthermore, both T and X_{CO} (as CO is an intermediate species) are parameters prone to the non-adiabaticity of the FWI process. Thus, additional knowledge on a major reaction species, e.g., a product like CO_2 or H_2O, which is less affected by enthalpy loss to the quenching wall would be desirable. Bohlin et al. [20] demonstrated an ultrabroadband one-dimensional CARS approach for simultaneously probing six major combustion species (N_2, O_2, H_2, CO, CO_2, and CH_4) along with thermometry to assess thermochemical state during atmospheric SWQ. This technique provided wall-normal profiles with 35 μm resolution with the wall-closest data at 30 μm above the solid surface. During SWQ, species information was given in terms of mole fraction ratios (with respect to N_2), while CO signal level was too low for quantification. To the author's best knowledge, this was the only experimental multi-parameter study in FWI that expanded beyond the previously presented (CO,T) thermochemistry. Thus, this thesis aimed closing that knowledge gap to a certain extent by simultaneously measuring the (CO_2,CO,T) thermochemistry in FWI, as recently presented for premixed, atmospheric SWQ under laminar [E11] and turbulent conditions [E8]. Please note that extractive sampling methods for species measurements were omitted in the above literature and references on such studies are reported by Luo and Liu [107] (see Table 1 in [107]).

Numerical Studies   As numerical studies are not within the scope of this thesis, FWI-related literature is summarized more briefly. Several aspects related with FWI-modeling are given by Poinsot and Veynante [128, p. 328 ff.] that should be accounted for, like the invalidity of adiabaticity assumptions, generation of near-wall pollutants, large wall heat fluxes or altering turbulent scales by the wall, to only name a few. Beside others, a major challenge in computational combustion investigations lies in the accurate description of the reaction chemistry [63, E5]. The most accurate approach is the application of *detailed chemistry* (DC, applied in [52, 63, E5] for laminar and [69] for turbulent flames) as this method directly solves the transport equations of all combustion-relevant species [63, E5]. Since this involves high computational effort, the DC approach is mostly suitable for generic FWI configurations [63, E5]. To facilitate the simulation of closer-to-reality applications or more complex geometries, the reaction chemistry needs to be reduced to lookup table-like *manifolds* that contain the full pre-calculated combustion chemistry accessed by few control variables [63, E5]. The application of such manifold-tabulated chemistry maintains the high accuracy of DC predictions, however, at much lower computational effort for the final simulation [E5]. In context of FWI simulation, different approaches to tabulate chemistry manifolds have been developed and applied, namely flamelet-generated manifolds (FGM, applied in [52, 63, E5]), quenching flamelet-generated manifolds (QFM, applied in [52, E5]) or reaction-diffusion manifolds (REDIM, applied in [63, 155, 156, E5]). Especially, when using the classical FGM method, prediction deficiencies in near-wall chemistry (regarding CO species) have been reported, while the others yielded better agreement with DC [52, 63, E5]. In some early FWI studies on turbulent conditions, a strongly simplified chemistry was applied [7, 8, 29, 129], e.g., the reduction of the entire combustion to a single-step reaction mechanism. If one is interested in merely capturing the combustion impact on the flow field, e.g., by the local viscosity change, this might be sufficient, however, not well-suited for detailed assessment of the reaction progress and its evolution during FWI. To ensure physical meaningful simulations of complex combustion applications it is evident that experimental data plays a crucial role for validation of computational models employed in simulations using both DC or reduced chemistry.

Similar to experimental FWI studies reported before, detailed numerical simulations are more frequently reported for laminar configurations [52, 62, 63, 75, 131, 155, 156, 168, E5] compared to turbulent conditions [2, 7, 8, 29, 69, 76, 129]. This is especially true with respect to a detailed treatment of the chemistry evolution in turbulent cases, which was only addressed by [69] (DC) and [76] (FGM). Relevant numerical studies on FWI under laminar conditions are summarized below. For instance, Popp et al. [131] conducted one-dimensional, atmospheric HOQ simulations for stoichiometric propane and methane fueled flames using DC. They investigated the impact of surface chemistry and found that it significantly participates in reaction for higher wall temperatures (600 K case in their study) and alters the near-wall flame structure. Ganter et al. [62] studied premixed, atmospheric SWQ (CH_4/air, $\Phi = 1.0$) using two-dimensional fully resolving simulations with DC, and discovered that near-wall CO (leading to correspondingly high concentrations) is transported there via diffusion from larger wall distance locations. For the same configuration and condition (premixed SWQ, CH_4/air, $\Phi = 1.0$) Heinrich et al. [75] evaluated the feasibility of FGM chemistry tabulation. They found that near-wall CO prediction by FGM suffers inaccuracy and pointed out that, despite a laminar configuration was stud-

ied, the flow has three-dimensional nature due to acceleration by the flame. Subsequently, reduced chemistry approaches were tested and evaluated for atmospheric, premixed SWQ using CH_4 [52, 63, E5] and DME fuel [E5]. Straßacker et al. [155, 156] demonstrated the application of REDIM chemistry tabulation in premixed HOQ for CH_4/air mixtures under varying pressure [155] and isooctane representative for complex fuels [156]. Recently, Zirwes et al. [168] assessed the computational sensitivity on quenching distances in atmospheric premixed SWQ (CH_4 and propane fuel) and pointed out potential shortcomings in the state-of-the-art formulations for diffusion models for near-wall application.

With respect to turbulent conditions, premixed FWI was studied in two dimensions by Poinsot et al. [129] and three-dimensional by Bruneaux et al. [29] using direct numerical simulation (DNS). They evaluated classical characteristics like quenching distances and wall heat flux as well as flame structures or assessed the importance of coherent structures to FWI. Alshaalan and Rutland [7, 8] investigated turbulent premixed SWQ in a Couette channel flow (V-shaped flame in channel) by DNS. The authors analyzed the reaction's influence on turbulent boundary layer, turbulent scalar fluxes and length scales, flame-surface density, wall heat flux and the impact of vortex structures. However, these early works mainly focused on the near-wall flame-flow interaction and applied simplified reaction mechanisms (e.g., single-step reaction), which in turn inhibited local thermochemistry assessment. A comprehensive three-dimensional DNS study of a turbulent premixed SWQ configuration for H_2/air combustion was presented by Gruber et al. [69] using detailed chemical kinetics as well as molecular transport models. Amongst other aspects, they pointed out potential regime changes of the flame when approaching the wall, as it thickens while flame speed decreases, and found that near-wall turbulent vortex structures govern FWI by pushing the reaction towards the wall or lifting it, which strongly affects the local wall heat flux. SWQ for turbulent premixed CH_4/air flames was investigated by Heinrich et al. [76] by three-dimensional Large Eddy Simulation (LES) and tabulated chemistry (FGM), who assessed several classical quantities like quenching distance and wall heat flux, but also evaluated the instantaneous interaction of vortex structures with the flame front. Ahmed et al. [2] performed three-dimensional DNS of turbulent premixed SWQ (CH_4/air) using single-step reaction chemistry and assessed the impact of wall boundary condition (i.e., isothermal or adiabatic wall). It needs to be noted that the majority of past simulation studies on turbulent FWI focused on aspects on fluid dynamics or thermal management (quenching distance, wall heat flux), while thermochemistry remained nearly unchartered field. Palulli et al. [123] recently presented a two-dimensional DNS for laminar premixed CH_4/air flames with DC in SWQ and superimposed unsteadiness to the combustion process by forcing the flame via velocity perturbations, and assessed (CO,T) correlations in state space of the unsteady case.

DME fuel   As pointed out above, novel fuel surrogates and additives are a further point of interest in future combustion research, like the diesel fuel additives DME and OMEs. DME is considered a promising candidate to replace petroleum-based fuels [149], despite it is stated less advantageous with respect to classical logistics for automotive fuels because it is gaseous at ambient conditions [105]. Still, DME represents a partially oxygenated hydrocarbon that is considered a promising low emission fuel pioneer, and its chemical

structure is closely related to the OMEs. For generic experimental studies the gaseous state is even desirable, as fuels are easier to handle and supply to the combustion facilities. From a theoretical point of view its low molecular complexity compared to OMEs is further beneficial for fundamental research, e.g., for building reaction mechanisms and models. For an application of more complex fuels with higher molecular weight, like DME or OMEs, it is well-known that such a molecular structure can significantly impact the FWI processes, especially, the formation of intermediate hydrocarbons where different chemical reaction pathways may become relevant. This was demonstrated early in numerical HOQ studies using detailed kinetics by Kiehne et al. [90] for propane or Hasse et al. [73] for iso-octane fuel, for example. Both studies emphasized that intermediate hydrocarbons need to be accounted for in the kinetics during flame quenching when using complex fuels. Evidently, the near-wall chemistry of novel low-emission fuels needs to be investigated thoroughly under quenching conditions.

Experimental and numerical studies on assessing the impact of DME fuel on FWI are scarce so far. Recently, Luo and Liu [106] investigated the effect of DME addition to ethylene fuel (C_2H_4) on soot formation, within a non-premixed flame impinging a cooled surface (HOQ configuration). By sampling and analyzing soot particles at the surface after combustion, they found that DME addition suppressed formation of soot. Lee et al. [98] studied premixed, lean DME/O_2 flames in a wall-stabilized, impinging HOQ arrangement and measured spatial formaldehyde distribution (by CH_2O-PLIF) as well as flame temperatures (by thermocouples), and performed comparison to simulation. Wan et al. [164] investigated the impact of wall chemical effects on lean DME/air flames ($\Phi = 0.85$) in an optically accessible micro flow reactor and applied extractive gas chromatography (for: DME, CO, CO_2) and PLIF (for: CH_2O, OH) to access species distributions. By varying the surface material in the channel, they found a strong wall chemical effect on the species evolution in both the low- and high-temperature oxidation regions. Kosaka et al. studied premixed DME/air combustion in an atmospheric SWQ burner by advanced, simultaneous laser diagnostics with scope on near-wall (CO,T)-thermochemistry (by CARS, CO-LIF and OH-PLIF) [E2] and the local heat release rate (by CH_2O-PLIF and OH-PLIF) [E3]. They performed comprehensive parametric sensitivity studies (wall temperature, Φ, laminar/turbulent inflow) and benchmarked the properties of DME quenching to common CH_4/air operation. A numerical study on premixed DME/air combustion in laminar SWQ was presented by Steinhausen et al. [E5] with focus on local heat release rate and near-wall thermochemistry as well as evaluation of different chemistry tabulation (including DC). Recently, Stagni et al. [153] further explored the role of near-wall chemistry during quenching of premixed DME/air flames in a laminar SWQ simulation. They assessed reduced chemistry models derived from DC and found that diffusion is the prevailing process in near-wall combustion and that low temperature chemistry in DME does not affect near-wall processes significantly (and thus may be neglected in mechanisms for lean to stoichiometric, atmospheric conditions). The sparse treatment of DME during FWI in the literature, especially with respect to near-wall resolved thermochemistry, demands further research activity to better understand its phenomenological behavior.

Open Scientific Questions The review article of Dreizler and Böhm [49] recently summarized several unresolved issues in the context of FWI studies: (1) exploring the structure of fluidic and thermal boundary layers under steady and unsteady FWI, and their interplay to near-wall and bulk flow turbulence; (2) evaluation of the turbulent heat flux contribution to the total heat flux; (3) clarification if capturing the chemistry-turbulence-wall interaction claims further advanced combustion models for description. For future experimental FWI studies, they stated the need for general methodological developments on the one hand and specific multi-parameter measurements (considered most urgent for thermochemistry) on the other hand as major tasks [49]. From these points, as well as the selected literature summarized above, the following open issues can be concretized for FWI experiments:

- Application of a well-selected multi-parameter diagnostic to further expand the instantaneous quantification of near-wall thermochemistry beyond (CO,T).

- Extend the experimental data and knowledge on turbulent thermochemistry.

- Gain further insight into the velocity boundary layer and clarify if a parametrization is possible.

- Further insights into near-wall characteristics of the perspective and promising low-emission fuel DME.

1.2 Aim, Structure and Novelty of this Thesis

The aim of this thesis is to address several open scientific questions in FWI, as outlined above, and to expand beyond the previous state-of-the-art experimental FWI research by the means of advanced laser diagnostics. Specifically, the following highlights and novelties will be pursued for this purpose:

- Gaining further detailed findings on thermochemistry during FWI by extension of the previously applied diagnostic (CARS and CO-LIF) to simultaneously quantify (CO,T) towards measuring three scalars at a time. For this purpose, CO_2 mole fraction X_{CO_2} was additionally measured via extension of the CARS setup to a *dual-pump* CARS arrangement, resulting in the accessibility of instantaneous, quantitative three-parameter thermochemical states (CO_2,CO,T). As stable major product species, CO_2 is expected less affected by enthalpy loss during quenching and monotonically rises with reaction progress, in turn making it a suitable progress variable component in numerical simulation for reduced chemistry manifolds for both DME [E5] and CH_4 [63, 75, 76]. Within the scope of this thesis, the capabilities to simultaneously measure (CO_2,CO,T) thermochemistry was recently presented in Zentgraf et al. [E8, E11] and allowed valuable novel insight into both laminar and turbulent FWI. This was the first time that dual-pump CARS was realized at RSM institute and, to the author's best knowledge, the first reported application of this combined diagnostic approach to study FWI environments.

- Detailed assessment of turbulent FWI that expands beyond previous classification of typical turbulence-related metrics, covering the following aspects: (1) Using the three-scalar thermochemistry approach to provide certain aid to the experimental lack on multi-scalar data during turbulent FWI; (2) Consideration of the instantaneous quenching topology for all analysis, classified to scenarios related either with SWQ or HOQ; (3) Proposing potential transport scenarios to explain instantaneous turbulent near-wall thermochemistry by coupling to detailed flow analysis; (4) Evaluation of the turbulent boundary layer down to the viscous sublayer during FWI.

- First insight into the impact of partially premixing on FWI with regards to thermochemistry and flame topology.

- Extending insight into processes during near-wall DME combustion in general, as a relevant novel fuel.

- Providing more comprehensive and highly resolved data sets for model validation in numerical combustion simulation.

All of the aspects listed above contain certain degree of novelty that is worth reporting.

Apart from this introduction, the following thesis is divided into six further chapters. Chapter 2 outlines fundamentals on fluid mechanics, combustion as well as laser diagnostics, which are relevant in context of this thesis. Subsequently, chapter 3 describes the studied combustion facility consisting of an atmospheric, fully premixed SWQ burner and provides a characterization for its operation within the scope of this work. The scientific
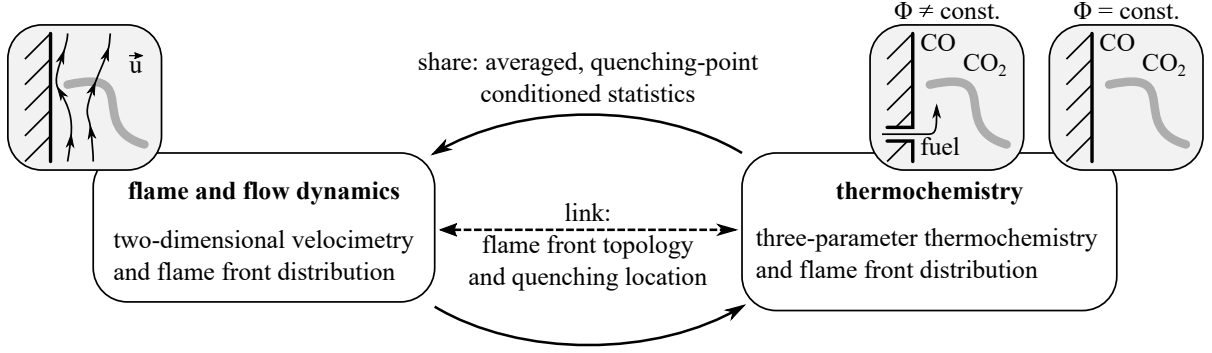
Figure 1.1: Graphical abstract of the applied approach using complementary experimental results to assess transport and reaction phenomena in FWI.

results are presented in chapters 4-6 (see also three embedded pictograms in the graphical abstract in Figure 1.1). First, the flame and flow dynamics are evaluated in chapter 4. Second, chapter 5 analyzes the near-wall thermochemistry in detail. Each of these chapters first introduces the aims, followed by the applied methods (diagnostics and data processing), then comprehensively presents and discusses all results, and concludes with a summary. Third, a first insight into partially premixed FWI in terms of a feasibility study is demonstrated by chapter 6. Finally, chapter 7 provides a conclusion of this work and draws an outlook. At the end of this thesis, a list of publications [E1–E12] is given to which the author made scientific contributions (as first author: [E7–E12], as coauthor: [E1–E6]; all peer-reviewed journal publications, except the conference contribution [E9]).

To best reach and discuss the above goals, this thesis takes the following approach drawn in the graphical abstract in Figure 1.1.[1] Basically, the two major campaigns on flame and flow dynamics (chapter 4) and thermochemistry (chapter 5, with partially premixed feasibility study in chapter 6) are stand-alone investigations. As the near-wall flame front is consistently captured during all measurements, data of both campaigns can be linked in terms of their statistic moments by conditioning on the instantaneous position of the quenching point and flame front topology. Such conditioning is done rigorously throughout the thesis. Including velocity data from a separate campaign for discussion of thermochemistry is not novel and was recently done by Jainski et al. [82] (laminar only, to assess near-wall flow boundary conditions and the local flame consumption speed) and Kosaka et al. [E2] (to compare near-wall integral time scales of the turbulent flow to those of CO production/oxidation). Both studies did not draw further detailed conclusions on the coupling of instantaneous fluid motion with thermochemistry, which is done more intensely here for turbulent conditions. As will be evident in the remainder of this work, this approach strongly supported the understanding and discussion on turbulent thermochemistry, as potential transport processes from the flame and flow dynamics campaign could be included.

---

[1]In this thesis, the free software Inkscape 0.91 (https://inkscape.org) was used to generate sketches and schematics or to finish annotations in processed result figures. The use of this valuable software is kindly acknowledged.

Chapter 2

Fundamentals

This thesis presents an experimental combustion study by means of laser diagnostics. As combustion processes are always coupled with flow phenomena, the chapter on fundamentals first covers fluid mechanical and combustion related basics. Subsequently, an insight into the applied laser diagnostics, including their governing quantum mechanics, is given. This chapter is not meant to provide a topical review but rather focuses the required aspects for the considerations in this thesis. Further literature is referred to at the appropriate places.

2.1 Fluid Mechanic Fundamentals

2.1.1 Continuum-Mechanical and Statistical Consideration

In fluid mechanics, the motion of flows is described by the conservation equations of continuum-mechanics and by using the means of statistics, as comprehensively outlined in the textbooks of Spurk and Aksel [152] and Pope [130].

Thus, corresponding equations can be given to describe the temporal and spatial motion of fluids. A first and important relation presents the conservation of mass by the *continuity equation*, taken from Spurk and Aksel [152, p. 37] as

$$\frac{\partial \rho}{\partial t} + \frac{\partial (\rho \cdot U_i)}{\partial x_i} = 0 \tag{2.1}$$

with the density ρ, time t, velocity U_i and location x_i in the i-th spatial direction. A second, leading equation captures the conservation of momentum, taken from [152, p. 45], by

$$\frac{\partial (\rho \cdot U_i)}{\partial t} + \frac{\partial (\rho \cdot U_i \cdot U_j)}{\partial x_j} - \frac{\partial \tau_{ji}}{\partial x_j} - \rho \cdot k_i = 0 \tag{2.2}$$

with the stress tensor τ_{ji} and k_i capturing the influence of mass- and volume forces (e.g., gravity). For the special case of Newtonian fluids and the corresponding formulation of τ_{ji}, Equation (2.2) can be emerged to the well-known *Navier-Stokes equations* [152, p. 103]. For a detailed and comprehensive discussion of conservation equations in fluid mechanics, the interested reader is referred to Spurk and Aksel [152] as well as Pope [130].

Evidently, a key parameter in those governing equations is the velocity field $U_i(\vec{x},t)$ with its spatial ($\vec{x}$) and temporal characteristics (t). Measuring flow velocities by experiments is thus of particular interest to describe the studied flows and also relevant for this thesis.

Depending on the flow conditions, the instantaneous flow velocity field $U_i(\vec{x},t)$ features quite different characteristics. Typically, the *laminar* and *turbulent* flow regime are distinguished [130, 152], whereat the dimensionless *Reynolds number* (see section 2.1.4 for definition) is an essential quantity to describe the flow and exceeding a critical value is relevant for transition towards the turbulent regime [152, p. 221 f.]. The laminar flow regime is associated with a deterministic and predictable fluid motion, e.g. straight and wall-parallel fluid trajectories in a pipe flow that only features molecular diffusion but no convective mixing in the lateral direction [152, p. 221]. In turn, the latter turbulent condition, which is most applicable for the majority of technical and practical flow configurations, is distinguished by a stochastic nature that is transient in time and evolves in all spatial dimensions [152, p. 221]. It furthermore features vortex structures and an increased diffusion [152, p. 221].

It is common practice to describe the influence of turbulence on the flow motion using statistical quantities and moments. For a fully developed turbulent flow, the instantaneous velocity $U_i(\vec{x},t)$ can be split into a contribution by an average velocity $\langle U_i(\vec{x},t)\rangle$ and a fluctuating fluid motion $u_i'(\vec{x},t)$, taken from [152, p. 224], as

$$U_i(\vec{x},t) = \langle U_i(\vec{x},t)\rangle + u_i'(\vec{x},t) \tag{2.3}$$

at a spatial location $\vec{x}$ and time t. This relation is commonly termed the *Reynolds decomposition* [130, p. 83]. According to Spurk and Aksel [152, p. 224], the average velocity results to

$$\langle U_i(\vec{x},t)\rangle = \lim_{N\to\infty}\left\{\frac{1}{N}\sum_{n=1}^{N}U_{i,n}(\vec{x},t)\right\} \tag{2.4}$$

for N realizations of the fluid motion. For experimental implementation, this is typically an *ensemble-average* over N finite samples. The operation $\langle...\rangle$ in Equation (2.4) can be applied for the averaging of any quantity. A further quantity that captures a measure for the velocity fluctuation in an ensemble is the *root mean square* (RMS) of the instantaneous velocity, taken from [130, p. 41], by

$$u_{i,\mathrm{RMS}}'(\vec{x},t) = \left\{\langle u_i'(\vec{x},t)^2\rangle\right\}^{\frac{1}{2}} = \sigma_{U_i}(\vec{x},t) \tag{2.5}$$

which equals the standard deviation $\sigma_{U_i}(\vec{x},t)$ of the instantaneous velocity $U_i(\vec{x},t)$, and can be resolved by inserting Equations (2.3) and (2.4). Applying the Reynolds decomposition in Equation (2.3) to the conservation equations, i.e. the continuity and Navier-Stokes equations, and performing an averaging operation $\langle...\rangle$ according to Equation (2.4) results in novel non-linear terms containing $\langle u_i'(\vec{x},t)\cdot u_j'(\vec{x},t)\rangle$, the so-called *Reynolds stresses*, in the averaged Navier-Stokes equations termed *Reynolds equations* [152, p. 224 ff.]. Because of these Reynolds stress terms, there are more unknowns in the equations as available equations to solve them, commonly referred to as the *closure problem* [130, p. 87].

The quantities discussed above can be used to derive further advanced measures for the fluid motion under investigation, as outlined in the following sections.

2.1.2 Scales and Structures in Turbulent Flow Motion

2.1.2.1 Energy Cascade and Integral Length Scales

A concept on relevant scales in turbulent flows is given by the ideas of the so-called *energy cascade* [130, p. 182 ff.]. In the following, this concept is briefly summarized using the explanations in Pope [130, p. 182 ff.] and based on that visualized in a schematic by Figure 2.1(a). The energy cascade assumes that large flow structures are containing the kinetic energy of the turbulent flow motion, as given by the big vortex with dimension L_0 by ① in Figure 2.1(a). With progression, this energy is increasingly distributed on smaller and smaller scales until it reaches the finest, Kolmogorov scales η (see ② in Figure 2.1(a)). At a certain point (L_{di}), length scales L reach the dissipation range ($\eta < L < L_{\mathrm{di}}$) and their energy dissipates due to the fluids viscosity ν (see ③ in Figure 2.1(a)).

A measure that represents larger, energy-containing flow scales, i.e., large eddies, is the integral length scale [130, p. 197]. It basically describes a range where velocity values are spatially correlated and thus are appointed to belong to a fluid bulk that uniformly moves [152, p. 226], see Figure 2.1(b). As the correlation within the fluid motion is the crucial factor, the two-point correlation, taken from [130, p. 196], forms the origin by

$$R_{ij}(\vec{x},\vec{r},t) = \langle u_i'(\vec{x} + \vec{r},t) \cdot u_j'(\vec{x},t) \rangle \tag{2.6}$$

with the spatial displacement $\vec{r}$. Note that the presentation in Pope [130, p. 196 f.] derives the equations for the case of homogeneous, isotropic turbulence that vanishes the $\vec{x}$-dependency. However, if this assumption is not valid, the $\vec{x}$-dependency remains in the equations, see Spurk and Aksel [152, p. 226] for example, and integral length scales can be assigned to each location $\vec{x}$ in the fluid motion. This was true for the presented thesis. Based on Equation (2.6), a longitudinal integral length scale

$$L_{11}(\vec{x},t) = \int_0^\infty \frac{R_{11}(\vec{x},\vec{r},t)}{\langle u_1'(\vec{x},t)^2 \rangle} \, dr = \int_0^\infty \frac{\langle u_1'(\vec{x} + r \cdot \vec{e_1},t) \cdot u_1'(\vec{x},t) \rangle}{\langle u_1'(\vec{x},t) \cdot u_1'(\vec{x},t) \rangle} \, dr \tag{2.7}$$

(a) visualization of the energy cascade
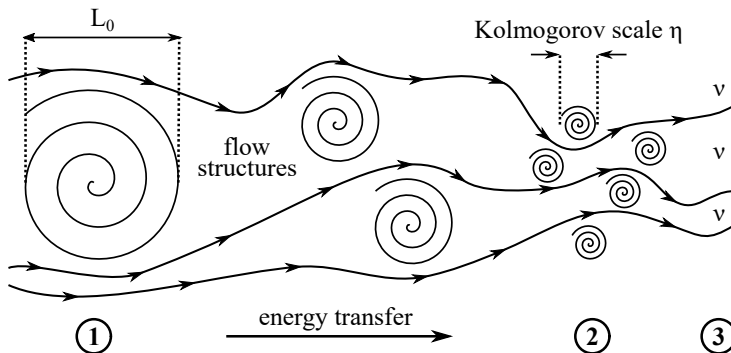
(b) two-point correlation
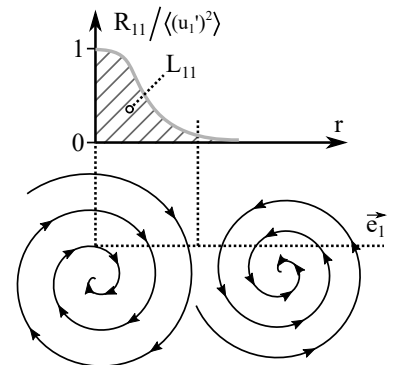
Figure 2.1: Visualization of (a) the energy cascade and (b) interpretation of the two-point correlation to derive the integral length scale L_{11} in Equation (2.7). Created from the descriptions in [130, p. 182 ff.] and adapted by own considerations.

and a corresponding transversal integral length scale can be defined

$$L_{22}(\vec{x},t) = \int_0^\infty \frac{R_{22}(\vec{x},\vec{r},t)}{\langle u_2'(\vec{x},t)^2 \rangle} \, dr = \int_0^\infty \frac{\langle u_2'(\vec{x} + r \cdot \vec{e_1},t) \cdot u_2'(\vec{x},t) \rangle}{\langle u_2'(\vec{x},t) \cdot u_2'(\vec{x},t) \rangle} \, dr \qquad (2.8)$$

according to Pope [130, p. 196 f.]. Here, $\vec{e_1}$ denotes the unit vector in the first direction of the coordinate system.

2.1.2.2 Anisotropy of Turbulence

Another convenient analytical tool assesses the anisotropy of turbulence by using an invariant map, that is often referred to as the *Lumley triangle*, as outlined by Choi and Lumley [35] for example. Originally, Choi and Lumley [35] used the invariant technique to investigate the so-called *return-to-isotropy* behavior in their work, that is of great importance for second-order turbulence models (see also Pope [130, p. 392 ff.]), but beyond the scope of this thesis. More general, the invariant map gives an interesting insight on how the turbulent kinetic energy is distributed to the spatial dimensions, i.e., within a three-dimensional energy ellipsoid, and allows some conclusions on the flow structure [35].

The invariants for the map are defined from the anisotropy tensor b_{ij} in Equation (2.9). The anisotropy tensor, taken from [35], is given by

$$b_{ij}(\vec{x},t) = \frac{\langle u_i'(\vec{x},t) \cdot u_j'(\vec{x},t) \rangle}{\langle u_k'(\vec{x},t) \cdot u_k'(\vec{x},t) \rangle} - \frac{1}{3} \cdot \delta_{ij} \qquad (2.9)$$

with δ_{ij} representing the *Kronecker delta* that is defined unity for $i = j$ and becomes zero for $i \neq j$ [130, p. 643]. Please note that Equation (2.9) is given in a modified way here, defining the tensor as a function of location $\vec{x}$ as well as time t and furthermore uses the notation introduced in the previous sections. Accordingly, the following three invariants, taken from [35], are defined as

$$I_1(\vec{x},t) = 0, \qquad (2.10)$$

$$I_2(\vec{x},t) = -\frac{1}{2} \cdot b_{ij}(\vec{x},t) \cdot b_{ji}(\vec{x},t), \qquad (2.11)$$

$$I_3(\vec{x},t) = \frac{1}{3} \cdot b_{ij}(\vec{x},t) \cdot b_{jk}(\vec{x},t) \cdot b_{ki}(\vec{x},t). \qquad (2.12)$$

Invariants $(-I_2, I_3)$ are located within the triangular invariant map shown in Figure 2.2. Corner points are defined by the state of three-dimensional (3D) isotropy in the origin $(-I_2, I_3) = (0,0)$, two-dimensional (2D) isotropy on the left-hand side and one-dimensional (1D) turbulence on the right-hand side [35]. Rearranging the equations taken from Choi and Lumley [35] leads to a formulation that specifies the edge for the state of 2D turbulence by

$$-I_2 = 3 \cdot I_3 + \frac{1}{9} \qquad (2.13)$$

and the edges for axisymmetric contraction (left) as well as expansion (right) by

$$-I_2 = \pm 3 \cdot \left\{ \frac{I_3}{2} \right\}^{\frac{2}{3}}. \qquad (2.14)$$
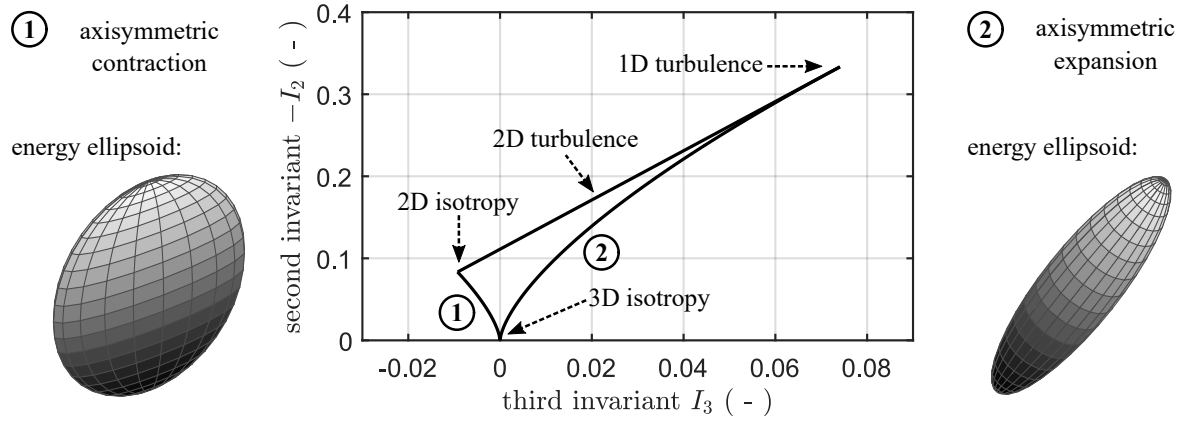
Figure 2.2: Invariant map for classification of turbulence anisotropy, with energy ellipsoids for the state of axisymmetric contraction ① and expansion ② sketched. Created from the visualizations and descriptions in [35] (Figure 1) and adapted by own considerations.

In Choi and Lumley [35], the boundary of axisymmetric contraction (Equation (2.14): negative algebraic sign) is given the designation *pancake shaped*, while the state of axisymmetric expansion (Equation (2.14): positive algebraic sign) was given the name *cigar shaped*. As already mentioned above, this denomination as well as the final classification in the triangular invariant map refers to a three-dimensional energy ellipsoid that undergoes certain deformation [35]. On the one hand, this deformation yields the dimension-dependent distribution of turbulent kinetic energy. On the other hand, an interpretation with respect to flow structures is possible. For example, the case of axisymmetric contraction features a flat energy ellipsoid, leading to elongated eddies [35], as visualized by ① in Figure 2.2 for an interpretation. In turn, the energy ellipsoid is stretched for the axisymmetric expansion state with corresponding eddies having no preferential structure or direction [35] (see ② in Figure 2.2).

2.1.2.3 Vortex Structures

As stated in the work of Chakraborty et al. [32] at the beginning, neither an accepted mathematical definition nor an universal criterion for identification of a *vortex* exists. This drawback is formulated in a similar way by Jeong and Hussain [85]. It directly emphasizes that vortex identification arises a challenging task and criteria should be used with caution and rather seen as a qualitative indicator than quantitative or ultimate measures. Nevertheless, vortex structures feature an essential characteristic of turbulent flow motion (see definition in section 2.1.1) and their classification provides insight to further understand specific flow phenomena, like mixing, heat transfer or combustion [85], to only name a few. Therefore, various possible criteria can be found in the literature, as comprehensively summarized and compared with one another in the works of Chakraborty et al. [32] as well as Jeong and Hussain [85]. For a more detailed insight into vortex identification schemes, the interested reader is referred to this literature.

One of these criteria is the so-called *Q-criterion* that was proposed by Hunt et al. [77] and defines a vortex by a coherent area with positive second invariant $Q > 0$ of the velocity gradient tensor $\partial U_i / \partial x_j$ [32, 85]. This invariant Q, taken from [85], is given by

$$
\begin{aligned}
Q = {} & -\frac{1}{2} \cdot \frac{\partial U_i}{\partial x_j} \cdot \frac{\partial U_j}{\partial x_i} \\
= {} & -\frac{1}{2} \cdot \left(\frac{\partial U_1}{\partial x_1} \right)^2 - \frac{1}{2} \cdot \left(\frac{\partial U_2}{\partial x_2} \right)^2 - \frac{1}{2} \cdot \left(\frac{\partial U_3}{\partial x_3} \right)^2 \\
& - \frac{\partial U_1}{\partial x_2} \cdot \frac{\partial U_2}{\partial x_1} - \frac{\partial U_1}{\partial x_3} \cdot \frac{\partial U_3}{\partial x_1} - \frac{\partial U_2}{\partial x_3} \cdot \frac{\partial U_3}{\partial x_2}
\end{aligned}
\tag{2.15}
$$

using the instantaneous velocities $U_i(\vec{x},t)$ (please note that the $(\vec{x},t)$-dependencies are not included in Equation (2.15) for reasons of clarity). Besides the prerequisite $Q > 0$, the Q-criterion further claims the pressure in the vortices below the ambient pressure [32, 85]. Chakraborty et al. [32] state that the first condition ($Q > 0$) often embraces the pressure condition, and correspondingly they only used the $Q > 0$ condition in their study. As outlined by Jeong and Hussain [85], the Q-criterion can alternatively be defined as

$$
Q = \frac{1}{2} \cdot \left(\| \Omega_{ij} \|^2 - \| S_{ij} \|^2 \right)
\tag{2.16}
$$

using the tensors $S_{ij} = \frac{1}{2} \cdot \left(\frac{\partial U_i}{\partial x_j} + \frac{\partial U_j}{\partial x_i} \right)$ and $\Omega_{ij} = \frac{1}{2} \cdot \left(\frac{\partial U_i}{\partial x_j} - \frac{\partial U_j}{\partial x_i} \right)$, named *rate-of-strain* (S_{ij}) and *rate-of-rotation tensor* (Ω_{ij}) by Pope [130, p. 23]. Considering the condition for vortices $Q > 0$, Equation (2.16) yields $\| \Omega_{ij} \|^2 > \| S_{ij} \|^2$. Thus, vortices are defined, where the contribution from rotation exceeds the corresponding strain contribution. The above Equations (2.15) and (2.16) are valid for incompressible flows, i.e., $\partial U_i / \partial x_i = 0$ [32].

One major advantage of the Q-criterion is that Q-values vanish at a solid surface and thus correctly capture the impact of a wall with respect to vortex structures [85]. This property is considered of particular importance for this thesis, as wall-bounded flows are in focus during flame-wall interaction. However, Jeong and Hussain [85] also pointed out a thorough discussion on potential inadequacy related with the Q-criterion. They documented that the Q-criterion is not always able to identify the right vortex cores but in conclusion stated that in most cases the Q-criterion resulted in similar results as their proposed novel λ_2-criterion [85]. At this point, it should be noted that the Q-criterion was successfully applied for numerical studies in near-wall reacting flow fields [69, 76].

Finally, an additional brief insight into the *vorticity* $\vec{\omega}(\vec{x},t)$ is given in the following. According to Pope [130, p. 22], vorticity is defined as

$$
\vec{\omega}(\vec{x},t) = \nabla \times \mathbf{U}(\vec{x},t) = \begin{pmatrix} \partial U_3 / \partial x_2 - \partial U_2 / \partial x_3 \\ \partial U_3 / \partial x_1 - \partial U_1 / \partial x_3 \\ \partial U_2 / \partial x_1 - \partial U_1 / \partial x_2 \end{pmatrix}
\tag{2.17}
$$

using the curl-operator $\nabla \times$. It is clearly evident from the outlines given in Jeong and Hussain [85] that the vorticity magnitude $|\vec{\omega}|$ is an inadequate mean for vortex identification for numerous reasons. However, vorticity features a valuable information that is no longer preserved by advanced criteria like the Q-criterion, namely a measure for the direction of rotation. Such information could be linked to vortex structures identified by advanced criteria.

2.1.3 Wall-Bounded Flows

Fluid mechanics close to a solid surface strongly deviate from considerations in a free-stream environment. The aspects on near-wall flows are covered in the majority of fluid-dynamical textbooks, like in Spurk and Aksel [152], Pope [130] and especially Schlichting and Gersten [145]. For detailed information on this topic it is referred to this literature.

In near-wall flows, the fluid's viscosity becomes a key parameter to be considered as it forces the fluid motion of the undisturbed bulk flow (U_∞) towards zero in a thin *boundary layer* to satisfy the no-slip condition at the surface [145, p. 27]. These boundary layers and their characteristics are of major interest when discussing wall-bounded flows, and, as in the classification of flow regimes in section 2.1.1, laminar and turbulent boundary layers can be distinguished [145, p. 27].

Assuming a flat plate with longitudinal inflow (U_∞) and laminar conditions, the resulting boundary layer continuously grows starting from the leading edge ($x = 0$ mm) of the solid surface [145, p. 28 f.]. Usual metrics define thicknesses of the evolving boundary layer, e.g., δ_{99} gives the location where $0.99 \cdot U_\infty$ is reached from the solid surface [145, p. 28 f.]. According to Schlichting and Gersten [145, p. 29], an analytical thickness

$$\delta_{99}(x) = 5 \cdot \sqrt{\frac{\nu \cdot x}{U_\infty}} \tag{2.18}$$

can be given for a laminar boundary layer, with the kinematic viscosity ν and length x in the direction of the solid surface. It needs to be noted that such laminar boundary layers undergo a transition into turbulent ones after a certain, *critical* length, accompanied with a sudden increase in the layer's thickness [145, p. 31].

To describe turbulent boundary layers, normalized parameters are usually applied; see Pope [130, p. 270 ff.] for example. In this context, there are several important variables and relations that are defined in the following. First, the *wall shear stress* is given by

$$\tau_{\mathrm{w}} = \rho \cdot \nu \cdot \left. \frac{d\langle U \rangle}{dy} \right|_{y=0 \text{ mm}} \tag{2.19}$$

with the density ρ, kinematic viscosity ν and the wall-normal gradient of the streamwise velocity $d\langle U \rangle/dy$ [130, p. 269]. Another quantity derived from τ_{w} is the *friction velocity*

$$u_\tau = \sqrt{\frac{\tau_{\mathrm{w}}}{\rho}} = \sqrt{\nu \cdot \left. \frac{d\langle U \rangle}{dy} \right|_{y=0 \text{ mm}}} \tag{2.20}$$

according to Pope [130, p. 269]. It further defines a normalized velocity [130, p. 272] by

$$u^+ = \frac{\langle U \rangle}{u_\tau} \tag{2.21}$$

as well as a dimensionless wall distance (so-called *wall units*) [130, p. 270]

$$y^+ = \frac{y \cdot u_\tau}{\nu} \tag{2.22}$$

within the near-wall region. While u_τ is considered a viscous velocity scale, the ratio ν/u_τ can be seen as a corresponding viscous length scale, and both are representative for the near-wall regime [130, p. 269 f.]. In this context, Pope [130, p. 270] points out that y^+ can be interpreted as a local Reynolds number. This again emphasizes the importance of viscosity on fluid motion in the vicinity of a solid surface. With decreasing y, this Reynolds number decreases while the viscosity ν maintains, means, that the viscous forces are getting increasingly important in the balance to the inertial forces (see definition of the Reynolds number in section 2.1.4).

Based on the above equations, near-wall turbulent flows are typically specified in the semi-logarithmic (y^+,u^+)-space, which is divided into different characteristic regions and described by certain universal laws, as outlined in Pope [130, p. 271 ff.]. A schematic of the classified (y^+,u^+)-space is given in Figure 2.3. In a superordinate classification, one can distinguish between a *viscous wall region* $(y^+ < 50)$ where viscosity has a significant impact and an *outer layer* $(y^+ > 50)$ where viscosity becomes insignificant [130, p. 275 f.]. Moving from the solid surface, the turbulent boundary layer first features the *viscous sublayer* $(y^+ < 5)$ that is transitioning into the *buffer layer* $(5 < y^+ < 30)$ and finally into the *log-law region* $(y^+ > 30)$ [130, p. 275 f.].

Following the *law of the wall*, the normalized velocity u^+ is merely a function of y^+, i.e., $u^+ = f_\text{w}(y^+)$, close to the solid surface [130, p. 272]. An important information, given in Pope [130, p. 272], is that this function f_w has universal character for non-transitional Reynolds numbers, i.e., can be applied to enclosed flows and free boundary layers similarly. Accordingly, a linear relation

$$u^+(y^+) = y^+ \tag{2.23}$$

can be given that well-describes the trend in the viscous sublayer for $y^+ < 5$ [130, p. 273]. The so-called *logarithmic law of the wall* (short: *log law*) well-captures the physical flow
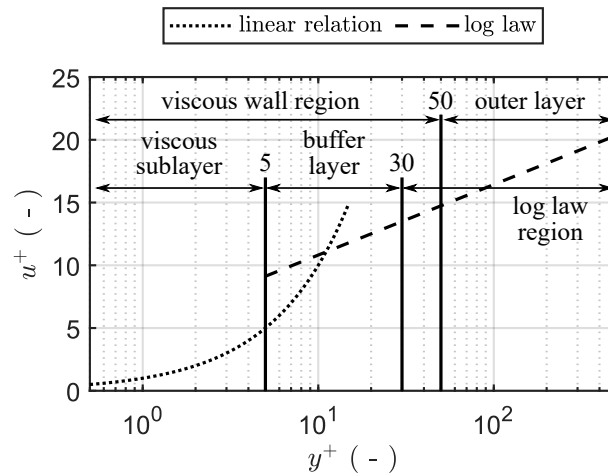
Figure 2.3: Schematic of the semi-logarithmic (y^+,u^+)-space with a distinction between the different layers. Both the linear relation and log law are shown according to Equations (2.23) and (2.24). Created from the visualizations and descriptions in [130, p. 273 ff.] (Table 7.1 and Fig. 7.8) and adapted by own considerations.

reality for wall units $y^+ > 30$ and is defined by

$$u^+(y^+) = \frac{1}{\kappa} \cdot \ln(y^+) + B \qquad (2.24)$$

with the von Kármán constant $\kappa = 0.41$ and a constant offset $B = 5.2$ [130, p. 274]. For further explanation and relations describing the behavior in the outer layer ($y^+ > 50$), where the viscosity gets negligible, it is referred to Pope [130, p. 275 ff.]. As evident from the discussion in Pope [130, p. 322 ff.], near-wall flows can further feature turbulent structures in various forms, like vortex structures, or *ejection* (fluid motion from wall) and *sweep* events (fluid motion towards wall), to only name a few.

2.1.4 Dimensionless Quantities

This final section on fluid mechanical fundamentals defines dimensionless quantities that are used in the remainder of this thesis. Figure 2.4 exemplifies the characteristic quantities for the definition of the dimensionless parameters by means of a cylinder.

First, the *Reynolds number* is defined by

$$Re = \frac{U \cdot L}{\nu} \qquad (2.25)$$

using both a characteristic velocity U and length L of the investigated flow as well as the kinematic viscosity ν according to Spurk and Aksel [152, p. 87]. The Reynolds number gives a ratio of inertial force (numerator) to frictional force (denominator) [145, p. 5].

Second, the *Strouhal number* can be given as outlined in Fey et al. [58] or Schlichting and Gersten [145, p. 19] by

$$Sr = \frac{f_{\mathrm{Sr}} \cdot L}{U} \qquad (2.26)$$

again with characteristic measures L, U and the frequency f_{Sr} of vortices shedding from the flow obstacle of dimension L. The Strouhal number is interpreted as a dimensionless frequency [145, p. 19]. In the case of a circular cylinder, U defines the oncoming flow, while L depicts the diameter of the cylinder [58]. In Fey et al. [58], a useful correlation $Sr = f(Re)$ is given for circular cylinders and a broad range of Reynolds numbers.
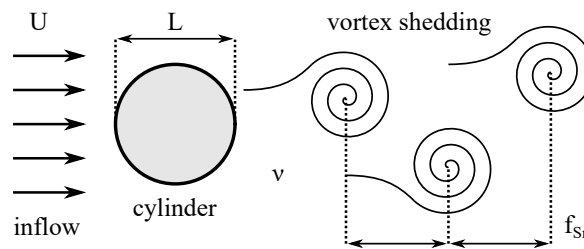
Figure 2.4: Characteristic flow quantities on a cylinder.

2.2 Combustion Fundamentals

Very general, combustion engineering considers the chemical transformation of reactants to products to make use of the global heat release [165, p. 2]. Combustion distinguishes two asymptotic types of flames, namely *premixed* flames, where fuel and oxidizer are mixed prior to combustion, and *non-premixed* flames (also called *diffusion* flames), where mixing and reaction happen at the same time [165, p. 4 ff.]. Between these asymptotic cases, *partially premixed* combustion with various intermediate mixing states exists (e.g., see Masri [111]), briefly presented in section 2.2.2.3. This fundamental section first outlines the role of reaction chemistry and subsequently focuses on the premixed combustion only and further aspects related with flame-wall interaction. A comprehensive insight into the most relevant aspects of combustion is provided by the textbooks of Warnatz et al. [165], Poinsot and Veynante [128] and Peters [127], where the reader is referred to for details.

2.2.1 The Role of Reaction Chemistry

The mathematical complete description of combustion processes requires the consideration of temporal and spatial changes caused by reaction, molecular and convective transport as well as radiation [165, p. 29]. Besides the previously introduced continuity Equation (2.1) and the conservation of momentum Equation (2.2), the set of conservation equations to describe such a *reactive flow* thus further demands the conservation of energy as well as species mass [165, p. 179 ff.]. For an arbitrary three-dimensional combustion process, the energy conservation equation in terms of enthalpy h, as taken from Poinsot and Veynante [128, p. 17], can be described by

$$\frac{\partial(\rho \cdot h)}{\partial t} + \frac{\partial(\rho \cdot U_i \cdot h)}{\partial x_i} = \frac{Dp}{Dt} - \frac{\partial q_i}{\partial x_i} + \tau_{ij} \cdot \frac{\partial U_i}{\partial x_j} + \dot{Q} + \rho \cdot \sum_{k=1}^{N} (Y_k \cdot f_{k,i} \cdot V_{k,i}) \qquad (2.27)$$

where q_i denotes an energy flux, $\dot{Q}$ a non-combustion-released heat source (e.g. by a radiation flux), $f_{k,i}$ the volume force, Y_k the mass fraction and $V_{k,i}$ the diffusion velocity of species k respectively. It is to be noted that there are several different formulations for the conservation of energy equation and some of them are more favorable for application in CFD than others [128, p. 16 ff.]. Using *Fick's law* to approximate diffusion velocities $V_{k,i}$, the mass conservation for species k can be given as

$$\frac{\partial(\rho \cdot Y_k)}{\partial t} + \frac{\partial(\rho \cdot U_i \cdot Y_k)}{\partial x_i} = \frac{\partial}{\partial x_i} \cdot \left(\rho \cdot D_k \cdot \frac{\partial Y_k}{\partial x_i} \right) + \dot{\omega}_k \qquad (2.28)$$

with D_k describing the diffusion coefficient of species k with respect to the entire mixture and the reaction rate $\dot{\omega}_k$ of species k [128, p. 14]. For a full description of all relevant conservation equations required to describe combustion processes, it is referred to the outlines of Warnatz et al. [165, p. 179 ff.] as well as Poinsot and Veynante [128, p. 12 ff.] (see also [128, p. 24 f.] for a convenient summary of these equations).

From the conservation of species mass in Equation (2.28), it is directly evident that actually *every* involved species k, including all intermediates, would be required for a mathematically complete description. Depending on the fuel used, the reaction processes

and involved species differ strongly. While the chemical mechanism of simple fuels like H_2 can be sufficiently described by approximately 40 elementary reactions, other hydrocarbon fuels feature up to several thousand reactions in their combustion process [165, p. 91]. As a consideration of all possible chemical pathways and species is technically not practical in many cases, *reduced mechanisms* are applied that use a few species to approximate the entire chemical reaction system [165, p. 107]. For combustion of methane/air mixtures, e.g., Peters [127, p. 25] outlines a reduced mechanism that consists of four global reaction steps. For dimethyl ether (DME) fuel, which is mainly used in the scope of this thesis, such mechanisms were recently proposed for premixed combustion by Stagni et al. [153] (31 species and 140 reactions) or Zettervall et al. [167] (30 species and 69 reactions). The mechanism of Stagni et al. [153] is reported feasible for application in atmospheric near-wall combustion environments, also in a further reduced version neglecting low-temperature chemistry (20 species and 93 reactions).

A prominent dimensionless parameter in the context of species diffusion is the so-called *Lewis number*

$$Le_k = \frac{\lambda}{\rho \cdot c_p \cdot D_k} \tag{2.29}$$

with heat diffusion coefficient λ and heat capacity c_p at constant pressure that finally relates thermal, i.e., $D_{\text{th}} = \lambda/(\rho \cdot c_p)$, and species diffusion speed with respect to species k (D_k: corresponding diffusion coefficient of species) [128, p. 7]. As stated by Poinsot and Veynante [128, p. 14], individual Lewis numbers Le_k only feature minor changes over the flame front and can be approximated constant for many flames. Furthermore, the assumption of $Le_k = 1$ for all species k is applied in many theoretical modeling approaches and valid for most combustion radicals, expect for very light ones [128, p. 34].

2.2.2 Premixed Combustion

A key parameter that characterizes premixed reactants for combustion is the *fuel equivalence ratio*

$$\Phi = \frac{1}{\lambda} = \frac{(X_{\text{fuel}}/X_{\text{air}})}{(X_{\text{fuel}}/X_{\text{air}})_{\text{stoichiom.}}} \tag{2.30}$$

that equals the reciprocal value of the *air equivalence ratio* λ and is defined from air and fuel mole fractions X, respectively [165, p. 6]. From this definition, $\Phi > 1$ is a (fuel) *rich* combustion, while $\Phi < 1$ describes a *lean* and $\Phi = 1$ the *stoichiometric* case [165, p. 6]. Please note that Φ is simply named *equivalence ratio* in the remainder of this thesis. Non-premixed combustion conditions cover the entire range $\Phi \in [0, \infty]$ [165, p. 8].

A further important quantity is the *laminar flame speed* u_{F} that defines the propagation speed of a laminar, premixed flat flame front into the unburnt, non-reacted quiescent gas mixture [165, p. 6]. It is directly evident that the balance between flame speed u_{F} and flow velocity of the unburnt, fresh gas mixture u_{U} determines the operation of premixed combustion systems. In case the flow velocity exceeds the flame speed, the flame is lifting and extinguishes by *blowoff* of the reaction [165, p. 6]. Another potential safety hazard of premixed flames that can cause severe technical damage is *flashback* of the reaction when u_{U} is too small compared to u_{F}.

2.2.2.1 General Flame Structure

An insight into the structure of premixed laminar flames, i.e., selected species mole fractions and temperature over distance x, is given by Figure 2.5 based on a lean combustion of DME/air ($\Phi = 0.83$, 1 atm). Traces presented in Figure 2.5 are extracted from the simulation of a freely propagating adiabatic flame introduced later in section 5.2.3 and are presented here in an equal manner as done for H_2 fuel in Warnatz et al. [165, p. 121] or qualitatively for CH_4 in Peters [127, p. 27]. As expected, reactant species (DME and O_2 in Figure 2.5) monotonically decrease while products (CO_2 and H_2O in Figure 2.5) and temperature monotonically rise over the flame front. Intermediates (only CO shown in Figure 2.5 as example) peak within the reaction area. For the case presented in Figure 2.5, at atmospheric pressure, most reaction progress appears in a narrow spatial range of several hundred microns. As discussed by Peters [127, p. 26 f.] for methane/air, the structure of premixed flames can be subdivided into (1) a *preheating zone*, (2) the *fuel consumption* or *inner layer* and (3) the *oxidation layer*. The fuel consumption layer maintains the reaction and in case this layer is impacted by turbulence, it will affect the entire structure of the flame [127, p. 27]. Peters [127, p. 28] estimates the fuel consumption layer's thickness to $\approx 18\ \mu$m for his presented methane/air flame, which is only a fraction of the flame thickness $l_F \approx 175\ \mu$m ($\Phi = 1.0$, 1 atm). In turn, l_F can be defined from scaling laws by thermal diffusivity of fresh gas and laminar flame speed as D_{th}/u_F describing a *diffusive thickness* [128, p. 56]. Poinsot and Veynante [128, p. 57] suggest a practical definition for a *thermal thickness* of premixed flames (most appropriate for mesh resolution in simulation) by

$$l_F = \frac{T_{burnt} - T_{fresh}}{\max(|\frac{\partial T}{\partial x}|)} \tag{2.31}$$

from the temperature difference between burnt and fresh gas, and maximum absolute value of its spatial gradient. From Figure 2.5 it is approximated to $l_F \approx 400\ \mu$m.
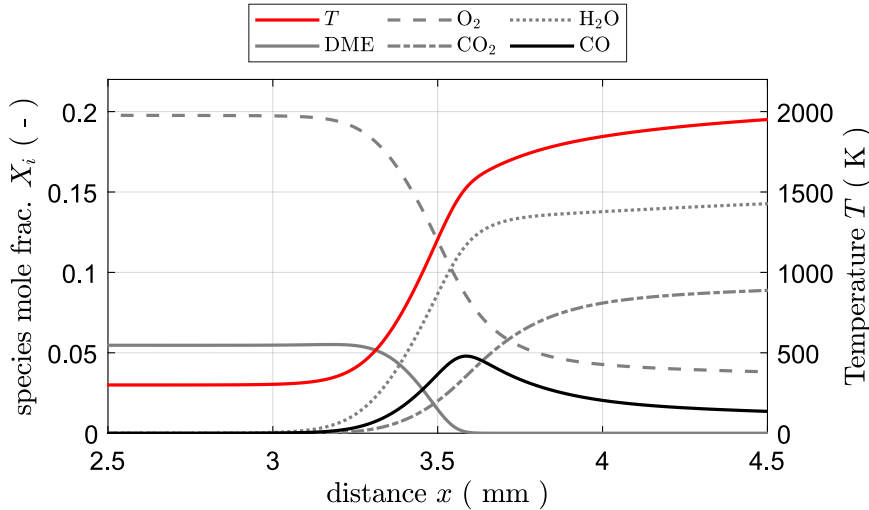
Figure 2.5: Structure of a premixed laminar flame for lean DME/air combustion at $\Phi = 0.83$ and 1 atm with selected species over distance x. Extracted from the numerical simulation of a freely propagating adiabatic flame introduced in section 5.2.3.

2.2.2.2 Classification of Turbulent Combustion Regimes

A prominent approach for the classification of premixed turbulent combustion regimes was introduced in the mid-1980s by Peters [126]. It modified a version originally proposed by Borghi [24] and, for this reason, is commonly referred to as the *Borghi-Peters diagram* in the combustion community. It features the capability to evaluate the regimes of a studied case with respect to the *flamelet*-concept, that is broadly used in numerical combustion simulation. According to the definition of Peters [127, p. 43], a *flamelet* describes a thin layer covering both reaction and diffusion processes that is located in a flow field. In other words, flamelets are meant to describe the local chemical reaction and diffusion in a combustion flow device. As previously pointed out in section 2.2.2.1 on the structure of premixed flames, most reaction activity is apparent in the thin fuel consumption layer, where very fast reaction is assumed [127, p. 43]. In case the fuel consumption layer is smaller than the Kolmogorov scale η of the flow, the local reaction is not affected (e.g. extinguished) by corresponding vortices and laminar flamelets can be assumed valid [127, p. 43]. From an experimental point of view, the Borghi-Peters diagram is thus considered valuable for an initial estimation of combustion regimes prior to set up a corresponding numerical simulation. Here, the regime diagram proposed in Peters [126] is used, but complemented with the descriptions in Borghi [24] for interpretation.

A blank Borghi-Peters diagram is visualized in Figure 2.6. The log-log diagram features a normalized scale measure l_t/l_F on the abscissa, while a normalized velocity u'/u_F spans the ordinate [126]. According to Peters [126] the numerator of the normalized length scale, l_t, describes a macroscopic, energy-containing length scale. This is consistent with the integral length scale, as stated by Borghi for this parameter [24]. Thus, the integral length scales L_{ii}, as introduced in section 2.1.2.1, can be used to quantify this variable. The numerator of the normalized velocity, denoted u', comprises statistically determined flow velocity fluctuations [24, 126]. Borghi [24] for example claims u' to be the square root of the turbulent kinetic energy that should contain an impact of combustion. The denominators of the normalized quantities are defined to be the laminar flame thickness l_F and laminar flame speed u_F. This is equally specified in both Peters [126] and Borghi [24]. Based on the normalized length and velocity scales, combustion regime boundaries in the regime diagram are defined by the following equations, taken from Peters [126]:

$$u'/u_F = Re \cdot (l_t/l_F)^{-1} \tag{2.32}$$

$$u'/u_F = Da^{-1} \cdot (l_t/l_F) \tag{2.33}$$

$$u'/u_F = Ka^{2/3} \cdot (l_t/l_F)^{1/3} \tag{2.34}$$

$$u'/u_F = 1 \tag{2.35}$$

Equations (2.32) to (2.35) feature the turbulent Reynolds (Re), Karlovitz (Ka) and Damköhler number (Da) and present the boundaries for separating the combustion regimes if the representative dimensionless quantity is set to unity [126]. Thus, the boundaries in Figure 2.6 are defined for $Re = 1$, $Da = 1$ and $Ka = 1$. Following the previously introduced Equation (2.25), the turbulent Reynolds number Re is defined using u' and l_t as characteristic velocity and length scales [126]. Correspondingly, turbulent Karlovitz and Damköhler numbers are given by $Ka = t_F/t_K$ and $Da = t_t/t_F$ from characteristic

time scales of the laminar flame t_{F} (flame time; depicts the laminar reaction), the macroscopic turbulent motion t_{t} and Kolmogorov time scale t_{K} [126]. A powerful feature of this regime diagram is that the interpretation of the used dimensionless quantities allows a direct conclusion on the existing flame structure and the reaction-flow coupling.

The region of *laminar flames* is mapped for $Re < 1$ [126]. The name suggests that the combustion characteristics are rather associated with a classical laminar behavior than a turbulent, means that neither the present fluctuation velocities nor the length scales of large eddies are big enough to significantly disturb, deform or stretch the flame front. This kind of flame-flow interaction is visualized by ① in Figure 2.6. For $Re > 1$, $Ka < 1$ and $Da > 1$, Peters [126] defines the so-called *flamelet regime* that is sub-classified into *corrugated flamelets* ($u'/u_{\text{F}} > 1$) and *wrinkled flamelets* ($u'/u_{\text{F}} < 1$) by Equation (2.35). Following the interpretation of Peters [126], $Ka < 1$ implies a low level of flame stretch and $Da > 1$ indicates fast reaction, while $Re > 1$ captures the turbulent character of the flow. This means that the flame front in this regime is mildly stretched by turbulent eddies causing a smooth wrinkling but the reaction progress is still faster than the disturbances by the flow. The closer states are getting to the $Ka = 1$ boundary, the more wrinkled their reaction zone gets. Consequently, the regime of corrugated flamelets features a higher degree of flame front wrinkling than the wrinkled flamelets do, as visualized by ② and ③ in Figure 2.6. The next regime is named *disturbed reaction zones* with dimensionless quantities defined to $Re > 1$, $Ka > 1$ and $Da > 1$ [126]. In contrast to the flamelet regime, the turbulent Karlovitz number further increases. According to Peters [126], the related increased flame stretch leads to eddies penetrating the flame front, causing a broadening of the reaction zone as well as local quenching. This is shown by pictogram ④ in Figure 2.6. Finally, $Re > 1$ and $Da < 1$ defines the *well-stirred reactor* regime [126]. Following the above interpretations, the $Da < 1$ relation implies that the time scales of the turbulent flow are smaller than those of reaction, i.e., of the laminar flame. This means that the flow is capable to break up the reaction zone in multiple small local reaction areas before it reaches the fully reacted state, as visualized by ⑤ in Figure 2.6.
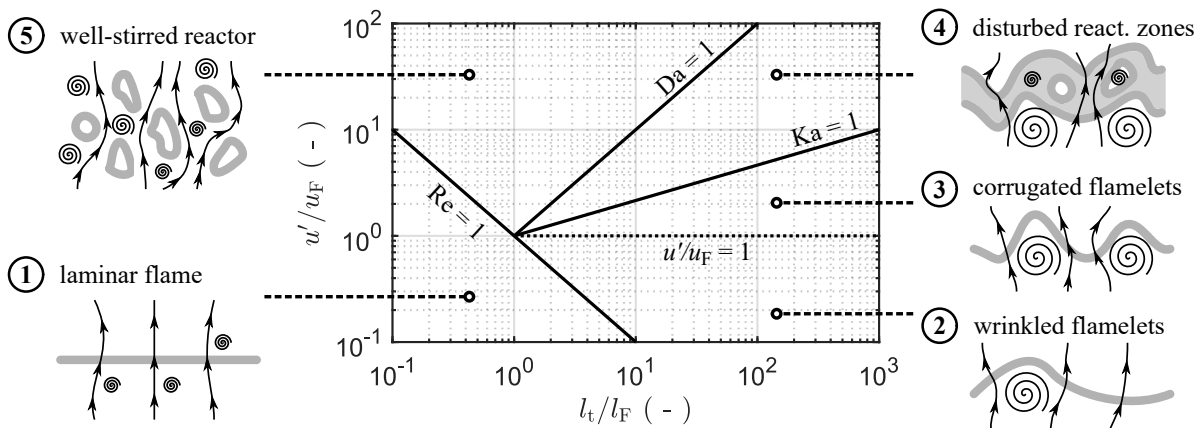
Figure 2.6: Borghi-Peters diagram classification of premixed turbulent combustion regimes, with regime boundaries by Equations (2.32) to (2.35) and visualizations of the flame-flow interaction by numbers ①-⑤. Created from the visualizations and descriptions in [126] (Fig. 7) and adapted by own considerations.

2.2.2.3 Impact of Partial Premixing

Combustion that combines features of premixed and non-premixed operation, e.g., in a stratified mixed medium, is named *partially premixed* and is frequently observed in technical combustion applications, like direct-injection gasoline engines or aviation gas turbines [127, p. 237 ff.]. If the interacting flows of the nonuniform medium are all either lean or rich, excluding the existence of stoichiometric conditions, the case is termed *stratified premixed* and local reaction behaves like premixed combustion, however, with local burning rate fluctuations [19]. If lean, rich and stoichiometric conditions exist within the involved mixtures, local combustion may feature both premixed and non-premixed behavior (called *premixed/non-premixed*) [19]. Partially premixed combustion can also involve novel flame structure phenomena, like so-called *triple flames* [127, p. 245 ff.]. Despite its practical relevance, partial premixing in combustion has not yet been studied in such a detail as the asymptotic cases (premixed or non-premixed). Insight into partially premixed turbulent flames, including a related literature review, is given in Peters [127, p. 237 ff.], Bilger et al. [19] or Masri [111], where the interested reader is referred to.

2.2.3 Flame-Wall Interactions

Combustion in practical technical applications mostly happens in enclosed devices with the presence of walls and thus features the potential for so-called *flame-wall interaction* (FWI) that arises a multitude of technical drawbacks and challenges regarding efficiency, pollutant formation and durability [128, p. 327]. If a flame propagates close to a solid cold surface, near-wall temperature gradients and thus wall heat fluxes become very large, which extracts heat from the flame in the vicinity of the wall and finally leads to a *quenching* of the local chemical reaction progress [128, p. 327]. As pointed out by Poinsot and Veynante [128, p. 328 ff.] FWI involves a complex coupling of wall, flame and turbulence (or more general: flow) that poses many challenges for the modeling in numerical simulation.
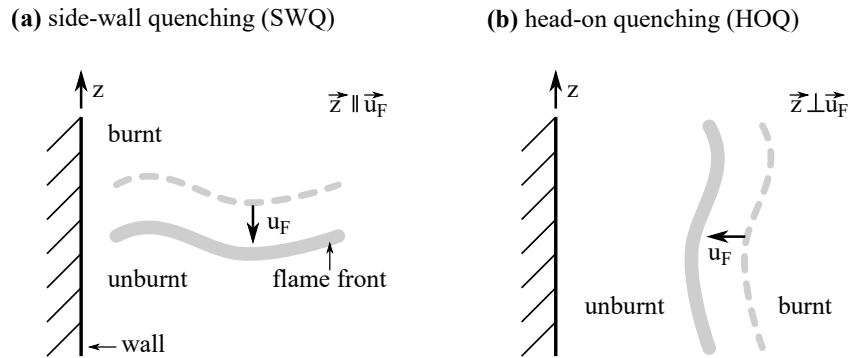
Figure 2.7: Schematic view of the most prominent generic scenarios of flame-wall interaction: (a) side-wall quenching (SWQ) and (b) head-on quenching (HOQ). Created from the visualizations and descriptions in [128, p. 332 f.] (Figure 7.5) and adapted by own considerations.

The phenomenon of flame-wall interaction can manifest in different geometrical configurations [128, p. 332]. Typically, the two generic forms of *side-wall quenching* (SWQ) and *head-on quenching* (HOQ) are discriminated [49], as shown in a schematic view in Figure 2.7. The distinguishing feature is the direction of flame propagation with respect to the wall. In SWQ, the flame front propagates parallel to the quenching wall ($\vec{u_\mathrm{F}} \parallel \vec{z}$) and locally extinguishes at the edge pointing to the wall [128, p. 332]. In contrast, HOQ appears when the flame propagates normal to the quenching wall ($\vec{u_\mathrm{F}} \perp \vec{z}$) and the reaction front extinguishes when reaching close to the surface [128, p. 332]. These events can exist in both stagnant or convective (laminar or turbulent) gas mixtures [49]. Besides SWQ and HOQ, Dreizler and Böhm [49] as well as Poinsot and Veynante [128, p. 333] classify *tube quenching*, while Warnatz et al. [165, p. 279 f.] briefly mention extinction in gaps. These additional configurations are rather associated with safety engineering, e.g., as flame arrestor application, than classical combustion engineering [49].

There are various measures that aim to describe and characterize near-wall quenching phenomena. For a first phenomenological description, two commonly used parameters are (1) the spatial distance between the flame and wall, (2) the wall heat flux, both typically evaluated in a normalized way and for quenching conditions [128, p. 330]. Quenching distances l_Q, i.e., the distance from the wall where the reaction extinguishes, can be expressed in a normalized way in terms of so-called *quenching Peclet numbers*

$$Pe_\mathrm{Q} = \frac{l_\mathrm{Q}}{l_\mathrm{F}} \tag{2.36}$$

with reference to a characteristic flame thickness l_F [128, p. 330 f.]. On the one hand, such a normalization suggests certain robustness to compare FWI results of different origin. On the other hand, Dreizler and Böhm [49] pointed out that different definitions of the flame thickness l_F, e.g., diffusive or thermal thickness introduced in section 2.2.2.1, can lead to deviations in this Peclet number. Typical quenching Peclet numbers are reported in the order of $Pe_\mathrm{Q} \approx 7$ for SWQ and $Pe_\mathrm{Q} \approx 3$ for HOQ phenomena [128, p. 332 f.]. In turn, the normalized wall heat flux is given by

$$\dot{Q}_\mathrm{W} = \frac{| -\lambda \cdot \frac{\partial T}{\partial y}\big|_\mathrm{W} |}{\rho \cdot Y_\mathrm{fuel} \cdot u_\mathrm{F} \cdot Q_\mathrm{R}} \tag{2.37}$$

with the instantaneous wall heat flux in the numerator (index W: at the wall) normalized by the so-called *flame power* of the laminar case in the denominator (density ρ and fuel mass fraction Y_fuel of fresh gas, laminar flame speed u_F, reaction heat Q_R) [128, p. 330 f.]. Specifically for quenching conditions, it is possible to relate the resulting wall heat flux $\dot{Q}_\mathrm{W,Q}$ to the corresponding quenching Peclet number Pe_Q, as outlined by Poinsot and Veynante [128, p. 332]. During quenching, a minimum in the Peclet number is observed along with a maximum in the normalized wall heat flux [128, p. 331].

However, studying FWI expands far beyond the above mentioned parameters for phenomenological description, as evident from the literature review given in section 1.1. For example, advanced studies dealt with the three-dimensional flow field or assessed detailed thermochemistry. For further insights into FWI, the reader is referred to the works of Dreizler and Böhm [49] for an experimental point of view using laser diagnostics as well as Poinsot and Veynante [128, p. 327 ff.] with scope on numerical simulation.

2.3 Laser Diagnostic Fundamentals

This fundamental section on laser diagnostics initially gives a brief insight into the underlying principles from quantum mechanics and lasers. Subsequently, basics on the application of the laser diagnostics used within this thesis are outlined in more detail.

2.3.1 A Brief Insight into Quantum Mechanics

Since quantum mechanics is a very extensive and highly complex subject, the following outlines will only cover some uttermost basic aspects to aid understanding of the applied laser spectroscopy descriptions in the remainder. For a deeper insight, the reader is referred to common textbooks, as presented by Elstner [54] or Hanson et al. [71].

A first important point to consider in a quantum mechanical view is that internal energy of all matter (i.e., atoms or molecules) is *quantized* in certain quantum states, which in turn feature discrete values of energy as well as angular momentum [71, p. 1]. This quantized internal energy of matter is composed of contributions from rotational (E_r), vibrational (E_v) and electronic energy (E_e) [71, p. 1], with varying magnitude in energy difference within each class ($\Delta E_\mathrm{r} < \Delta E_\mathrm{v} < \Delta E_\mathrm{e}$) [71, p. 3 f.]. This is schematically depicted by the energy structure of matter in Figure 2.8(b).

Another basic aspect in quantum mechanics is covered by *Planck's law*, which defines a photon's energy

$$E_\mathrm{ph} = h \cdot \nu = h \cdot \frac{c}{\lambda} = h \cdot c \cdot \omega = h \cdot c \cdot \tilde{\nu} \tag{2.38}$$

from Planck's constant $h = 6.63 \cdot 10^{-34}$ Js and its frequency ν (dimension t^{-1}), or speed of light $c \approx 3 \cdot 10^8$ m/s and wavelength λ (dim. l) or wavenumber ω, $\tilde{\nu}$ (dim. l^{-1}) [71, p. 3 ff.]. While the consideration of radiation as a photon involves the idea of a particle, parameters like ν, λ or ω are associated with the idea of electromagnetic waves, i.e., Equation (2.38) describes the coexisting particle- and wave-character of radiation [71, p. 3]. This property is commonly referred to as the *wave-particle dualism* in quantum mechanics.
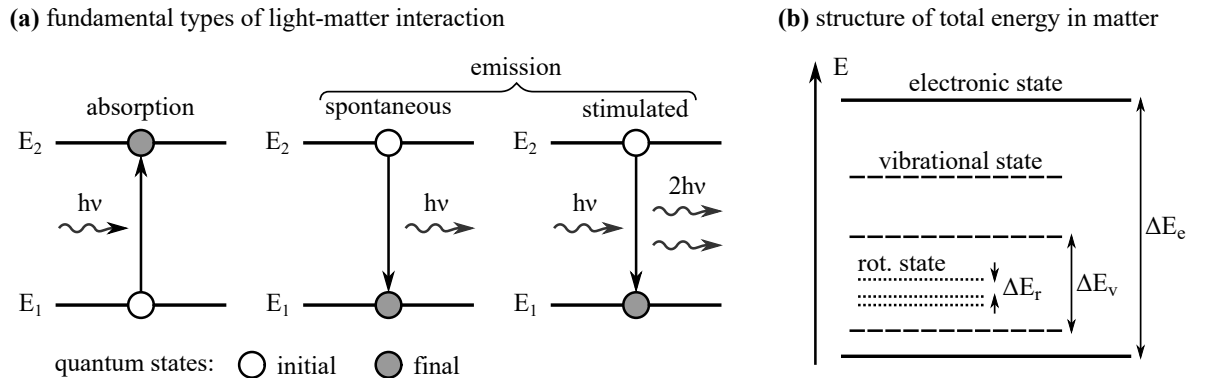
Figure 2.8: Schematic of (a) basic types of light-matter interaction and (b) structure of internal energy in matter. Created from the visualizations and descriptions in [133, p. 29] (Fig. 2.17) as well as descriptions in [71, p. 3 ff.] and adapted by own considerations.

A further important point is that matter may undergo interaction with photons. The principles can be depicted by a simplified energy scheme shown in Figure 2.8(a) featuring two quantum states at different energies E_1 (lower) and E_2 (upper). In accordance with Equation (2.38), the energy gap between the two quantum states needs to correspond the energy of interacting photons ($\Delta E = E_2 - E_1 = h \cdot \nu$). Typically, three fundamental types of light-matter interaction are distinguished [133, p. 29]:

1. *absorption*: An incident photon with energy ΔE transfers the system from a lower (E_1) to an excited energetic state (E_2).

2. *spontaneous emission*: The excited system (E_2) releases energy ΔE by emission of a corresponding photon and returns to a lower energetic state (E_1).

3. *stimulated emission*: An incident photon with energy ΔE induces the system to transfer from an excited (E_2) to a lower energetic state (E_1) by releasing a second photon, coherent to the incident one.

As outlined in Raffel et al. [133, p. 30 ff.], the interaction path of stimulated emission enables laser operation (together with the so-called *population inversion*, i.e., the higher energetic state has a larger population than the corresponding lower energetic state).

Moreover, the distribution of quantum states within a certain atomic or molecular species under equilibrium conditions is given by the *Boltzmann distribution* [71, p. 8]. With respect to occupation of the i-th level of energy E_i, the Boltzmann fraction yields

$$f_i = \frac{g_i \cdot e^{-E_i/(k \cdot T)}}{\sum_j g_j \cdot e^{-E_j/(k \cdot T)}} \tag{2.39}$$

depending on degeneracy factors g_i (number of quantum states with same energy), the temperature T [71, p. 8] and Boltzmann's constant $k = 1.38 \cdot 10^{-23}$ J/K [136, p. 25].

Since a specific notation is commonly applied for description of quantum states in diatomic molecules, which is used later in the text for some laser diagnostic implication, it will be briefly introduced. Overall states can be described in the notation

$$^{2S+1}\Lambda_{\mathrm{g/u}}^{+/-} \tag{2.40}$$

which are the so-called *term symbols* [54, p. 615]. Here, Λ depicts the total angular momentum $\Lambda = |\sum m_l|$ by summing up the orbital angular momentum of all involved electrons m_l, and resulting Λ-values 0, 1, 2,... are assigned to symbols Σ, Π, Δ, and so on [54, p. 615]. Furthermore, $2S+1$ describes the spin multiplicity, subscripts "g" and "u" capture inversion symmetry of the wave function, while superscript signs $+/-$ specify if there is a change of sign in the wave function ($-$) or not ($+$) [54, p. 615]. A more detailed description of this notation is beyond the scope of this thesis and can be found in the textbook of Elstner [54, p. 614 ff.].

2.3.2 Laser Diagnostics Application

The term *laser* is originally an acronym that stands for *light amplification by stimulated emission of radiation* [136, p. 4]. The experimental demonstration of the first working laser source is attributed to the work of T. H. Maiman [109] in 1960, who presented a flash lamp-pumped, coherently emitting ruby laser [43, p. 271].

The main features of radiation emitted from a laser source are its *coherence* in space and time as well as the high degree of directionality [136, p. 3]. Basically, a working laser requires three main components [43, p. 271 f.], as shown in Figure 2.9: (1) a laser-active medium that is capable to realize the above mentioned *population inversion* with larger population of a higher energetic state compared to the lower energetic state; (2) an energy pumping mechanism that generates and maintains the population inversion; (3) an optical resonator that forces spontaneous emission processes in the medium towards stimulated, amplified emission along the resonator axis. However, practical laser implementation is much beyond those three main elements and numerous different realizations are possible, depending on the individual application, e.g., if the laser-active medium has gaseous, liquid or solid state, or if continuous wave or pulsed laser operation is desired. As mainly commercially available Nd:YAG solid-state and dye lasers are used for the applied diagnostics in this thesis, a detailed description of the underlying technology is omitted at this point. For technical insights on the laser principle, the interested reader is referred to the textbook of Renk [136].

Using laser radiation for diagnostic purpose is accompanied with numerous advantages. First, it can provide extremely high resolution in space (as the radiation is well-focusable) and time (if a short-pulsed laser is applied, e.g., with nanosecond pulse width). Second, laser radiation probes an investigated system non-intrusively. Third, laser techniques are highly selective. A comprehensive overview on numerous laser spectroscopy techniques is given in the textbooks of Demtröder [44] or Hanson et al. [71] for example.

Within the scope of this thesis, the applied diagnostics comprises the techniques *particle image velocimetry* (PIV), *coherent anti-Stokes Raman spectroscopy* (CARS) including the special implementation of *dual-pump* CARS (DP-CARS), *laser-induced fluorescence* (LIF) and *thermographic phosphor thermometry* (TPT). Those diagnostic approaches will be further outlined in the following.
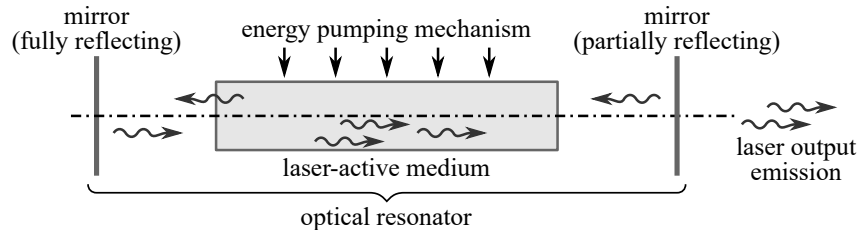
Figure 2.9: Schematic of the three main components required for laser operation. Created from the visualizations and descriptions in [43, p. 271 f.] (Fig. 8.1 and 8.4) and adapted by own considerations.

2.3.2.1 Particle Image Velocimetry (PIV)

As the name *particle image velocimetry* (PIV) inherently suggests, this experimental technique provides a measure of velocity by means of imaging particles. A schematic for the PIV principle is shown in Figure 2.10 that comprises both a draft of an optical setup (a) and a brief graphical description of the data evaluation (b). Following the outlines of Raffel et al. [133, p. 4 ff.], a working PIV system requires several aspects:

1. Small particles to trace the velocity, often called *seeding* particles, need to be dispersed to the fluid flow under investigation, provided they are not already present in a sufficient manner (e.g., as possible in multi-phase flows). Reacting environments require thermally stable and chemically inert particles, like metal oxides [133, p. 25].

2. An illumination of these dispersed particles in a plane or volume by a light source has to be done that yields at least two consecutive exposures of the particles in the flow within a short time separation Δt.

3. A spatially resolved detection of the resulting scattered emission is required.

4. A data processing is needed that derives the local particle displacement $\Delta \vec{x}$ between the consecutive exposures and together with Δt finally assesses a corresponding projected velocity $\mathbf{U}$ of the flow field, on small spatial *interrogation windows* (IRWs).

As PIV is an indirect approach that assesses the flow velocities via velocity of tracer particles, their properties are of particular importance for the technique [133, p. 15]. In order to estimate the suitability of tracer particles for a certain fluid, a *relaxation time*

$$t_\mathrm{R} = \frac{d_\mathrm{P}^2 \cdot \rho_\mathrm{P}}{18 \cdot \mu_\mathrm{F}} \tag{2.41}$$

can be given that describes a measure for the time required for velocity equilibrium between particles and fluid (particle diameter d_P and density ρ_P; dynamic viscosity of the fluid μ_F) [133, p. 16]. In other words, t_R is the time that passes until a particle again follows the fluid motion after a rapid change in flow. This suitability on temporal response of tracer particles actually needs to be assessed for each individual flow configuration.
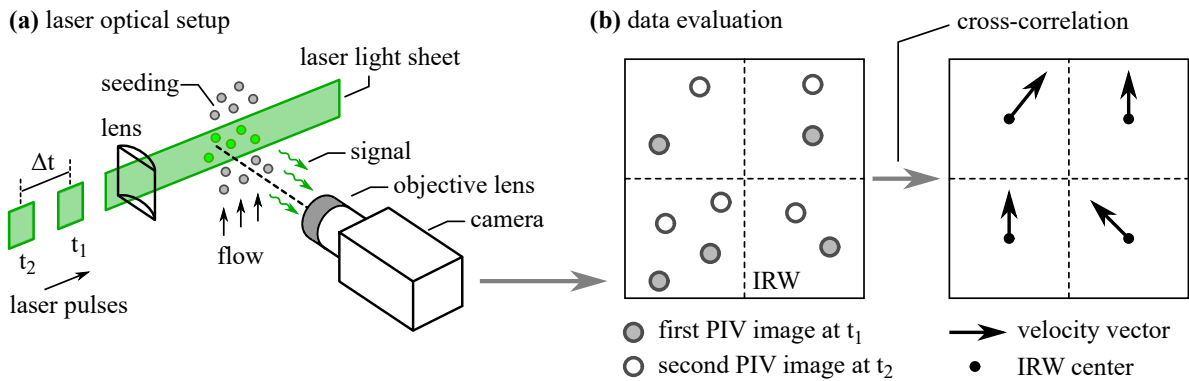
Figure 2.10: Schematic of the PIV principle. Created from the visualizations and descriptions in [133, p. 4 ff.] (Fig. 1.4) and adapted by own considerations.

From the outlines in Raffel et al. [133, p. 16 ff.] it appears practicable to use tracer particles in the physical order of a micrometer for gas phase flows. The smaller the particles are, the better their ability to correctly trace the fluid motion, however, too small diameters d_P impact the light scattering properties [133, p. 16]. Thus, the scattering behavior is another important aspect to consider with respect to the tracer particles. For small particles, it is a function of involved refraction indices (particle and fluid), particle geometry (size, shape and orientation), polarization of incident light and observation angle of detection [133, p. 18]. Typically, these properties are discussed by means of the Mie scattering theory, valid for spherical particles with $d_P > \lambda$ (λ: laser wavelength), and the scattered intensity features an observation angle dependency with approximately $\pi \cdot d_P / \lambda$ local angular maxima [133, p. 18], whereas the average energy of scattered light is proportional to $(d_P / \lambda)^2$ [133, p. 51]. While an increase in d_P implies larger scattering intensities, the scattered light emission also becomes more susceptible to the selection of observation angle [133, p. 19]. This tradeoff needs to be further considered for proper selection of seeding particles. Technical approaches on how to disperse particles to flows are outlined in Raffel et al. [133, p. 21 ff.].

For illumination, lasers are commonly applied due to their coherent properties as well as high output energies and formed to planar light sheets or volumes by different combinations of cylindrical and/or spherical lenses [133, p. 28 ff.]. Following Raffel et al. [133, p. 97 ff.], two major types of recording approaches are available: the first one uses a single camera frame to record multiple illuminations of the particles, the second one uses a separate frame for each illumination (e.g., laser pulse). The latter approach is preferable, as it directly preserves the temporal order of particle information, i.e., which particle image belongs to which illumination, and is easier to process [133, p. 97]. It covers the commonly used concept of *singly illuminated double frames*, i.e., two consecutive camera frames, each capturing one of two consecutive laser illuminations of the particle field. Nowadays, detection is mainly done by digital CCD or CMOS cameras with various chip architectures, as comprehensively summarized in Raffel et al. [133, p. 101 ff.].

The evaluation of singly illuminated double frame digital PIV raw images is done by means of discrete cross-correlation functions

$$R(\Delta x, \Delta y) = \sum_{i=-K}^{K} \sum_{j=-L}^{L} I_1(i,j) \cdot I_2(i + \Delta x, j + \Delta y) \qquad (2.42)$$

to detect the best match between consecutive particle images I_1 and I_2 (intensity values) on a local IRW [133, p. 133 f.]. For a certain range of possible shifts Δx and Δy, the maximum correlation value $R(\Delta x, \Delta y)$ is assessed and the corresponding shifts finally describe a measure for the particle displacement $\Delta \vec{x}$ [133, p. 134]. As stated above, the displacement can be turned into a velocity information by relating it to the known time separation Δt.

In general, there are lots of aspects to consider for proper PIV experiments. For a detailed insight into PIV fundamentals and these application related aspects the reader is referred to the comprehensive textbook of Raffel et al. [133]. In the past years, the PIV diagnostic has widely been used in combustion studies with different implementations and for various applications, as recently reviewed by Chen and Liu [33] for example.

2.3.2.2 Coherent anti-Stokes Raman Spectroscopy (CARS)

Coherent anti-Stokes Raman spectroscopy (CARS) is a *four-wave parametric mixing process* and classified as a nonlinear Raman spectroscopy approach [44, p. 169]. For high incident light intensities, the dipole moments $p(\vec{E})$ induced in molecules become a nonlinear function $\propto \vec{E}^n$ of higher orders n of the electric field $\vec{E}$ that cannot be neglected [44, p. 161 f.]. For N oriented dipoles, the overall medium's polarization is then given by $\vec{P}(\vec{E}) = N \cdot \vec{p}(\vec{E})$ [44, p. 162]. In turn, this polarization

$$\vec{P}(\vec{E}) = \epsilon_0 \left\{ \chi^{(1)}\vec{E} + \chi^{(2)}\vec{E} \cdot \vec{E} + \chi^{(3)}\vec{E} \cdot \vec{E} \cdot \vec{E} + ... \right\} \tag{2.43}$$

describes the nonlinear reaction of the medium resulting on incident electric fields $\vec{E}$, with the vacuum permittivity ϵ_0 and susceptibility tensors $\chi^{(n)}$ (rank $n + 1$) [53]. The electrical susceptibility $\chi^{(1)}$ describes physical effects like light absorption or spontaneous Raman scattering, $\chi^{(2)}$ is responsible for frequency doubling of incident waves (i.e., second harmonic generation) but vanishes in isotropic media (e.g., fluids or symmetric crystals), while the $\chi^{(3)}$ tensor causes processes like third harmonic generation or CARS [53]. The medium's nonlinear polarization, as proposed in Equation (2.43), basically features the potential to generate new waves [44, p. 168 f.].

In CARS, three electric fields (pump and probe beams: ω_{P1}, ω_{P2}; Stokes beam: ω_S) interact with a medium and cause its third-order polarization that generates a coherently scattered forth wave at the anti-Stokes frequency

$$\omega_{aS} = \omega_{P1} + \omega_{P2} - \omega_S \tag{2.44}$$

whereat the difference of pump and Stokes frequency $\omega_{P1} - \omega_S$ should match Raman active transitions ω_R [53]. The corresponding energy scheme of the CARS process is shown in Figure 2.11(a). First, the pump beam ω_{P1} transfers the system from its energy ground state $|v,J\rangle$ to a virtual energy level and the Stokes beam ω_S subsequently forces a transition to the rotational-vibrational state $|v',J'\rangle$, followed by another transfer to a
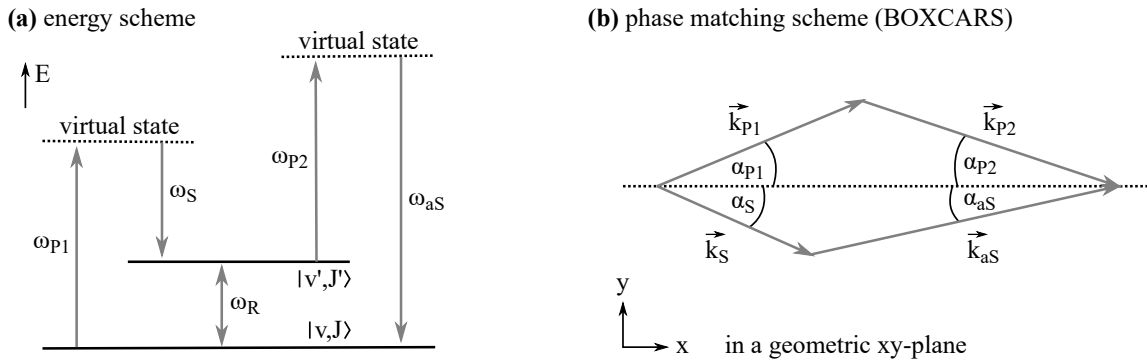
Figure 2.11: Schematic of the CARS principle: (a) energy scheme for single-photon interaction and (b) phase matching scheme in terms of a planar BOXCARS arrangement. Created from the visualizations and descriptions in [53] (Fig. 1 and 3) as well as [139] (Fig. 1) and adapted by own considerations.

virtual level induced by ω_{P2} that finally results in the anti-Stokes emission at ω_{aS} by returning back to the energy ground state $|v,J\rangle$ [53]. In addition to this energy scheme, the so-called *phase matching* condition needs to be met for CARS. It can be described by the phase mismatching

$$\Delta\vec{k} = \vec{k}_{P1} + \vec{k}_{P2} - \vec{k}_{S} - \vec{k}_{aS} \tag{2.45}$$

from corresponding wave vectors $\vec{k}$ and should become $\Delta\vec{k} = 0$ for an ideal phase matching [53]. A schematic for *planar BOXCARS* phase matching is given by Figure 2.11(b) and the required phase matching angles α_i can be calculated from the drawn geometrical configuration. Other phase matching arrangements are *collinear CARS* (all beams overlapped on one path; simplest application at high anti-Stokes signal; bad spatial resolution), *folded BOXCARS* (three-dimensional overlap of beams; smaller anti-Stokes signal; good spatial resolution), as shown in El-Diasty [53], or *USED CARS* phase matching (USED: unstable-resonator spatially enhanced detection) that utilizes the annularly shaped output of pump lasers with unstable resonator [28,51]. Equations (2.44) and (2.45) describe energy and momentum conservation for the CARS process, respectively. The CARS signal intensity, i.e., the anti-Stokes intensity, and its parameter dependencies can be expressed by

$$I_{CARS} \propto \frac{\omega_{aS}^2}{c^4} \cdot \left[\chi^{(3)}(\omega_{P1} - \omega_{S})\right]^2 \cdot I_{P1}I_{P2}I_{S} \cdot L^2 \cdot \left\{\frac{\sin(\Delta k L/2)}{\Delta k L/2}\right\}^2 \tag{2.46}$$

with vacuum speed of light c, laser intensities I and interaction length L [53,74]. The two major recording modes to acquire CARS spectra, i.e., I_{CARS} as function of ω_{S}, are [53]: (1) *scanning CARS*, where a narrowband dye laser is used to scan ω_{S} step by step and the signal is captured by a single-channel detector (e.g., photodiode or photo multiplier tube); (2) *broadband CARS* that uses a broadband dye laser to instantaneously cover the entire spectral range required for ω_{S} and a multi-channel detector (allows single-shot realizations). The latter approach is the method of choice for practical combustion environments that feature transient behavior.

An example for a common optical CARS setup is shown in Figure 2.12. A lens focuses the incident laser beams to a probe volume (interaction length L) where the coherent anti-Stokes signal is locally induced (shown in blue). It is then collimated by another lens, guided to a multi-channel detector (spectrometer and camera) and additionally conditioned by optional filters, e.g., to reject remaining pump or Stokes laser radiation or to attenuate too high intensities. For diagnostic purpose, CARS spectra can be evaluated in terms of thermometry, as the temperature-dependent Boltzmann distribution for equilibrium conditions directly determines the population of rotational and vibrational states measured in frequency domain, and species concentrations can be assessed via the proportionality $I_{CARS} \propto N^2$ for a probed species [139]. Evaluation of recorded CARS data is typically done by spectral fitting algorithms, like for example by the widely known CARSFT code [122], the algorithm to fit WIDECARS spectra by Cutler et al. [40] or the MARSFT code proposed by Greifenstein and Dreizler [68].

A detailed description of further theoretical and practical aspects on CARS is given in the comprehensive articles by Druet and Taran [50], Roy et al. [139] as well as El-Diasty [53], where the reader is referred to for a deeper insight. The CARS diagnostic has been used frequently in the past decades for combustion studies. Recent advances in
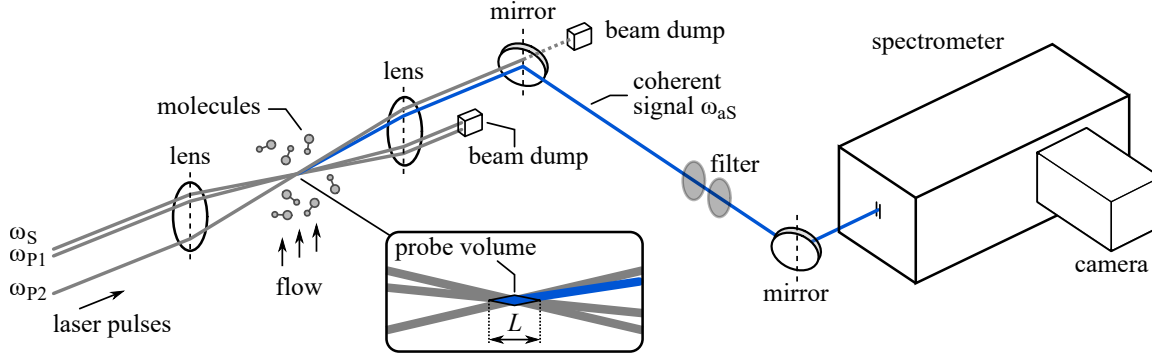
Figure 2.12: Typical optical setup for nanosecond, single-shot, broadband CARS using a planar BOXCARS phase matching. Based on the setup used in this thesis that is introduced later in section 5.2.1.1 and Figure 5.2.

this context were summarized by Roy et al. [139], who broadly covered developments and applications on nano- (including dual-pump CARS), pico- and femtosecond CARS. The application of nanosecond CARS lately emerged to the development of so-called *width-increased dual-pump enhanced CARS* (WIDECARS), which employs a Stokes laser with increased spectral width and facilitates simultaneous measurement of temperature and most major species concentrations in combustion (N_2, O_2, H_2, CO, CO_2, C_2H_4) [40, 159]. While conventional nanosecond CARS approaches mainly provided pointwise information, femto-/picosecond approaches recently extended the CARS diagnostic to highly resolved one-dimensional [20, 22, 23] or even two-dimensional [21] instantaneous, single-shot measurements in combustion environments.

Dual-Pump CARS (DP-CARS)   As this thesis applies the dual-pump CARS (DP-CARS) technique to target both the N_2 and CO_2 molecules, this approach is further outlined in the following. Especially, N_2 is a suited species to probe for thermometry in combustion systems using air as the oxidizer [139]. In general, DP-CARS is characterized by the use of two spectrally different pumping beams with the purpose to measure CARS spectra of two molecular species within a close frequency range at a time [103, 104]. The first presentation of DP-CARS is ascribed to R. E. Teets ("Laser mode effects on coherent anti-Stokes Raman spectroscopy"; presented at the First International Laser Science Conference, Dallas, Texas, November 18-22, 1985), as stated in [103, 139, 160], however, he used two fixed pumping frequencies, which strongly limited the potential molecular species to probe [139]. Shortly after, a more flexible and frequently used DP-CARS approach was introduced by Lucht [103], where the two pump beams were supplied by the second harmonic of an Nd:YAG laser ($\lambda_{P1} = 532$ nm, $\omega_{P1} = 18800$ cm^{-1}) and a narrowband, tunable dye laser (grating tuned to $\lambda_{P2} \approx 555$ nm, $\omega_{P2} \approx 18000$ cm^{-1}). Along with a broadband dye laser as Stokes beam (centered at $\lambda_S = 607$ nm, $\omega_S = 16470$ cm^{-1}), he demonstrated the capability to simultaneously capture the transitions of both N_2 around 2330 cm^{-1} ($\approx \omega_{P1} - \omega_S$) and O_2 around 1556 cm^{-1} ($\approx \omega_{P2} - \omega_S$) on a single detector, measured in a cell (400 K, 1.6 atm). As stated by Roy et al. [139], this three-laser DP-CARS approach is highly flexible and capable to target nearly any combination

of two molecular species. With spectral modifications, it has been demonstrated to probe three species at a time in flames, like $N_2/O_2/CO$ [18], $N_2/O_2/H_2$ [119] or $N_2/H_2/CO$ [166], to only name a few. This experimental three-laser setting (first pump: Nd:YAG at $\lambda_{P1} = 532$ nm; second pump: narrowband dye; Stokes: broadband dye centered around $\lambda_S = 607$ nm) is also capable to simultaneously target N_2 and CO_2 (around 1380 cm^{-1}, conforms the symmetric stretch vibrational mode [71, p. 67 ff.]) by tuning the wavelength of the narrowband dye laser to $\lambda_{P2} \approx 560$ nm [28, 70, 104, 140]. Thariyan et al. [160] generated their tunable second pump radiation around 561 nm by application of an injection-seeded optical parametric oscillator (OPO) to measure the DP-CARS spectra of the N_2/CO_2 pair.

The concept of DP-CARS can be explained by the energy schematic shown in Figure 2.13 with transitions of N_2 in (a) and CO_2 in (b) respectively. Please note that in contrast to Figure 2.11, a multi-photon process is shown here with consideration of the broadband nature of the Stokes laser (see broadened arrows). The influence of tuning the narrowband dye laser is presented by $\Delta\omega_{P2}$ at the respective virtual states. Basically, a variation $\Delta\omega_{P2}$ leads to a slight spectral shift of the N_2 anti-Stokes signal with respect to the CO_2. The N_2 molecule in Figure 2.13(a) is pumped by the 532 nm beam (ω_{P1}) and probed using the narrowband dye radiation at 560 nm (ω_{P2}), while CO_2 in Figure 2.13(b) is targeted vice versa (pumped: 560 nm, probed: 532 nm) [140]. The resulting anti-Stokes signals of both molecular species are detected around 496 nm [104, 140]. Examples for resulting emission spectra are shown in Figure 2.14 in terms of calculated spectra for fixed mole fractions $X_{N_2} = 0.7$ and $X_{CO_2} = 0.1$ representative for a fully reacted, adiabatic DME/air mixture at $\Phi = 0.83$. These calculations were done using the spectral fitting code of Cutler et al. [40], as referred to in section 5.2.2.1 later, and used for the setting of the experiment described in section 5.2.1.1. At first, it is evident from Figure 2.14 that both N_2 and CO_2 information are spectrally very close and can easily be captured within ≈ 200 cm^{-1}. Furthermore, the impact of temperature is observed. Especially, anti-Stokes intensities of the shown CO_2 transitions decrease quickly when temperature rises. From ambient to adiabatic flame temperatures at constant mole fractions, as depicted in Figure 2.14(a), a total intensity drop (I instead of $\sqrt{I}$) of ≈ 560 times for the N_2 band head at ≈ 2330 cm^{-1}
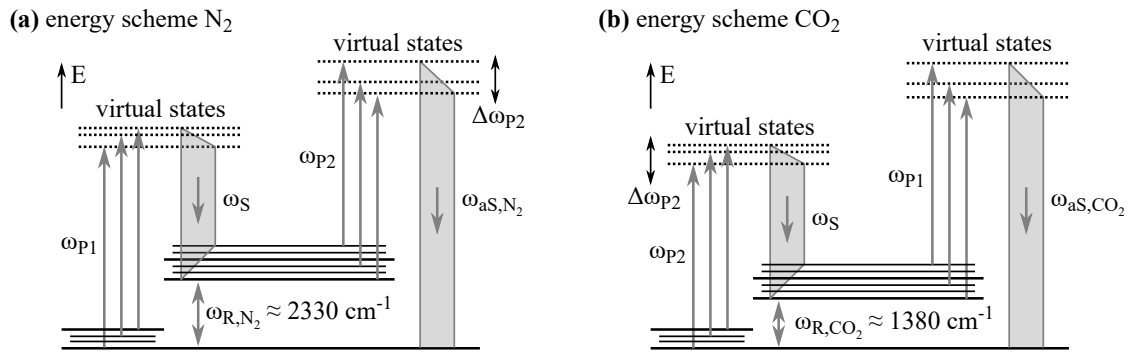
Figure 2.13: Schematic of the DP-CARS principle: energy scheme for (a) N_2 and (b) CO_2, considering multi-photon interaction and broadband Stokes laser. Created from the visualizations and descriptions in [140] (Fig. 2) and adapted by own considerations.

is observed, while the most prominent CO_2 feature near 2374 cm^{-1} drops by a factor of $\approx 1.1 \cdot 10^5$. Of course, the signal intensity is not exclusively determining the mediums response in CARS, but also the spectral pattern. Yet it emphasizes the broad dynamical signal range of the CO_2 anti-Stokes signal that needs to be covered in combustion-related environments. On the other hand, the anti-Stokes CO_2 signal is very strong for lower temperatures and thus promising to evaluate in near-wall combustion, e.g., where the reacting gas is quenched and cooled down by wall heat losses.

From the above outlines, the major advantages of the DP-CARS technique are as follows: (1) a broad variety of possible molecular species combinations can be detected, due to the spectral flexibility provided by the narrowband and tunable second pump source; (2) the molecular species are measured exactly at the same time and location, as their anti-Stokes signals originate from the identical three laser beams [104]; this means that the derived information features excellent correlation, which in turn is a very strong advantage for the thermochemistry study presented in this thesis in chapter 5; (3) the signals of both molecular species are spectrally very close and can be recorded instantaneously using a single detector [103, 104].

2.3.2.3 Laser-Induced Fluorescence (LIF)

Fluorescence describes a radiating transition between electronical states at unchanged total spin S that manifests as spontaneous emission [54, p. 762 f.]. It thus follows the selection rule $\Delta S = 0$ for transitions [54, p. 703], commonly referred to as *spin-allowed* ones. It needs to be mentioned that literature often explains fluorescence based on singlet states (and phosphorescence by including triplet states) [54, 95, 146]. However, transitions between states of higher multiplicity are always possible, as long as they are spin-allowed by the above selection rule. For example, this is true for the CO molecule discussed below,
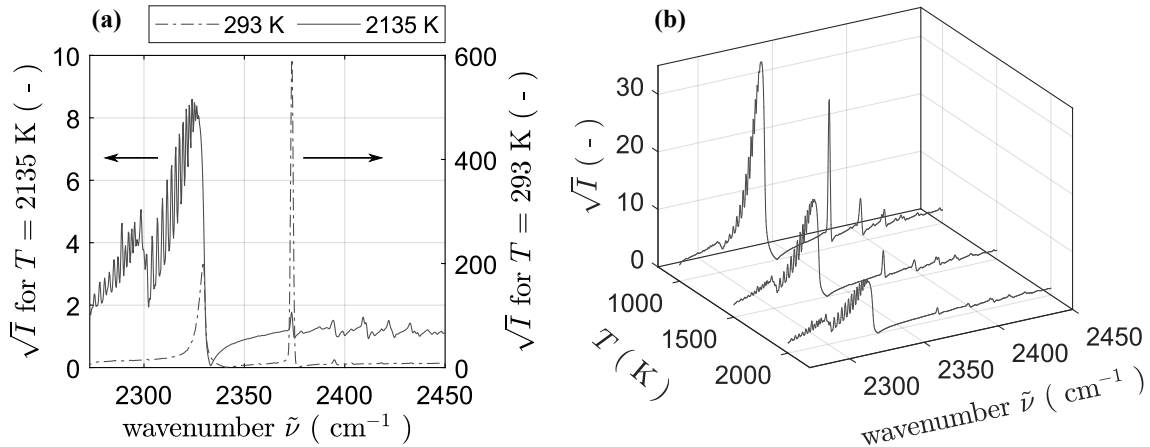
Figure 2.14: Calculated DP-CARS spectra for constant mole fractions $X_{N_2} = 0.7$ and $X_{CO_2} = 0.1$ representative for fully reacted, adiabatic DME/air mixture at $\Phi = 0.83$ (extracted from underlaying data of Figure 2.5): (a) 293 K (ambient temperature) and 2135 K (adiabatic flame temperature) as well as (b) intermediate temperatures 1000 K, 1500 K and 2000 K. Spectral axes given with respect to N_2 Raman shift.

with potential fluorescence emission in the so-called *third positive bands*, which is a triplet-triplet transition and thus satisfies $\Delta S = 0$. For the basic introduction to the phenomenon of fluorescence (and also phosphorescence in section 2.3.2.4) the descriptions are limited to the example of singlet and triplet states here, in accordance with common literature. The fluorescence process can be explained using the energy schematic in Figure 2.15(b) that shows the energy E qualitatively with respect to the distance between atomic nuclei r_n, and numbers ①-⑦ depict major sub-processes for discussion. It needs to be noted that Figure 2.15(b) exemplifies the schematic for a diatomic molecule (more generally referred to as *dimer* in [54, p. 757 f.]) that can be described by one dimension r_n, however, more complex molecules need to consider more degrees of freedom [54, p. 757 f.]. The considerations on electronical states further take into account that the electron mass is much smaller than the mass of corresponding atomic nuclei and therefore both the *Born-Oppenheimer approximation* (electrons do instantaneously follow the atomic nuclei motion, i.e., change in r_n, and feature corresponding steady state) and *Franck–Condon principle* (energy transitions happen vertically at constant r_n) apply [54, p. 758 f.].

By absorption of an incident light photon with energy $h\nu_A$, the system is initially transferred from its ground state S_0 (S: singlet) to an electronically excited state S_1 (higher vibrational level v' typical, see ①) [54, p. 763]. Once the system under study is electronically excited, its energy depopulation is possible on various radiative and non-radiative pathways, as pointed out by Schulz and Sick [146]. Via so-called *relaxation* the system is subsequently transferred to lower vibrational levels within the electronic excited state S_1 (see ②) [54, p. 763]. This relaxation involves both vibrational and rotational energy transitions [146], often referred to as *vibrational energy transfer* (VET) and *rotational energy transfer* (RET) (e.g., see [42]). It results from collisions with surrounding molecules and is thus very likely to occur (typically down to $v' = 0$; not necessarily for gases) [146]. After relaxation, the system can undergo a transition back to a certain vibrational level v'' in the electronical ground state S_0 by emission of the actual fluorescence photon with less energy than the incident one ($h\nu_F < h\nu_A$, so-called *Stokes-shift*, see ③) [54, p. 763].

Figure 2.15: Schematic of the LIF principle: (a) typical optical setup, as used in this thesis (e.g., see OH-LIF setup introduced in section 4.2.1.1); (b) energy scheme with major sub-processes ①-⑦, exemplified for singlet states. Created from the visualizations and descriptions in [146] (Fig. 3) as well as [10, p. 605 f.] (Fig. 11.64) and adapted by own considerations.

The fluorescence lifetime is typically in the order of nanoseconds [54, 146]. Depending on the resulting vibrational level v'' after photon emission, further relaxation within the S_0 state might follow (see ④).

As mentioned before, further radiating and non-radiating loss paths exist besides the actually *desired* fluorescence process that cause a de-excitation of S_1 states and significantly determine the fluorescence phenomenon. Following the outlines of Schulz and Sick [146] the major mechanisms in this context comprise: (1) non-radiative, spin-allowed *internal conversion* $S_{n+1} \rightarrow S_n$ (states of same multiplicity, see ⑤) that is more relevant for higher electronical states $n \geq 1$ due to the smaller energy gaps compared to ground states; (2) non-radiative, spin-forbidden *intersystem crossing* $S_n \rightarrow T_n$ (states of different multiplicity, T: triplet, see ⑥), which in turn is a prerequisite for the potential subsequent radiative transition $T_1 \rightarrow S_0$ (so-called *phosphorescence*, see following section 2.3.2.4 for more details); (3) inter-molecular collisonal quenching with electronic energy transfer to the collider can occur (in turn leading to electronical excitation of collider, see ⑤), especially O_2 (ground state T_0) is an efficient and strong quenching partner of some molecules (e.g., organics or aromatics) as it promotes triplet state transition [146]. Furthermore, mechanisms like predissociation and ionization may occur (see ⑦), as will be outlined for the CO molecule below. These deactivation processes are yet superimposed by relaxation and various combinations are furthermore possible, e.g., an intersystem crossing that is followed by collisional quenching. This underlines the complexity and arising challenges when trying to quantitatively study the fluorescence emissions.

For diagnostics purpose, fluorescence emission can be selectively excited by the means of laser radiation, named *laser-induced fluorescence* (LIF), and applied to yield a measure for species concentration, temperature, pressure or even velocity of a probed system [71, p. 177 f.].

A typical optical setup for LIF is depicted in Figure 2.15(a). Usually, radiation in the visible (VIS) or ultraviolet (UV) spectral range is used for LIF excitation [146]. The incident laser radiation is formed to lines, sheets or volumes in the probed region by laser optics, respectively, and the resulting fluorescence emission is typically captured perpendicular to the principal beam direction. Additional filters may be applied for signal conditioning, e.g., suppression of unwanted background. Recording is done by single-point or array photodetectors with optional additional signal intensification [71, p. 178]. The application of intensifiers is not simply meant to increase the signal strength but often act as *UV-converters* to turn LIF emission in the UV range to VIS radiation and thus make it detectable by common silicon-based scientific camera systems. Furthermore, intensifiers allow a well-defined time gating of the LIF signal, e.g., to suppress luminescence from the combustion process [146].

An equation for the recorded LIF signal intensity can be given as

$$I_{\text{LIF}} = \frac{I_{\text{L}}}{h\nu_{\text{L}}} \cdot V \cdot N_{\text{F}} \cdot \sigma_{\text{A}} \cdot \phi_{\text{F}} \cdot \frac{\Omega}{4\pi} \eta \tag{2.47}$$

with photon flux $I_{\text{L}}/h\nu_{\text{L}}$, probed volume V, number density of targeted molecule N_{F}, absorption cross-section σ_{A}, fluorescence quantum yield ϕ_{F}, observation angle $\Omega/4\pi$ and

detector efficiency η [146]. Due to these dependencies, a calibration is required if one wants to quantify LIF signals [71, p. 195 ff.]. Typically, absorption cross-section $\sigma_A = f(\lambda_L, T)$ and fluorescence quantum yield $\phi_F = f(\lambda_L, T, p, X_i)$ are considered to feature parameter dependencies on excitation wavelength λ_L, temperature T, pressure p and mole fractions X_i of the present bath gas species [162]. The fluorescence quantum yield

$$\phi_F = \frac{k_F}{k_F + \underbrace{\sum_i k_i}_{\text{intra-molecular}} + \underbrace{\sum_j k_{j,Q} \cdot X_j}_{\text{inter-molecular}}} = \frac{1/\tau_{F,\text{rad}}}{1/\tau_{F,\text{eff}}} \qquad (2.48)$$

describes a ratio of fluorescence rate k_F in the numerator and overall de-excitation rates in the denominator, including all further intra-molecular deactivation rates $\sum_i k_i$ as well as inter-molecular collisional quenching rates $k_{j,Q} \cdot X_j$ for each species j [121, 146]. It is further possible to express ϕ_F by characteristic fluorescence lifetimes for the *undisturbed* radiation $\tau_{F,\text{rad}}$ and the actually observed, effective one $\tau_{F,\text{eff}}$ [146]. It becomes directly evident from Equations (2.47) and (2.48) that these influences need to be considered in case the fluorescence signal should be quantified, e.g., by in-situ calibration for a studied configuration. For a more detailed insight into basics, the interested reader is referred to the comprehensive textbook of Lakowicz [95] that covers fluorescence in general, and to the review article on tracer LIF diagnostics by Schulz and Sick [146].

Fluorescence processes are very specific with respect to the electronical configuration of the species to be targeted. So the question arises, where to best excite and detect desired species for technical realizable LIF application. As this thesis applies the LIF diagnostic to probe the CO, OH and NO molecules during combustion processes, their most important photophysical properties are summarized in the following.
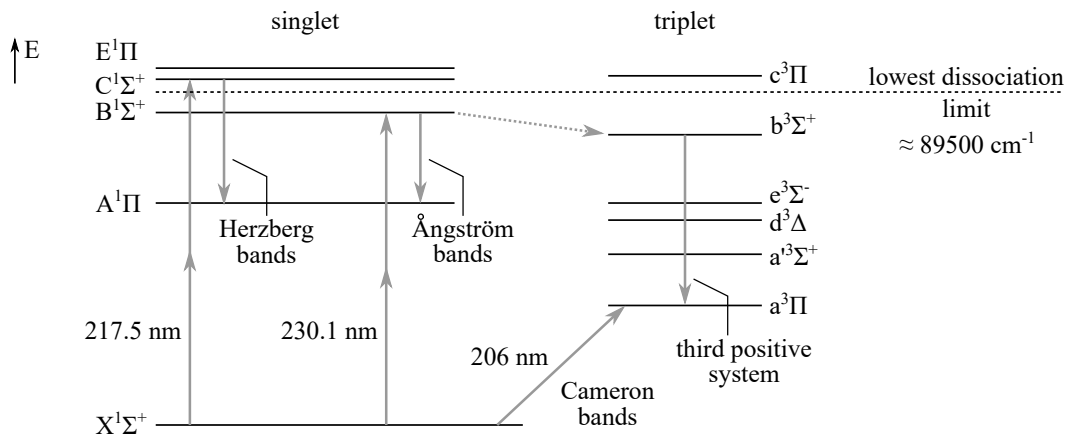
Figure 2.16: Energy scheme for LIF in CO molecules with selected transitions. For the sake of clarity, the presentation is limited to electronic energy levels only. Created from the visualizations and descriptions in [30, 102, 138] (Fig. 1) and adapted by own considerations.

CO-LIF   Potential transitions to be used by LIF in the CO molecule are summarized by the energy scheme in Figure 2.16. An essential photo-physical characteristic of the CO molecule is that the spin-allowed electronical transitions are located in the vacuum UV (VUV, about 100-200 nm) range [30, 138]. A one-photon excitation of the spin-allowed $A^1\Pi \leftarrow X^1\Sigma^+$ transition from the energetic ground state requires to span an energy gap in the order of ≈ 65000 cm^{-1} (see Fig. 1 in [102]), which would correspond a radiation around 150 nm. Such a wavelength is by no means simple to handle, as transmittance in common optical substrates can be restricted (see for example Fig. 1 in [150] or Fig. 4 in [87]), nor practical to use in real combustion environments, as the flame medium directly absorbs the VUV [163]. As reported in Linow et al. [102] as well as Carrivain et al. [30], the only non-VUV one-photon excitation is the spin-forbidden $a^3\Pi \leftarrow X^1\Sigma^+$ transition within the *Cameron bands* around 206 nm and, due to its spin-forbidden nature, too weak in signal for practical application in flames. Consequently, two-photon excitation is reported to be the method of choice to excite CO-LIF in combustion environments [30, 102, 138]. The straightforward way one could think of would be a two-photon excitation of the $A^1\Pi \leftarrow\leftarrow X^1\Sigma^+$ transition. However, Linow et al. [102] state that the resulting UV fluorescence emission ($\approx 200 - 250$ nm) is basically possible to detect in combustion environments but too weak for reliable concentration measurements. Different schemes for two-photon CO-LIF in combustion environments were compared by Linow et al. [102] and recently by Rosell et al. [138]. These two studies report three potential transitions for CO-LIF detection for combustion applications: (1) fluorescence from the $B^1\Sigma^+ \rightarrow A^1\Pi$ transitions in the *Ångström bands* (400-700 nm) that follow the $B^1\Sigma^+ \leftarrow\leftarrow X^1\Sigma^+$ excitation by two photons with $\lambda \approx 230.1$ nm [102,138]; (2) detection of $C^1\Sigma^+ \rightarrow A^1\Pi$ transitions within the *Herzberg bands* (360-600 nm) that originate from an initial $C^1\Sigma^+ \leftarrow\leftarrow X^1\Sigma^+$ excitation by two photons $\lambda \approx 217.5$ nm [102,138]; (3) an initial $B^1\Sigma^+ \leftarrow\leftarrow X^1\Sigma^+$ excitation (two photons, $\lambda \approx 230.1$ nm), followed by an energy transfer to the close $b^3\Sigma^+$ triplet state and final emission $b^3\Sigma^+ \rightarrow a^3\Pi$ in the *third positive bands* (282-380 nm) [138]. The excitations of these LIF schemes do all take place in the so-called *Hopfield-Birge system* [102, 138]. In this context it needs to be noted that an ionization of CO molecules is possible by absorbing a third excitation photon [30], which is often referred to as a 2+1 photo-ionization process [102, 148] and can be used for *resonance-enhanced multiphoton ionization* (REMPI) [45]. Basically, the first option listed above, i.e., excitation with two photons around 230.1 nm and detection in the Ångström bands, was commonly used in past and present combustion studies [5, 61, 67, 82, 110, 148, E2], to only name a few. Linow et al. [102] consider a detection within the Herzberg bands favorable, as it is less affected by C_2-LIF crosstalk compared to the Ångström bands. The study of Rosell et al. [138] recently pointed out that also the Herzberg bands feature certain bias from present C_2 as well as broadband emission originating from polycyclic aromatic hydrocarbons (PAHs), i.e., soot precursors. They rather suggest a simultaneous detection of multiple lines within both the Ångström and third positive bands for CO concentration measurements. However, in combustion configurations with low C_2 concentrations and minimal sooting tendency, like in fully premixed lean flames studied in this thesis, it appears well-justified to apply the commonly used detection scheme over the Ångström bands. Furthermore, the results of Rosell et al. [138] suggest that a detection of the $v' = 0 \rightarrow v'' = 1$ transition in the Ångström bands near 485 nm is free from C_2 interference.

This transition was detected within the CO-LIF measurements in this thesis, as presented later in section 5.2.1.2.

Following the outlines of Carrivain et al. [30], the equation for corresponding two-photon LIF signal intensity features a proportionality

$$I_{\text{LIF,2P}} \propto \left(\frac{I_{\text{L}}}{h\nu_{\text{L}}}\right)^2 \cdot \frac{k_{\text{F}}}{k_{\text{F}} + k_{\text{Q}} + k_{\text{P}} + \sigma_{\text{ion}}\frac{I_{\text{L}}}{h\nu_{\text{L}}}} \tag{2.49}$$

with the fluorescence quantum yield in the second term expressed by the fluorescence rate k_{F} (or Einstein A coefficient), overall collisonal quenching rate k_{Q}, predissociation rate k_{P} and ionization cross-section σ_{ion}. The competing deactivation processes finally result in $I_{\text{LIF,2P}} \propto I_{\text{L}}^n$ with $1 < n < 2$ [30]. Exponents close to $n = 2$ indicate negligible impact of ionization, while the fluorescence signal gets independent of collisional quenching for $n = 1$ (as ionization dominates) [30]. This trade-off is further discussed in section 5.2.1.2 that deals with the application of CO-LIF in context of this thesis. In this context, it should also be noted that photolytic production of CO from CO_2 is possible. This has particular importance in combustion environments and is thus discussed in more detail in section 5.2.2.2.

To completely circumvent two-photon excitation for the VUV transitions in CO molecules, Kirby and Hanson [91] proposed a linear planar LIF scheme with both excitation and detection in the infrared using vibrational transitions only, and demonstrated the feasibility for quantitative two-dimensional CO imaging in gas flows. They excited the $v' = 2 \leftarrow v'' = 0$ transition of CO by a tunable high-power infrared source at 2.35 μm and detected the emission around 4.7 μm.

OH-LIF   Probing of the hydroxyl radical OH by LIF diagnostic was frequently applied in combustion studies in the past decades and is thus considered a well-established approach. As summarized in a statement by Atakan et al. [9], OH features the advantages that it is straightforward to probe via LIF technique, is available at high concentrations in most flames and can yield suitable insight into flame structures. Typically, OH-LIF has been applied for qualitative imaging of the flame front structure or reaction zone distribution in one-dimensional profiles [3], planar configurations [9, 158] and recently advanced to three-dimensional (so-called *tomographic*) imaging by volumetric illumination [100, 124] or rapid laser scanning applications [101]. Furthermore, it found application for thermometry in flames [9, 96]. As evident from common literature, the electronical transitions in the $A^2\Sigma^+ - X^2\Pi$ system are used for OH-LIF in flames [3, 9, 48, 89, 96, 158]. A very comprehensive work on the available UV bands of OH was presented by Dieke and Crosswhite [46], and can be used for selection or identification of potential transitions. Dreier et al. [48] explored the capabilities of Raman-shifting excimer laser radiation for LIF excitation in flames and successfully accessed the vibrational bands $(v',v'') = (3,1)$ and $(2,0)$ near 268.5 nm, $(1,0)$ and $(2,1)$ around 291.5 nm as well as $(1,1)$ and $(0,0)$ around 313 nm of the $A^2\Sigma^+ - X^2\Pi$ electronical transition in OH by using a KrF excimer laser (around 248 nm) with different Raman mediums to realize the shift. Ketterle et al. [89] compared different OH-LIF imaging schemes using a XeCl

excimer laser at 308 nm to excite the (0,0) band with detection in the (0,0) or (0,1), while a KrF around 248 nm was applied for excitation of the (3,0) vibrational band. They concluded that XeCl excimer laser radiation is rather appropriate for qualitative visualization of flame structures, while KrF lasers could be used for quantitative studies, as the predissociation caused by the short wavelength yields a signal less sensitive to collision quenching (but also much less signal strength). Besides excimer lasers, the radiation of frequency doubled dye lasers has been applied to excite the (1,0) vibrational band of the $A^2\Sigma^+ - X^2\Pi$ transition, like the $Q_1(6)$ line around 283 nm for flame structure visualization [3, 82, E2, E3] or various lines near 280 nm for thermometry purpose [9, 96]. As stated by Atakan et al. [9], the three schemes exciting the vibrational bands (0,0), (1,0) and (3,0) of the $A^2\Sigma^+ - X^2\Pi$ system are frequently applied, each of them having specific characteristics. Excitation of the (0,0) vibrational band features largest Franck-Condon factors [9] (means: highest probability to populate a vibrational state [54, p. 761]) but suffers *radiation trapping* of the emitted fluorescence [9], i.e., re-absorption of these photons by other OH radicals on their path to the detector. This re-absorption issue can be avoided by exciting the (1,0) or (2,1) vibrational band [48]. However, as demonstrated by Sadanandan et al. [142], excitation of the (1,0) band for OH-LIF also features certain radiation trapping in flames, but could be minimized by detecting in the (1,1) emission band. As already mentioned above, a (3,0) transition of OH causes predissociation in the $v' = 3$ state that yields a fluorescence signal less affected from collision quenching, however, for elevated pressures (≥ 10 bar) predissociation does no longer dominate over quenching [9, 89]. The predissociation implies reduced fluorescence quantum yields (potentially compensated by high excitation power, e.g., from excimer lasers) and for higher pressures a strong interference from O_2 fluorescence furthermore occurs [9]. In contrast, high-pressure bias from O_2 interference is avoidable by using the (1,0) band for excitation [9].

From the above outlines, it is evident that a proper selection of the excitation/detection strategy is important when aiming to quantify the OH-LIF signal, e.g., in terms of temperature measurements [9, 96]. However, when performing visualization of the flame front, it appears justified to simply select the lines with high intensity in the studied configuration. Excitation of the (1,0) vibrational band system appears well-suited for this purpose. Thus, this thesis applies frequency doubled dye laser excitation within the (1,0) vibrational band and targets the line $Q_1(6)$ around 283 nm as well as the $Q_1(9)+Q_2(8)$ line pair near 284 nm.

NO-LIF   Nitric oxides (NO_x), like nitric monoxide (NO), are crucial pollutants in combustion processes that demand continuous reduction and are subject to strict governmental emission restrictions. Evidently, NO is an interesting chemical species to understand in combustion studies and can be accessed conveniently by the LIF technique [17]. Besides the study on formation of NO as a pollutant, this species can further be used in LIF diagnostics for the purpose of thermometry [61, 99] or as tracer for mixture fraction evaluation (typically additionally seeded to the flows under investigation) [141, 143]. Bessler et al. [17] provide an overview on different NO-LIF excitation schemes (including a valuable literature review) and draw some selection guidelines for specific combustion applications,

especially in context of elevated pressure environments. Major excitation schemes are [17]: (1) Transitions in the $A^2\Sigma^+ - X^2\Pi$ electronic system by using the (0,0), (0,1) and (0,2) vibrational bands around corresponding wavelengths of 225 nm, 236 nm and 247 nm; (2) the (0,1) band in the $D - X$ electronical transition (192-195 nm) that is accessible by ArF excimer lasers with a wavelength near 193 nm. The latter approach suffers strong attenuation of both laser and signal radiation in typical combustion environments that could completely vanish detectable signal [17]. In general, the shorter a wavelength is, the more susceptible it is to absorption by the medium it transits. The standard approach, which is most frequently applied, is excitation of the $A^2\Sigma^+ - X^2\Pi(0,0)$ system (224-227 nm) and is seen as the preferred method for combustion applications, as it features strong signal and selectivity (even at higher pressures) [17]. In the temperature range of 1500-2500 K the vibrational ground state $v'' = 0$ of the electronical ground state X features highest population [17]. This is equally true for ambient temperature gases, and the (0,0) transition originating from the vibrational ground state appears thus most efficient. This excitation approach is typically used for studies on mixture fraction [141, 143]. Drawbacks of exciting the (0,0) band are increased laser attenuation by absorption of the probed medium (e.g., by CO_2 and H_2O at flame temperatures; especially for longer pathways) and possible interference with broadband emission from PAHs in the red-shifted detection region [17]. In contrast, the schemes exciting the (0,1) and (0,2) vibrational bands of the $A^2\Sigma^+ - X^2\Pi$ transition are capable to mitigate these drawbacks to a certain extent, however, at lower signal strength of the fluorescence emission [17]. Please note that both red- and blue-shifted detection is possible if excitation is done from a higher vibrational level in the electronic ground state, i.e., for the schemes using either the (0,1) or (0,2) bands, which basically allows for more customized detection approaches [17]. Suited bandpass filters are mandatory in any case for detection to suppress LIF of interfering species (O_2, CO_2, PAHs) [17]. For a deeper insight into these above topics, the interested reader is referred to the work of Bessler et al. [17]. A more specific discussion on the favorable (0,0) excitation in particular can be found in [16].

Within the scope of this thesis, NO was applied with the purpose to trace pre-flame mixture processes. Thus, the *standard approach* in the (0,0) vibrational band of the $A^2\Sigma^+ - X^2\Pi$ electronic system is used and excitation is performed around 226.26 nm.

2.3.2.4 Thermographic Phosphor Thermometry (TPT)

The laser diagnostic *thermographic phosphor thermometry* (TPT) uses the emission characteristics of laser-induced phosphorescence from special materials, so-called *thermographic phosphors* (TGPs), to evaluate their temperatures. These phosphors consist of a *host* (ceramic materials, e.g., Al_2O_3) doped by small amounts of *activators* (rare earth or transition metal ions, e.g., Eu^{+3}) that emit radiation on excitation [27]. As the non-radiative de-activation is a function of temperature [27], so is their phosphorescence emission and they are termed *thermographic*. As pointed out in section 2.3.2.3 on laser-induced fluorescence, *phosphorescence* is a potential process involved in de-population of the electronically excited state. For this reason, the basics on activation of the excited state are omitted here (see section 2.3.2.3) and focus is on the specific de-activation pro-
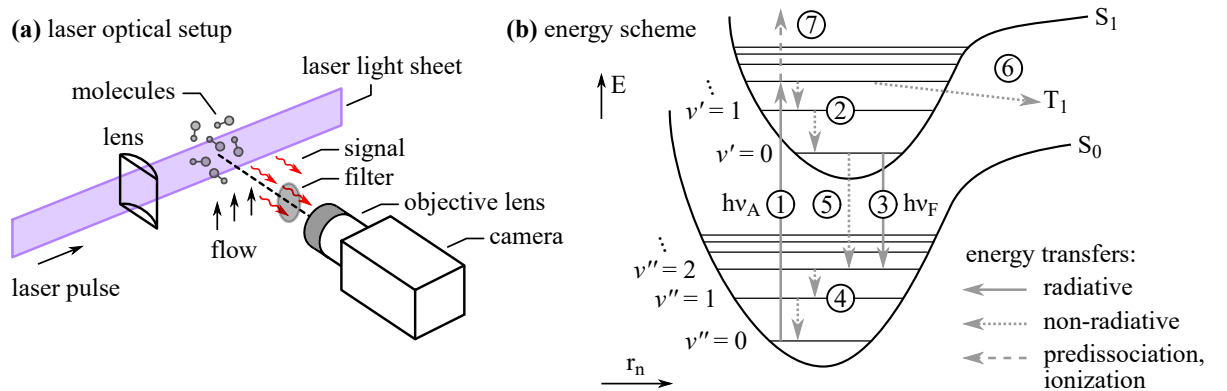
(a) laser optical setup
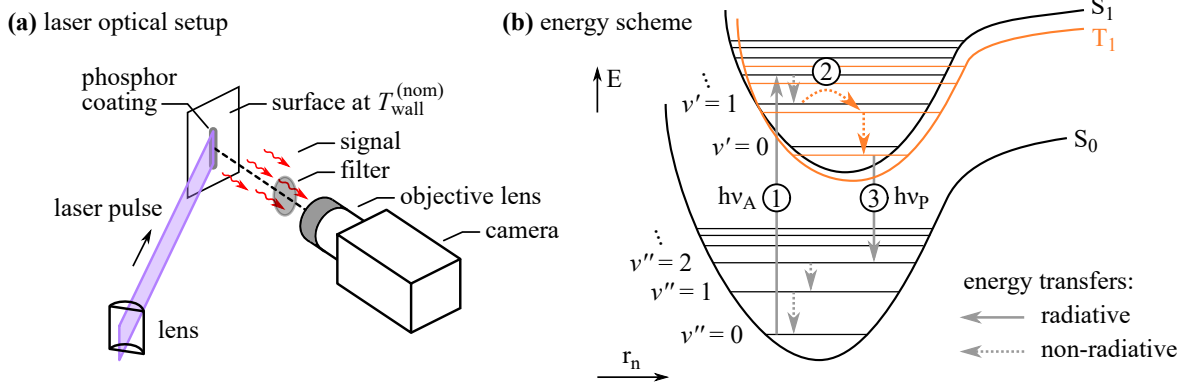
(b) energy scheme

Figure 2.17: Schematic of the TPT principle: (a) typical optical setup, as used in this thesis (e.g., see TPT setup introduced in section 5.2.1.4); (b) energy scheme, exemplified for singlet-triplet states. Please note that the energy scheme was simplified for the sake of clarity and focuses the phosphorescence phenomenon; for further potential de-activation processes please see Figure 2.15. Created from the visualizations and descriptions in [146] (Fig. 3) as well as [10, p. 605 ff.] (Fig. 11.67) and adapted by own considerations.

cess itself. The principle of phosphorescence is depicted in terms of its energy scheme by Figure 2.17(b), assuming that excitation already occurred (see ①).

As previously stated in section 2.3.2.3 on LIF, the phenomenon of phosphorescence will be explained in the following for the example of singlet (S) and triplet states (T). The requirement for this de-activation path is a previous energy transfer between states of different multiplicity $S_n \rightarrow T_n$ by intersystem crossing (see ②) [54, p. 764] [146]. The following spontaneous, *spin-forbidden* radiative transition $T_1 \rightarrow S_0$ is then termed phosphorescence (see ③) [54, p. 764] [146]. The change in spin during singlet-triplet-transitions violates the $\Delta S = 0$ selection rule, which in turn harms the conservation of angular momentum [54, p. 764]. As spin momentum $\hat{S}$ and orbit momentum $\hat{L}$ are coupled to a total angular momentum $\hat{J}$ in multi-electron systems [54, p. 591 ff.], the violation caused by spin momentum can be compensated over a strong spin-orbit coupling by a corresponding change in orbit momentum (e.g., via collision) [54, p. 764]. This strong coupling is the case when heavy atoms (starting around atomic number $Z \geq 40$ [54, p. 591]) are present in a molecule, like in TGPs [27]. However, due to the actually spin-forbidden nature of this transition, the triplet state is a long-lived one [54, p. 765] [146]. Typical lifetimes of thermographic phosphor emission can easily vary from 10^{-9} s to 10^{-2} s (see Table 3 in [27]), depending on the probed material itself and strongly on its temperature [27], making TGPs suitable for thermometry application.

For technical realization, the solid thermographic phosphors are supplied as small particles and need to be inserted in the system to probe, e.g., at a surface by a coating [27] or dispersed to a fluid phase [1]. In this context, one always needs to remember that the particle's temperature is actually probed, which is assumed in equilibrium with its surrounding and thus to mimic a surface or fluid temperature. Basically, two major thermometry schemes are distinguished using TGPs that either use temporal or spectral change in the phosphorescence emission with temperature [27]: (1) a time-resolved approach that either

assesses the time domain by rise or decay times (most common), or utilizes the system's response behavior in frequency domain; (2) a time-integrated method that evaluates the intensity of a single band or ratio of multiple spectral bands (most common). In any case, the complex nature of photophysics in TGPs requires a calibration of the measured values to temperatures [27]. A typical laser diagnostic TPT setting to measure surface temperatures by means of TGPs is shown in Figure 2.17(a). A laser pulse is shaped by optics and guided to a TGP coating at a surface with nominal wall temperature $T_{\text{wall}}^{(\text{nom})}$. The resulting emission is collected and recorded by appropriate detectors. As thermographic phosphor thermometry was extensively studied and found various applications in the past decade, the interested reader is referred to the comprehensive review articles of Aldén et al. [4], Brübach et al. [27] and Abram et al. [1] for further details.

In this thesis, TPT only finds minor application by a pointwise decay time approach for simple control purpose of the studied quenching wall at elevated temperatures, i.e., to benchmark the surface temperature to the temperature measured by embedded thermocouples (see following section 3).

Chapter 3

Burner Facility

The phenomenon studied within the scope of this thesis is atmospheric, premixed side-wall quenching (SWQ), assessed using a special *SWQ burner* facility. This burner was developed, built and investigated within the previous dissertation of Jainski [79], and further analyzed in the subsequent thesis of Kosaka [94]. Basically, it is a well-defined generic reference case that was studied frequently over the past years by the RSM group in various contexts [81–83, E2, E3], to only name a few (see previous section 1.1 on state of research for further information). The burner facility thus became established in the experimental FWI community and was therefore also used in this thesis to further explore the SWQ phenomenon. This chapter comprises a first section on the general design of the SWQ burner and its installation in the RSM laboratory, while a second section summarizes the operation conditions, including major characteristics. Parts of the content of chapter 3 were published in Zentgraf et al. [E8,E11] and are reused with permission (see appendix B), in a modified wording and partially extended by further technical and scientific details to fit the structure of this thesis. This concerns parts of sections 3.1 (reported in [E8,E11]) and 3.2 (reported in [E8,E11]), excluding subsection 3.2.3.

3.1 Installation

A schematic of the SWQ burner is shown in Figure 3.1 for the overall construction in (a) as well as for selected details in (b). The following description is based on the current burner configuration as it was mounted in the RSM laboratory for the research presented in this work. Descriptions of this burner device (with varying extent and details) may also be found in the references given in the above paragraph.

The burner is operated stationary with its main flow under fully premixed conditions. Continuous flows of dehumidified air and fuel are initially mixed, guided to the device, split up and enter the burners inlet plenum (see ①) via eight opposed ports from the side. Subsequently, the inflow passes a homogenization section, which consists of different structures. At both the entrance and outlet (see ② and ④), a fine square mesh (mesh width ≈ 0.5 mm) is inserted between two coarse hexagonal grids. In the center, a honeycomb structure is arranged (see ③, height ≈ 25 mm, distance between opposed edges ≈ 3 mm). Downstream the homogenization, a converging nozzle (Morel-type, see ⑤) reduces the flow cross-section from 120×120 mm^2 to approximately 40×40 mm^2 (corner radius: 5 mm),
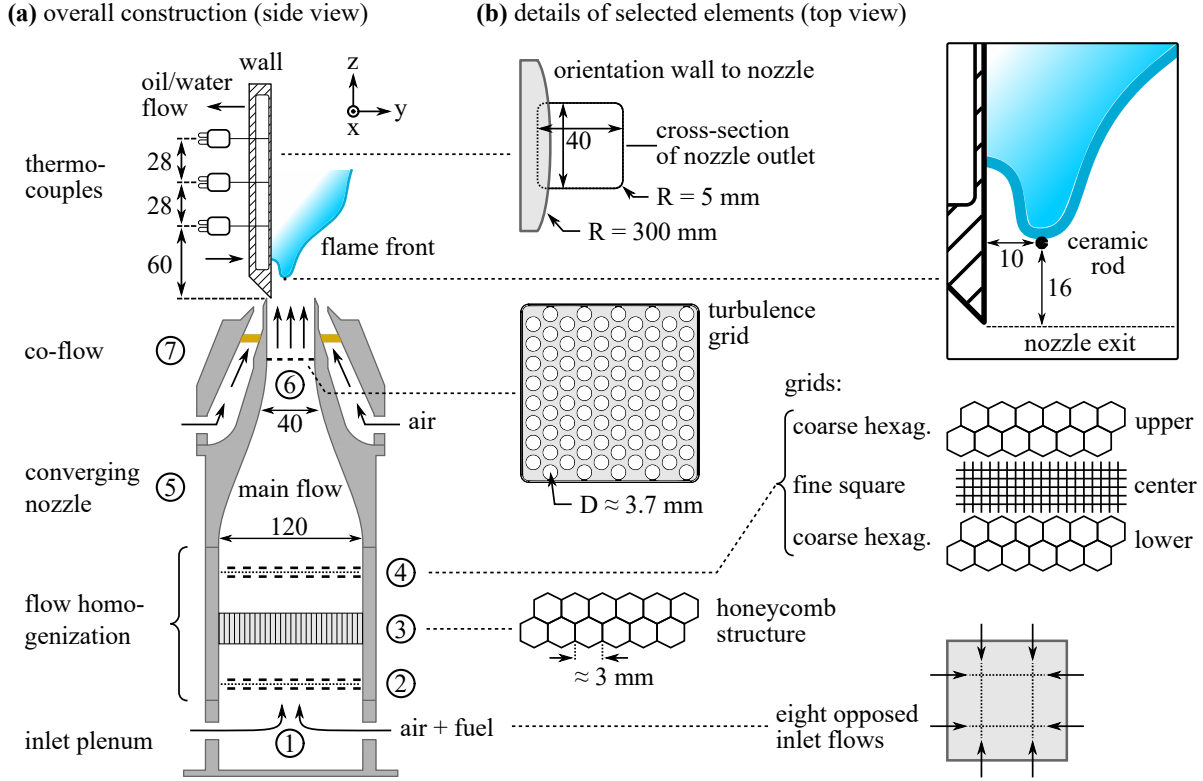
Figure 3.1: Schematic of the SWQ burner: (a) overall construction; (b) selected details. All dimensions without unit are given in millimeters. Parts of this figure were published in Zentgraf et al. [E11] (parts of Fig. 1) and are reused with permission of Elsevier; reproduced in an adapted, extended version.

corresponding to a contraction ratio of 9. This yields a velocity profile of the premixed main flow that is close to a top-hat at the nozzle exit (see section 3.2.3). After contraction, the flow passes a short straight channel section and finally enters to environment through a nozzle (sharp edges at the nozzle's outlet minimize flow recirculation). The central main flow is shielded from the laboratory environment by a co-flow operated with dehumidified air (see ⑦), which is homogenized prior to outlet by a sintered structure made of bronze. A turbulence grid (see ⑥) can be optionally inserted in the main flow, about 50 mm upstream the nozzle exit. It is designed as a perforated plate (individual hole diameter ≈ 3.7 mm) that features $\approx 50\%$ solidity in the active flow cross-section. Without insertion of the grid, laminar operation of the SWQ burner is realized. Details on resulting velocities at the nozzle exit can be found in section 3.2.3. Downstream the nozzle exit, the reaction is stabilized on a cylindrical ceramic rod with 1 mm diameter that is placed about 10 mm from the quenching wall and 16 mm downstream the nozzle exit. The stabilized reaction is forming a V-shaped flame with two branches: (1) a flame branch that can be assumed approximately adiabatic; (2) a wall-bounded branch that extinguishes at the solid surface of the quenching wall. The quenching wall is manufactured from stainless steel and features a curved surface in the xy-plane (radius $R = 300$ mm, see details in top view in Figure 3.1(b)) for an improved optical access. Thus, lasers can probe very close to the wall along the x-direction. Furthermore, the wall is slightly ranging into the cross-

section of the nozzle exit (see details in top view in Figure 3.1(b)). During combustion operation, the temperature of the quenching wall is stabilized and controlled by continuously flushing its cooling duct with water at ambient temperature for a *cold-wall* case (nominal wall temperature $T_{\mathrm{wall}}^{(\mathrm{nom})} = 60$ °C) or tempered thermal oil for a corresponding *hot-wall* condition (nominal wall temperature $T_{\mathrm{wall}}^{(\mathrm{nom})} = 360$ °C; bath circulation thermostat: Peter Huber Kältemaschinenbau AG, CC-304B, operated with thermofluid SilOil P20.275.50). Wall temperatures are monitored by the values from three type K sheath thermocouples (diameter 1.5 mm). They are arranged on the wall's centerline ($x = 0$ mm) with their tips embedded in the wall, approximately 200 μm to 400 μm underneath the surface. A benchmark of these temperature values to surface temperatures can be found in section 3.2.1. The combustion flue gas is handled by the laboratory's exhaust duct.

All gas flows are defined and controlled by calibrated mass flow controllers (Bronkhorst High-Tech B.V.). Their operation also determines the equivalence ratio of the premixed main flow. An uncertainty of $\delta\Phi = 0.01$ can be given for lean DME-air mixtures ($\Phi = 0.83$). It results from error propagation of fuel and air flow rate deviations during calibration. A similar error magnitude is expected for CH_4 operation. The SWQ burner device, as shown in Figure 3.1(a), is assembled in a triaxial, computer-controlled traversing system (x: out of plane direction, y: wall-normal direction, z: streamwise, wall-parallel direction). Within the scope of this thesis, a new traversing system was built up and allowed to synchronize burner movement with recording and to automatize data acquisition[2]. Besides the SWQ burner, additional devices are arranged in the traversing unit for calibration purpose, like an available quasi-adiabatic flat flame burner that follows the design of Gregor and Dreizler [65], as well as an inline heater tube to seed test gases.

To facilitate discussion in the remainder of this thesis, Figure 3.2 graphically summarizes the nomenclature used in near-wall context. Please note that many coordinate systems shown in sketches or pictograms, like in Figure 3.1(a), do not represent the absolute origin but indicate the coordinates orientation only. In most instances, data analysis defines $x = 0$ mm at the wall's centerline, $y = 0$ mm at its surface and $z = 0$ mm as the instantaneous quenching height (see ①). In a few cases, the streamwise direction is referred to the nozzle exit at $z_{\mathrm{abs}} = 0$ mm (see ②). These procedures will be defined later in more detail at the appropriate places.

---

[2]The implementation of this valuable LABVIEW software was done by Dr.-Ing. Max Greifenstein from Technical University of Darmstadt (RSM) and was used in this thesis with permission. His kind contribution is acknowledged here.
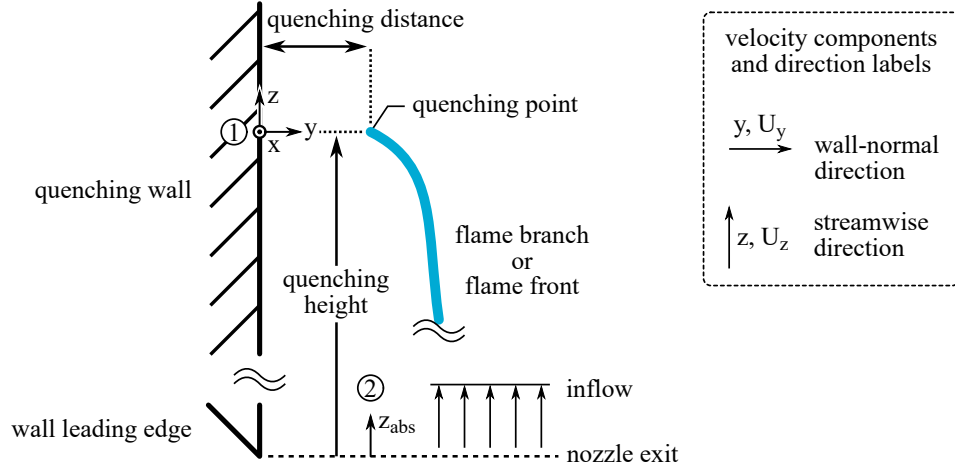
Figure 3.2: Graphical outline of the used near-wall nomenclature.

3.2 Operation Conditions

A summary of the operation conditions measured for this thesis is shown in Table 3.1. It involved a comprehensive parameter variation in fuel (CH_4 or DME), equivalence ratio Φ, inflow condition (either laminar or turbulent) and nominal wall temperature $T_{wall}^{(nom)}$. The table furthermore distinguishes the performed measurement campaigns on flame and flow dynamics (F&F, see chapter 4), thermochemistry (TC, see chapter 5) and partially premixed FWI (PP, see chapter 6). Crosses ($\times$) indicate if an operation condition case was measured. Please note that the hot wall case at 360 °C was not feasible to measure within the flame and flow dynamics campaign, as no particles were evident close to the wall's surface, which finally impeded PIV measurements (denoted by *); most likely due to thermophoresis of the very small seeding particles. The campaign on partially premixed FWI is seen as feasibility study and was thus performed for OP5 only, however, for four subsets available with 0, 2, 3.5 and 4.5 ln/h secondary CH_4 seeding to generate the partial premixed conditions (denoted by **). The impact of such parameter variations on

Table 3.1: Major operating conditions used with the SWQ burner for the research presented in this thesis. OP: operation point; * not measurable, as no seeding for PIV apparent within the boundary layer (most likely due to thermophoresis); ** four subsets available with 0, 2, 3.5 and 4.5 ln/h secondary CH_4 seeding.

OP	fuel	Φ	inflow	$T_{wall}^{(nom)}$	campaigns		
					F&F	TC	PP
1	DME	0.83	laminar	60 °C	$\times$	$\times$	-
2	DME	0.83	turbulent	60 °C	$\times$	$\times$	-
3	DME	0.95	laminar	60 °C	$\times$	$\times$	-
4	DME	0.83	laminar	360 °C	-*	$\times$	-
5	CH_4	1.00	laminar	60 °C	$\times$	$\times$	$\times$**
6	CH_4	1.00	turbulent	60 °C	$\times$	$\times$	-
7	CH_4	1.00	laminar	360 °C	-*	$\times$	-

FWI was studied previously, e.g., in the thesis of Kosaka [94]. In the dissertation presented here, the focus is especially on (1) DME fuel, (2) a detailed assessment of turbulence related phenomena and (3) to explore the capabilities from novel diagnostics application. For this reason, the parameter domain measured in Table 3.1 is reduced to OP1, OP2 and OP5 for presentation in this thesis.

As the SWQ burner features an *open* configuration, its combustion operates under atmospheric conditions, i.e., at 1 bar. For comparability in the operating points, the main flow Reynolds number $Re = U \cdot L/\nu$ is kept constant at ≈ 5900 between all studied cases. It is assessed from the bulk flow velocity U of the main flow (assumed spatially homogeneous as $U = \dot{V}/A$, $\dot{V}$: total flow rate), the nozzle exit's hydraulic diameter $L \approx 41.7$ mm and the mixture's kinematic viscosity ν at the nozzle exit for 20 °C conditions. This corresponds $Re \approx 5500$ at 0 °C. Despite the elevated Reynolds number, velocities at the burner exit are not yet transitional, due to the burner design featuring a convergent nozzle with only a short straight flow section to the nozzle exit. This configuration yields a nearly top hat, laminar velocity profile with very thin boundary layers. Please note that for practical reasons, the outlet Reynolds number in this thesis was slightly increased by 10% in contrast to $Re = 5000$ (for 0 °C [81–83]) in previous studies in this device. This was mainly to guarantee a more stable operation when the burner is fueled with DME, which features a higher laminar flame speed than CH_4 at a given equivalence ratio (see Fig. 3 and 5 in [132] for example). This slight increase did not cause any undesired flow instability nor transitional behavior. The constant Reynolds number in turn leads to approximately constant bulk velocities of 2.1-2.2 m/s in the main flow. Minor deviations exist with fuel and Φ variation, as the mixture's viscosity slightly changes. The co-flow was operated at 2 m/s bulk velocity. To further aid comparability between the two fuels DME and CH_4, equivalence ratios in Table 3.1 are chosen in a way that the laminar flame speed u_F is approximately equal, i.e., $u_{F,DME\ 0.83} \approx u_{F,CH_4\ 1.00}$. As evident from a comparison of different experimental data and mechanisms by Qin and Ju [132] $u_{F,CH_4\ 1.00}$ ranges between 0.35-0.37 m/s (see Fig. 3 in [132]), while $u_{F,DME\ 0.83}$ is in the equal order of 0.35-0.39 m/s (see Fig. 5 in [132]), for fuel-air premixtures at atmospheric pressure.

In the following three subsections, some further metrics on the burner operation are given, which were derived with the laser diagnostics applied in this thesis. As these findings are rather associated with basic characteristics than results on flame-wall interaction, they are reported here briefly. Values may serve as boundary conditions for corresponding numerical simulation or to reproduce the experimental SWQ burner operation.

3.2.1 Quenching Wall Temperatures

Table 3.1 gives the *nominal* wall temperatures $T_{wall}^{(nom)}$ for the studied operation points, i.e., the actually desired wall temperatures that should be reached during operation. Please note that superscript labels in the wall temperature parameter denote the origin (nom: nominal, TC: from thermocouples, TPT: from thermographic phosphor thermometry). The near-wall heat release, which determines the wall temperature, depends on fuel, equivalence ratio and also whether a laminar or turbulent inflow is present. To best reach the desired nominal values of $T_{wall}^{(nom)}$ in the experiment, the flow rate in the cooling duct

had to be well-controlled and the resulting wall temperatures continuously checked. As already stated above in section 3.1, this was done by thermocouples embedded closely underneath the wall's surface (downstream of quenching event). To check their correlation with temperatures measured directly at the surface, a benchmark with thermographic phosphor thermometry (TPT) was performed during the thermochemistry campaign (see section 5.2.1.4 for experimental setting and 5.2.2.4 for processing). For a conservative consideration, this was done for the higher wall temperature case at 360 °C nominal value only, i.e., OP4 in Table 3.1, and expected to well-reflect the other operation points. Here, thermocouple temperatures yielded $T_{\mathrm{wall}}^{(\mathrm{TC})} = 626$ K $\pm$ 6 K (mean $\pm$ standard deviation), while the TPT measurements resulted in $T_{\mathrm{wall}}^{(\mathrm{TPT})} = 670$ K $\pm$ 0.7 K. These values are considered to agree well. The 44 K higher value in the average TPT results, which corresponds $\approx 7\%$ deviation in absolute value, is considered physical as these probes are measured directly at the wall's surface, while thermocouples are embedded underneath. Consequently, thermocouple values well-reflect the temperature of the wall surface within an uncertainty of 7%. This is considered sufficiently accurate, also in the cold wall case at nominal temperature of 60 °C, as temperature gradients are less pronounced compared to the benchmark case. Typically, thermocouple temperatures met the nominal temperature in Table 3.1 during operation within a few Kelvin and values given in the table can be seen as representative boundary conditions.

3.2.2 Flame Front Unsteadiness

Residual fluctuation of the flame is observed under laminar inflow conditions. This unsteadiness has been ascribed to Helmholtz resonances in past studies [81, 82, E3]. A measure for this effect is the movement of the instantaneous quenching point location in wall-parallel z-direction (see Figure 3.2). This quenching point motion can be derived from OH-PLIF data, as described later in section 4.2.2.3. For OP1 in Table 3.1, the fluctuation in the quenching point's z-location was about ± 500 μm ($\pm 1\sigma$ standard deviation) in the flame and flow dynamics measurement (see chapter 4) and approximately ± 310 μm for the thermochemistry campaign (see chapter 5). Comparable values are expected for the other laminar operation points in Table 3.1. Values assessed from the flame and flow dynamics campaign might be slightly increased due to potential bias from involved seeding particles, e.g., minor agglomerations at the wall or in the flow homogenization section may increase unsteadiness. Nevertheless, both fluctuation values are considered well-consistent with previous studies in this burner device (± 200 μm) [81, 82, E3]. The instantaneous quenching point location derived from OH-PLIF can be applied to correct for these remaining fluctuations in the laminar inflow case by statistic conditioning. This conditioning procedure will be introduced later in this thesis (see section 4.2.2.3). A further discussion on the remaining unsteadiness during laminar operation, including vortex shedding frequency from the ceramic flame holder rod and Helmholtz resonance frequency, is presented in section 4.3.1.2.

3.2.3 Velocity Profiles at Nozzle Exit

Another important boundary condition is the experimental velocity profile at the nozzle exit of the premixed main flow, derived by PIV measurements. The velocimetry results shown here were not measured as part of the campaigns presented in chapters 4-6, but in a separate realization. Basically, this PIV setup closely matched the one used within the flame and flow dynamics campaign as presented in section 4.2.1.2, however, using low-speed systems instead of high-speed. For this reason, only major features are summarized in the following. PIV seeding was supplied to the main flow in an equal manner as described in section 4.2.1.2 later, i.e., the same seeding particles using the same seeder device. A frequency-doubled Nd:YAG PIV laser system (New Wave Research, Gemini PIV, G200) operated at 10 Hz repetition rate served as light source. The two consecutive laser pulses ($\Delta t = 40$ μs) were energy controlled by a combination of half-wave plate and polarizing beam splitter cube, formed to light sheets by cylindrical lenses and introduced to the burner from top, as presented later in section 4.2.1.2. They featured energies around 10 mJ/pulse in the FOV with ≈ 50 mm height and ≈ 750 μm thickness ($1/e^2$-value). The Mie-scattered PIV signal was collected by an objective lens (Sigma, APO Macro DG HSM D, 180 mm, f/8) equipped with a narrowband bandpass filter (Edmund Optics Inc., #65-216, central wavelength 532 nm, FWHM 10 nm) and recorded by a low-speed sCMOS camera (LaVision GmbH, Imager sCMOS, 15 μs exposure). In contrast to the highly resolved high-speed setting presented later (see section 4.2.1.2), the detection side did neither feature an extension tube nor a Scheimpflug arrangement. Particle raw images were processed using the software DaVis 10.0.5 (LaVision GmbH) with a 32×32 interrogation window at 75% overlap in the final passes. This resulted in a vector spacing of ≈ 150 μm.

The nozzle exit velocities were measured exemplary for CH_4 fuel at $\Phi = 1.00$ for both laminar and turbulent inflow conditions (equals OP5 and OP6 in Table 3.1) under non-reacting conditions, i.e., not ignited. These profiles do equally represent the DME fueled conditions, as total flow rates did only drop by ≈ 4% when switching from CH_4 to DME operation in Table 3.1. Velocity profiles are presented in Figure 3.3 over the full 40 mm width of the nozzle exit in y-direction ($y = 0$ mm denotes the nozzle's center), extracted in a z-range of 2-4 mm above the nozzle exit and averaged in this region. An ensemble of 1000 statistically independent samples was considered. Due to reflections from the vertical pole of the ceramic flame holder rod, minor artifacts remained in the velocity fields between $y = 1$-4 mm that had to be masked in some RMS profiles. The laminar inflow configuration is given in Figure 3.3(a) for ensemble-averages $\langle...\rangle$ and (b) for the fluctuation velocity's RMS values. In an equal manner, (c) and (d) present the turbulent condition. Velocity components in nozzle-radial y-direction, i.e., $\langle U_y \rangle$ and $u'_{y,\,\mathrm{RMS}}$, are shown by gray lines, while the streamwise z-components, i.e., $\langle U_z \rangle$ and $u'_{z,\,\mathrm{RMS}}$, are depicted in black. The flow velocities were measured at the wall's centerline $x = 0$ mm (solid lines) and for two off-centerline locations ($x = -10$ mm as dashed lines and $x = 10$ mm as dotted lines). In the ensemble-averaged profiles in Figures 3.3(a) and (c) $\langle U_y \rangle$ vanishes, while the streamwise components $\langle U_z \rangle$ evidently feature shapes that closely match top-hat profiles across the majority of nozzle width. The values are around 2.5 m/s in the constant region of the profiles. This is well-consistent with values around 2.3 m/s observed in
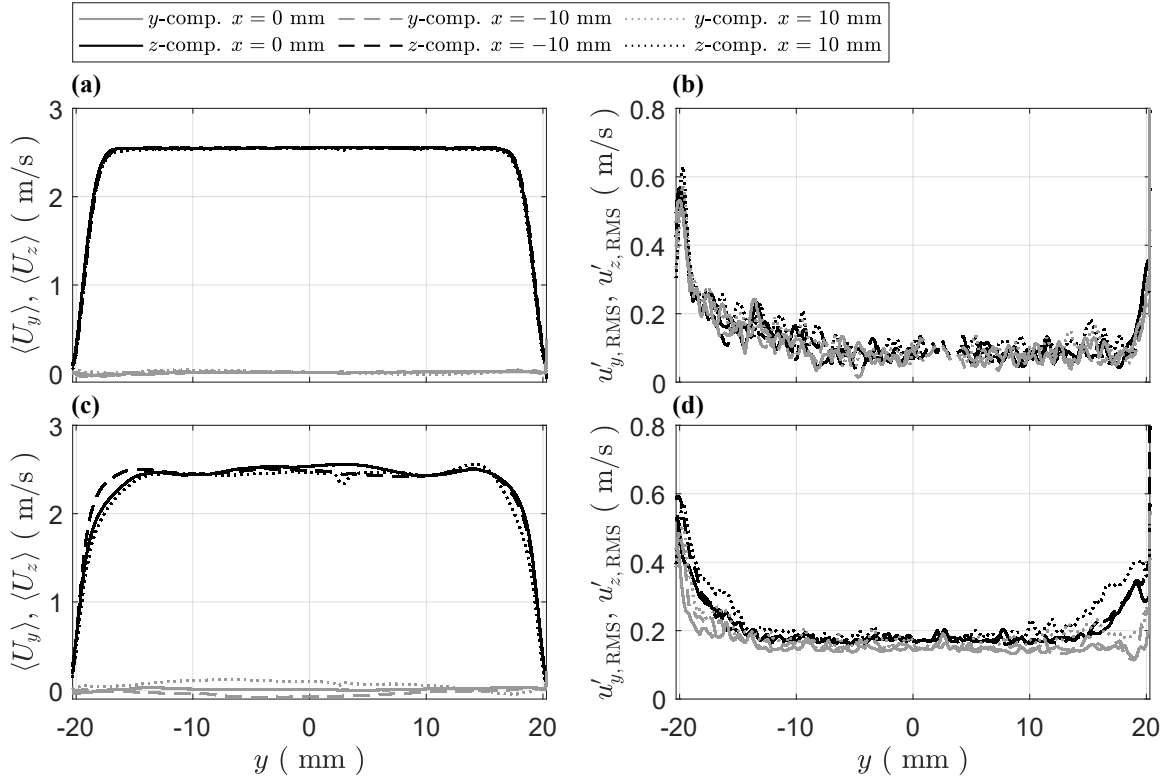
Figure 3.3: Velocity profiles at the nozzle exit of the premixed main flow for laminar (a,b) and turbulent (c,d) inflow conditions. Ensemble-averages are presented in (a) and (c), while (b) and (d) depict the fluctuation velocity's RMS values respectively. Statistics of 1000 samples presented.

previous works [79, p. 67] [94, p. 66] and perfectly reflects the 10% increase in Reynolds number. Velocity fluctuations feature an average value around 0.18 m/s in the nozzle core ($y \in [-10 \text{ mm}, 10 \text{ mm}]$) for the turbulent case in Figure 3.3(d), which corresponds a turbulence intensity of $u'_{z,\text{RMS}}/\langle U_z \rangle \approx 7.2\%$ for the streamwise component. In the laminar case in Figure 3.3(b) fluctuations in the order of 0.09 m/s remain in average (equals $u'_{z,\text{RMS}}/\langle U_z \rangle \approx 3.6\%$, most likely due to the Helmholtz resonances reported above). For the turbulent case, these values are also in good agreement with previous observations, where the turbulence intensity is reported around 6-7% [83] or 6-8% [94, p. 66] at the nozzle exit. However, in the laminar case values around 0.4% were reported in the past [79, p. 66] [94, p. 66]. Please note that higher values of velocity metrics in this thesis are most likely due to the slight increase in Reynolds number. Furthermore, profiles recorded aside the centerline, i.e., at $x = -10$ mm and $x = 10$ mm, do well match the center profile ($x = 0$ mm). Overall, the presented velocity profiles do feature good symmetry.

Chapter 4

Flame and Flow Dynamics

4.1 Aim of the Investigation

As initially outlined in Chapter 1, a major scope of this thesis is on further exploring turbulent FWI. This involves studying individual transport mechanisms and an evaluation of the turbulent boundary layer in detail. To gain the best possible understanding of combustion physics in generic SWQ, a sophisticated approach, shown by the graphical abstract in Fig. 4.1, is followed that combines information on both near-wall flame and flow dynamics with thermochemistry originating from complementary experimental studies. This chapter focuses on the first experimental campaign on flame and flow dynamics, mainly dealing with the topic of transport processes (framed red in Figure 4.1).

The investigation covers basic flame and flow characteristics of the studied SWQ burner, resolves near-wall boundary layers, assesses length scales and combustion regimes as well as near-wall anisotropy and vortex structures. Finally, temporally resolved transients are discussed. On the one hand, the aim is to explore novel, independent results on the flow physics governing SWQ. On the other hand, potential transport theories are postulated in order to better understand the thermochemical phenomena presented in chapter 5. Several contents of chapter 4 were published in Zentgraf et al. [E8, E9, E11], and are reused in this thesis in part and with permission (see appendix B for permission of Elsevier and declarations of the author's contribution). In the remainder of this chapter, corresponding passages are pointed out at the beginning of superordinate sections, respectively.
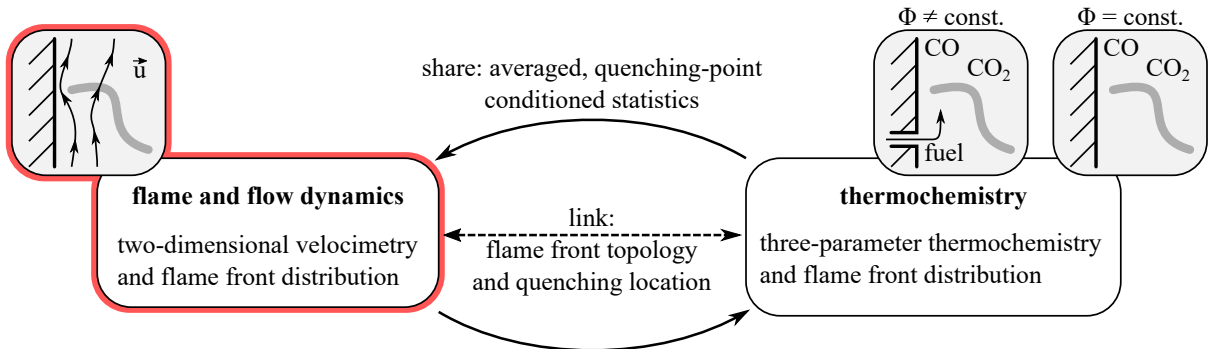
Figure 4.1: Graphical abstract of the applied approach using complementary experimental results to assess transport and reaction phenomena in FWI.

4.2 Methodology

The objectives of this investigation are pursued experimentally with the aid of high-speed and high-resolution laser diagnostics, specified in section 4.2.1. This enables the physical aspects to be investigated down to the relevant near-wall boundary layer scales and up to the temporal dynamics of their transient behavior. The processing of the experimental data is described in section 4.2.2.

4.2.1 Laser Diagnostics

An outline of the laser diagnostics applied to the SWQ burner is shown in Figure 4.2. A planar laser-induced fluorescence (PLIF) of the hydroxyl radical OH served as flame front marker, while two-dimensional, two-component particle image velocimetry (2D2C-PIV) was used to access the flow field. Both the OH-PLIF and 2D2C-PIV were applied simultaneously and spatially matched for correlated planar flame and flow field information at repetition rates up to 4 kHz. They probed the yz-plane of the burner device at the central line of the quenching wall ($x = 0$ mm). The individual diagnostics and their implementation are presented in the following subsections. Parts of the content of section 4.2.1 were published in Zentgraf et al. [E8] and are reused with permission (see appendix B), in a modified wording and partially extended by further technical and scientific details to fit the structure of this thesis. This concerns parts of sections 4.2.1.1, 4.2.1.2 and 4.2.1.4.
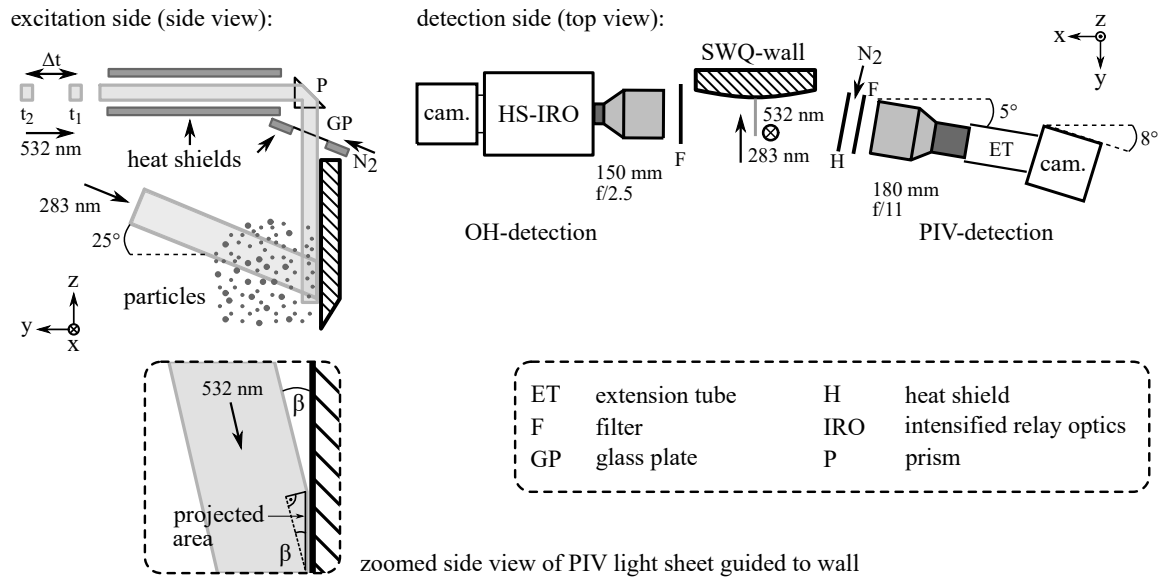
Figure 4.2: Laser diagnostic setup with the excitation shown in a side view and the detection optics in a top view. A zoomed view of guiding the PIV laser light sheet to the wall is embedded. Parts of this figure were published in Zentgraf et al. [E8] (parts of Fig. 1) and are reused with permission of Elsevier; reproduced in an adapted, extended version.

4.2.1.1 OH-PLIF

The implementation of the applied high-speed OH-PLIF diagnostics bases on the theoretical principles previously described in section 2.3.2.3 on laser-induced fluorescence. The electronic states of the combustion-formed OH radicals were excited by ultraviolet (UV) radiation at 35334.04 cm^{-1} ($\approx$ 283 nm), corresponding to their $Q_1(6)$ transition [46]. The required radiation around 283 nm was provided by a high-speed dye laser (Sirah Lasertechnik GmbH, Allegro), operated with Rhodamine R590 laser dye solved in ethanol. The resulting fundamental dye laser radiation around 566 nm was frequency-doubled to 283 nm using two consecutive, temperature-stabilized BBO crystals. The high-speed dye laser was optically pumped at 4 kHz pulse rate by a frequency-doubled Nd:YAG high-speed laser (Edgewave GmbH, Innoslab, IS 8II-E, 532 nm). The UV beam was guided to the SWQ burner facility using laser mirrors with high-reflective dielectric coating and fused silica prisms. To obtain a laser light sheet with spatially homogeneous intensity, the beam was initially expanded and collimated by a telescope of spherical lenses (focal length $f = -40$ mm and $f = +200$ mm) and subsequently cut by a spherical aperture to pick its high-intensity region. Then, the beam was compressed to a thin light sheet by a cylindrical lens ($f = +500$ mm) and additionally expanded in its height (cylindrical lens, $f = -200$ mm). Within the field of view (FOV), the light sheet finally featured a thickness of 450 μm by its $1/e^2$-bounds and a height of $\approx$ 35 mm. It had approximately 1 W laser power in the FOV, corresponding to an average pulse energy of $\approx$ 250 μJ/pulse. The UV sheet was guided to the FOV along the y-axis from top, inclined by an angle of $\approx$ 25° to the horizontal, as shown in Figure 4.2. This was necessary due to the limited available space near the SWQ burner facility.

The resulting OH-PLIF emission was captured perpendicular to the light sheet along the x-axis, as shown in the top view of Figure 4.2. The entire detection setup was mounted inclined by $\approx$ 10° to the horizontal for space reasons (not shown in Figure 4.2). The signal was collected by a customized UV lens (B. Halle Nachfl. GmbH, 150 mm, f/2.5) equipped with an interference filter (Laser Components, BP300-325, 305-340 nm transmission) to suppress ambient light and flame luminosity. A high-speed CMOS camera (Photron, Fastcam SA-X2, 480K-M4, 64 GB, 5 μs exposure) combined with a two-stage high-speed image intensifier (LaVision GmbH, HS-IRO, 100 ns gate) recorded the emission with one camera pixel corresponding to $\approx$ 22.5 μm in the FOV.

4.2.1.2 2D2C-PIV

The diagnostic application based on the fundamentals presented in section 2.3.2.1 and captured the y- and z-components of the velocity field. To trace the fluid motion, alumina nanoparticles (Al$_2$O$_3$, MSE Supplies LLC, nominal diameter 300 nm) were seeded to the premixed main flow of the SWQ burner. For this purpose, a special vibration bed seeder device was designed (see appendix A.1). The vibration was switched off directly prior to measurements to avoid potential flow oscillations by the seeder. For safety reasons, only the combustion air was laden with particles by the seeder and mixed with fuel afterwards. Following Equation (2.41), the seeding's relaxation time is $t_R \approx 1$ μs (20 °C) to $t_R \approx 0.3$ μs (2000 °C), estimated for air [31, p. 948] and $\rho_{Al_2O_3} = 3970$ kg/m^3 [113].

Mie-scattering at the dispersed particles was excited by two individual frequency-doubled Nd:YAG high-speed lasers (Edgewave GmbH, Innoslab, IS 16II-E) operated at 4 kHz with 532 nm output radiation. Each laser provided one pulse required for PIV, with both pulses temporally separated by $\Delta t = 10$ μs. High-reflective dielectric mirrors were used to guide the 532 nm beams in the optical setup. Further optical elements (e.g., lenses) featured an appropriate anti-reflection coating. A polarizing beam splitter plate was used to overlap both lasers and to control their energies by additional half-wave-plates arranged in each beam path prior to the splitter. Unused radiation was trapped by a water-cooled beam dump. Two cylindrical lenses (focal length $f = -30$ mm and $f = +250$ mm) were used to expand and subsequently collimate the height of the laser light sheet. Additionally, an approximately homogeneous intensity region was selected from both laser shots by cutting the edges with a vertical slit aperture. These light sheets were guided to a level above the burner facility by a periscope and their thickness was compressed using a cylindrical lens ($f = +700$ mm). Afterwards, light sheets were directed through the exhaust gas of the burner, approximately 300 mm above the FOV, and deflected downwards to the FOV by a fused silica prism (see side view in Figure 4.2). The prism's angle was set that the light sheets impacted the vertically aligned wall surface under a very shallow angle β, as shown in the zoomed side view in Figure 4.2. This procedure strongly expands the projected area of the laser light sheet at the wall. Thus, the laser power is disposed over a broad area on the wall. This minimized reflections at the wall on the one hand and ensured to properly illuminate the FOV all the way to the wall's surface on the other hand. The optical path through the exhaust gas as well as optical elements were protected by water-cooled heat shields to prevent damage and avoid additional beam steering bias to the light sheets. The prism was additionally shielded by a fused silica window, purged with a nitrogen flow (for cooling and cleaning from seeding particles). The concept of introducing laser light sheets from top of the SWQ burner was originally applied in Kosaka et al. [E3] for simultaneous OH and formaldehyde PLIF and proved feasible in suppressing wall reflections. It was adapted from Kosaka et al. [E3] in this thesis and applied to PIV. In the FOV, the resulting sheets had a thickness of ≈ 250 μm (within $1/e^2$-bounds) at 12 mm height with $\approx 225 - 390$ μJ/pulse (derived from average laser power of 0.9-1.55 W). The laser powers dropped by 20-25% over a few hours of operation. This was attributed to seeding contamination of the fused silica window progressively increasing during operation despite purging. The energy drop did not cause any apparent deterioration of the raw image quality or PIV results.

The Mie-scattered radiation was collected by a customized imaging optics consisting of an objective lens (Sigma, APO Macro DG HSM D, 180 mm, f/11) and an extension tube (≈ 180 mm length). The use of an extension tube allowed for an image magnification by a factor of ≈ 2.25. Consequently, each camera pixel (13.5 μm) represented ≈ 6 μm in the physical near-wall FOV. A bandpass filter (Edmund Optics Inc., #86-963, central wavelength 525 nm, FWHM 50 nm) in front of the objective lens aided suppressing both flame luminosity and ambient light. An additional heat shield, purged with nitrogen, was arranged in front of the filter to protect the imaging optics from thermal radiation (only ≈ 170 mm between filter and centerline of the wall). The signal was finally captured using a high-speed CMOS camera (Vision Research Inc., Phantom v2640, 288 GB RAM) operated in double frame mode. As depicted in the top view in Figure 4.2, the detection

setup was aligned in a Scheimpflug arrangement with 5° (objective lens) and 8° (camera) inclination to the x-axis, adapted from Renaud et al. [135]. This aided in minimizing the vignetting impact of near-surface seeding particles by the wall.

All laser systems were run at 4 kHz, while the imaging systems (OH-PLIF and 2D2C-PIV) either acquired at 50 Hz or 4 kHz. However, to avoid multiple exposures, cameras were always gated with 4 kHz. The 50 Hz recordings served as statistically independent samples while the 4 kHz recordings enabled investigation of transients.

4.2.1.3 Field of Views

The arrangement of the combined field of views (FOVs) for both the OH-PLIF and PIV diagnostic is shown in Figure 4.3. While the OH-PLIF extended over a range $(\Delta y,\ \Delta z) = (23.1\ \text{mm},\ 23.6\ \text{mm})$, the PIV FOV spanned $(\Delta y,\ \Delta z) = (10.6\ \text{mm},\ 10.9\ \text{mm})$. The smaller FOV of the PIV technique was centered to the FOV of OH-PLIF, as depicted in Figure 4.3(a). Both FOVs were arranged at the wall's centerline, i.e., apex of the curved plane, at $x = 0$ mm and included a certain proportion of the wall to ensure proper wall detection in the post-processing. To best cover the motion of the near-wall flame under turbulent conditions, two spatially overlapping FOVs were measured at different streamwise z-locations, as outlined in Figure 4.3(b). The OH-PLIF FOV is not shown in this schematic for reasons of clarity, however, it was arranged with respect to PIV as shown in Figure 4.3(a). For DME fuel, the spatial overlap was ≈ 5 mm (OP1 to OP3 in Table 3.1), while CH_4 operation (OP5 and OP6 in Table 3.1) overlapped by ≈ 2 mm. Basically, data of overlapping FOVs can be combined to increase ensemble statistics, however, this was not required for analysis in this thesis.

(a) combined FOVs   **(b)** overlapping upper and lower PIV FOVs

OH-PLIF
PIV
10.6
10.9   23.6
23.1
flame branch

flame front fluctuation
upper PIV FOV
overlap ≈2-5 mm
lower PIV FOV

□ PIV   ⊏⊐ OH-PLIF
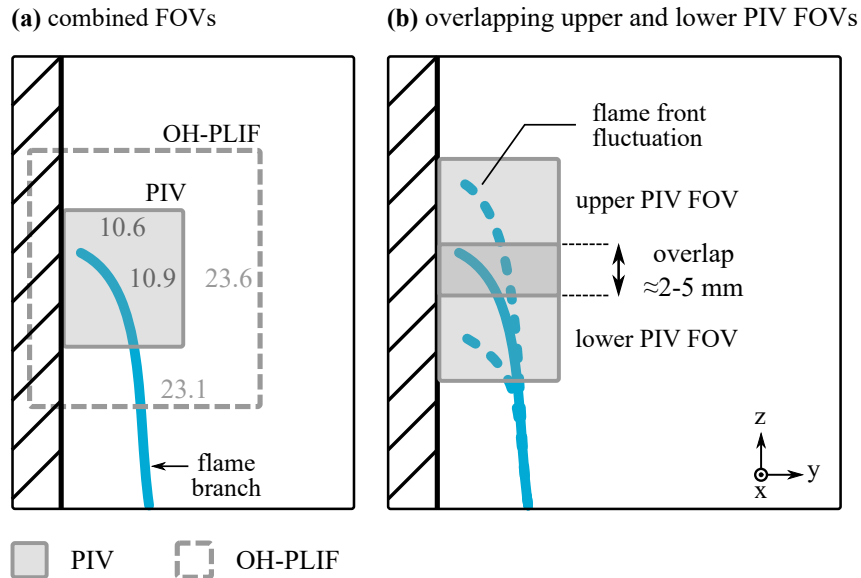
Figure 4.3: Spatial arrangement of the combined OH-PLIF and PIV FOVs for the flame and flow dynamics campaign (a) and the overlapping of upper and lower PIV FOVs for turbulent operation (b). All dimensions without unit are given in millimeters.

4.2.1.4 Synchronization and Matching

The lasers and detection systems were temporally synchronized as outlined by the schematic in Figure 4.4(a), using a digital pulse generator (Quantum Composers Inc., 9520 Series) and a PTUX hardware (LaVision GmbH). The laser pulse for OH-PLIF was temporally placed in the center between both PIV laser pulses, separated by $\Delta t = 10~\mu$s. This guaranteed for a proper temporal matching of both diagnostics. Exposures of the detection systems were correspondingly aligned to capture the pulses as shown in Figure 4.4(a). The temporal synchronization was checked by photodiodes (Thorlabs Inc., DET10A, 200-1100 nm), which were permanently mounted in both the OH-PLIF and PIV optical paths capturing low-energy reflections, and by a digital oscilloscope (Tektronix GmbH, TDS 3034B, 300 MHz).

The laser light sheets were spatially overlapped in the region of the FOV by using a specially designed detection optics shown in Figure 4.4(b). Both the PIV (532 nm) and OH-PLIF (283 nm) light sheets were guided to a fused silica cuvette ($20 \times 10 \times 45$ mm^3) filled with a mixture of purified ethanol and Pyrromethene 567 laser dye. The dye tracer concentration was kept very low to avoid significant laser absorption over the penetration depth of light sheets in the solution. As the high repetition rates of the lasers bleached the dye rapidly, the mixture had to be stirred during alignment. This was applied by a small stirrer coupled to an electrical motor. The resulting fluorescence signal was collected by a combination of achromatic lens ($f = +200$ mm) and objective lens (Nikon AF Nikkor, 50 mm, f/16, focused near infinity) and captured by a CMOS camera (Thorlabs Inc., DCC1545M-GL). Finally, light sheets of both diagnostics were overlapped by live monitoring the recorded fluorescence signal. Both the cuvette and detection optics were spatially fixed during alignment.

For spatial scaling of the recorded images, i.e., the transfer from pixels to mm-units, spatial calibration targets were applied (LaVision GmbH, 058-5 and a customized high-resolution target). The PIV and OH-PLIF detection setups were matched by a customized cone target manufactured from brass that was recorded simultaneously with both systems. The tip of the cone was set as common origin.

(a) temporal synchronization scheme:
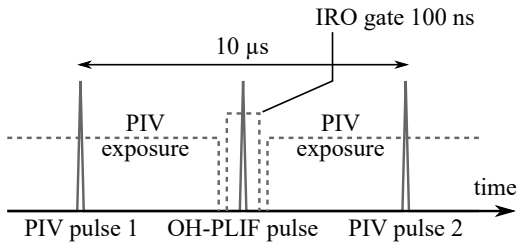
(b) optics for light sheet overlap (side view):
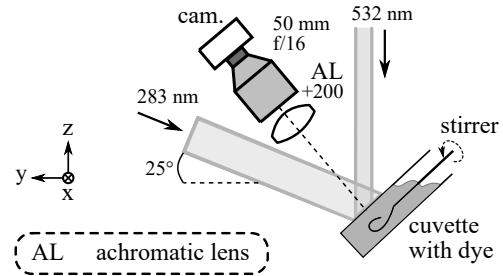
Figure 4.4: Schematic for (a) the temporal synchronization of lasers and detection systems and (b) customized detection system for light sheet overlap in the FOV region.

4.2.2 Data Processing

This section summarizes the data processing that was applied to derive the presented results. The entire data processing in this chapter was implemented using the software MATLAB R2020b[3] (The MathWorks, Inc.), unless otherwise stated. Parts of the content of section 4.2.2 were published in Zentgraf et al. [E8, E11] and are reused with permission (see appendix B), in a modified wording and partially extended by further technical and scientific details to fit the structure of this thesis. This concerns parts of sections 4.2.2.1 (reported in [E8]), 4.2.2.3 (reported in [E8, E11]) and 4.2.2.6 (reported in [E8]).

4.2.2.1 PIV Processing

For the evaluation of PIV raw images and the calculation of corresponding velocity fields, the commercial software DaVis 10.0.5 (LaVision GmbH) was applied in this thesis.

Prior to executing the actual PIV algorithm, several pre-processing steps were performed. As the quenching wall featured a minor angle relative to the detection system (either the wall or camera were not perfectly aligned vertical), raw images were first rotated slightly ($\approx 0.5 - 0.6°$) to exactly match the wall surface to the vertical axis of the camera chip. This step is not necessarily required, but convenient for any further post-processing. Subsequently, a time filter was applied to subtract the minimum over all images in the considered ensemble (equals ambient background subtraction). A geometric mask was applied to exclude the locations within the wall from further processing. Then, values below zero (due to previous filtering) were set to zero intensity. A non-linear *min-max filter* with 9 pixels width was applied for intensity normalization. Again, resulting values below zero were set to zero intensity, followed by a 3×3 Gaussian smoothing filter.

Finally, the PIV operation was performed. The algorithm executed 2 initial passes on a 48×48 interrogation window (IRW) with 50% overlap followed by 3 final passes on a 16×16 IRW at 75% overlap. This results in a final vector spacing of 23.5 μm with one IRW corresponding to ≈ 94 μm. Furthermore, a lower resolution case was processed with 96×96 initial passes, while final passes featured a 48×48 IRW (final vector spacing of 94 μm). The latter low-resolution case provided reduced spatial noise and was used for the visualization of vortex structures only (see sections 4.2.2.6 and 4.3.2.5). An intermediate level of anisotropic denoising (level 4/7) was selected. Common vector post-processing steps were applied to exclude erroneous velocities (vectors with correlation values < 0.9 and groups with less than 5 vectors were removed, universal outlier detection applied and empty spaces filled up).

This processing workflow applied for all data (laminar/turbulent, reactive/non-reactive) presented in this thesis. It was developed iteratively and provided the best possible PIV results, i.e., high correlation values at low velocity uncertainties.[4]

---

[3]Additional colormaps in this thesis were provided by the "matplotlib" MATLAB function [37].

[4]The PIV processing workflow used in this thesis was developed in close consultation with M.Eng. Alexander Nicolas and Dr. Brian Peterson from The University of Edinburgh. The fruitful discussions, advice and support is acknowledged here.

4.2.2.2 Estimation of the Wall Position

In FWI research, a proper determination of the quenching wall position is crucial. This planar imaging study estimated the wall position from non-reactive, non-seeded PIV raw images, as shown in Figure 4.5. Since a fraction of particles agglomerated at the wall's surface during operation, the wall is well visible in the recordings. The wall surface was assumed at the outer surface of wall-agglomerated particles, as depicted by the red dashed line in the zoomed view in Figure 4.5(b). This position was assigned $y = 0$ mm within this chapter and the wall is depicted by a gray rectangle in all views of two-dimensional fields. Based on this estimation, the wall-closest PIV vector information is located around 30 ± 10 μm (mean $\pm$ standard deviation) from the wall surface. As the PIV detection system featured a pixel resolution of ≈ 6 μm, this is expected sufficiently accurate. However, this is a first estimation of the wall-closest velocimetry positions, which will be refined by the turbulent boundary layer processing in section 4.2.2.4. As both PIV and OH-PLIF systems are spatially superposed, the wall position is thus equally known for OH-PLIF.

4.2.2.3 Flame Front and Quenching Point Detection

The detection of flame front and quenching point from OH-PLIF images in this thesis followed the basic ideas described in Jainski [79, p. 76]. The approach was modified to best fit to the data measured here and enhanced to classify different quenching topologies. A detailed description of the applied detection procedure is given in the following, with selected steps shown in Figure 4.6. All steps were applied to each individual sample recorded. Starting with the raw OH-PLIF image in Figure 4.6(a), it is evident that artifacts from the planar laser sheet remained in the PLIF recording. These involve the non-uniform global distribution of the excitation energy in the light sheet (see ① in Figure 4.6(a)), as well as local hot spots resulting in high-intensity stripes (see ② in Figure 4.6(a)). The latter observation is appointed to beam steering that is caused when the laser was passing the free flame branch opposite the quenching wall.
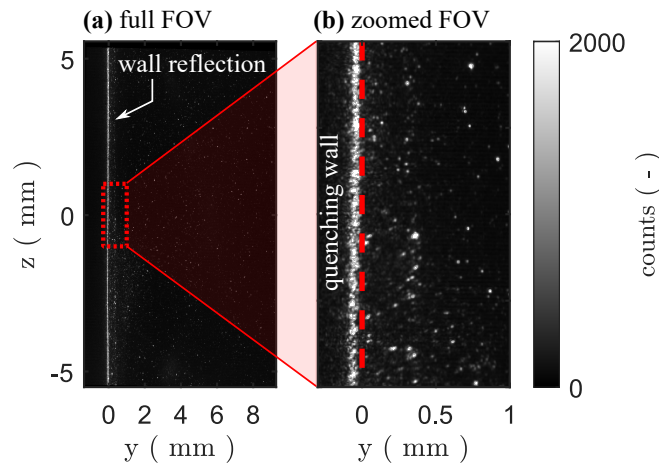
Figure 4.5: Estimation of the wall position $y = 0$ mm from PIV raw images: (a) global view of the entire FOV, (b) zoomed view with estimated wall position as red dashed line.
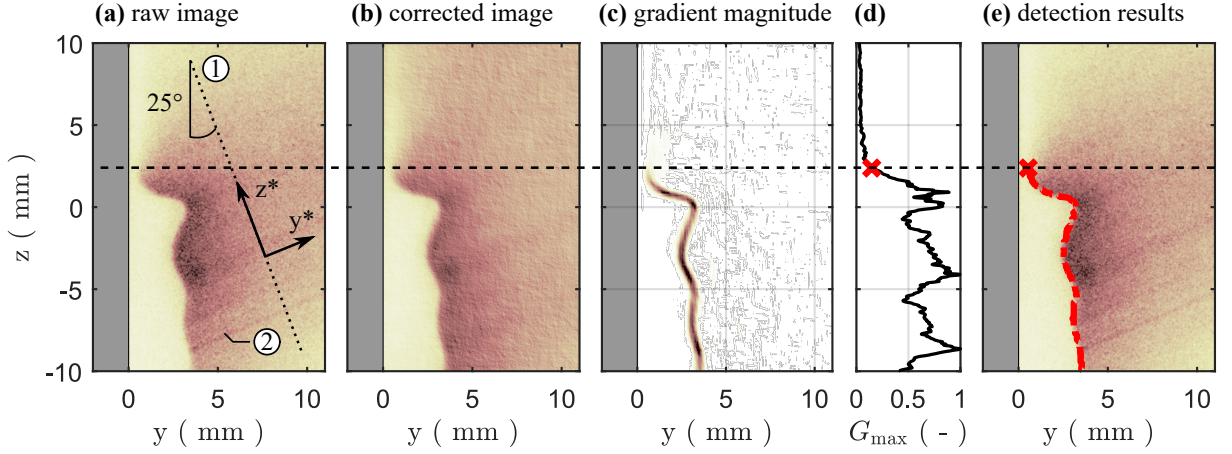
Figure 4.6: Visualization of selected steps for flame front and quenching point detection from OH-PLIF: (a) raw image, (b) intensity-corrected image, (c) gradient magnitude image $G(y,z)$, (d) z-trace of the line-wise maximum gradient magnitude G_{max} and (e) raw image with detected flame front (red dash-dotted line) and quenching point (red cross). Shown on an exemplary single shot with intensity in arbitrary units.

First, a laser-profile correction was performed. Since the laser light sheet was introduced to the ROI by 25° relative to the horizontal, all operations were done in a (y^*,z^*)-coordinate system rotated by 25°. For laser-profile extraction in z^*-direction, a region in the post-flame was selected where homogeneous OH concentration is assumed, i.e., only laser profile influences are apparent in the OH-PLIF signal (see ① in Figure 4.6(a)). To increase the robustness, the profile was not extracted at a single line but averaged over 50 pixels in the y^*-direction and additionally fitted by a Gaussian. For correction, each z^*-line was divided by the derived laser profile. Afterwards, the entire pre-processed OH-PLIF image was normalized to intensity values in the range $[0, 1]$. Second, remaining hot spots (see ② in Figure 4.6(a)) were removed by filtering the image in its Fourier-domain. As the hot spot artifacts were consistently aligned by 25° to the y-axis in the physical space, they could be identified in the corresponding Fourier-space and erased, i.e., by setting them zero. This selective filtering retained image resolution in the physical space best possible and finally resulted in an intensity-corrected image shown in Figure 4.6(b).

Subsequently, a 21×21 moving average filter was applied to further remove spatial noise. The image gradients in both spatial directions were calculated and formed to the two-dimensional field $G(y,z) = [(\partial I/\partial y)^2 + (\partial I/\partial z)^2]$ of the quadratic gradient magnitude. High gradient magnitudes, as depicted in Figure 4.6(c), appear to well capture the flame front shape. Hence, the flame front position was defined by the maximum of $G(y,z)$ in y-direction for each z-location. The resulting values G_{max} on the flame front trace were normalized ($\in [0, 1]$) and the quenching point was defined at the location, where the normalized values first exceeded a threshold when approaching from downstream. This is shown in Figure 4.6(d) with the trace of G_{max} as black solid line and location where the threshold is first exceeded as red cross. The threshold is set empirically and depends on the characteristics of the detection setup as well as the experimental conditions, like for example the flame structure. Here, the laminar cases were best captured using a threshold

at 0.35, while the turbulent featured 0.15. Finally, Figure 4.6(e) visualizes the OH-PLIF raw image with the flame front (red dash-dotted line) and quenching point (red cross) detected with the described procedure.

As will be evident from the results on flame dynamics discussed later in section 4.3.1, the quenching topologies do not always feature a well-defined side-wall quenching event with one prominent quenching point, as shown in Figure 4.7(a). In turbulent operation of the burner facility, the flame front is often flapping to the wall, forming a wall-parallel reaction zone. This is shown in Figure 4.7(b). In the scope of this thesis, it appeared practical to separate both phenomena and individually discuss their nature. Once, the flame front (red dash-dotted line) and quenching point (red cross) were detected, as outlined above, the flame front trace upstream the quenching point was scanned for further areas that were closer to the wall than the quenching point itself. Starting from the wall-closest point on the flame front trace, a corridor of 5 pixels in wall-normal y-direction was allowed as detection uncertainty of wall-parallel reactions and minor gaps (≤ 10 pixels in z-direction) between individually detected reaction zones were connected. In the end, an existence of at least one extended reaction zone (> 50 pixels in z-direction) was required to finally assign the sample to the class with wall-parallel reaction zones and only the biggest one was considered for further analysis. This is shown in Figure 4.7(b) with the onset and end of the wall-parallel reaction zone marked by blue circles. Otherwise, it was considered to be a typical side-wall quenching event (see Figure 4.7(a)). This distinction and the naming of these two cases will be discussed in detail in the results section 4.3.1.

For the evaluation of statistical ensembles, it appears practical to assess results using a coordinate system fixed to the quenching event, i.e., having the quenching onset at one common streamwise location $z = 0$ mm for all samples. This allows to analyze results with a sharp transition across the quenching event, from the unburnt to the burnt. Furthermore, it is expected to reduce bias from flame intermittency. This was achieved by shifting each sample in z-direction by its instantaneous position of quenching onset, as
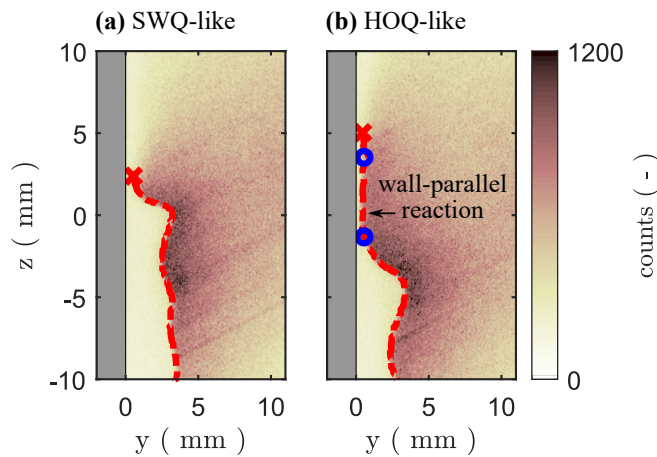
Figure 4.7: Exemplary classification of samples with respect to their instantaneous quenching topology: (a) a typical SWQ event with one prominent quenching point, (b) an extended wall-parallel reaction zone. Symbols: flame front (red dash-dotted line), quenching point (red cross), bounds of wall-parallel reaction zone (blue circles).
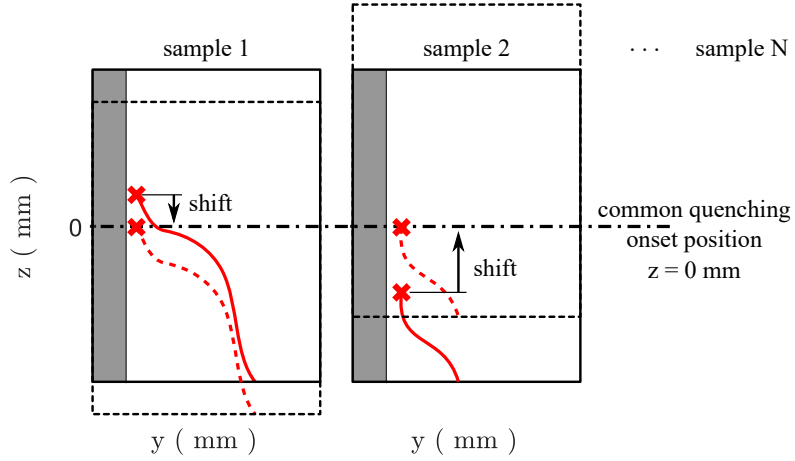
Figure 4.8: Schematic outlining the shift of fields in the quenching-point conditioning. Shifted fields are depicted with dashed lines, while original fields are shown as solid lines.

outlined by the schematic in Figure 4.8. For cases featuring a typical side-wall quenching event the quenching point served for conditioning, while for the cases with a wall-parallel reaction zone the quenching onset (lower blue circle in Figure 4.7(b)) was used. Ensemble statistics were then applied to these conditioned fields, named *quenching-point conditioned* in the remainder of this thesis. It is emphasized that quenching-point conditioning can be applied to all fields or measured scalars related to OH-PLIF or recorded simultaneously, e.g., derived from the simultaneous PIV. However, this conditioning leads to different field statistics in the z-direction, i.e., samples available at one z-location after shifting. The capabilities of this approach are presented in sections 4.3.1 and 4.3.2.

4.2.2.4 Turbulent Boundary Layer Processing

Turbulent boundary layers were processed using the fundamentals from section 2.1.3. The key parameter for assessing turbulent boundary layers in their (y^+,u_z^+)-space[5] is the friction velocity $u_{\tau, z}$. Following Equation (2.20), $u_{\tau, z}$ is defined at the wall's surface $y = 0$ mm. Thus, the gradient $d\langle U_z \rangle/dy$ should be defined as close to the wall as possible with the experimental data. Since the wall-closest region, i.e., the viscous sublayer, features a linear relation between velocity and wall distance, the near-wall gradient is assumed a constant that equals the slope of this linear curve.

In a first pre-processing step, a $(y, z) = (1, 11)$ moving average filter was applied to the velocity fields to reduce spatial noise in the streamwise z-direction, while preserving resolution in the wall-normal y-direction. Then, a linear fit was applied to the near-wall data on the first data points from the wall, with $d\langle U_z \rangle/dy$ set to its slope. This was an adaptive, iterative procedure and performed for each z-location separately. The number of considered points for fitting was scaled by the local kinematic viscosity ν. For ambient temperature T_0, 11 wall-closest data points were used (≈ 260 μm wall-normal

---

[5]According to the nomenclature in Figure 3.2, the streamwise velocity component is denoted by U_z. Thus, normalized values are termed u_z^+ in this thesis instead of u^+ common in literature.
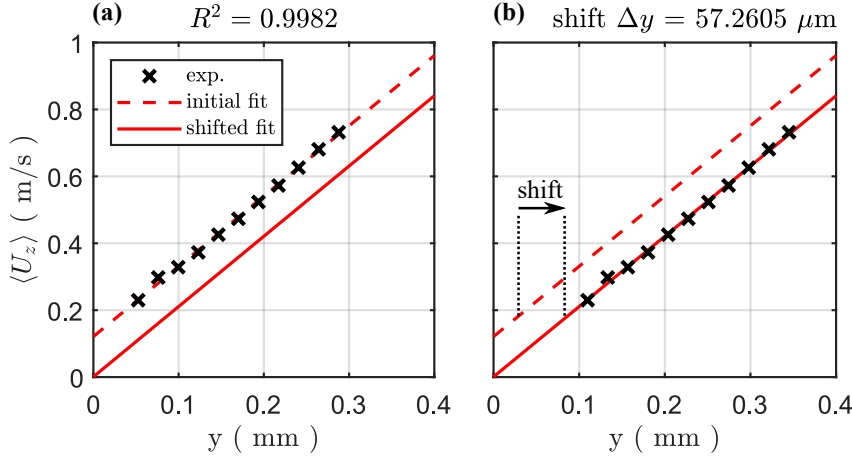
Figure 4.9: Exemplary linear fitting of near-wall data for estimation of $u_{\tau, z}$ from non-reacting experimental data: (a) initial fit featuring $R^2 = 0.9982$, (b) after a shift by Δy.

range), while for higher gas phase temperatures $1 + 10 \cdot \nu(T)/\nu(T_0)$ points were applied. This procedure proved very practical in the data analysis of reacting cases and enabled a robust estimation of $u_{\tau, z}$, as the boundary layer is thickening with rising temperature, i.e., increasing viscosity ν. As a quality factor, a coefficient of determination $R^2 \geq 0.99$ of the fit was demanded in processing to accept the fit results and assign $d\langle U_z\rangle/dy$ to the fit's slope. The iterative algorithm was moreover allowed to remove near-wall data points to optimize the R^2-values (up to maximum of 10 iterations). If the $R^2 \geq 0.99$ condition was not fulfilled, the respective z-location was excluded from further analysis in terms of turbulent boundary layers. Since such an approach is obvious for the problem at hand, similar interactive fitting procedures to determine the near-wall gradient $d\langle U_z\rangle/dy$ were previously applied by Jainski et al. [80] and Renaud et al. [135] in engine environments.

In addition to its linear behavior, the velocity u_z^+ needs to vanish at the wall's surface ($y^+ = 0$). However, as clearly evident from Figure 4.9(a), this was not perfectly the case with the experimental data. To correct this minor physical inconsistency, the data was additionally shifted in wall-normal direction by Δy to ensure that the fitted linear curve meets the origin (y^+, u_z^+) = (0,0), as shown in Figure 4.9(b). The final y^+ values were calculated on the shifted coordinate. In this example profile, a shift of $\Delta y \approx 57$ μm was applied. In average, correction-shifts of 70 ± 10 μm (mean $\pm$ standard deviation) for non-reacting and 105 ± 55 μm for reacting data were observed. Referring back to section 4.2.2.2, this offset Δy could also be interpreted as an uncertainty in estimating the real wall-position $y = 0$ mm from the PIV raw images.

4.2.2.5 Classification of Turbulence Anisotropy

For assessment of the turbulence anisotropy, the basics in section 2.1.2.2 were used. The application of these basics actually requires three-dimensionally resolved velocity information. However, the experimental velocimetry data measured in this thesis only featured two spatial components in the y- and z-direction. For this reason, it was assumed that the velocity fluctuation in x-direction is zero. Even though z is the streamwise direction and
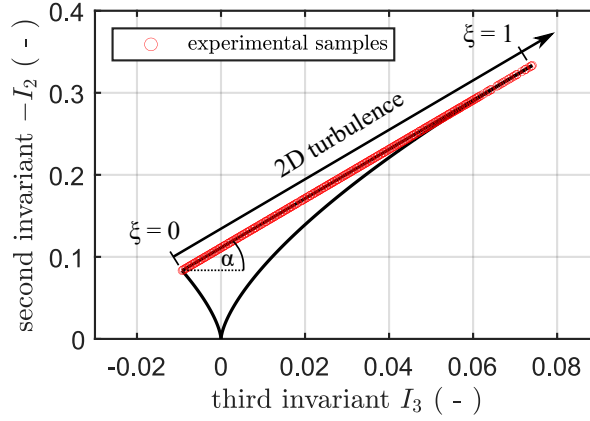
Figure 4.10: Exemplary invariant map for experimental, near-wall velocimetry data with only two velocity components and under non-reacting conditions.

the wall-normal coordinate y is most important for FWI studies, still some processes occur in x-direction. Thus, the simplification is not expected to entirely capture the nature of turbulence here but to provide a valuable insight into the contributions of the governing y- and z-components.

This simplification, i.e., $u'_x = 0$ (note: index notation u'_i used here for practical reasons), finally allowed to calculate the invariants I_2 and I_3 for experimental SWQ operation as

$$I_2(y,z) = -\frac{1}{2} \cdot \left[b_{yy}^2 + b_{zz}^2 + 2 \cdot b_{yz}^2 \right], \tag{4.1}$$

$$I_3(y,z) = \frac{1}{3} \cdot \left[b_{yy}^3 + b_{zz}^3 + 3 \cdot b_{yz}^2 \cdot (b_{yy} + b_{zz}) \right] \tag{4.2}$$

with the anisotropy tensor

$$b_{ij} = \frac{\langle u'_i \cdot u'_j \rangle}{\langle u'_y \cdot u'_y \rangle + \langle u'_z \cdot u'_z \rangle} - \frac{1}{3} \cdot \delta_{ij} \tag{4.3}$$

and both b_{ij} and u' being functions of the coordinate (y,z). As a direct consequence of the projection to the yz-plane, only states within the 2D turbulence region exist in the invariant map, as shown for experimental data in Figure 4.10. This limits the informative value of the invariant map and impeded an assessment of the turbulence anisotropy in its classical sense. For this reason and for further simplification, the states within 2D turbulence were expressed by a coordinate transformation [114, p. 39]

$$\xi(y,z) = I_3(y,z) \cdot \cos(\alpha) - I_2(y,z) \cdot \sin(\alpha) \tag{4.4}$$

that maps each state (I_3, I_2) to a scalar value ξ, as shown in Figure 4.10. In addition, values were normalized to $\xi \in [0, 1]$, with zero describing the state of 2D isotropy and unity the 1D turbulence. In the results section 4.3.2.4, the parameter ξ is used as measure for the dimension-related distribution of the turbulent kinetic energy on the one hand. On the other hand, it serves as an indicator for the structure of present vortices. As stated in the corresponding fundamentals section 2.1.2.2, flat energy ellipsoids near the 2D isotropy state could indicate elongated eddies (here $\xi \to 0$), while no preferred structure is likely for a stretched energy ellipsoid, i.e., near 1D turbulence (here $\xi \to 1$).

4.2.2.6 Identification and Characterization of Vortex Structures

Instantaneous vortex structures were identified by the Q-criterion as discussed in section 2.1.2.3. As this criterion bases on a calculation of local gradients, it is thus very sensitive to remaining spatial noise in the velocity fields. To minimize the impact of spatial noise on vortex detection, a PIV processing with 48×48 IRW size was used (see section 4.2.2.1). This procedure has proven robust for vortex detection and, despite the lower resolution, is considered feasible to reliably capture strong, energy containing vortex structures.

First, Q-value fields were calculated from the velocity fields by Equation (2.15). Equal to the previously discussed anisotropy (section 4.2.2.5) the Q-criterion requires three-dimensional velocimetry input, but the presented experimental data is two-dimensional. Again, a simplification was adapted and both the velocity component and the spatial gradient in x-direction were assumed to zero, i.e., $U_x = 0$ and $\partial/\partial x = 0$. This resulted in a kind of two-dimensional projection of the Q-criterion and Equation (2.15) simplified to

$$Q(y,z) = -\frac{1}{2} \cdot \left(\frac{\partial U_y}{\partial y}\right)^2 - \frac{1}{2} \cdot \left(\frac{\partial U_z}{\partial z}\right)^2 - \frac{\partial U_y}{\partial z} \cdot \frac{\partial U_z}{\partial y} \tag{4.5}$$

as a function of the spatial location (y,z). Despite this deviates from the original definition of the criterion and simplifies the three-dimensional nature of turbulence, it is considered to yield a valuable indicator for vortices. This is evident in the results discussed later in sections 4.3.2.5 and 4.3.2.6. As pointed out in section 2.1.2.3, the formulation in Equation (2.15) is only valid for incompressible flows. Despite combustion environments feature strong variations in local temperature and thus density, the flow can be considered incompressible if its *Mach number Ma* meets the condition $Ma^2 \ll 1$, according to Warnatz et al. [165, p. 21]. The Mach number $Ma = U/U_s$ defines a ratio of flow velocity U to its speed of sound U_s (for air: 347 m/s at 300 K, 634 m/s at 1000 K) [31, p. 50]. As the studied SWQ device features velocities up to about 5 m/s in the burnt exhaust gas, corresponding Mach numbers are very low and the flow is considered incompressible here. In turn, the used equations for the Q-criterion are valid.
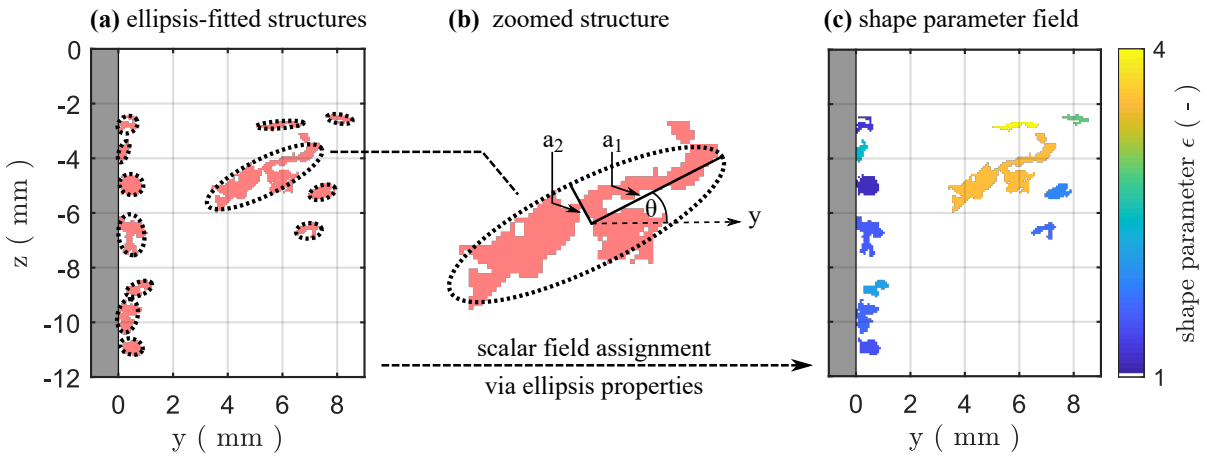
Figure 4.11: Further processing of vortex structures identified by Q-criterion. Exemplary, near-wall single-shot under reacting conditions.

As outlined in section 2.1.2.3, vortices are defined for values $Q > 0$. However, as experimental data always features some uncertainty, it is recommended to apply a threshold value larger than zero in order to ensure a robust detection of vortex structures. The empirical threshold used in this thesis is defined to the median of values $Q > 0$, means that only the stronger half of locations identified as vortices is taken into account. This threshold is derived from the entire ensemble, i.e., all samples, considered for a specific case (thresholds: non-reacting $\approx 13800 \text{ s}^{-2}$, SWQ-like $\approx 28000 \text{ s}^{-2}$, HOQ-like $\approx 30400 \text{ s}^{-2}$).

In a second step, the Q-value fields were binarized by the above thresholds, leading to fields featuring the value 1 at locations with detected vortex structures and 0 elsewhere. Subsequently, individual structures with less than 20 pixels on their boundary were removed. An example for a resulting binarized field describing vortex structures is shown in Figure 4.11(a) as light red areas. Averaging these binarized fields over samples of an ensemble resulted in a spatial vortex probability field ($\in [0, 1]$).

Binarized fields were further assessed by the MATLAB-function "regionprops" (MATLAB R2020b, The MathWorks, Inc.) that provides an advanced tool to measure properties of spatial features in binarized images. It was applied to assess the major and minor axis of an ellipse that fits to each individual structure, as well as the orientation of major axis to abscissa. The resulting fitted ellipsis assigned to each structure are shown in Figure 4.11(a) and Figure 4.11(b) in a zoomed view for one structure. Evidently, structures are approximated by their ellipse. Based on the ellipsis dimensions and orientation, each identified structure was assigned further characteristic values. This is visualized in detail by the zoomed view of one vortex structure in Figure 4.11(b). Here, a shape parameter $\epsilon = a_1/a_2$ was given by the ratio of major (a_1) to minor axis (a_2). The value $\epsilon = 1$ indicates spherical vortices, while $\epsilon > 1$ implies elongated structures. The bigger ϵ is, the more one-dimensional the structure is. An orientation parameter $\Theta = |\theta \cdot \frac{2}{\pi}|$ defined the absolute and normalized value of angle θ. Values at $\Theta = 0$ represent an orientation of the structures along the y-axis, i.e., in wall-normal direction, while $\Theta = 1$ would specify the major axis to be aligned in streamwise z-direction. These parameters (ϵ and Θ) were finally assigned to the corresponding vortex structures in two-dimensional fields, as outlined for ϵ in Figure 4.11(c). This enabled an ensemble-evaluation of these parameters in their spatial field. For example, the elongated structure shown in the zoomed view in Figure 4.11(b) was assigned a spatially constant value $\epsilon \approx 3.5$.

In addition, the vorticity $\vec{\omega}$, given by Equation (2.17), was used and simplified by

$$\omega_x(y,z) = \frac{\partial U_z}{\partial y} - \frac{\partial U_y}{\partial z} \tag{4.6}$$

to two dimensions and served to complement the Q-criterion with an information on rotation direction. For a two-dimensional flow in a right-handed coordinate system, positive vorticity is assigned to a counterclockwise rotation, while negative values indicate a clockwise rotation with respect to the out-of-plane direction [31, p. 156 ff.], here the x-direction. Each identified vortex structure was assigned a spatially averaged ω_x-value of the vorticities located within this individual structure. Finally, a positive averaged value was interpreted as a counterclockwise motion of the individual structure, while a negative average indicated that the structure likely rotates clockwise.

4.3 Results and Discussion

The results initially assess the flame dynamics for the studied burner in section 4.3.1. Consecutively, the related flow dynamics are comprehensively analyzed in section 4.3.2. This is done for operation conditions OP1 and OP2 in Table 3.1. Thus, the following consideration covers both a laminar and turbulent case. The turbulent condition is studied in more detail, while the laminar case serves for reference and is given for completeness. Parts of the content of section 4.3 were published in Zentgraf et al. [E8,E9] and are reused with permission (see appendix B), in a modified wording and partially extended by further technical and scientific details to fit the structure of this thesis. This concerns parts of sections 4.3.1 (reported in [E8]) and 4.3.2.2 (reported in [E9], however only minor aspects reused here and significantly extended with modified data processing).

4.3.1 Flame Dynamics

For the analysis of flame dynamics, only the transient OH-PLIF data recorded at 4 kHz are used. The near-wall flame front motion is first visualized for a selected time series and subsequently assessed in the transient's ensemble, including fluctuation characteristics.

4.3.1.1 Selected Time Series

Figure 4.12 outlines the instantaneous motion of the near-wall flame front (red dash-dotted line) for laminar inflow conditions by showing four consecutive single-shot images of an acquired transient. The time separation between the single-shots is chosen to 1 ms (every fourth image of the 4 kHz data shown). The flame branch quenching at the wall is clearly exhibiting a classical side-wall quenching scenario, with the near-wall flame front forming an acute angle to the wall. Flame front and quenching point hardly exhibit temporal fluctuation (see horizontal dashed line at $z = 0$ mm or previous section 3.2.2).
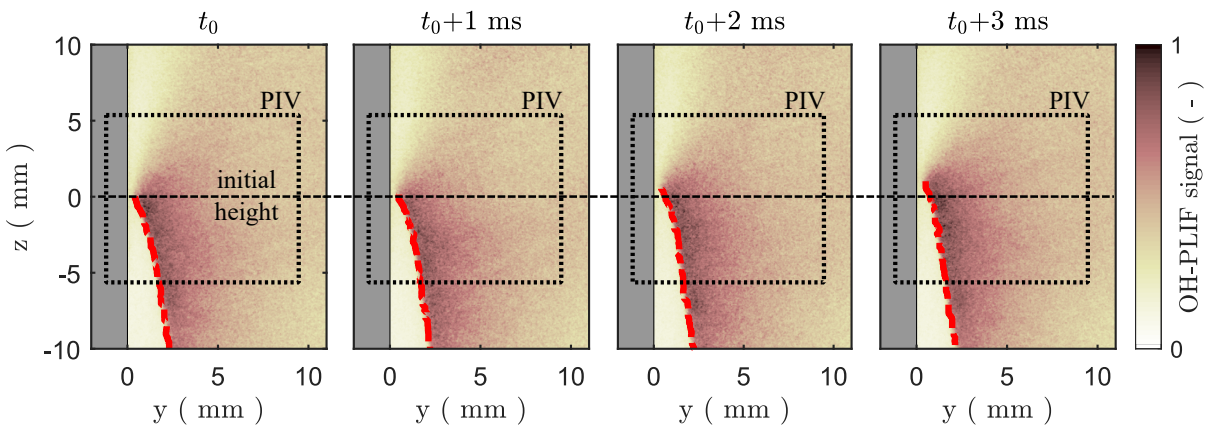
Figure 4.12: Transient OH-PLIF recordings for laminar inflow conditions from 4 kHz data with 1 ms increment shown (every fourth recording). Detected instantaneous flame front (red dash-dotted line), PIV-FOV (black dotted rectangle) and wall (gray area) superimposed.
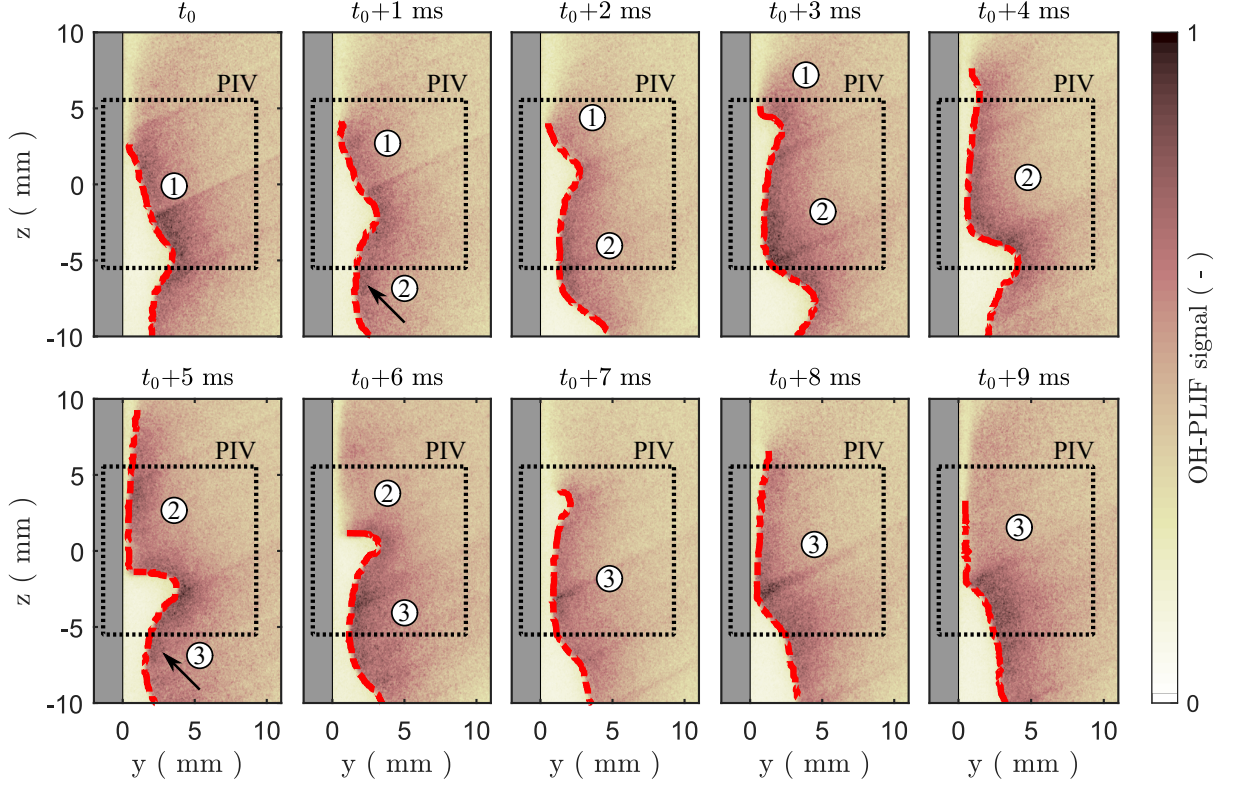
Figure 4.13: Transient OH-PLIF recordings for turbulent inflow conditions from 4 kHz data with 1 ms increment shown (every fourth recording). Detected instantaneous flame front (red dash-dotted line), PIV-FOV (black dotted rectangle) and wall (gray area) superimposed. This figure was published in Zentgraf et al. [E8] (parts of Fig. 3) and is reused with permission of Elsevier; reproduced in an adapted, extended version.

In Figure 4.13, the corresponding case under turbulent inflow conditions is visualized by ten consecutive images from the transient. In contrast to the laminar case, the turbulent features pronounced motion in the near-wall flame front and quenching point location within the 1 ms time increments. The flame front approaches the wall in wave-like, flapping movements. These *waves* can be seen as individual local reaction zones, labeled by ① to ③ in Figure 4.13. The transient sequence starts at t_0 with the zone ① developing a classical side-wall quenching topology, similar to the laminar operation. For this reason, such quenching topologies are named *SWQ-like* in the remainder of this thesis. With the sequence temporally emerging, the SWQ-like reaction zone ① moves downstream and extinguishes around $t_0 + 4$ ms. At the same time, a new reaction zone ② approaches the wall but rather quenches over a broad front, parallel to the wall, at $t_0 + 5$ ms. As this quenching topology is reminiscent of a head-on quenching (HOQ) phenomenon, the related scenarios are named *HOQ-like* here. This is supported by the decreasing OH signal behind the flame front from $t_0 + 5$ ms to $t_0 + 6$ ms, indicating stopped production and enthalpy loss. While this local HOQ-like event is transported further downstream and extinguishes around $t_0 + 7$ ms, another reaction zone ③ reaches the wall and forms a rather HOQ-like flame front at $t_0 + 9$ ms. However, effects are less pronounced than in zone ② and the OH signal behind the wall-parallel zone is lower, more typical for SWQ-like cases.

From the transient sequence in Figure 4.13, it is first evident that individual local reaction zones impact the wall with a time separation in the order of ≈ 5 ms ($\hat{=} 200$ Hz). These reaction zones are considered as independent local quenching events, suggesting statistical independence. Thus, results from 10 Hz and 50 Hz data used in this thesis are considered statistically independent with respect to the instantaneous quenching event. Second, it is observed that the quenching topology under turbulent conditions alters between SWQ- and HOQ-like scenarios. Such an alternating combination of both SWQ and HOQ phenomena was previously observed in numerical FWI studies in SWQ configurations by Heinrich et al. [76] for three-dimensional highly resolved LES and Palulli et al. [123] for an unsteady laminar flame at intermediate forcing frequencies (also termed SWQ-like and HOQ-like in [123]). In this thesis it is assumed that these two topologies are governed by different local transport processes and, besides a varying flame structure, are expected to result in different near-wall thermochemistry (see chapter 5). Therefore, a distinction between the two cases is considered of great importance and is consistently done in the remainder of this work by applying the classification in section 4.2.2.3.

4.3.1.2 Transient Ensemble Consideration

The near-wall flame motion is analyzed in a statistical ensemble by considering 4000 consecutive samples recorded at 4 kHz. This corresponds to a time series of one second and is expected to contain at least 200 statistical independent quenching realizations. The ensemble is used to derive a two-dimensional flame front probability, here called *flame brush*, and to assess the frequency of the wall-normal flame front fluctuation.

First, the (y,z)-locations of the detected flame front for each individual sample were turned into binary flame front fields (flame front locations: 1; outside: 0). The flame brush field was then derived by averaging all binary flame front fields, resulting in a probability of flame front occurrence (0: never observed; 1: always observed). Second, the wall-normal flame front fluctuation was derived from the temporal y-coordinate movement of the detected flame front within an upstream location shown by the two dashed, black lines in Figures 4.14(a) and 4.15(a), spanning ≈ 1 mm in z-direction. For robustness, the y-values of each individual flame front were averaged in this 1 mm z-range. A fast Fourier transform (FFT) was used to turn this information in the frequency domain.

Results for laminar inflow conditions are shown in Figure 4.14. The observation from transients in section 4.3.1.1, suggesting the laminar flame hardly fluctuates, manifests here, as the flame brush in Figure 4.14(a) forms a thin line. However, minor fluctuation remains due to Helmholtz resonances from the used SWQ burner geometry, as concluded in Jainski et al. [81]. Here, the standard deviation of the quenching point position in z-direction is $\sigma \approx \pm 495$ μm, slightly larger as the ± 200 μm previously reported for laminar operation of this burner [81, E3]. To minimize biasing influences of this sample-to-sample fluctuation, quenching-point conditioning (see section 4.2.2.3) is applied in Figure 4.14(b) to the detected flame fronts prior to flame brush calculation. This evidently results in a much sharper flame brush tip at $z = 0$ mm compared to the non-conditioned in Figure 4.14(a). Figure 4.14(c) visualizes the frequency of the wall-normal flame front fluctuation. As expected for laminar operation, only small amplitudes are observed in
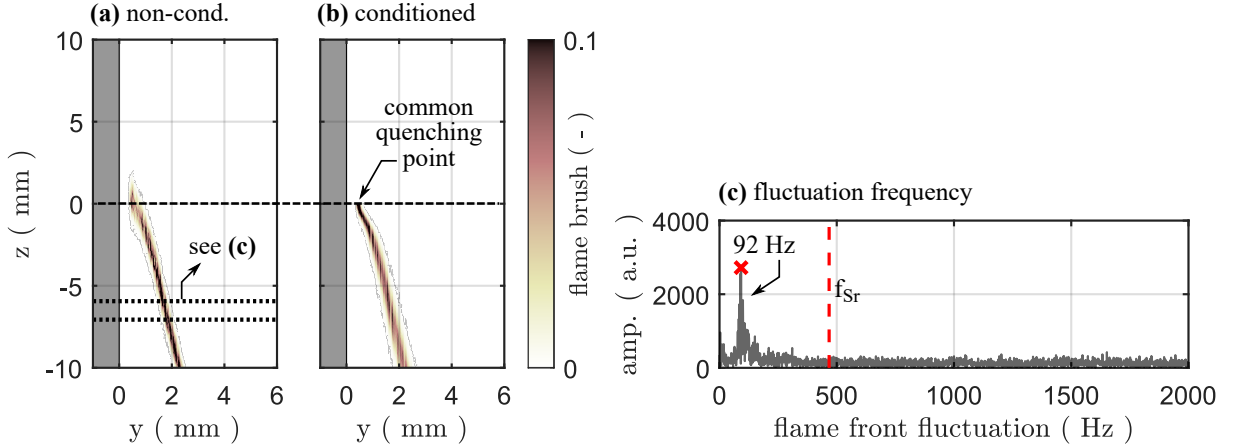
Figure 4.14: Flame brush for laminar inflow conditions for (a) all samples, (b) quenching-point conditioned samples. Frequency spectrum of wall-normal flame front fluctuation in (c). 4000 consecutive samples from 4 kHz data.

most frequencies. The pronounced frequency around 92 Hz is attributed to Helmholtz resonances reported above and compares well to 104 Hz stated in Jainski et al. [81]. The minor deviation is attributed to differences in the operation setpoint and data processing. As the flame is stabilized on a cylindrical ceramic rod, periodic vortex shedding in terms of a Kármán vortex street is expected and could impact the flame motion. Following the fundamentals in section 2.1.4, a vortex shedding frequency $f_{Sr} \approx 468$ Hz is derived from the rod's diameter $L = 1$ mm and an inflow velocity $U_z \approx 2.5$ m/s (see Figure 3.3). The corresponding Strouhal number is derived to $Sr \approx 0.187$ according to Fey et al. [58] with $Re \approx 165$ for the cylindrical rod. In Figure 4.14(c), no increased amplitude is evident in the frequency spectrum around f_{Sr} (see red dashed line), i.e., there is no impact of vortex shedding from the flame-holder rod to the near-wall flame front motion.

For turbulent inflow conditions, Figure 4.15(a) outlines the flame brush for all 4000 samples without any classification in SWQ-/HOQ-like topologies or quenching-point conditioning. Figure 4.15(b) shows the flame brush for non-conditioned SWQ-like samples, while Figure 4.15(c) depicts the corresponding quenching-point conditioned flame brush. Similarly, Figure 4.15(d) and (e) outline flame brushes of non-conditioned and quenching-point conditioned HOQ-like samples. This consideration underlines the capability of the quenching-point conditioning. While the non-conditioned SWQ- and HOQ-like flame brushes extend $10 - 15$ mm in z-direction close to the wall and do not feature a defined quenching onset, the corresponding quenching-point conditioned cases result in a sharp, well-defined transition from the unburnt to the burnt at $z = 0$ mm. Thus, quenching-point conditioning is expected to significantly aid the statistical evaluation in the following sections. Using non-conditioned fields is expected to wash out spatial information and very likely impedes a proper discrimination of the SWQ- and HOQ-like phenomena. No pronounced frequencies are evident in flame motion in Figure 4.15(f). The amplitudes are ≈ 5 times higher compared to the laminar case and continuously decrease reaching 1000 Hz. There is no peak observed near the vortex shedding frequency f_{Sr} (see red dashed line). This behavior suggests that the fluctuations originate from turbulence.

75
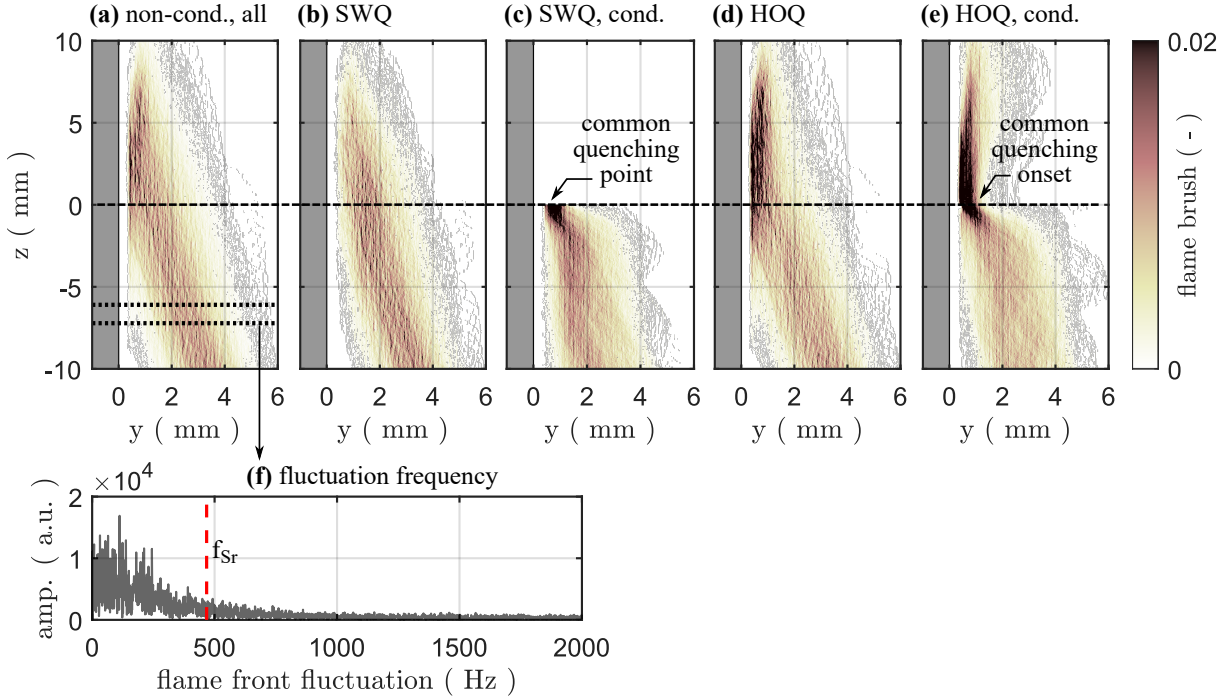
Figure 4.15: Flame brush for turbulent inflow conditions for (a) all samples, (b) non-conditioned SWQ-like, (c) quenching-point conditioned SWQ-like, (d) non-conditioned HOQ-like, (e) quenching-point conditioned HOQ-like. Frequency spectrum of wall-normal flame front fluctuation in (f). 4000 consecutive samples from 4 kHz data.

4.3.2 Flow Dynamics

The section on flow dynamics evaluates different transport processes governing the near-wall quenching reaction. Particular attention is on a distinction between SWQ- and HOQ-like cases, as classified for turbulent operation in section 4.3.1. Here, the considered statistical ensemble comprises 868 samples with SWQ-like operation (equals 43.4%) and 1132 HOQ-like samples (equals 56.6%), which approximates an equal share between both events. The laminar case is only discussed briefly as a general benchmark case and for completeness. The section first gives a basic characterization of the governing flow fields. One focus is on accessing the boundary layers in the near-wall regions. Length scales are analyzed and used to classify the present combustion regimes. Furthermore, near-wall anisotropy and vortex structures are assessed. The section finally concludes with a consideration of transient phenomena. All results discussed in this section, except the last section 4.3.2.6 on transients, apply statistically independent, quenching-point conditioned data at 50 Hz.

4.3.2.1 Basic Flow Characterization

Fundamental flow field metrics are given in Figure 4.16, for laminar inflow conditions. Figure 4.16(a) outlines the quenching-point conditioned flame brush as derived in section 4.3.1 but for 1000 samples recorded at 50 Hz, with the trace of its centroid superimposed as red dash-dotted line. It is derived by calculating the flame brush centroid in y-direction
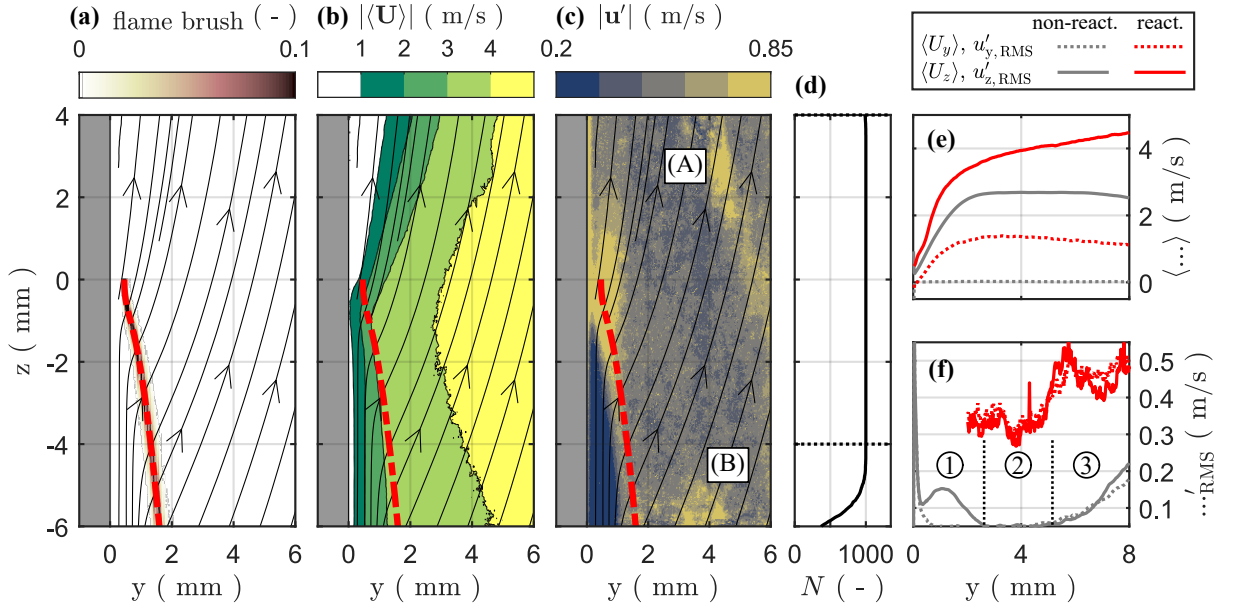
Figure 4.16: Basic, quenching-point conditioned flow field metrics for laminar inflow: (a) flame brush, (b) ensemble-averaged $|\langle\mathbf{U}\rangle|$ and (c) fluctuating velocity magnitude $|\mathbf{u}'|$, (d) samples N. (a)-(c) reacting case with flame brush centroid (red dash-dotted line) and ensemble-average velocity streamlines. Ensemble-averaged (e) and fluctuating velocity profiles (f) at $z = 0$ mm. Samples: 300 non-reacting; 1000 reacting.

for each z-location. As evident from Figure 4.16(a) this trace well-matches the narrow flame brush (i.e., fully overlaps it) and thus appears to provide a good measure of the mean flame front. Figure 4.16(b) shows isolines of the ensemble-averaged velocity magnitude defined as

$$|\langle\mathbf{U}\rangle| = \sqrt{\langle U_y\rangle^2 + \langle U_z\rangle^2} \tag{4.7}$$

with the ensemble-averaged, quenching-point conditioned y- and z-velocity components $\langle U_y\rangle$ and $\langle U_z\rangle$. It is observed that the isolines of $|\langle\mathbf{U}\rangle|$ contract approaching the quenching point and expand downstream $z = 0$ mm. Within the unburnt pre-quenching areas, streamlines are wall-parallel and perfectly follow the streamwise z-direction. Approaching the flame front, thermal expansion is accelerating the flow in flame-normal direction, forcing an increase in both velocity components. Thus, streamlines are moving from the wall. Figure 4.16(c) outlines the related fluctuating velocity magnitude, expressed by

$$|\mathbf{u}'| = \sqrt{(u'_{y,\,\text{RMS}})^2 + (u'_{z,\,\text{RMS}})^2} \tag{4.8}$$

with $u'_{y,\,\text{RMS}}$ and $u'_{z,\,\text{RMS}}$ defining the RMS of the instantaneous fluctuations u'_y and u'_z according to Equation (2.5). Despite Figure 4.16(c) presents laminar conditions, velocity fluctuations exist due to a remaining unsteadiness from the inflow (Helmholtz resonances) and intermittency of the flame. In the near-wall unburnt flow, values are < 0.2 m/s and increase to $0.3 - 0.55$ m/s in the burnt. They are highest near the quenching point ($z = 0$ mm, $y < 1$ mm), likely influenced by the prehistory of the tip movement. Some high values are appointed to either imaging artifacts (A) or low statistical samples (B) and need to be evaluated carefully. Figure 4.16(d) gives the number of available velocimetry

samples N for averaging with respect to z-direction, which is $N = 1000$ within the majority of locations but decreases for $z < -5$ mm due to quenching-point conditioning. Figure 4.16(e) outlines profiles of the components $\langle U_y \rangle$ (dashed lines) and $\langle U_z \rangle$ (solid lines) in wall-normal y-direction at the common quenching height $z = 0$ mm, averaged over 500 μm in z-direction. Figure 4.16(f) correspondingly reports the velocity fluctuations $u'_{y,\,\mathrm{RMS}}$ and $u'_{z,\,\mathrm{RMS}}$. Gray lines depict non-reacting conditions, while red lines visualize the corresponding reacting cases. Like in Zentgraf et al. [E8], three characteristic zones are defined for non-reacting conditions. First, a zone closest to the wall where the boundary layer evolves, called *boundary layer zone* (see ①). Second, a region that is expected to represent an undisturbed flow, called *bulk zone* (see ②). For turbulent inflow conditions, this area features the impact of grid-generated turbulence only, while it captures a measure for remaining flow unsteadiness for laminar operation. Third, an area where the influence of the ceramic rod wake for flame stabilization gets apparent, called *wake zone* (see ③). For the non-reacting flow (gray lines), the boundary layer zone ① features increasing $\langle U_z \rangle$ and elevated $u'_{z,\,\mathrm{RMS}}$ values. The wall-normal component remains at $\langle U_y \rangle \approx 0$ m/s for all wall distances. In the bulk zone ②, a constant value of $\langle U_z \rangle \approx 2.7$ m/s is reached, while $u'_{z,\,\mathrm{RMS}}$ and $u'_{y,\,\mathrm{RMS}}$ remain close to zero. This underlines that the underlying bulk flow features negligible fluctuation and can be appointed to a laminar behavior. Finally, $\langle U_z \rangle$ is slightly decreasing and both fluctuation components are increased in an equal manner within the wake zone ③. Under reacting conditions (red lines), both $\langle U_z \rangle$ and $\langle U_y \rangle$ rise due to the reaction's thermal expansion. Velocity fluctuations are only considered for $y > 2$ mm, to minimize the impact of flame intermittency, with their values around $0.3 - 0.55$ m/s.
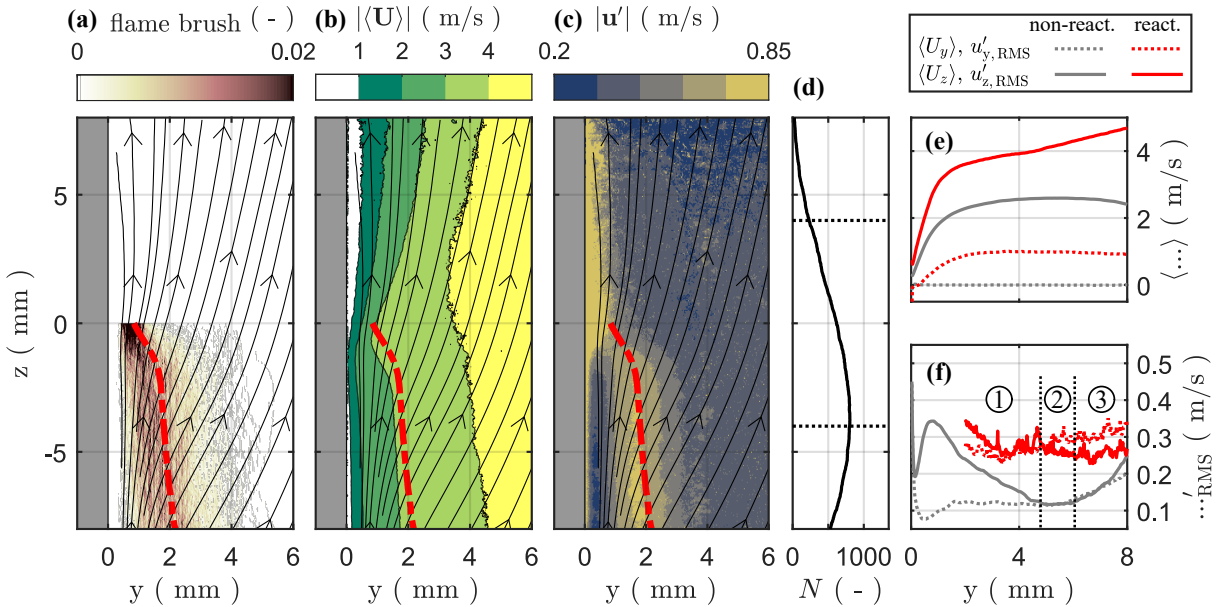
Figure 4.17: Basic, quenching-point conditioned flow field metrics for turbulent inflow, SWQ-like: (a) flame brush, (b) ensemble-averaged $|\langle \mathbf{U} \rangle|$ and (c) fluctuating velocity magnitude $|\mathbf{u}'|$, (d) samples N. (a)-(c) reacting case with flame brush centroid (red dash-dotted line) and ensemble-average velocity streamlines. Ensemble-averaged (e) and fluctuating velocity profiles (f) at $z = 0$ mm. Samples: 300 non-reacting; 868 reacting.

Corresponding flow metrics for turbulent inflow conditions are visualized in Figures 4.17 (SWQ-like) and 4.18 (HOQ-like). Comparing these turbulent cases to the laminar, it is evident that they reproduce several basic characteristics found in the laminar. First, the flame brush centroid appears to well-capture a measure for the mean flame front position. Second, the streamlines are aligned wall-parallel in the unburnt flow and are forced in wall-normal direction approaching the flame front. Third, isolines of $|\langle \mathbf{U} \rangle|$ are contracted approaching the quenching location and expand beyond. However, some differences to the laminar are observed. First, the fluctuating velocity magnitudes $|\mathbf{u}'|$ are more pronounced within the flame brush area, directly evident by comparing Figures (a) to (c). These increased $|\mathbf{u}'|$-values are clearly appointed to the more intense flame intermittency in the turbulent cases. Second, the non-reacting y-profiles of the fluctuating velocity, observed in Figures (f), feature increased values. The impact of the boundary layer zone ① emerges to $y = 5$ mm at approximately 2.5 times higher values for $u'_{z,\text{RMS}}$, clearly characterizing the presence of a turbulent boundary layer. Also within the bulk zone ②, values are ≈ 2.5 times higher than in the laminar, appointed to the turbulence generating grid used. This corresponds to a turbulence intensity $u'_{z,\text{RMS}}/\langle U_z \rangle \approx 4.5\%$ in zone ② [E8]. Due to a decay of the free-stream turbulence, it is slightly decreased compared to the 6-7 % stated in Jainski et al. [83] for the burner's nozzle exit (see also section 3.2.3).

Comparing the SWQ-like topology (Figure 4.17) with the HOQ-like (Figure 4.18), it is first observed that both cases behave quite similar for the pre-quenching regions ($z < 0$ mm). However, for $z \geq 0$ mm, several features are observed that clearly distinguish both cases. Isolines of the ensemble-averaged velocity magnitude $|\langle \mathbf{U} \rangle|$ are located closer to the wall
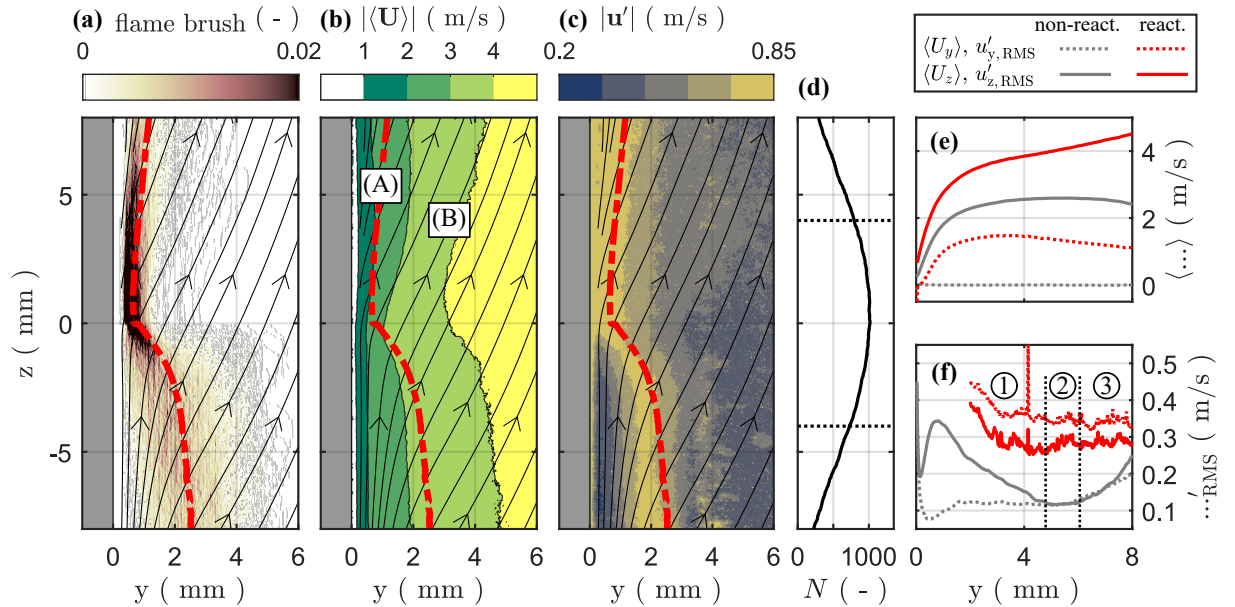
Figure 4.18: Basic, quenching-point conditioned flow field metrics for turbulent inflow, HOQ-like: (a) flame brush, (b) ensemble-averaged $|\langle \mathbf{U} \rangle|$ and (c) fluctuating velocity magnitude $|\mathbf{u}'|$, (d) samples N. (a)-(c) reacting case with flame brush centroid (red dash-dotted line) and ensemble-average velocity streamlines. Ensemble-averaged (e) and fluctuating velocity profiles (f) at $z = 0$ mm. Samples: 300 non-reacting; 1132 reacting.

for the HOQ-like case (see Figure 4.18(b), marked by (A)) compared to the SWQ-like in Figure 4.17(b). This suggests higher near-wall velocities and a potentially increased convective z-transport for HOQ-like topologies in the vicinity of the wall. Also, the fluctuating velocity magnitudes $|\mathbf{u'}|$ are stronger in the HOQ-like, indicating higher mixing rates. Additionally, streamlines in HOQ-like topologies are more forced to the wall-normal direction than for the SWQ-like, marked by (B), suggesting a transport with preferential y-direction. Finally, slightly more velocimetry samples N are available for the HOQ-like scenario in the range $z \in [-4\text{ mm}, 4\text{ mm}]$, which is focused in the following sections.

From this initial comparison of fundamental flow metrics, it is already evident that the SWQ- and HOQ-like topologies are likely different in their transport behavior. The major finding of this section is that the HOQ-like case suggests increased convective transport in both y- and z-direction and higher mixing rates than the SWQ-like.

4.3.2.2 Boundary Layers

Initially, boundary layers for the laminar case are briefly discussed by their streamwise evolution in Figure 4.19, with (a) and (c) showing the FWI region and wall leading edge under non-reacting conditions, while (b) outlines the FWI region with reaction. Solid black lines depict the analytical δ_{99}-thickness of a laminar boundary layer, as defined by Equation (2.18), using $x = z_{\text{abs}}$ and $U_\infty = \langle U_{z,\infty} \rangle$. The relevant length for boundary layer evolution is defined as z_{abs} starting at the leading edge of the wall, while the relevant bulk flow velocity $\langle U_{z,\infty} \rangle \approx 2.6$ m/s is extracted at a position $y \in [8.5\text{ mm}, 9.5\text{ mm}]$ and $z_{\text{abs}} \in [0\text{ mm}, 2\text{ mm}]$ as spatial average. Since this analytical solution is only derived for comparison of non-reacting conditions, the kinematic viscosity is approximated by air at ambient conditions (1 atm, 20 °C) as $\nu = 1.516 \cdot 10^{-5}$ m^2/s [31, p. 948]. The dotted black line describes δ_{99} directly derived from the experimental data, i.e., the isoline, where 99% of the non-reacting bulk flow velocity $\langle U_{z,\infty} \rangle$ is reached. For the reacting case this isoline at $0.99 \cdot \langle U_{z,\infty} \rangle \approx 2.57$ m/s is equally shown as a measure for the boundary layer, following the idea of Jainski et al. [83] who used a 95%-criterion for robustness.

Starting with the non-reacting case at the leading edge of the wall (Figure 4.19(c)), both traces of δ_{99} deviate. The analytical boundary layer thickness is smaller than the value directly derived from the experiment. The deviation originates from the sharp leading edge of the wall in the experiment that cuts the oncoming flow and causes an acceleration (see feature ① in Figure 4.19(c)), vortex shedding and some recirculation near the edge. However, in the FWI region in Figure 4.19(a), both boundary layer traces of the δ_{99}-thickness match perfectly. This suggests that the imperfection caused by the leading edge of the wall vanishes until reaching the FWI region. It is concluded that the theoretical view of a flat plate with longitudinal inflow well fits to the laminar operation conditions in the investigated SWQ burner, despite the wall features a slight curvature in x-direction (see section 3.1). Under reacting conditions shown in Figure 4.19(b), the experimentally derived δ_{99}-trace is contracting when approaching the quenching point and expands downstream. However, as δ_{99} is defined by an isoline, this boundary layer evolution merely mimics the isoline behavior previously discussed in section 4.3.2.1.
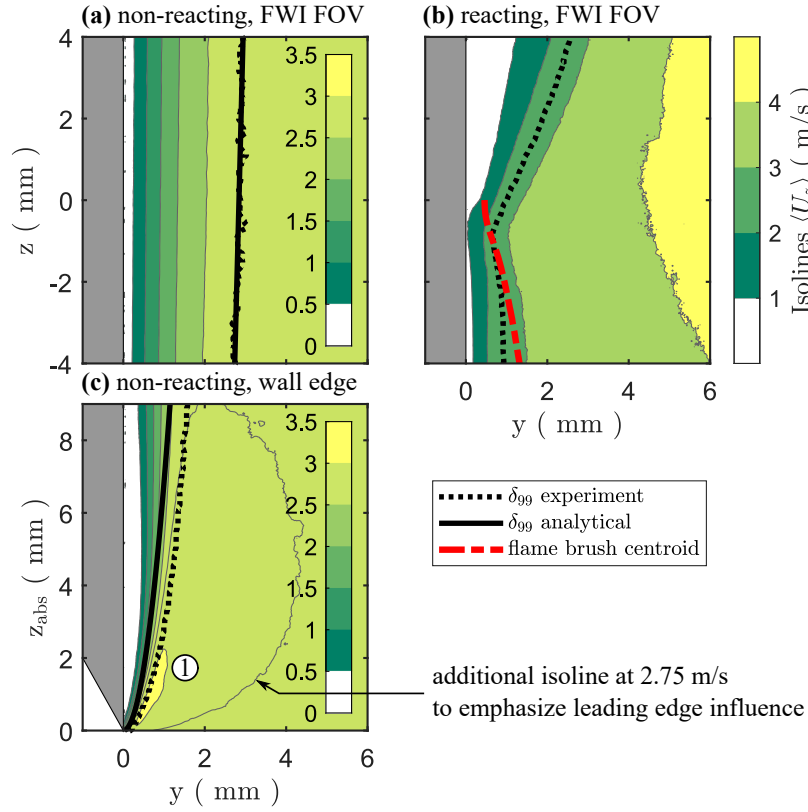
Figure 4.19: Isolines of $\langle U_z \rangle$ with streamwise boundary layer trace for different FOVs at laminar inflow: FWI region (a) non-reacting, (b) reacting and the wall leading edge, non-reacting (c). Fields in (a) and (c) feature own color scale embedded. Samples: 300 non-reacting; 1000 reacting.

In the following, a detailed analysis of the turbulent boundary layer is given. These considerations base on the fundamentals in section 2.1.3 and the post-processing outlines in section 4.2.2.4.

The streamwise evolution of turbulent boundary layers is discussed by Figure 4.20, for different FOVs and both non-reacting and reacting conditions. Dotted black lines outline the $y^+ = 5$ trace, while solid black lines give the $y^+ = 10$. Normalized values in the (y^+, u_z^+)-space are used according to Equations (2.20)-(2.22). For reacting cases, the kinematic viscosity in these equations is considered a function of local gas phase temperature $\nu(T)$. This approach follows the descriptions in Alshaalan and Rutland [8], who considered the locally calculated friction velocity $u_{\tau, z}$ for each streamwise location as the appropriate value for normalization. First, the evolution under non-reacting conditions in Figure 4.20(d) and (a) is discussed. Similar to the laminar case, the leading edge of the wall ($z_{\mathrm{abs}} = 0$ mm) disturbs the early development of the boundary layer (see feature ①). For this reason, only y^+-traces for $z_{\mathrm{abs}} > 1$ mm are given in Figure 4.20(d). Beyond $z_{\mathrm{abs}} > 5$ mm the evolution seems unbiased and the y^+-traces appear to be converged to constant values of ≈ 465 μm for $y^+ = 5$ and ≈ 935 μm for $y^+ = 10$. These values do only change slightly as the turbulent boundary layer further evolves to the corresponding FWI region, shown in Figure 4.20(a). At $z = -4$ mm, $y^+ = 5$ equals ≈ 440 μm, while at
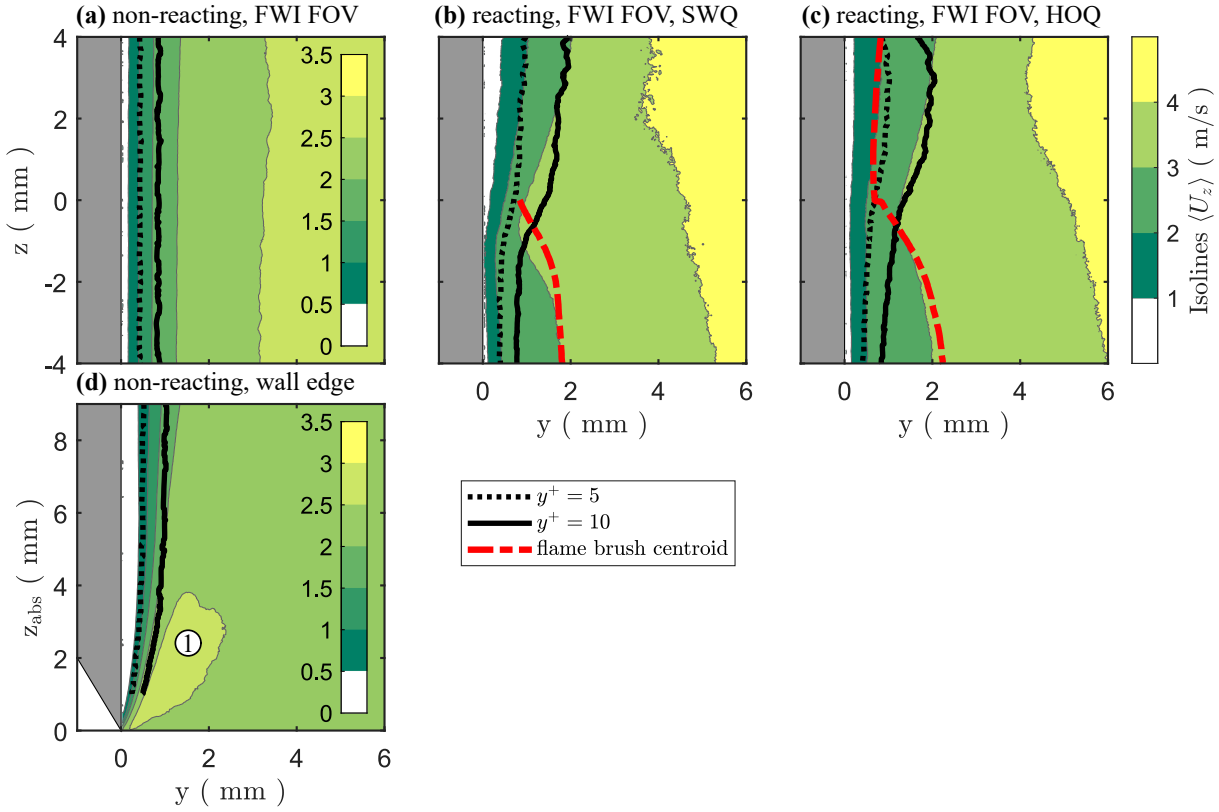
Figure 4.20: Isolines of $\langle U_z \rangle$ with streamwise boundary layer trace for different FOVs at turbulent inflow: FWI region (a) non-reacting, (b) reacting SWQ-like, (c) reacting HOQ-like and the wall leading edge, non-reacting (d). Fields in (a) and (d) feature own color scale embedded. Samples: 300 non-reacting; 868 SWQ-, 1132 HOQ-like reacting.

$z = 4$ mm, it corresponds to ≈ 425 μm. At a flat plate, literature [145, p. 31 ff.] would actually expect a slowly growing viscous sublayer with thickness $\delta_v \propto \ln(z)$ for increasing z-distance. This is not evident in the studied burner. One reason could be that the turbulent boundary layers are not resulting from a transition of laminar ones but rather from an inflow with grid-generated turbulence cut by the wall's leading edge. Thus, they may behave different to a classical turbulent boundary layer that develops from a laminar one.

For reacting, SWQ-like conditions the z-evolution is shown in Figure 4.20(b). Approaching the quenching point, it is clearly observed that the y^+-traces feature constant thickness up to $z = -1$ mm. Here, $y^+ = 5$ equals $y \approx 480$ μm and well-matches to the non-reacting values reported above. Therefore, it is concluded that the inner structure of turbulent boundary layers upstream of quenching is not affected by the SWQ-like reaction. However, quenching impacts the traces for $z > -1$ mm and forces increasing boundary layer thickness. The increase is strongest for $z \in [-1 \text{ mm}, 1 \text{ mm}]$. A similar behavior is evident in the HOQ-like case in Figure 4.20(c). However, boundary layers already start to thicken further upstream the quenching onset, clearly observed in the continuously growing $y^+ = 10$-trace. Both Cheng et al. [34] and Ng et al. [118] experimentally studied combustion in turbulent boundary layer flows (velocity by *laser Doppler velocimetry*, LDV)

and, among other aspects, found that the presence of combustion thickens the boundary layer due to the reaction's heat release. This corresponds well to the observations made in this thesis.

Figure 4.21 directly compares the turbulent boundary layer traces for the SWQ- and HOQ-like case and benchmarks them with the non-reacting. As pointed out above, the reacting SWQ-like perfectly matches the non-reacting up to $z = -1$ mm. For $y^+ = 5$, the HOQ-like well-follows the SWQ-like evolution but features a slightly increased thickness for $z \in [-3 \text{ mm}, -1 \text{ mm}]$. This trend clearly manifests in the trace at $y^+ = 10$ (see ① in Figure 4.21(b)). These results suggest that SWQ-like topologies feature a slightly steeper thickening of the boundary layer when evolving across the quenching location.

This behavior is examined in more detail by analyzing individual factors influencing the y^+-evolution of turbulent boundary layers in Figures 4.22 (SWQ-like) and 4.23 (HOQ-like). Following the governing Equations (2.20)-(2.22), key parameters to determine the (y^+, u_z^+)-dependence are the kinematic viscosity ν and the wall-normal gradient of the streamwise ensemble-averaged velocity $d\langle U_z \rangle / dy$. As the kinematic viscosity is a function of temperature $\nu(T)$, the local gas phase temperature needs to be accounted for, considering reacting conditions. The gas phase temperature used in Figures 4.22(a) and 4.23(a) originates from the thermochemistry data measured in the complementary campaign discussed later in chapter 5, under identical operation conditions. This data is used in advance here, as it perfectly complements the boundary layer investigation. The temperature data was similarly quenching-point conditioned. Resulting single-shot values at $y = 120$ μm are depicted as red scattering in Figures 4.22(a) and 4.23(a). The pronounced fluctuation with respect to temperature is caused by the turbulent nature of the flame and does not reflect the measurement's precision. For robust viscosity estimation, temperature averages were calculated on spatial z-increments with 200 μm width. The trace of averages was additionally smoothed by a moving average spanning 9 bins and finally fit by
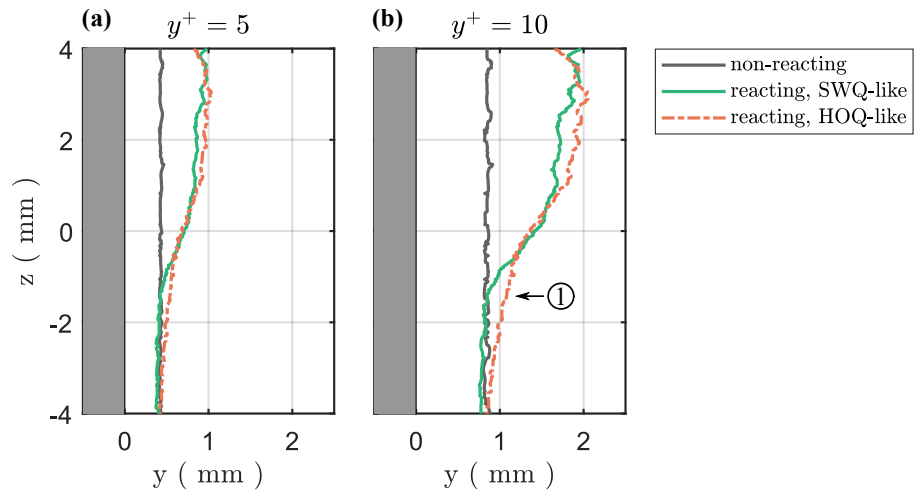
Figure 4.21: Direct comparison of the streamwise boundary layer traces at (a) $y^+ = 5$ and (b) $y^+ = 10$ from Figure 4.20 for the FWI region: non-reacting (gray solid line), reacting SWQ-like (green solid line) and HOQ-like topology (orange dash-dotted line).
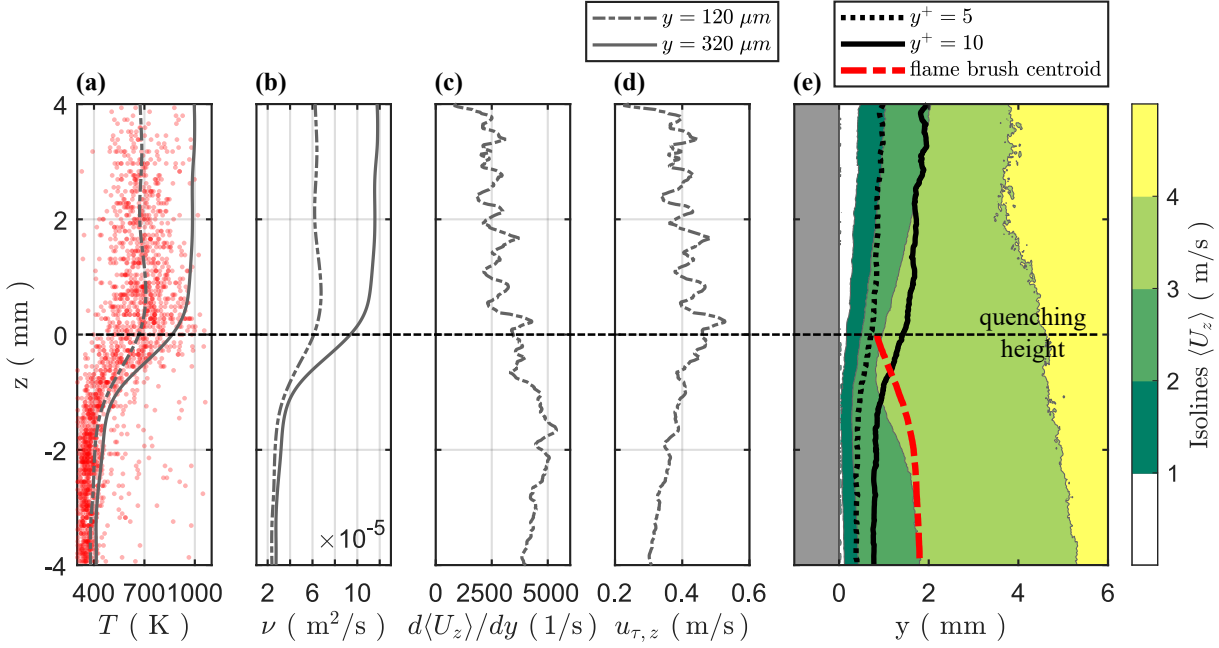
Figure 4.22: Key parameters of the turbulent boundary layer evolution for SWQ-like case. Ensemble-averaged profiles of (a) gas temperature T, (b) kinematic viscosity $\nu(T)$, (c) wall-normal gradient of the streamwise velocity $d\langle U_z \rangle/dy$, (d) friction velocity $u_{\tau,z}$ and (e) isolines of $\langle U_z \rangle$ with boundary layer traces from Figure 4.20(b). Samples: 868. Parts of this figure were published in Zentgraf et al. [E9] (parts of Fig. 2 (a,b)) and are reused; reproduced in an adapted, extended version with different processing in (c)-(e).

a smoothing spline to derive $T(z)$ (gray curves). For kinematic viscosity shown in Figures 4.22(b) and 4.23(b), tabulated values of air (1 atm) in the range $T \in [-150\,°\text{C}, 2000\,°\text{C}]$ were taken from Çengel and Cimbala [31, p. 948]. A piecewise cubic interpolation was applied to derive a function $\nu(T)$.

When approaching the quenching point from the unburnt for a SWQ-like topology, gas phase temperatures (Figure 4.22(a)) and thus kinematic viscosity (Figure 4.22(b)) do rise within a narrow region of $z \in [-1\,\text{mm}, 1\,\text{mm}]$. Beyond this interval, variables are approximately constant. The evolution of T and ν in y–direction is captured by presenting two profiles at $y = 120\,\mu\text{m}$ and $y = 320\,\mu\text{m}$. Overall, a gradient in z–direction is present for $z \in [-1\,\text{mm}, 1\,\text{mm}]$, while an additional, pronounced y-gradient exists for $z > -1\,\text{mm}$. As the friction velocity $u_{\tau,z}$ needs to be defined as close to the wall as possible (see section 4.2.2.4), the wall-closest temperature location at $y = 120\,\mu\text{m}$ is chosen to extract values for calculating $u_{\tau,z}$. Figure 4.22(c) outlines the evolution of the wall-normal gradient $d\langle U_z \rangle/dy$ in z–direction. It is observed that the gradient drops when approaching the quenching point from the unburnt. This can be explained by the expansion of the velocity isolines downstream the quenching point, as reported in Figure 4.22(e), associated with reaction-induced thermal expansion. The finally resulting friction velocity $u_{\tau,z}$ in Figure 4.22(d) rises when approaching the quenching point and, despite some fluctuations, appears to slightly drop in the post-quenching area ($z > 0\,\text{mm}$). The final impact on y^+, i.e., thickening of the y^+-boundary layer traces over the quenching

event, as shown in Figure 4.22(e), is appointed to the streamwise, temperature-induced viscosity gradient. This gets evident from rewriting Equation (2.22) to

$$y = y^+ \cdot \nu/u_{\tau, z} \tag{4.9}$$

and considering y^+ as a constant on the traces respectively. With streamwise evolution in the z-coordinate, ν increases by a factor of 5-6 from pre- to post-quenching areas, while $u_{\tau, z}$ changes by ≈ 1.5. Consequently, the y-locations corresponding to a fixed y^+ value, e.g., 5 or 10, do increase over the quenching event, with the viscosity change in z-dimension being the main contributor.

A corresponding evaluation is done for the HOQ-like scenario by Figure 4.23. Gas phase temperatures in Figure 4.23(a) are taken and conditioned for HOQ-like cases here. Evidently, the single-shot temperatures at $y = 120$ μm (see red scatter) are distributed over a much broader range in z-direction compared to the SWQ-like case. This originates from the nature of HOQ events. For the quenching onset $z > 0$ mm the flame front approaches the wall perpendicularly. Thus, locations at a fixed y-position can cover values from ambient to nearly burnt gas temperatures. This washes out spatial gradients, directly reflected by the viscosity in Figure 4.23(b). Since the applied quenching point-conditioning, according to section 4.2.2.3, is not considering the y-coordinate, the observed y-gradients are smoothed compared to the SWQ-like. Moreover, some high temperature scatter is apparent within the pre-quenching region at $y \in [-2 \text{ mm}, 0 \text{ mm}]$ (see feature ①). Most likely, the HOQ-like wall-parallel reaction already approaches close to the wall in some cases but its final onset of the wall-closest zone is detected further downstream. It is
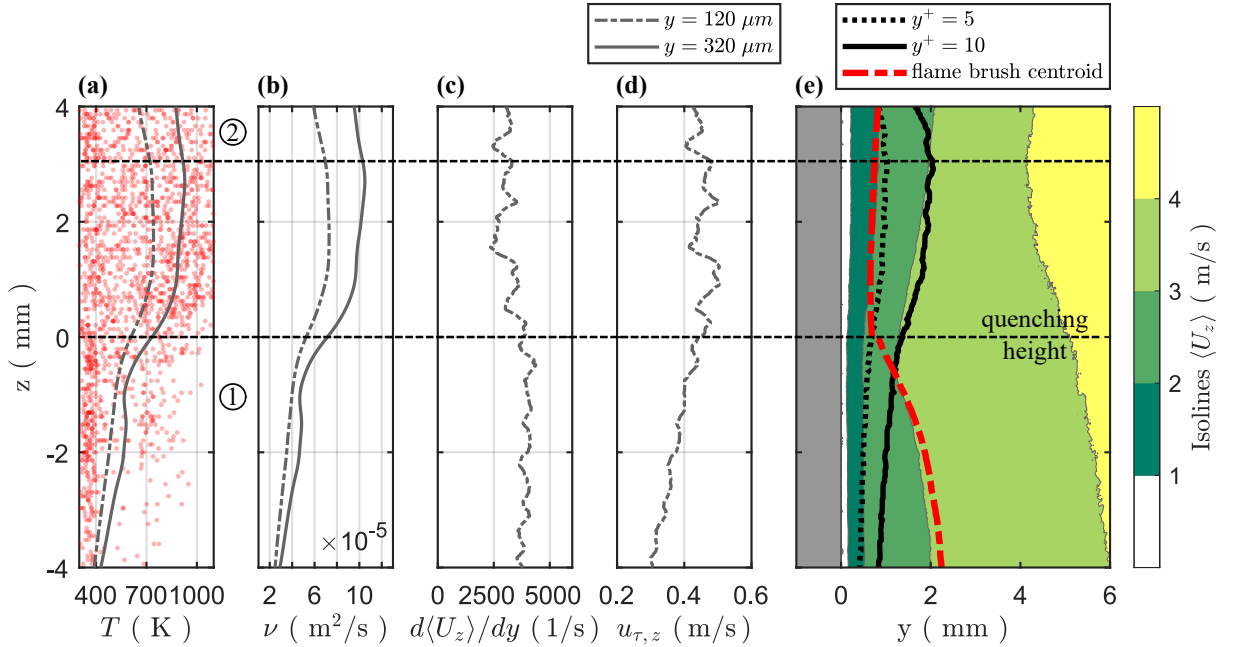
Figure 4.23: Key parameters of the turbulent boundary layer evolution for HOQ-like case. Ensemble-averaged profiles of (a) gas temperature T, (b) kinematic viscosity $\nu(T)$, (c) wall-normal gradient of the streamwise velocity $d\langle U_z \rangle/dy$, (d) friction velocity $u_{\tau, z}$ and (e) isolines of $\langle U_z \rangle$ with boundary layer traces from Figure 4.20(c). Samples: 1132.

furthermore observed that for $z > 3$ mm, the average temperatures are again slightly dropping (see feature ②). In turn, this leads to decreasing thickness of the y^+-traces in Figure 4.23(e). One needs to recall that instantaneous HOQ-like events do only feature a finite wall-parallel extent in streamwise z-direction. This gets evident from the HOQ-like quenching-point conditioned flame brush in Figure 4.15(e), which shows that the probability to observe a wall-parallel flame front appears to drop for $z > 3$ mm. Thus, it is expected that the average length of HOQ-like reaction zones is reached around $z \approx 3$ mm and that conditioned fields at $z > 3$ mm increasingly contain individual samples downstream the actual HOQ-like wall-parallel reaction zone. Results at $z > 3$ mm should therefore only be interpreted with caution. The wall-normal gradient $d\langle U_z \rangle / dy$, shown in Figure 4.23(c), features a nearly constant trace and only slightly drops downstream the quenching onset. Friction velocity $u_{\tau,z}$ features a smooth increase in z-direction and appears constant downstream quenching. As stated above, the evolution of $y^+ = 5$ and $y^+ = 10$ traces is appointed to the behavior in the streamwise viscosity. The smoother increase in ν with respect to z clearly reflects in the spatial traces shown in Figure 4.23(e), causing a smoother thickening of the turbulent boundary layer for HOQ-like topologies.

So far, the above consideration focused on the impact to y^+. However, also normalized velocities u_z^+ are expected to be affected by the reaction. To further complement this
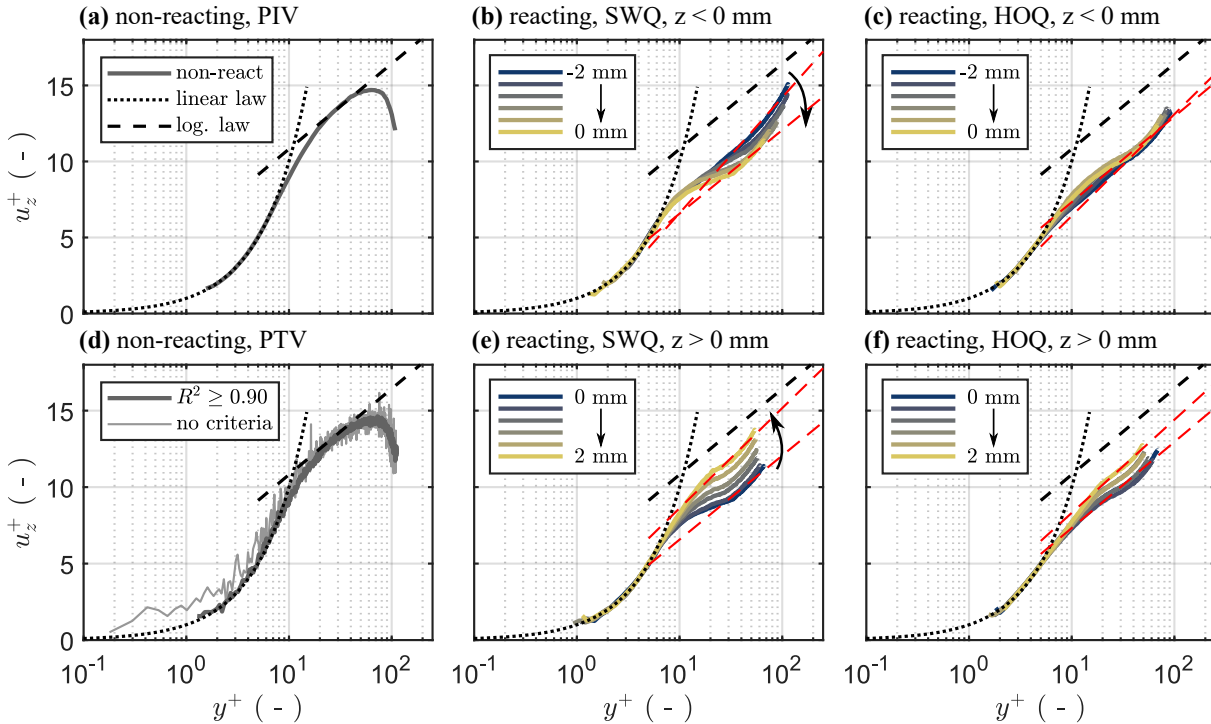
Figure 4.24: Near-wall turbulent boundary layer profiles in (y^+, u_z^+)-space: non-reacting PIV (a) and PTV (d), reacting SWQ-like pre-quenching (b) and post-quenching (e), reacting HOQ-like pre-quenching (c) and post-quenching (f). Samples: 300 non-reacting; 868 SWQ-, 1132 HOQ-like reacting. This figure follows the design of the visualization published in Zentgraf et al. [E9] (Fig. 3), however, is not reproduced from [E9] as the processing is different.

insight, (y^+, u_z^+)-profiles are presented in Figure 4.24, for non-reacting and SWQ-/HOQ-like reacting conditions at different streamwise locations. From the non-reacting case in Figure 4.24(a), it is evident that the boundary layer can be resolved down to values of $y^+ \approx 1.5$, i.e., the viscous sublayer. The experimental data does well-align with the linear relation (see Equation (2.23)) and the log law region (see Equation (2.24)) up to $y^+ \approx 50$. A typical transition region within the buffer layer is observed between $y^+ = 8$ and $y^+ = 20$. Values $y^+ > 50$ suffer the impact of the Kármán vortex street of the ceramic rod and thus deviate from the law of the wall. Overall, the non-reacting behavior present in the studied SWQ burner is very well-captured by the universal laws for turbulent boundary layers, despite a turbulent inflow impinges the leading edge of the wall. The wall-closest boundary layer location around $y^+ \approx 1.5$ equals $y \approx 130 \ \mu$m. To further assess if values can be probed closer to the wall, a feasibility analysis by *particle tracking velocimetry* (PTV) was done for this non-reacting case in a subsequent processing step[6] to the PIV using DaVis 10.0.5 (LaVision GmbH). The PTV data was ensemble-averaged on a resampled $(\Delta y, \Delta z) = (10 \ \mu$m, $23.5 \ \mu$m$)$ grid[7], to provide increased resolution in y-direction and preserve the PIV vector spacing in z-dimension, while having a sufficient number of statistical probes in the sampling region. This idea for spatially resampling the near-wall PTV data on a rectangular grid bases on a study presented by Renaud et al. [135] for velocimetry in a motored engine, assessing boundary layers in $20 \ \mu$m$ \times 500 \ \mu$m bins. The PTV data in this thesis is technically capable to probe the velocity field as close as $\approx 5 \ \mu$m to the wall, as defined in section 4.2.2.2. Results are visualized in Figure 4.24(d) for a $R^2 \geq 0.90$-criterion (dark gray curve) and without any criteria (light gray line) to fit the linear regime within the viscous sublayer. It is first evident that PTV data is more noisy than the PIV. Furthermore, the data with $R^2 \geq 0.90$ is not capable to resolve u_z^+ closer to the wall than $y^+ \approx 1.5$. The data with no criteria for quality assurance reaches values down to $y^+ \approx 0.2$ (equals $y \approx 16 \ \mu$m). However, it overrates near-wall u_z^+ and does not well-follow the linear relation for $y^+ < 1$. Potential reasons are that (1) the velocimetry computation might be limited approaching the wall surface, as the particle shift approximates zero at the given $\Delta t = 10 \ \mu$s, (2) near-wall imaging artifacts could exist (e.g., reflections of particles at the stainless steel wall appearing as ghost particles). Consequently, PTV evaluation did not provide further valuable insight into the near-wall boundary layer for the SWQ burner operation studied here. PIV results do sufficiently resolve and describe the near-wall behavior and, for this reason, PTV processing was not further applied in this thesis.

For the reacting cases, SWQ-like topologies are shown in Figures 4.24(b) and (e) at different selected z-locations (equidistant, $\Delta z = 0.4$ mm) approaching the quenching point from the upstream (Figure 4.24(b)) and from quenching onset in downstream direction (Figure 4.24(e)). This is equally done for the HOQ-like in Figures 4.24(c) and (f). It is first evident that the linear regime is retained up to $y^+ \approx 5$ for all profiles in the reacting cases. Thus, the viscous sublayer is unaffected by the quenching reaction. Beyond $y^+ = 5$, the profiles exhibit smaller, *flattened*, u_z^+-values, as expected from the log law. Since curves at different z-locations do not coincide, no universal law is longer valid at this point. The

---

[6]PTV from PIV using correlation with 1-8 pixels particle size range, 55 counts intensity threshold, 6 pixels correlation window size, 2 pixels allowed range to reference and no consecutive post-processing.
[7]Spatial sampling was done by the "histcn" MATLAB function [108].

(y^+, u_z^+)-profiles are increasingly flattening when approaching the quenching point, where the lowest u_z^+-values are yielded. Evolving from the quenching point to downstream z-locations, the values of u_z^+ are again increasing. In the HOQ-like case, the behavior is similar but less pronounced than for the SWQ-like topology. This is appointed to the smaller z-variation in $u_{\tau, z}$ in the HOQ-like, supported by the below discussion. The flattening with regard to the logarithmic law of the wall can be explained by Equation (2.21). The normalized velocity u_z^+ is defined as the ratio of $\langle U_z \rangle$ and $u_{\tau, z}$. The observed progression is based on an interplay between $\langle U_z \rangle$ and $u_{\tau, z}$, and their variation from non-reacting to reacting conditions. In the bulk flow ($y \in [1 \text{ mm}, 8 \text{ mm}]$, $z \in [-4 \text{ mm}, 4 \text{ mm}]$), $\langle U_z \rangle$ rises in average by ≈ 1.6 (reaction-induced expansion), while the friction velocity $u_{\tau, z}$ increases by a factor of ≈ 2 in average (viscosity change by reaction heat). Consequently, u_z^+ values decrease by $\approx 20\%$ in average, compared to the non-reacting flow, and underrate the universal log law. As the impact of friction velocity predominates, the observation is governed by the influence of streamwise near-wall viscosity. Furthermore, these effects feature a z-variation. The thermal impact is considered highest near quenching and may reduces further downstream. In contrast to SWQ-like cases, $z = 0$ mm marks the transition to wall-parallel reaction in HOQ-like events. Thus, the variability in z-progression is inherently less for HOQ-like topologies.

The observation that reacting (y^+, u_z^+)-traces undershoot the log law for a turbulent boundary layer near the quenching location was made in comparable manner by Al-shaalan and Rutland [8], who numerically studied an SWQ configuration. Likewise, they appointed this behavior to the stronger increase in $u_{\tau, z}$ compared to the rise in streamwise velocity. They furthermore observed that the u_z^+-profile returns to the universal log law of the non-reacting case at farther downstream locations from quenching (see also Fig. 2 in [8]). Overall, their findings are in excellent agreement to the observations made here. Such a trend was furthermore found in literature for different, primarily non-reacting, application cases. Bae et al. [11] numerically studied the impact of large density variation on the turbulent boundary layer in an air flow within a wall-heated pipe. For higher heat fluxes near onset of the thermal source, i.e., where the temperature gradient is high, Bae et al. [11] observed the normalized velocity profile is lower than the log law (see Fig. 10(a) left, run 445 in [11]) and appointed this to an increase in the skin friction coefficient $C_\mathrm{f} \propto \tau_\mathrm{w} \propto \rho \cdot \nu \propto \mu$ near the heating onset. The analysis of Ng et al. [118] also suggested a rise in friction coefficient during combustion process due to the increasing viscosity of the fluid. Overall, this appears consistent with the explanation via viscosity given above. As the gas temperature increases in z-direction, the dynamic viscosity μ rises (see [31, p. 948]), leading to an increase in C_f. A similar trend undershooting the log law was observed for turbulent boundary layers with *adverse* pressure gradients, as discussed experimentally in Nagano et al. [116] or numerically by Lee and Sung [97]. In turn, *favorable* (i.e., negative) pressure gradients, which are associated with an acceleration of the fluid, tend to overrate the log law [84]. As the studied configuration is atmospheric and the V-flame expands undisturbed to the environment, the impact of pressure gradient is considered less prominent than the effect of strong heat source by reaction here. But, both influences could be superimposed in physical reality of the studied SWQ burner.
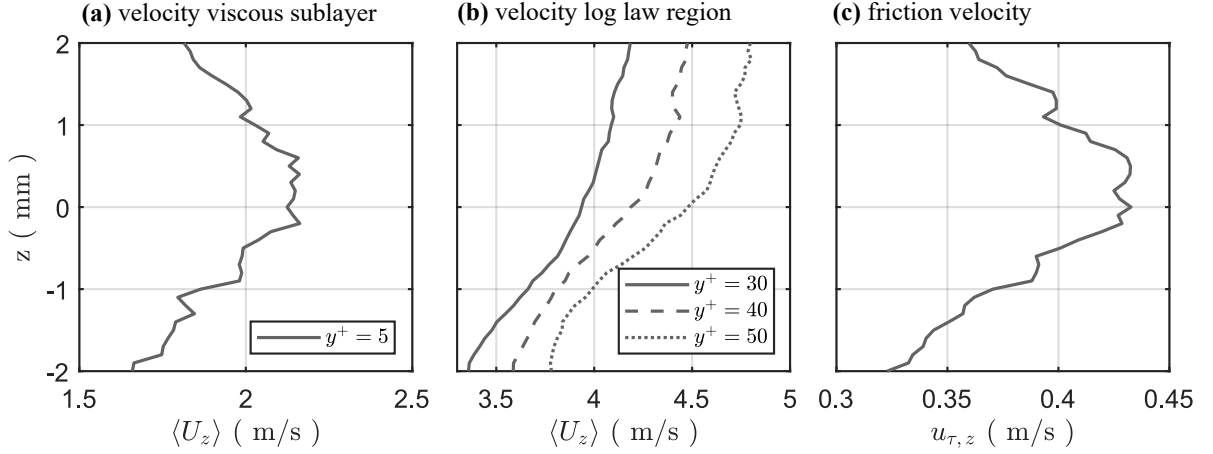
Figure 4.25: Streamwise interplay between values of $\langle U_z \rangle$ (a,b) and $u_{\tau, z}$ (c) for reacting SWQ-like cases. Samples: 868.

This yields first explanation for the observations within the region $y^+ > 20$ under reacting FWI conditions. However, further unraveling the streamwise evolution and its parameter dependence in this region is more complex. It requires a deeper insight into the above mentioned interplay between $\langle U_z \rangle$ and $u_{\tau, z}$, as presented for SWQ-like conditions by Figure 4.25. It is evident that $\langle U_z \rangle$ at farther locations from the wall features pronounced variation in both spatial directions, which is clearly appointed to thermal expansion by the reaction. While all $\langle U_z \rangle$ traces in Figure 4.25(b) do monotonically rise with z, the friction velocity $u_{\tau, z}$ in Figure 4.25(c) first increases towards the quenching point ($z < 0$ mm) and again drops further downstream ($z > 0$ mm). Overall, this leads to the observed behavior with first flattening and then rising curves in the region $y^+ > 20$. In contrast, streamwise velocity $\langle U_z \rangle$ within the viscous sublayer, as shown in Figure 4.25(a) exemplary, well follows the trace of $u_{\tau, z}$. In a further step, the presumed parameter dependence may be broken down by the proportionality

$$u_z^+(y^+, \ z) = \frac{\langle U_z \rangle (y^+, \ z)}{u_{\tau, z}(z)} \propto \frac{K \cdot \left(\frac{T(y^+, z)}{T_0} \right)}{\sqrt{\left(\frac{T(y=120 \ \mu m, z)}{T_0} \right)^{1.5} \cdot \frac{d\langle U_z \rangle}{dy} \Big|_{y=0 \ mm}}} \tag{4.10}$$

where the numerator expresses the change in streamwise velocity by thermal expansion via ideal gas law, in which the volume change, and thus velocity change, correlates linearly to local temperature $T(y^+, z)$. However, a factor K needs to be introduced that considers the impact of geometry and three-dimensional nature of expansion, e.g., a closed geometry will strongly force the flow in streamwise direction, while an unbounded configuration will less. This factor reflects that the volume expansion does not lead to equally increased velocities in all three spatial directions. The denominator covers the impact on kinematic viscosity in its first term, which changes with the near-wall temperature $T(y = 120 \ \mu m, \ z)$ by an exponent 1.5 (derived from $\nu = \mu/\rho$ [165, p. 229] with the dynamic viscosity $\mu \propto T^{0.5}$ [165, p. 63] and density $\rho \propto T^{-1}$ via ideal gas law), as well as the velocity gradient in the second term (which most likely also possesses a certain temperature dependence). To represent a measure of change, temperatures are referenced to the ambient temperature T_0. Evidently, the evolution of $u_z^+(y^+, \ z)$ within the log law range features a permanent

interplay between the contributions of (1) thermal expansion by the reaction (influenced by local temperature and geometry), (2) near-wall viscosity (determined by near-wall temperature) and (3) near-wall velocity gradient.

In turn, this impedes a straightforward parametrization of both κ and B by thermodynamic quantities for a log law that captures the FWI influences. As a first attempt of an FWI log law, Figure 4.26 provides these parameters with respect to relative distance to the quenching point z, i.e., $\kappa(z)$ and $B(z)$. They were derived by fitting the experimental curves for wall units $y^+ > 20$ to a log law following Equation (2.24) with κ and B as free fitting parameters. Fits for the extreme values $z \in \{-2\,\text{mm}, 0\,\text{mm}, 2\,\text{mm}\}$ are included in Figure 4.24 as red dashed lines. Evidently, both SWQ- and HOQ-like cases possess similar traces. For the SWQ-like case, values of κ may be captured by a parabolic function

$$\kappa(z) = -\left(\frac{z}{6.6\,\text{mm}}\right)^2 + 0.41 \tag{4.11}$$

and B could be described by a stepwise linear function

$$B(z) = \begin{cases} 1.91/\text{mm} \cdot z + 2.92 & z \leq -0.7\,\text{mm} \\ 0.25/\text{mm} \cdot z + 1.14 & z \geq -0.7\,\text{mm} \end{cases} \tag{4.12}$$

as outlined by the dashed green curves in Figure 4.26. As mentioned above, an universal log law is not valid for the reacting case and Equations (4.11) and (4.12) do merely provide a first attempt to parametrize log laws for reacting FWI conditions. Further research on this topic is required to fathom the real parameter dependency, e.g., by numerical simulation.
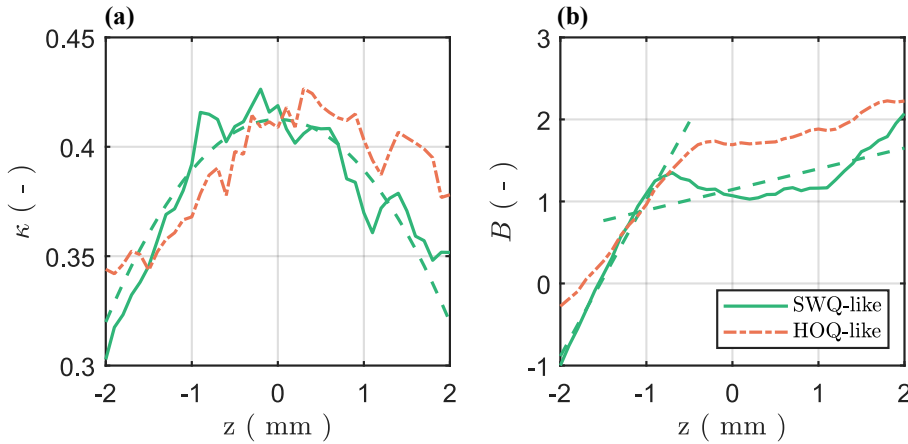
Figure 4.26: Potential parametrization of both κ (a) and B (b) for a log law under reacting FWI conditions. Derived from the boundary layer evolution in Figure 4.24.

4.3.2.3 Length Scales and Combustion Regimes

A further revealing evaluation is the assessment of length scales in the near-wall reacting flow and based on them an estimation of the present combustion regimes. This is addressed within this section by calculation of integral length scales (see section 2.1.2.1) and a regime classification using the Borghi-Peters diagram (see section 2.2.2.2).

For the sake of clarity, only the two longitudinal integral length scales $L_{yy,+y}$ (for the y-velocity component in positive y-direction) and $L_{zz,+z}$ (for the z-velocity component in positive z-direction) are considered in the following (corresponds to two of four possibilities here). They were derived for each (y,z)-location in the near-wall flow, according to Equation (2.7). Results are shown in Figure 4.27, considering non-reacting as well as SWQ- and HOQ-like reacting conditions. For orientation and discussion purpose, traces of the boundary layer evolution at constant values $y^+ = 5$ (dotted black line) and $y^+ = 10$ (solid black line) as well as averaged flame front location (dash-dotted red line) are superimposed. Correlations were performed in positive y- and z-coordinate direction. First of all, it is noted that Figure 4.27 features pronounced blank areas (displayed white). This is due to missing correlation length in the limited available FOV that would be required for proper assessment. According to the governing Equation (2.7), there should be a
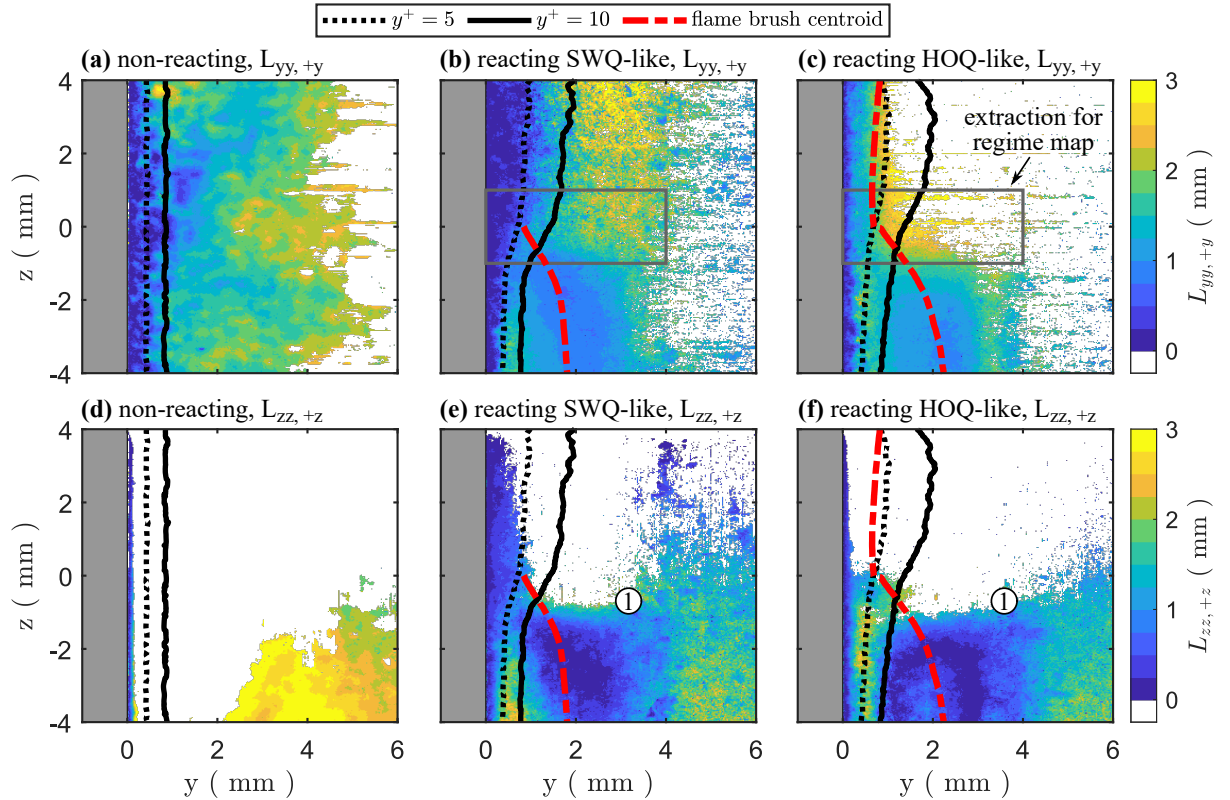
Figure 4.27: Integral length scales $L_{yy,+y}$ (top line) and $L_{zz,+z}$ (bottom line) for non-reacting (a,d) as well as SWQ- (b,e) and HOQ-like (c,f) reacting cases at turbulent conditions. Gray solid rectangle in (b,c) outlines region where $L_{yy,+y}$ is extracted for Borghi-Peters diagram. Samples: 300 non-reacting; 868 SWQ-, 1132 HOQ-like reacting.

semi-infinite range $r \in [0, \infty]$ available for correlation. However, it is clearly evident from the two samples in Figure 4.28 that structures in the instantaneous fluctuating velocities range in the order of $y \approx 2 - 4$ mm in the u'_y-fields (Figure 4.28(a) and (c)) and easily extend to $z > 9$ mm in the u'_z-fields (Figure 4.28(b) and (d)). Zones, where the length scale calculation did not converge were thus excluded from evaluation. For this purpose, an empirical criterion was introduced and the normalized two-point correlation $R_{ii}/\langle (u'_i)^2 \rangle$, that ranges between 0 and 1 (see section 2.1.2.1), was required to drop below 0.1 to consider the length scale converged. Otherwise, this location was assigned to a blank value in Figure 4.27. In particular, this is evident when approaching the limits of the FOV (y-direction for $L_{yy,+y}$ at right hand side and z-direction for $L_{zz,+z}$ at top). In these blank areas, it can only be concluded that the integral length scales would have been too large to be clearly determined within the available space to the FOV boundary.

For the non-reacting case, the length scales $L_{yy,+y}$ in Figure 4.27(a) start at values close to zero near the wall ($y = 0$ mm) and grow for increasing wall-distances, reaching values $L_{yy,+y} \geq 2$ mm around $y = 4$ mm. For the scales $L_{zz,+z}$, only sparse information is captured in Figure 4.27(d). As pointed out above and shown in Figures 4.28(b) and (d), the underlying instantaneous structures close to the wall nearly cover the full z-height of the velocimetry FOV. This complicates the convergence of the correlation in z-direction and inherently leads to the huge blank areas observed for $L_{zz,+z}$. The corresponding instantaneous structures, denoted by ① and ② in Figure 4.28, are so-called *ejections* ($u'_y > 0$ and $u'_z < 0$) with fluid motion from the wall contributing to turbulent energy production [130, p. 323 ff.]. In the area $y > 3$ mm and $z < -3$ mm, length scales $L_{zz,+z}$ can reach values around 3 mm and above. For the remaining blank areas, it is considered very likely that the near-wall energy containing structures in $L_{zz,+z}$ extend beyond 3 mm. This is supported by the instantaneous u'_z-fields in Figures 4.28(b) and (d).

Length scales $L_{yy,+y}$ in the SWQ-like case start at $L_{yy,+y} \approx 0$ mm near the wall and quickly increase to $L_{yy,+y} \approx 1$ mm approaching the $y^+ = 5$ boundary, as depicted in Figure 4.27(b). It is remarkable that the streamwise evolution of the $y^+ = 5$ value of
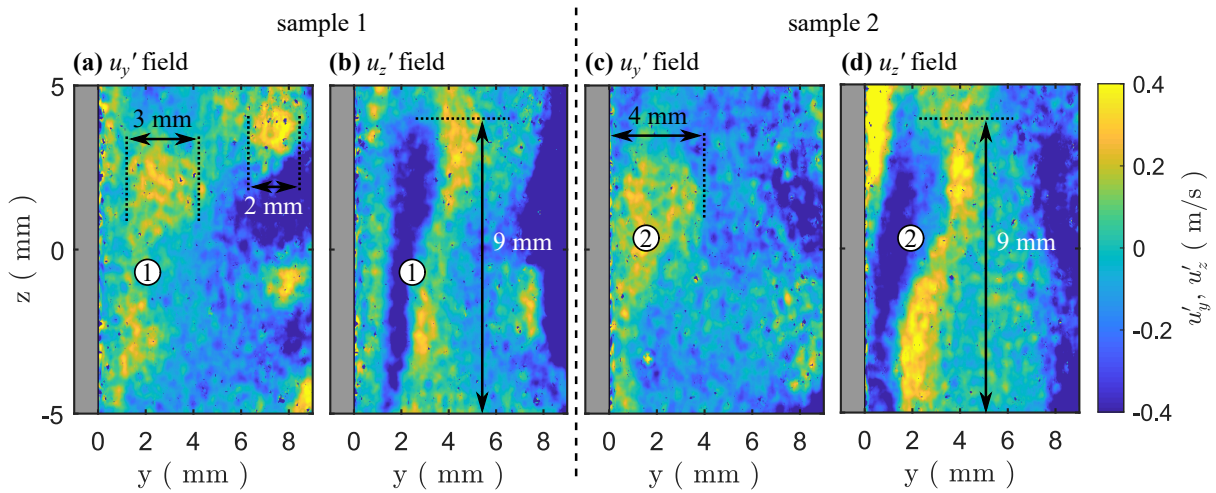
Figure 4.28: Instantaneous fields of u'_y (a,c) and u'_z (b,d) for two arbitrary samples under non-reacting conditions.

the turbulent boundary layer well-aligns with low values of $L_{yy,+y}$ in the entire z-range displayed (note: this is not the case for the HOQ-like events). Between the $y^+ = 5$ and $y^+ = 10$ boundary, values further evolve to $L_{yy,+y} \leq 2$ mm but again decrease to values $L_{yy,+y} \leq 1$ mm across the flame brush region. In the far post-flame, values are rising again. This trend is consistently observed in both the SWQ- and HOQ-like topology (Figure 4.27(c)), however, length scales appear to grow faster for increasing wall distances in the HOQ-like case than for SWQ-like events. For example, regions close to the $y^+ = 5$ boundary already feature values near $L_{yy,+y} = 2$ mm. The same observation is made for the post-quenching areas ($z > 0$ mm). While the HOQ-like case in Figure 4.27(c) already reaches values of $L_{yy,+y} \approx 3$ mm at $y = 1$ mm, the SWQ-like in Figure 4.27(b) takes up to $y = 3$ mm. One overall conclusion from this is that the energy containing structures in y-direction are smaller for the SWQ-like case compared to the HOQ-like in the near-wall area. This implies that the governing velocity fluctuations are correlated on a smaller spatial scale for the SWQ-like, suggesting a further progressed decay of the governing turbulence. Consequently, the HOQ-like cases contain more energy near-wall than the SWQ-like. Thus, a more intense instantaneous mixing is assumed in the HOQ-like, finally suggesting a more intense wall-normal convective transport and mixing in the HOQ-like cases than in the SWQ-like cases. For $L_{zz,+z}$, SWQ-like and HOQ-like topologies feature a similar trend with respect to the increase/decrease behavior in the near-wall length scale values in Figures 4.27(e) and (f). It is again remarkable that values are quite high near the $y^+ = 5$ boundary in the pre-quenching ($z < 0$ mm). However, their fields appear quite equal in spatial distribution and a considerable part of information is missing within the post-quenching zone ($z > 0$ mm). This suggests only minor differences in the streamwise transport between both quenching topologies. It is noticeable that $L_{zz,+z}$-values close to the blank regions are quite low (≈ 1.5 mm, see feature ①), despite more than 4 mm are left to the FOV z-limit. Here, one needs to recall that length scales result from integration over the correlation length r and thus have smaller values than r (see Equation (2.7)).

Once the existing integral length scales have been calculated and discussed, an evaluation of the combustion regimes in the Borghi-Peters diagram, as introduced in section 2.2.2.2, follows. First of all, the diagram's parameters l_F (laminar flame thickness), u_F (laminar flame speed), $l_t = L_{ii}$ (integral length scale) and u' (turbulence intensity) need to be defined in a well-considered way to best fit the experimental SWQ burner operation. Both variables l_F and u_F are characteristic quantities for the used DME fuel at $\Phi = 0.83$. Thus, they are derived from results of a laminar, adiabatic freely propagating flame. The flame thickness results to $l_F \approx 400$ μm from the consideration in section 2.2.2.1, while the laminar flame speed is estimated to $u_F \approx 0.35$ m/s from Qin and Ju [132] (see Fig. 5 in [132]). For definition of the values u' and l_t it appears most reasonable to consider the multi-dimensional nature of turbulence and include x-, y- and z-components, e.g., by using the turbulent kinetic energy as stated in Borghi [24] and some kind of directional-averaged value for the integral length scale. However, planar diagnostics were applied in the measurement presented here, which only provide the y- and z-values respectively. Furthermore, it is evident from the above assessment of integral length scales that the $L_{zz,+z}$ fields are only filled very sparsely, especially in the region of the quenching onset that is of interest here. For this reason, the evaluation of turbulent premixed combustion

regimes via Borghi-Peters diagram in this thesis is limited to the wall-normal y-quantities. Consequently, u' is set to $u'_{y,\,\mathrm{RMS}}$ while l_t is described by $L_{yy,\,+y}$. This is not considered a drawback. As the classification in combustion regimes relies on the interaction of local flame and flow conditions, it appears reasonable to consider the relevant parameters in vicinity of the reaction zone and preferably normal to the flame. Since the flame front in the SWQ burner operation often features a very steep angle to the wall or is even parallel, e.g., see Figure 4.13, the wall-normal y-direction can be seen as a good approximation of the flame front-normal. Thus, analyzing the Borghi-Peters diagram by using y-direction components only is considered to provide a valuable insight into existing regimes.

However, defining the regime diagram on experimental data of a quenching flame near a solid surface arises further open issues. First, a change in u_F and l_F occurs when approaching the wall and values can actually no longer be derived from freely propagating flames. For a turbulent, premixed H_2/air flame in an SWQ-configuration Gruber et al. [69] pointed out that the flame is thickening when approaching the wall as well as a near-wall drop in flame displacement speed by a factor of ≈ 2 for $y^+ \leq 15$ (would equal approximately 1.3 mm here). However, their wall-closest displacement speed remained at $\approx 50\%$ of the undisturbed laminar flame speed. They interpreted both circumstances as an indicator for a possible regime change near the quenching wall from "thin flamelet" towards "thickened wrinkled". For laminar CH_4/air SWQ-operation Jainski et al. [82] observed that the flame consumption speed is close to the undisturbed laminar flame speed up to 2 mm above the wall surface, but then rapidly drops by a factor of 4 reaching 1 mm wall distance. Despite absolute values in both studies deviate (most likely due to the different fuels used), the decreasing trend in near-wall flame speed is qualitatively consistent. Flame thickening close to the quenching wall ($y^+ = 0.6$) was also observed in the numerical study of Ahmed et al. [2] for conditions representative for a CH_4/air mixture ($\Phi = 1.0$, single-step reaction). However, at $y^+ = 20$ ($y/h = 0.18$, would equal approximately 1.7 mm here) they observed a behavior very close to a freely propagating laminar flame (see Fig. 5 in [2]). It is assumed that both the laminar flame thickness and speed remain constant at their undisturbed freely-propagating value for $y \geq 2$ mm also for the lean DME combustion analyzed here. For wall distances $y \in [0\,\mathrm{mm}, 2\,\mathrm{mm}]$ it would be possible to estimate the decreasing u_F approaching the wall, like done by a linear fit in [82] for example. However, as an estimation for the near-wall thickening of l_F was missing, locations $y < 2$ mm were omitted in the following evaluation. It was limited to $y \geq 2$ mm, where values of both the laminar flame thickness and speed are assumed constant, as $l_\mathrm{F} \approx 400\,\mu$m and $u_\mathrm{F} \approx 0.35$ m/s given in the above paragraph. A second, related open issue is about the spatial region where the data for evaluation should be extracted from the experimental FOV. As stated by Borghi [24], the influences of combustion should be covered. Thus, it appears to be most practical to use a spatial region that includes the unburnt, flame front and ranges to the burnt gas. For this reason, the below analysis uses values close to the quenching point from $y \in [0\,\mathrm{mm}, 4\,\mathrm{mm}]$ and $z \in [-1\,\mathrm{mm}, 1\,\mathrm{mm}]$ (gray rectangle in Figure 4.27). However, only values at $y \geq 2$ mm for presumably constant l_F and u_F were considered (samples displayed color-coded). Additionally inspecting the location of the flame brush centroid in Figures 4.27(b) and (c), it is directly evident that the majority of data with $y \geq 2$ mm is located within the burnt gas.

As evident from the above outlines, an application of the Borghi-Peters classification on experimental, near-wall flame quenching conditions is accompanied by a number of trade-offs and features multiple potential sources of uncertainty. For this reason, results are only considered to provide a raw estimation of the combustion regimes during turbulent FWI but not an ultimate classification. Again, it is emphasized that these challenges are not seen as a major drawback impeding this analysis. In particular, it is considered of interest to further discriminate the SWQ-like from HOQ-like topology here.

Figure 4.29 visualizes the Borghi-Peters regime analysis under flame quenching conditions with the above assumptions. This is done in terms of a scatter plot (top row) showing one data point for each (y,z)-location in the extraction rectangle in Figures 4.27(b) and (c) for values $y \geq 2$ mm (color-coded by the wall distance). Corresponding probability density functions (PDFs, bottom row) are given in a zoomed view to show the distribution's focus. The analysis is limited to reacting conditions, since it should include the impact of combustion (e.g., see [24]).

The SWQ-like topologies in Figure 4.29(a) are classified in the regime of wrinkled flamelets at the boundary next to corrugated flamelets. The PDF in Figure 4.29(c) underlines that the majority of spatial probes is within the wrinkled flamelets. Following the color-coding from $y = 2$ mm to $y = 4$ mm, the trace appears to bend downwards and again upwards, as visually indicated by the black curved arrow in Figure 4.29(a). This suggests a trend of re-laminarization when evolving further from the reaction zone towards the fully burnt. Potentially, it could emerge back to the laminar regime in the further progression, i.e.,
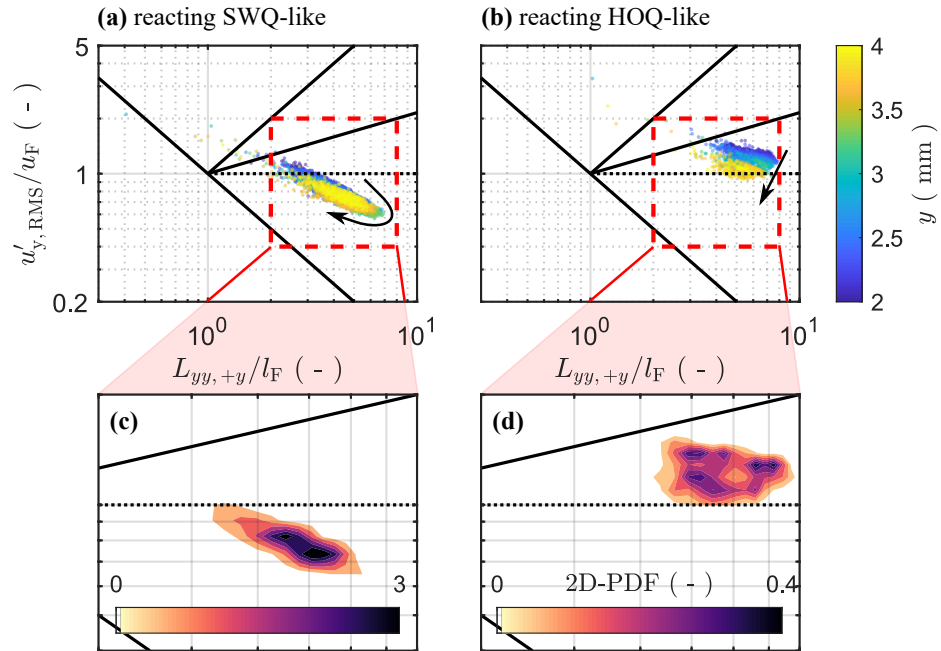
Figure 4.29: Borghi-Peters diagram for SWQ- (a,c) and HOQ-like (b,d) reacting cases at turbulent inflow conditions. (a) and (b): scatter plot for all spatial probes at $y \geq 2$ mm, y-distance color-coded; (c) and (d): corresponding PDF for the zoomed regions indicated by red dashed rectangles. Samples: 868 SWQ-, 1132 HOQ-like reacting.

for $y > 4$ mm. The HOQ-like topology, shown in Figure 4.29(b), is predominantly located within the regime of corrugated flamelets for spatial probes featuring $y > 2$ mm. Again, this is clearly revealed by the corresponding PDF in Figure 4.29(d). The majority of spatial samples is located in the corrugated flamelets but very close to the wrinkled flamelets. In Figure 4.29(b) the progress of color-coded samples suggests that the states emerge from the corrugated ($y \approx 2$ mm) to the wrinkled flamelets for increasing y, as shown by the straight black arrow in Figure 4.29(b). This means that the Karlovitz number and thus the flame stretch decrease with increasing wall distance. It is very likely that spatial samples would be located within the wrinkled flamelet regime for $y > 4$ mm. As pointed out above for the SWQ-like case, this again underlines a tendency of re-laminarization when approaching the burnt regions.

Overall, both topologies range very close to each other at the $u'_{y,\,\mathrm{RMS}}/u_\mathrm{F} = 1$ boundary that separates wrinkled from corrugated flamelets. It needs to be noted that this boundary is not meant a sharp transition between two combustion regimes. Emerging from wrinkled to corrugated flamelets is rather considered a continuous process of increasing wrinkling, as the Karlovitz number rises. Despite differences are minor, the fact that HOQ-like cases are predominantly within the corrugated flamelet regime, while the SWQ-like topology is located in the wrinkled, suggests that the HOQ-like case is governed by a higher level of turbulence interacting with the local quenching reaction. It thus features more wrinkled flame front structures. This in turn could imply a slight tendency towards higher mixing and transport as well as an increased reaction rate and eventually higher near-wall heat release in the HOQ-like compared to the SWQ-like topology. Most likely, this is due to the HOQ-like samples approaching the wall in y-direction, featuring higher fluctuation in this coordinate.

4.3.2.4 Near-Wall Anisotropy

A further interesting insight is provided by the anisotropy of turbulence in the near-wall region, based on the invariant map introduced in section 2.1.2.2. Unlike to the original purpose of the invariant map, as shown by Choi and Lumley [35] for example, it is not used to evaluate the *return-to-isotropy* behavior here. As outlined by the processing implications in section 4.2.2.5, it is rather used to provide further interpretation on the direction-dependent distribution of near-wall turbulent kinetic energy by an anisotropy coordinate $\xi \in [0, 1]$. As the parameter ξ results from a projection on the yz-plane and information in the third spatial direction is missing, it cannot be conclusively determined whether $\xi = 1$ is actually one-dimensional turbulence and $\xi = 0$ describes two-dimensional isotropy, as originally defined in the vertices of the invariant map (see Figure 2.2). For this reason, the states are termed *isotropic* ($\xi = 0$) and *anisotropic* ($\xi = 1$) with respect to the applied two-dimensional projection.

Figure 4.30 presents fields of the normalized anisotropy coordinate ξ. To complement the discussion below, corresponding fields of $u'_{y,\,\mathrm{RMS}}$ (Figures 4.30(d)-(f)) as well as $u'_{z,\,\mathrm{RMS}}$ (Figures 4.30(g)-(i)) are included. In line with the previous presentations, boundary layer traces ($y^+ = 5$ and $y^+ = 10$, black lines) and the averaged flame front location (dash-dotted red line) are shown for orientation.
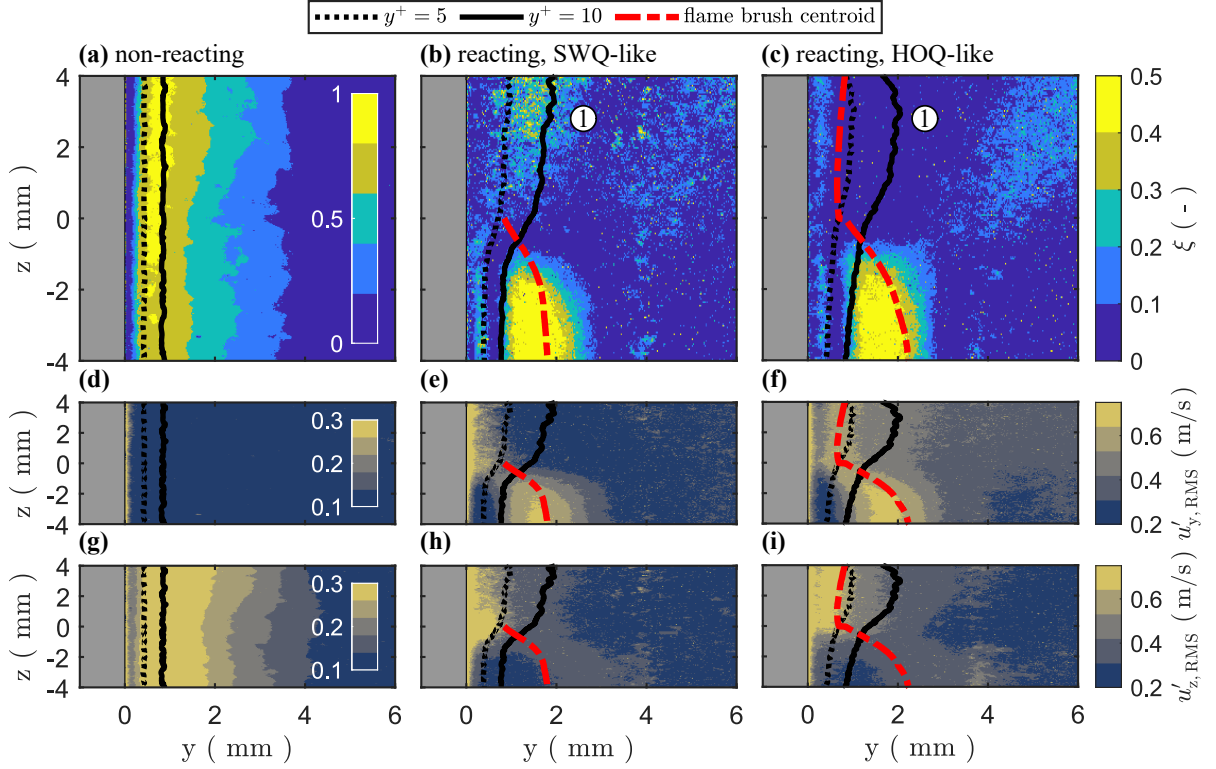
Figure 4.30: Anisotropy coordinate ξ (top line), corresponding fields of $u'_{y,\,\mathrm{RMS}}$ (center line) and $u'_{z,\,\mathrm{RMS}}$ (bottom line) for non-reacting (a,d,g) as well as SWQ- (b,e,h) and HOQ-like (c,f,i) reacting cases at turbulent inflow conditions. Samples: 300 non-reacting; 868 SWQ-, 1132 HOQ-like reacting.

For the non-reacting reference case in Figure 4.30(a) values $\xi \approx 0$ are observed very close to the quenching wall ($y^+ < 5$), indicating isotropy. For increasing distance y, values quickly rise and reach a peak of $\xi > 0.8$ between the $y^+ = 5$ and $y^+ = 10$ trace of the turbulent boundary layer. This suggests pronounced anisotropic behavior. Further from the boundary at $y^+ = 10$, values are continuously decreasing with $\xi < 0.1$ for $y > 4$ mm, again approaching towards isotropy. Comparing Figures 4.30(d) and (g) it is directly evident that the velocity fluctuation in the streamwise z-direction is the dominating component in the regions with high ξ-values. So, the anisotropic turbulence character observed in the non-reacting case suggests that near-wall turbulent kinetic energy is almost exclusively stored in streamwise z-direction.

For the reacting cases in Figures 4.30(b) and (c), the behavior differs completely from the non-reacting case. High ξ-values in the turbulent boundary layer, between $y^+ = 5$ and $y^+ = 10$, are no longer developed. In contrast, values in this zone are close to zero under reacting conditions. Only a very thin layer with $\xi \approx 0.1 - 0.3$ remains next to the $y^+ = 5$ boundary. This is appointed to slightly larger $u'_{z,\,\mathrm{RMS}}$ values in Figures 4.30(h) and (i). Despite the boundary layer thickness remains nearly unchanged for pre-quenching regions at $z < -1$ mm from non-reacting to reacting cases, the anisotropy characteristics inside the boundary layer appear completely different. At this point, it is remarkable that the boundary layer traces at $y^+ = 5$ as well as $y^+ = 10$ clearly delimit certain physical phe-

nomena observed in Figure 4.30. The flame brush region (for pre-quenching, $z < -1$ mm) features values $\xi \approx 0.5 - 0.6$. These values are clearly appointed to the impact of the wall-normal component $u'_{y, \text{RMS}}$, as evident from Figures 4.30(e) and (f). Unequivocal, this effect can be attributed to the flame front, causing (1) an acceleration of the fluid normal to the flame front (approximately equals y-direction) and (2) intermittency of the flame, fluctuating in its position from sample to sample. As the latter intermittency biases the flow's velocity fluctuations in the classical understanding of turbulence, an interpretation with respect to the anisotropy of turbulence should be omitted here. However, turbulent kinetic energy within the flame brush is rather contained in the wall-normal y-direction. For $y > 3$ mm values do again approach $\xi \approx 0$, suggesting a return to isotropy with respect to the two-dimensional projection. In the aspects described above, both the SWQ- and HOQ-like case do well-align in their spatial anisotropy characteristics for the pre-quenching regime ($z < 0$ mm). The only significant difference between both quenching topologies is observed within the post-quenching regime for $z > 0$ mm (see region ①). The SWQ-like features elevated values for ξ between $y^+ = 5$ and $y^+ = 10$, suggesting a tendency towards anisotropic turbulence in the streamwise z-dimension (evident by comparing Figures 4.30(e) and (h)). In turn, the HOQ-like quenching topology possesses $\xi \approx 0$ from the trace of the flame brush centroid to at least $y = 3$ mm. This gives rise to a behavior close to isotropy and suggests that the turbulent kinetic energy is similarly stored in both spatial dimensions. In turn, this could suggest the presence of elongated eddies, as stated in section 2.1.2.2. Potential presence of vortex structures could be supported by the fact that both fluctuations $u'_{y, \text{RMS}}$ and $u'_{z, \text{RMS}}$ within this zone are more intense in the HOQ- than in the SWQ-like case. This gets clear by comparing both Figures 4.30(e) and (h) to Figures 4.30(f) and (i). Especially, these more intense fluctuations for the HOQ-like case behind the flame front could point to a potential driving mechanism to push the flame front closer to the wall. However, these fluctuations need to be interpreted carefully, as they could also originate from flame intermittency. A separate evaluation on vortex structures is thus recommendable.

4.3.2.5 Near-Wall Vortex Structures

As already indicated at the end of the previous paragraph, the identification and analysis of vortex structures is another interesting point to yield valuable insight into governing transport processes and mixing. Indeed, previous numerical studies [7,29,69] pointed out the importance of near-wall coherent vortex structures as governing mechanisms in turbulent FWI operation. Both Alshaalan and Rutland [7] as well as Gruber et al. [69] report of vortices, which simultaneously push the reaction closer to the wall on one side (wall heat flux increases) and on the other side lift it from the wall (wall heat flux decreases). This corresponds well to the description of so-called *horseshoe* vortices during flame quenching reported by Bruneaux et al. [29] in an earlier study. Basically, such *horseshoe* or *hairpin* vortices are considered important structures in boundary layer flows, as mentioned and illustrated in Pope [130, p. 325 f.] for example. It needs to be noted that the reported structures [7,69] were elongated in streamwise direction (z-axis here) and the main alteration in pushing and lifting the flame front with respect to the wall was observed along the spatial direction that corresponds the out-of-plane x-axis in this thesis (not assessed

by measurements). Even though this specific phenomenon reported cannot be captured by planar measurements in the *yz*-plane presented here, the importance of structures in turbulent FWI is still clearly evident. In this thesis, an assessment of coherent vortex structures using a simplified, two-dimensional projection of the *Q*-criterion is performed, as outlined in section 4.2.2.6, and further characteristics are derived.

The results of the analysis are outlined in Figure 4.31 by two-dimensional ensemble-averaged fields of the vortex probability (top row), shape parameter ϵ (center row) and orientation parameter Θ (bottom row), as introduced in section 4.2.2.6. Again, boundary layer traces ($y^+ = 5$ and $y^+ = 10$, black lines) and the averaged flame front location (dash-dotted red line) are included for discussion and orientation purpose.

In the non-reacting reference case, shown in Figure 4.31(a), vortex structures are observed with a high probability of $0.3 - 0.4$ within the viscous sublayer of the turbulent boundary layer up to $y^+ < 10$. For increasing distances from the wall, the probability to observe a vortex decreases rapidly. An analysis of vorticity yields 73% of the structures turn counterclockwise, while 27% turn clockwise. As evident from Figure 4.31(d), structures are rather elongated from the wall up to $y = 3$ mm. There seems to be a transition towards spherically shaped vortices for $y > 3$ mm. From the orientation parameter in Figure 4.31(g) the entire field appears to homogeneously feature values around $\Theta \approx 0.5$.
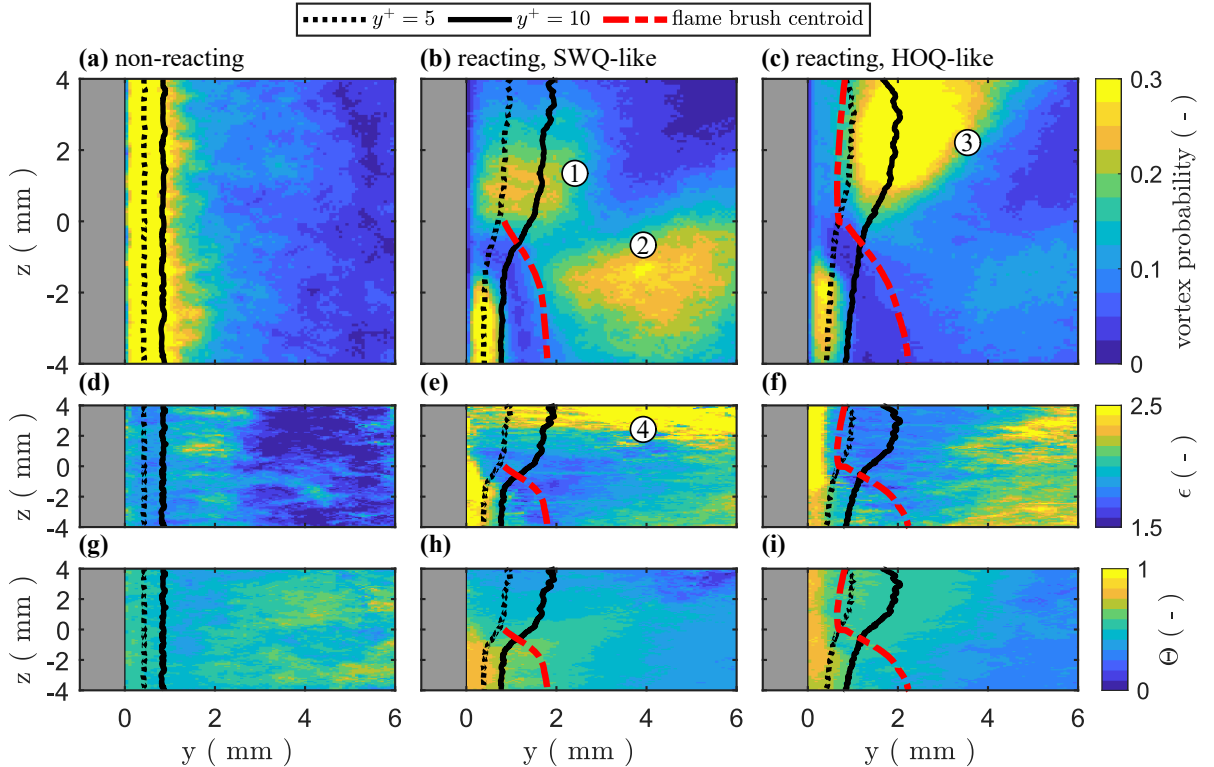
Figure 4.31: Ensemble-averaged fields of vortex probability (top row), corresponding shape parameter ϵ (center row) and orientation parameter Θ (bottom row) for non-reacting (a,d,g) as well as SWQ- (b,e,h) and HOQ-like (c,f,i) reacting cases at turbulent inflow conditions. Samples: 300 non-reacting; 868 SWQ-, 1132 HOQ-like reacting.

In average, the orientation of vortex structures thus possesses an in-between stage of y- and z-direction.

In the unburnt pre-quenching region ($z < -2$ mm), both the reacting SWQ- and HOQ-like cases in Figures 4.31(b) and (c) reflect the non-reactive behavior within the turbulent boundary layer for $y^+ \leq 10$ by featuring high vortex probabilities up to $0.3 - 0.35$. However, near the quenching event and in the post-flame areas, the behavior of reacting cases is quite different. In the SWQ-like topology in Figure 4.31(b), high probabilities for vortex structures are apparent directly downstream the quenching point ($z > 0$ mm, see ①) and behind the flame front (around $(y,z) \approx (4$ mm$, -2$ mm$)$, see ②). Both regions feature probabilities up to 0.25, means every fourth SWQ-event features vortex structures at those positions. In contrast, the HOQ-like case in Figure 4.31(c) features one pronounced region of high vortex probability up to nearly 0.4 directly behind the flame brush centroid of the wall-parallel reaction zone ($y > 1$ mm, $z > 0$ mm, see ③). It is noteworthy that $> 99\%$ of all vortex structures identified turn counterclockwise in both reacting topology cases. This pronounced counterclockwise behavior was already evident from the transient consideration in Zentgraf et al. [E8] (see color-coded vortex structures in Fig. 3 in [E8]). As the SWQ- and HOQ-like topology do alternate in a certain way during transient operation of the burner, vortices within region ② could be precursors for the events observed in location ③.

From the shape parameter ϵ (Figures 4.31(e) and (f)) and orientation parameter Θ (Figures 4.31(h) and (i)) it is evident that near-wall vortex structures during FWI at $y^+ < 5$ are preferentially elongated (ϵ high) and oriented in streamwise z-direction (Θ approaching unity). Despite identified with other criteria, this corresponds very well to the observations on near-wall shape and orientation reported in previous studies [7, 69]. For the SWQ-like topology it needs to be noted that this is only evident up to the quenching point, while apparent over the full z-height for the HOQ-like. This is most likely a phenomenon related with the unburnt, fresh gas, which is occasionally present in HOQ-like cases in wall proximity (depending on how far the flame is already propagated to the wall).

Farther from the wall, structure's shape is apparently getting more spherical up to a wall distance of $y = 3$ mm, as ϵ drops, but again starts to elongate for $y > 3$ mm. Regions ①-③ with high vortex probability possess rather spherical than elongated vortex shape in the yz-plane. For the SWQ-like case in Figure 4.31(e) there is a pronounced region at $z > 2$ mm (see ④) with $\epsilon > 2.5$. However, this is expected to be an image artifact. Following Figure 4.17(d), the number of available samples N is already dropping significantly approaching $z = 4$ mm in the SWQ-like. So, the locations $z > 2$ mm are expected to frequently contain edges of the FOV for individual samples and to cut identified structures, hence appearing one-dimensional along the y-direction. This assumption is confirmed by the orientation parameter in Figure 4.31(h) approaching values close to zero in this region (see ④). Such issues are not evident from the HOQ-like topology. Overall, the orientation parameter Θ decreases with increasing wall distances, which suggests that structures are increasingly aligned towards the y-direction. From the shape and orientation evaluation, it can be concluded that structures appear elongated in z-direction within the unburnt gas, approach spherical shapes in the flame bush region and in the near burnt, and finally get elongated in y-direction for the far burnt gas.

However, features in ϵ and Θ are less significant than observations in the vortex probability. It can be concluded that the presence of vortices at the right location appears to be the decisive element whether a case develops into SWQ- or HOQ-like, rather than the shape or orientation. In the SWQ-like, it is suggested that the coherent structure located directly downstream the quenching point promotes exhaust gas recirculation, influencing the local quenching event. For the HOQ-like, the vortices behind the flame front are expected to push the reaction zone close to the wall, leading to the actual HOQ phenomenon. This in turn could be related with the vortex reported in the literature [7, 29, 69], which was pushing the reaction closer to the quenching wall. These two topology-related phenomena were already presumed on the basis of the transient observation in Zentgraf et al. [E8].

4.3.2.6 Transient Phenomena

After the available data has been analyzed in detail from a statistical point of view using the statistically independent 50 Hz data, a brief evaluation of transient phenomena using samples acquired at 4 kHz will be given to complement the investigation on flame and flow dynamics. This is done by discussing one continuous transient that contains both an HOQ- and an SWQ-like event in the following. For reasons of clarity, the transient is shown in two separate Figures 4.32 (first half) and 4.33 (second half). Each column presents an individual time step with $\Delta t = 250$ μs increment in the sequence, as indicated in the title on column's top. The top row outlines OH-PLIF images superimposed with the detected flame front (red dash-dotted line), streamlines and identified vortex structures by Q-criterion (blue filled areas). The largest vortex structure is colored in a dark blue, while smaller structures feature a light blue. This aids temporal tracking of the biggest, i.e., strongest, existing vortex phenomenon in the FOV. The fact that structures are temporally traceable suggests a certain robustness of the implemented processing, like the use of Q-criterion for this combustion application and the empirical thresholding. To facilitate discussion on the instantaneous fluid transport, relative velocity fields are derived as $U_{z,\mathrm{rel}}(y,z) = U_z(y,z) - \langle U_z \rangle(y,z)$ by subtracting the temporal average velocity field $\langle U_z \rangle(y,z)$ from the instantaneous $U_z(y,z)$. The same is applied for the fields $U_y(y,z)$ that describe the y-direction velocity component. These velocities give a measure for the instantaneous, relative fluid motion with respect to the global temporal average movement. In the following visualizations, corresponding negative values in the blue regions mean that fluid is slowed down with respect to the temporal average, while positive values in yellow regions indicate a relative speed up. If yellow and blue areas are located next to each other, fluid in those regions is expected to increasingly depart from each other with evolving time. The center rows in Figures 4.32 and 4.33 depict $U_{z,\mathrm{rel}}$, while the bottom rows outline $U_{y,\mathrm{rel}}$ respectively. These views depict the biggest vortex as black solid line for reference.

The transient in Figure 4.32 first starts with a HOQ-like event at $t = 0$ ms (time t is defined to zero at this point to facilitate discussion). As observed in the top row, the largest vortex structure (dark blue area) is clearly identified behind the reaction zone that aligns parallel to the wall. This is fully consistent with the statistical analysis provided in Figure 4.31(c), predicting vortices at this location with high probability values of $0.3 - 0.4$. The observed HOQ-like topology temporally evolves to a typical scenario that is classified as an SWQ-
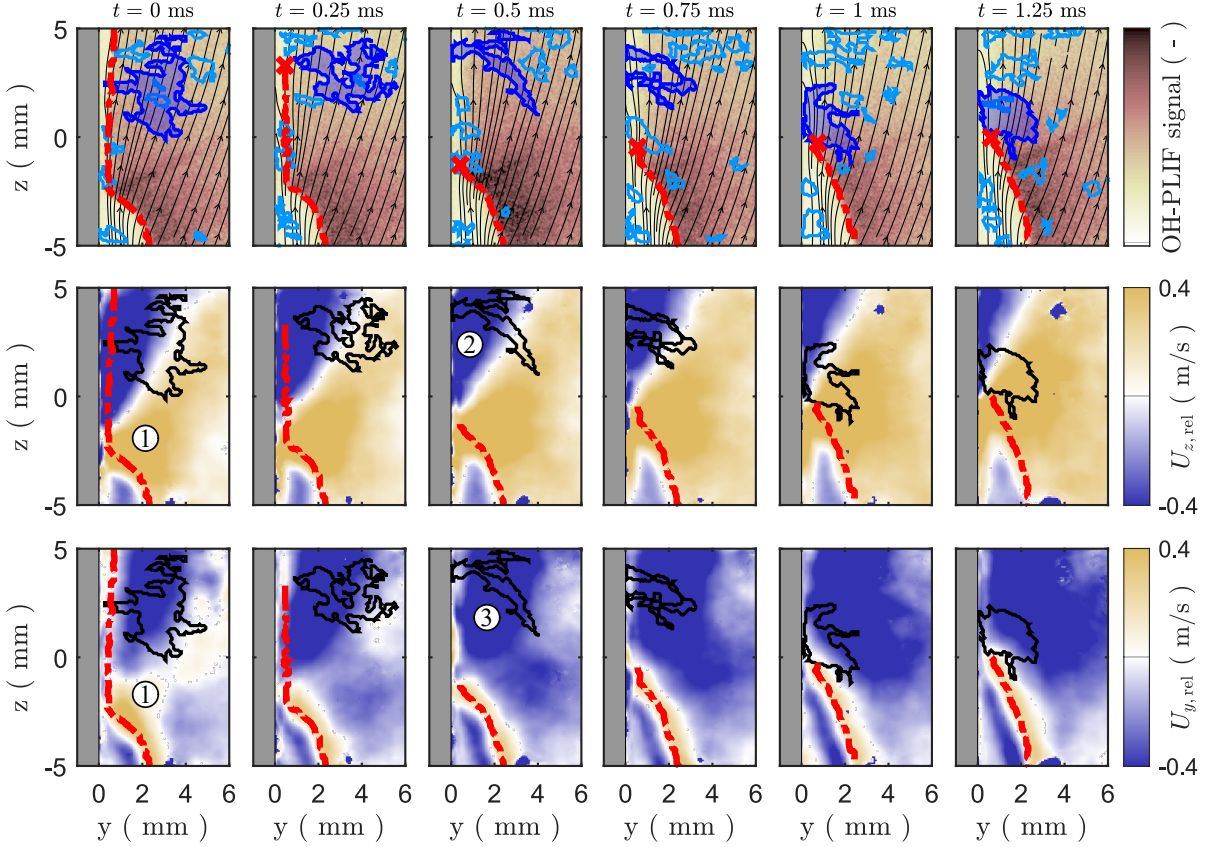
Figure 4.32: Transient sequence (first half) at 4 kHz (250 μs between images) containing the transition from HOQ-like to SWQ-like topology. Top row: OH-PLIF images; center row: $U_{z,\,\mathrm{rel}}$; bottom row: $U_{y,\,\mathrm{rel}}$. Superimposed: detected flame front (red dash-dotted line), streamlines, identified vortex structures by Q-criterion (dark blue filled area: largest structure, light blue filled areas: smaller structures).

like case. The algorithm that detects the flame front from OH-PLIF images starts to classify an SWQ-event from $t = 0.5$ ms on. From $t = 0$ ms to $t = 0.75$ ms the biggest vortex right behind the wall-parallel reaction zone increasingly shrinks, most likely as it temporally decays. Finally, at $t = 1$ ms it is no longer significant and the biggest vortex structure is detected directly downstream the quenching point. This well-aligns with the previous statistical analysis on vortex structures in Figure 4.31(b), where increased vortex probability values (> 0.2) are apparent directly downstream the quenching point location. As expected, the flame front promotes a relative fluid movement in positive y- as well as z-direction in the fields of $U_{y,\,\mathrm{rel}}$ and $U_{z,\,\mathrm{rel}}$ (see zone ① in Figure 4.32). This suggests certain physical robustness of the derived relative velocity fields as a measure for instantaneous fluid transport with respect to the temporal average and they can be used for this interpretation. From spatial $U_{z,\,\mathrm{rel}}$-distributions, shown in the center row, basically a wedge-shaped zone with relative movement in negative z-direction, i.e., upstream, is observed within wall-parallel quenching or right above the quenching point (see zone ② in Figure 4.32). In turn, the $U_{y,\,\mathrm{rel}}$-fields suggest a slowed down relative movement of fluid in wall-normal direction, i.e., in negative y-coordinate, in the post-quenching areas (see zone ③ in Figure 4.32).
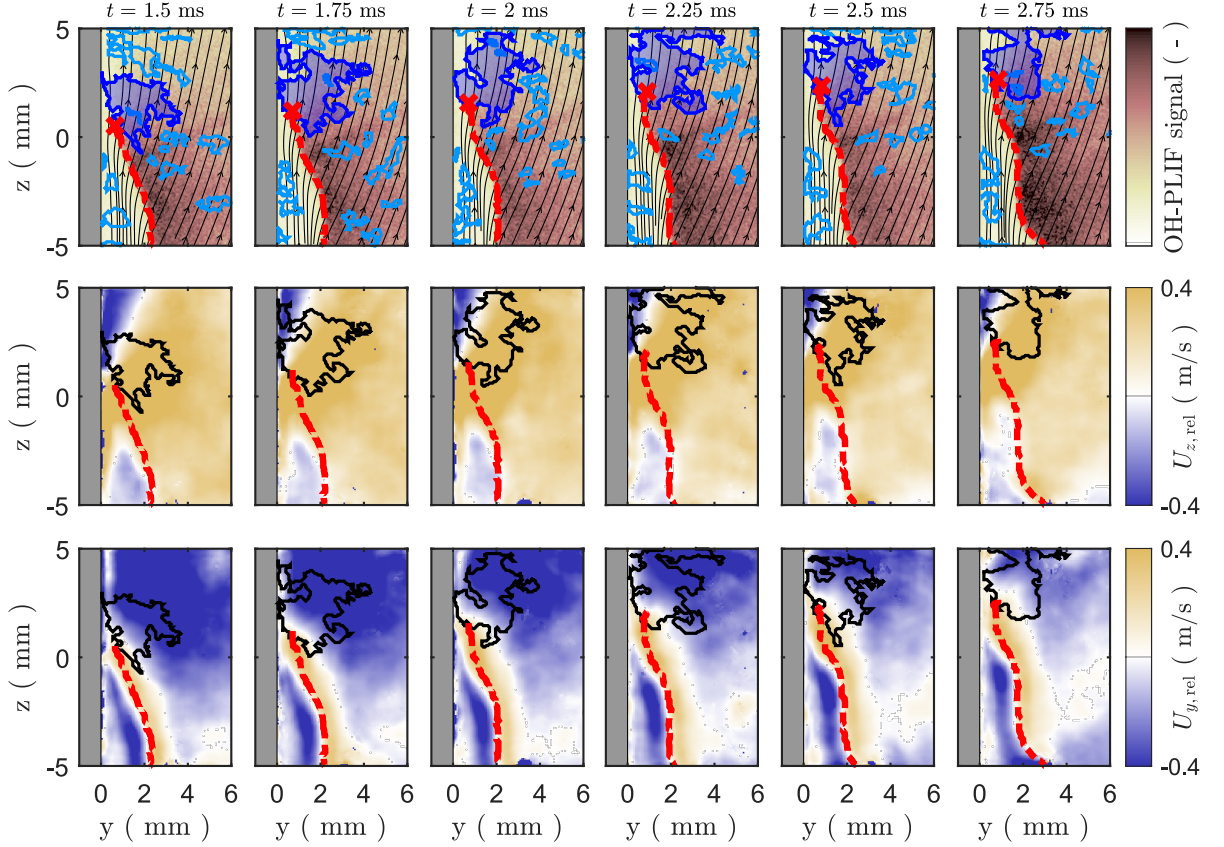
Figure 4.33: Transient sequence (second half) at 4 kHz (250 μs between images) containing the transition from HOQ-like to SWQ-like topology. Top row: OH-PLIF images; center row: $U_{z,\,\mathrm{rel}}$; bottom row: $U_{y,\,\mathrm{rel}}$. Superimposed: detected flame front (red dash-dotted line), streamlines, identified vortex structures by Q-criterion (dark blue filled area: largest structure, light blue filled areas: smaller structures).

Continuing the sequence of the selected transient from Figure 4.32 in Figure 4.33, it is observed that the biggest detected vortex structure moves further downstream with temporal evolution, spatially synchronized with the quenching point. As pointed out in section 4.3.2.5, more than 99% of the identified vortex structures rotate counterclockwise in the SWQ-like case. A very interesting aspect in the observed SWQ-like events is that the apparent wedge-shaped zone sometimes appears to extend upstream the instantaneous quenching event. In this area the $U_{z,\,\mathrm{rel}}$-fields spatially change sign. While both flame front and quenching point are associated with regions of positive $U_{z,\,\mathrm{rel}}$, the neighboring wall-closest fluid is characterized by negative $U_{z,\,\mathrm{rel}}$ values. This means that, for progressing time in the instantaneous sequence, the flame front and quenching point move downstream, while near-wall fluid is decelerated relative to them. This can be seen as a transport in negative z-direction, relative to the downstream movement of the quenching point. In turn, this would indicate that reacted gas phase is transported upstream the SWQ-like quenching point causing local exhaust gas recirculation (EGR), as presumed in Zentgraf et al. [E8]. This is for example the case in the time step $t = 2.75$ ms shown in the last column of Figure 4.33. As this phenomenon is hard to observe from the global view in Figure 4.33, a magnified view is shown in Figure 4.34(a) besides two further se-
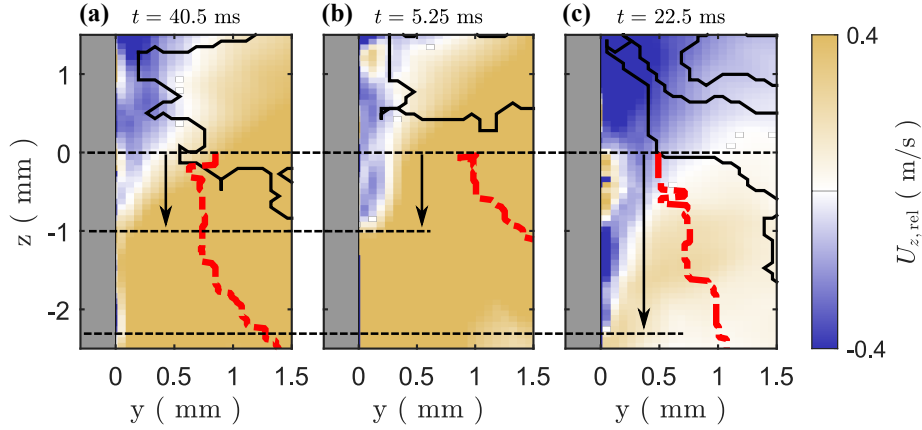
Figure 4.34: Magnified selected fields of $U_{z,\mathrm{rel}}$ to visualize upstream transport relative to the quenching point of SWQ-like events.

lected fields with similar effect. In the visualization in Figure 4.34 the quenching height is fixed at $z = 0$ mm for better comparison and t at the top indicates absolute time in the transient. While the blue region, indicating relative transport in negative z-direction, in Figures 4.34(a) and (b) reaches less than one millimeter upstream the quenching point, it can also extend more than 2 mm, as shown in (c). Thus, a typical dimension of this wedge-shaped zone that could cause upstream transport relative to the quenching point may be estimated as $(\Delta y, \Delta z) \leq (0.5\ \mathrm{mm},\ 2\ \mathrm{mm})$.

4.4 Summary

This chapter presented a detailed analysis of the near-wall flame and flow dynamics during operation of an SWQ burner. Fields of flow velocity and flame front distribution were measured simultaneous by PIV (two-dimensions, two-components) and OH-PLIF. All acquired data was (1) conditioned to the instantaneous quenching onset and (2) classified with respect to the near-wall quenching topology (either SWQ-like or HOQ-like) prior to statistical analysis. Scope of the analysis was to gain further insights into the underlying near-wall transport effects, especially with respect to the distinguished quenching topologies observed for turbulent conditions. Operation points OP1 and OP2 presented in Table 3.1 were studied, i.e., both laminar and turbulent DME/air flames at $\Phi = 0.83$ and $T_{\mathrm{wall}}^{(\mathrm{nom})} = 60\ ^\circ\mathrm{C}$ (main focus on the turbulent case).

From the flame dynamics analysis, it became evident that turbulent operation of the SWQ burner leads to alternating SWQ- and HOQ-like quenching topologies. In the set of statistical independent data (2000 samples in total) 43.4% featured SWQ-like and 56.6% HOQ-like topology, which approximates an equal share between both events. Thorough conditioning on the quenching onset and classification of both topologies yielded the capability for robust statistical analysis, which preserved spatial features relative to the quenching event. A first characterization of basic flow metrics indicated that the SWQ- and HOQ-like quenching topology is different in the individual near-wall transport behav-

ior. In the vicinity of quenching, HOQ-like cases suggested increased convective transport in both y- and z-direction as well as higher mixing rates than the SWQ-like topology.

The measured highly-resolved PIV data was capable to resolve the turbulent boundary layer down to its viscous sublayer to at least $y^+ = 1.5$ (equals 130 μm). Further PTV processing was thus not required, despite it proved possible. The non-reacting reference case well-reflected the universal laws (linear relation and log law), which are common to describe turbulent boundary layers. Upon reacting operation, the inner structure of turbulent boundary layers remained nearly unaffected by combustion in the pre-quenching area, but thickened with evolution in streamwise z-direction over the quenching onset. The change in near-wall viscosity in z-direction due to the reaction's heat release was appointed as major contributor for this thickening. SWQ-like cases featured slightly steeper thickening than HOQ-like topologies in streamwise direction. It was furthermore evident that the viscous sublayer remained unaffected by quenching events, as the linear regime was retained up to $y^+ = 5$. However, for $y^+ > 5$ the u_z^+ velocity profiles underrated the log law values. This tendency increased when approaching the quenching onset in streamwise direction and partially recovered further downstream. The observation was appointed to a permanent interplay between mean velocity in streamwise direction $\langle U_z \rangle$ (thermal expansion) and $u_{\tau, z}$ (change of viscosity and wall-normal velocity gradient). Both parameters were driven by heat release and the local gas temperature distribution was seen as key parameter. However, a detailed unraveling of the parameter dependence turned out complex and a potential parametrization of log laws for reacting FWI conditions requires further research.

An analysis of near-wall integral length scales revealed that wall-normal scales ($L_{yy, +y}$) rise for increasing distance from the wall. As this increase is observed faster for HOQ- than SWQ-like cases, it suggested bigger, energy containing near-wall structures in HOQ-like topology, which could imply increased instantaneous mixing and more intense wall-normal convective transport than in SWQ-like cases. Well-selected regime analysis within the quenching area showed that SWQ-like events are rather focused within the wrinkled flamelets regime, while HOQ-like cases are predominantly located in the corrugated flamelets. However, both processes are observed very close to each other near the regime boundary. In turn, this suggested that the HOQ-like is associated with higher level of turbulence interacting with the local quenching reaction, i.e., more wrinkling. This implied potentially higher mixing, transport and reaction rates of HOQ-like topologies in the wall-normal direction than the SWQ-like cases.

A simplified, two-dimensional projection of turbulence anisotropy states yielded insight on the direction-dependent distribution of turbulent kinetic energy during flame quenching. Basically, SWQ- and HOQ-like topologies did behave similarly in their turbulence anisotropy characteristics within the pre-quenching regions ($z < -1$ mm). A striking difference was observed in the post-quenching, where the SWQ-like case possessed rather anisotropic behavior with respect to the projection, while HOQ-like topologies featured isotropy in the projection directly behind the flame front, with more intense velocity fluctuations than the SWQ-case. The latter observation in the HOQ-like could suggest elongated eddies.

Accordingly, near-wall vortex structures were assessed in terms of vortex probability, shape and orientation by using a simplified two-dimensional Q-criterion projected to the yz-plane. It was first evident that rather elongated structures in z-direction prevail at high probability within the undisturbed boundary layer in the pre-quenching areas. SWQ-like topologies featured high vortex probability directly downstream the quenching point that could promote near-wall EGR. In HOQ-like cases high probability was observed close to the wall-parallel reaction zone in the burnt gas, presumably pushing the reaction closer to the wall. In the reacting cases, nearly all vortices turned counterclockwise ($> 99\%$). The significantly different local presence of vortices was assumed to determine the actual quenching topology. Furthermore, structures seemed to be elongated in z-direction within the unburnt gas, rather spherical in/behind the flame brush and elongated in y-direction for the far burnt gas.

A final consideration of a transient evolving from an HOQ- to SWQ-like event confirmed the proposed view on major vortex structures as previously concluded from the statistical analysis. Biggest structures were temporally well-traceable. An evaluation of instantaneous relative fluid movement suggested potential near-wall transport of fluid upstream the quenching event, possibly causing near-wall EGR.

Chapter 5

Thermochemistry

5.1 Aim of the Investigation

This chapter presents a comprehensive experimental campaign on fully-premixed thermochemistry during SWQ to access the coupled reaction-transport processes governing near-wall flame quenching. Within the graphical abstract in Figure 5.1, summarizing the complementary measurements performed in this thesis, the relevant thermochemistry topic is framed red.

Initially, an advanced three-parameter laser diagnostic is introduced to simultaneously quantify gas phase temperature, carbon dioxide and monoxide mole fractions during flame-wall interaction. The novel approach is thoroughly quantified in terms of accuracy and precision by benchmarking it to simulation data. Near-wall thermochemistry data is studied for laminar operation to assess species diffusion effects. Turbulent cases are analyzed for the impact of convection and mixing on thermochemistry, whereat focus is on the previously classified SWQ- and HOQ-like topologies. A major aim is to postulate theories on potential near-wall transport-reaction coupling during quenching, and to point out that near-wall thermochemistry changes with respect to the quenching topology. Several contents of chapter 5 were published in Zentgraf et al. [E8, E11], and are reused in this thesis in part and with permission (see appendix B for permission of Elsevier and declarations of the author's contribution). In the remainder of this chapter, corresponding passages are pointed out at the beginning of superordinate sections, respectively.
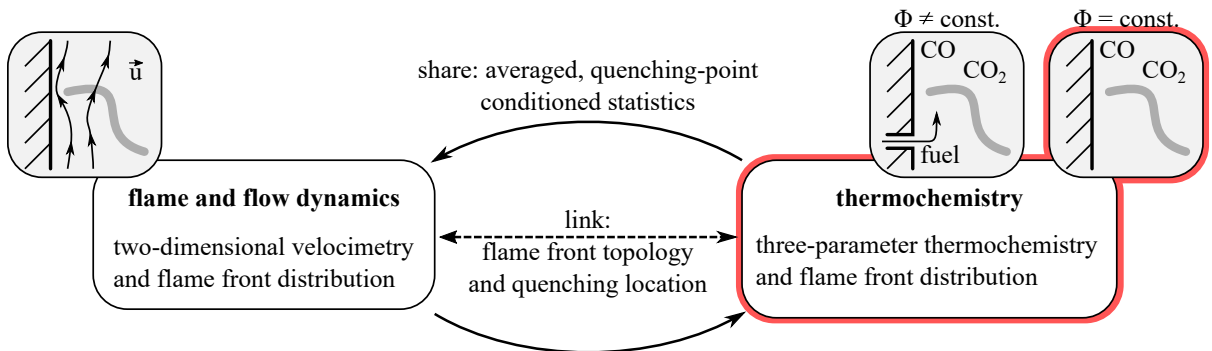
Figure 5.1: Graphical abstract of the applied approach using complementary experimental results to assess transport and reaction phenomena in FWI.

5.2 Methodology

For a detailed assessment of thermochemistry, an advanced combination of quantitative and qualitative laser diagnostics is applied simultaneously. The experimental realization is outlined in section 5.2.1 with the subsequent data processing given in section 5.2.2 and a numerical benchmark case in section 5.2.3. Parts of the content of section 5.2 were published in Zentgraf et al. [E11] and are reused with permission (see appendix B), in a modified wording and partially extended by further technical and scientific details to fit the structure of this thesis. This concerns parts of sections 5.2.1, 5.2.2 and 5.2.3.

5.2.1 Laser Diagnostics

The laser diagnostic setup is summarized by the schematic given in Figure 5.2. The comprehensive realization comprised four individual approaches, applied simultaneously. Dual-pump coherent anti-Stokes Raman spectroscopy (DP-CARS) quantified gas phase temperature T and carbon dioxide mole fraction X_{CO_2} by instantaneously targeting N_2 and CO_2 molecules, while a two-photon laser-induced fluorescence probed carbon monoxide (CO-LIF) to assess CO mole fraction X_{CO}. The spatial flame front distribution was measured by planar laser-induced fluorescence of the OH radical (OH-LIF) and thermographic phosphor thermometry (TPT) yielded wall surface temperatures for control purpose. Basically, this simultaneous multi-parameter approach followed former studies, like Kosaka et al. [E2], who used N_2-CARS instead of DP-CARS. A detailed description on the experimental implementation of each individual approach is given in the following.

5.2.1.1 DP-CARS

The applied DP-CARS approach involved the quantum mechanical fundamentals given in section 2.3.2.2. This thesis followed the study of Lucht et al. [104] and their optical setup to implement the DP-CARS technique on the SWQ burner facility here. The N_2 molecules Raman shift $\Delta\tilde{\nu} \approx 2330$ cm^{-1} was accessed by pumping with 532 nm and probing around 560 nm, while CO_2 at $\Delta\tilde{\nu} \approx 1380$ cm^{-1} was pumped by 560 nm radiation and probed at 532 nm, both transitions using a broadband Stokes laser around 607 nm [140]. The three required wavelengths λ_1 to λ_3 were provided by two dye lasers and two Q-switched, frequency-doubled Nd:YAG lasers (Spectra-Physics PIV 400, 10 Hz, 5-8 ns pulse width, custom-modified[8]) as excitation source. Pulses of the first Nd:YAG laser were split into two paths to provide radiation at $\lambda_1 = 532$ nm in the region of interest (ROI) on the one hand, and to optically pump a custom-built broadband, modeless Stokes laser on the other hand that generated the $\lambda_3 = 607$ nm beam. The Stokes laser applied in this thesis basically followed a design principle by Ewart [56] and was first implemented at RSM by the work of Kissel [92]. It consisted of a transversally pumped oscillator and two longitudinally pumped amplifier stages (pre- and main amplifier). Further details on the design can be found elsewhere [92]. A dye mixture of Rhodamine 610 and 640 solved in ethanol (oscillator: ≈ 69 mg/L R610, ≈ 60 mg/L R640; amplifiers: ≈ 27 mg/L R610,

---

[8]The PIV-overlap was removed and individual Nd:YAG cavities were split with independent second harmonic generation stages, finally resulting in two independent lasers at 532 nm.

AL	achromatic lens	GP	glass plate	L/2	half-wave plate
DM	dichroic mirror	H	heat shield	PMT	photomultiplier tube
F	filter	IRO	intensified relay optics	SL	spherical lens
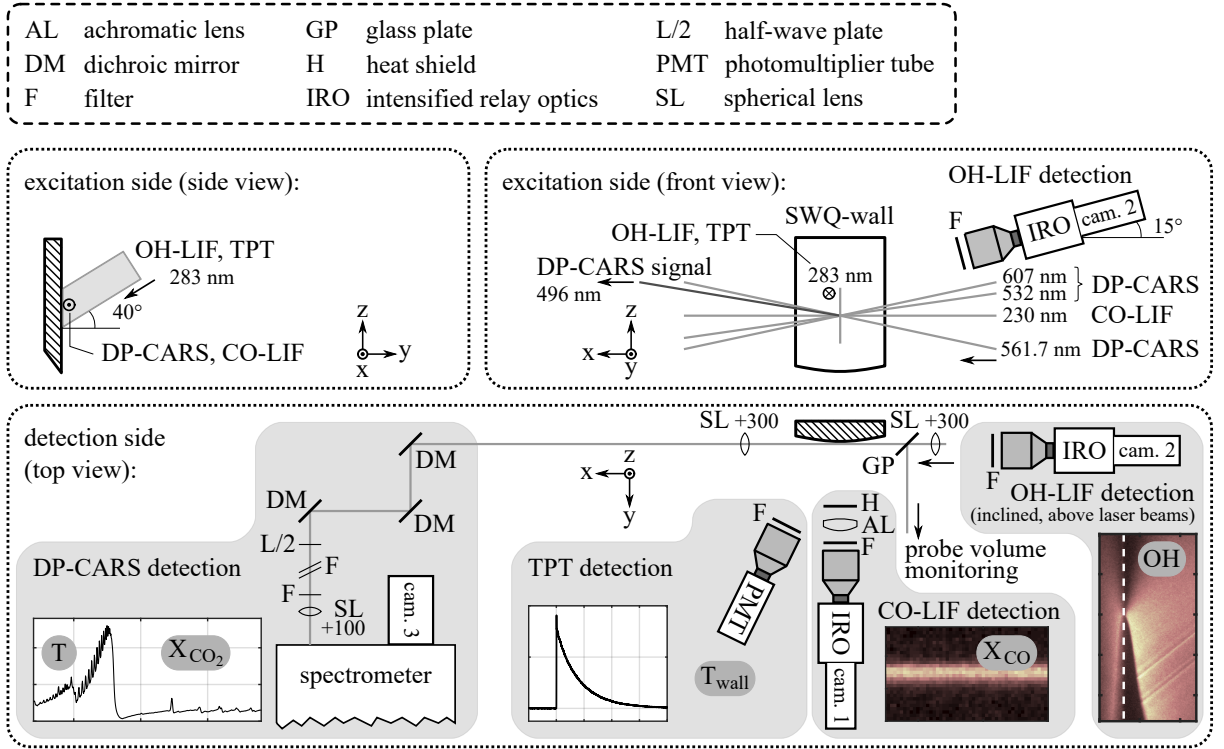
Figure 5.2: Laser diagnostic setup with the excitation side shown in a side as well as front view and the detection side in a top view. Exemplary signals are shown in embedded views for each detection setup respectively. Numbers at spherical lenses denote focal length in millimeters. This figure was published in Zentgraf et al. [E11] (Fig. 2) and is reused with permission of Elsevier; reproduced in an adapted version.

$\approx$ 8 mg/L R640) provided a broadband spectral profile centered around 607 nm with $\approx$ 8 nm full width at half maximum (FWHM). To generate radiation at $\lambda_2 = 561.7$ nm, the second Nd:YAG laser was used to optically pump a narrowband dye laser (Radiant Dyes Laser & Accessories GmbH, NarrowScan) operated with Rhodamine 590 dye dissolved in ethanol. To attain a good separation of the N_2 and CO_2 spectral features on the recorded DP-CARS spectra in this work, $\lambda_2 = 561.7$ nm was used instead of the 560 nm reported in Roy et al. [140] or 561 nm used by Lucht et al. [104]. Laser beams were guided through the optical setup by high-reflective dielectric mirrors as well as anti-reflective coated prisms. All further optics had respective anti-reflective coatings. The individual beams, i.e., radiations at λ_1, λ_2 and λ_3, were energy-controlled by a combination of zero-order half-wave plate and polarizing beam splitter. Their divergence was adjusted by Galilean telescopes of spherical lenses to create well-defined foci in the ROI of each laser beam, respectively. After passing delay lines, the three individual beams were overlapped in a planar BOXCARS arrangement along the vertical axis (z-direction in Figure 5.2), guided to the SWQ burner and focused to the ROI by a spherical lens with $f = +300$ mm focal length. A fused silica flat glass plate (see GP in Figure 5.2) was positioned after the focusing lens to deflect a fraction of the DP-CARS beams to a probe volume monitoring system (explained in detail in section 5.2.1.6). To meet the DP-CARS phase matching condition, the focusing angles were set to $\alpha_{532} \approx 2.0°$, $\alpha_{561} \approx -1.9°$ and $\alpha_{607} \approx 2.2°$

with respect to the principal beam direction, i.e., x-direction in Figure 5.2. Within the ROI, final average pulse energies E were $E_{532} \approx 25$ mJ (1% coefficient of variation (CV)), $E_{561} \approx 24$ mJ (3% CV) and $E_{607} \approx 13$ mJ (2% CV), which were $\approx 15\%$ decreased from those used by Lucht et al. [104]. The dimensions of the interaction volume Δx, Δy and Δz were derived to further assess the DP-CARS measurement resolution in the ROI. First, a thin glass plate (100 μm thickness) was moved through the probe volume in x-direction. The resulting $1/e^2$-values of its integrated non-resonant signal were used to estimate the interaction length in x-direction to $\Delta x \approx 2.4$ mm. Second, a beam monitor (DataRay Inc., WinCam D; neutral density filters of OD9 in front) was used to measure the individual pulse intensities I in the central measurement plane of the SWQ burner ($x = 0$ mm). The CARS probe volume was derived as the $1/e^2$-value of the convolved intensity $I_{\mathrm{CARS}} \propto I_{532} \cdot I_{561} \cdot I_{607}$ and spanned $(\Delta y, \Delta z) \approx (67 \ \mu m, 54 \ \mu m)$. In the scope of this thesis, the entire excitation system for DP-CARS, i.e., lasers as well as optics for beam control and overlap, was constructed and arranged on a mobile lab table (Nd:YAG pump lasers on a lower floor, dye lasers on an upper floor above; see appendix A.2 for details). This was done to prepare the diagnostic system for future applications at other test rigs at RSM institute.

After passing the ROI, the coherent DP-CARS emission ($\lambda_4 \approx 496$ nm) was collimated by another spherical lens with $f = +300$ mm. As the DP-CARS signal featured a significant spatial overlap with $\lambda_2 = 561.7$ nm, it had to be split from this high laser intensity prior to spectroscopic detection. This was done by three lowpass dichroic mirrors (Thorlabs Inc., DMLP550L, 50% transmission/reflection at 550 nm), each transmitting $\approx 90\%$ of λ_2 while the DP-CARS signal was reflected. To further optimize the polarization of the DP-CARS emission λ_4 with respect to the spectrometer, it passed an additional achromatic half-wave plate (Thorlabs Inc., AHWP10M-600, for 400-800 nm). Afterwards, three filters were arranged in the beam path for further signal conditioning. First, a notch filter was applied to remove scattered radiation at $\lambda_1 = 532$ nm. Second, residuals of $\lambda_2 = 561.7$ nm were suppressed by a short pass filter (Thorlabs Inc., FESH0550, cutoff wavelength 550 nm). Third, optional neutral density filters (arranged in a motorized filter wheel: 0.5%, 10% transmission or no filter) were moved in the signal path. As the DP-CARS signal significantly increases at lower temperatures (e.g., see Figure 2.14 for reference), this was required to avoid saturating the detector at certain measurement locations. After filtering, a spherical lens ($f = +100$ mm) focused the DP-CARS emission to the entrance slit of a spectrometer (SPEX Industries Inc., 1704, 1 m spectrometer, 2400 lines/mm grating) and the resulting spectra were recorded by a cooled, backside-illuminated CCD camera (Princeton Instruments, Pixis 400). The camera was operated with 1 ms exposure time using all 1340 pixels in the horizontal direction, i.e., wavelength-dimension, on the camera chip, while only 25 pixels in vertical chip-direction were used, as the signal did not expand further. To reduce noise, these 25 vertical pixels were hardware-binned prior to readout, resulting in one spectrum for each measurement. To correct for the spectral profile of the Stokes laser, non-resonant DP-CARS spectra were recorded in pure argon gas (specification: argon 4.6, purity 99.996%) several times during measurements. For this purpose, the DP-CARS probe volume was centered in a T-fitting that was flushed with argon gas. This avoided the presence of any remaining ambient species, like N_2, and exclusively yielded a non-resonant spectrum.

5.2.1.2 CO-LIF

The implemented CO-LIF technique based on the fundamentals outlined in section 2.3.2.3. Carbon monoxide was excited by two UV photons at $\lambda = 230.09$ nm for the transition $B^1\Sigma^+ \leftarrow\leftarrow X^1\Sigma^+(0,0)$ in the Hopfield-Birge bands and its resulting emission $B^1\Sigma^+ \rightarrow A^1\Pi(0,1)$ in the Ångström bands was captured, as outlined by Linow et al. [102]. The implementation of this well-established approach in this thesis followed the outlines of previous FWI investigations [67, 82, 110, E2]. The required UV pulse at 230.09 nm was generated by a narrowband dye laser (Sirah Lasertechnik GmbH, PrecisionScan, 2400 lines/mm grating). The operation with Pyridine 1 laser dye yielded 690.27 nm fundamental radiation that was turned into its second harmonic at 345.135 nm by a first frequency conversion unit. A further stage mixed remaining fundamental (690.27 nm) and second harmonic (345.135 nm) to form the desired radiation at 230.09 nm, i.e., a frequency tripling of the fundamental. A wavelength meter (HighFinesse GmbH, WS6) continuously monitored the 690.27 nm radiation and stabilized the laser's grating position by a control loop, finally keeping the 230.09 nm radiation constant within 0.025-0.036 cm^{-1} deviation (minimum to maximum wavenumber difference over a measuring day, based on temporal averages for each spatial recording position). The dye laser was optically pumped by a Q-switched, frequency-doubled Nd:YAG laser (Spectra-Physics GCR 4, 10 Hz, 5-7 ns FWHM-pulse width, 532 nm). High reflectivity dielectric mirrors were used to direct the 230.09 nm radiation to the ROI. First, the radiation was energy-controlled by a half-wave plate and a subsequent Glan-laser double escape polarizer (Lattice Electro Optics Inc., PCGL-a-BBO-04). Second, reflections of a flat fused silica glass plate (≈ 10 mm thickness, not shown in Figure 5.2) were deflected from the beam path to an energy meter (front side reflex; Coherent Inc., EM USB J-10MT-10KHZ) and a beam monitor (back side reflex; DataRay Inc., WinCam D) with additional UV-converter (Star Tech Instruments Inc., BSF23) for control and reference purpose. This was a separate measure to the probe volume monitoring system introduced in section 5.2.1.6 below. The energy values were required to correct pulse-to-pulse fluctuations of the excitation energy in the CO-LIF signal, as outlined in the processing section 5.2.2.2. The beam profile references were not acquired shot-to-shot but from time to time to check the UV laser's spatial position and intensity distribution. Deviations could indicate a change in the laser operation and in the worst case a mismatch of the spatial overlap with the DP-CARS probe volume (in case the spatial location shifts) or bias the CO-LIF calibration required for quantification (in case the intensity distribution alters). This was not evident from the beam profile references during the performed measurements. Afterwards, a spherical lens ($f = +300$ mm) focused the UV beam to the probe volume, while the 90°-deflection by a small rectangular mirror (10×20 mm^2) placed it between the DP-CARS beams for overlap (see front view of the excitation side in Figure 5.2), right after the DP-CARS focusing lens. Within the ROI, average pulse energies were $\approx 0.7 - 0.9$ mJ (5% CV), but slightly dropped during a measuring day by about 10-18%. This did not affect the data processing and was corrected for using the acquired energy reference values, as pointed out above. The UV beam diameter in the ROI spanned $(\Delta y, \Delta z) \approx (260 \ \mu\text{m}, 200 \ \mu\text{m})$ ($1/e^2$-value of Gauss-fitted profiles, measured with above mentioned beam monitor equipped with UV-converter). However, this is not considered the effective probe volume size of the CO-LIF diagnostic. As the applied excitation scheme is a two-photon process, the resulting LIF signal features an

energy dependency by an exponent $n \leq 2$ (here: $n = 1.68$). Thus, an estimation of the CO-LIF-effective probe volume size needs to consider the laser fluence dependency $I^n = I^{1.68}$ leading to $(\Delta y, \Delta z) \approx (140~\mu m, 140~\mu m)$ ($1/e^2$-value of Gauss-fitted profiles of $I^{1.68}$). In principal beam direction, a CO-LIF probe volume of $\Delta x \approx 2$ mm is extracted for data analysis to fit the DP-CARS interaction length.

The resulting CO-LIF signal was captured by an imaging optics consisting of achromatic lens (Qioptiq Photonics GmbH & Co. KG, G322267000, $f = +160$ mm, 80 mm diam.) and objective lens (Canon, EF 135 mm f/2L USM, focused to infinity). An interference bandpass filter (Laser Components GmbH, LC-HBP 490/20-75, >95% transmission at 480-500 nm) removed ambient light and flame luminosity impact. It was mounted between achromatic and objective lens, in the region of parallelized collected light, to avoid potential bias to the filter band by varying angle of incidence (AOI) of the transmitting signal. To protect the detection system from thermal radiation of the burner, an anti-reflection coated heat shield was placed in front of the collection lens and purged by a N_2-flow for cooling purpose (between heat shield and achromatic lens). The collected and filtered CO-LIF emission was amplified by an intensified relay optic (IRO, LaVision GmbH, low speed IRO) gated at 100 ns and operated in the linear regime. The intensified signal was finally recorded by a 4×4 hardware-binned CCD camera (LaVision GmbH, Imager E-Lite 1.4M) applying 10 ms exposure time to capture the entire phosphorescence decay of the IRO emission. Recordings were limited to a cropped 70 (horizontal) by 30 (vertical) bin-region on the camera chip centered at the CO focus. This equaled a physical area of $(\Delta x, \Delta z) \approx (3.5$ mm, 1.5 mm$)$ in the ROI, considering a bin size of $\approx 50~\mu m$.

5.2.1.3 OH-PLIF

The diagnostic implementation followed the fundamentals in section 2.3.2.3 and is well-comparable to the previously described high-speed OH-PLIF application in section 4.2.1.1. In turn, this realization in context of the thermochemistry study applied low-speed laser and imaging systems and is thus reported for completeness. Here, excitation and detection are done by transitions in the $A^2\Sigma^+ - X^2\Pi$ system [9]. The OH radical was excited in the UV at $\tilde{\nu} \approx 35210.04$ cm^{-1} ($\lambda \approx 283.93$ nm), which corresponds to its Q$_1$(9) transition [46]. The required UV radiation was generated by frequency-doubling the fundamental output $\lambda \approx 567.86$ nm (in air) of a narrowband dye laser (Sirah Lasertechnik GmbH, Double Dye, 2400 lines/mm, only one cavity used) operated with Rhodamine 590. The dye laser was optically pumped by a Q-switched, frequency-doubled Nd:YAG laser (Spectra-Physics PIV 400, 10 Hz, 5-8 ns FWHM-pulse width, only one cavity used, 532 nm). The energy of UV pulses was set and controlled by rotating the polarization of the fundamental dye laser radiation (using an achromatic half-wave plate) prior to the second harmonic generation. This lowered the UV conversion efficiency, i.e., pulse energy at $\lambda \approx 283.93$ nm, while preserving its beam profile. High reflective dielectric mirrors were used to deflect the UV radiation in the beam path. For light sheet forming, the UV pulse was first expanded and collimated using a Galilean telescope of spherical lenses ($f = -100$ mm and $f = +200$ mm). A subsequent cylindrical lens ($f = +500$ mm) compressed the light sheet thickness, while its height was expanded by an additional cylindrical lens ($f = -300$ mm) prior to the ROI. Latter expansion was required to spatially probe both the FWI region

and the thermographic phosphor coating (see section 5.2.1.4) with one laser light sheet. Due to the limited space around the SWQ burner, the UV-sheet had to be guided to the ROI along the y-axis from top, by an angle of $\approx 40°$ to the horizontal. Within the ROI, average pulse energies were $\approx 0.3 - 0.4$ mJ (10% CV), with the laser light sheet featuring a thickness of $\Delta x \approx 220$ μm ($1/e^2$-value of profile measured with beam monitor and UV-converter as done for CO-LIF in section 5.2.1.2) and ≈ 60 mm height.

A customized UV-objective lens (B. Halle Nachfl. GmbH, 150 mm, f/2.5) collected the OH-PLIF emission. To suppress ambient light and flame luminosity, a bandpass interference filter (Laser Components, BP300-325, 305-340 nm transmission) was mounted in front. A combination of low-speed IRO (LaVision GmbH, gated at 100 ns) and 3×3 hardware-binned CCD camera (LaVision GmbH, Imager E-Lite 1.4M, 10 ms exposure) acquired the signal. One bin on the camera chip corresponded to ≈ 69 μm in the physical space. As the OH-PLIF was detected along the x-axis, it had to be mounted above the DP-CARS excitation beams and inclined by an angle of $\approx 15°$ to capture the FWI-region (see front view of excitation side in Figure 5.2).

5.2.1.4 TPT

Basics of the TPT approach can be found in section 2.3.2.4. In this thesis, the TPT diagnostic was applied for control purpose, i.e., to benchmark the derived wall surface temperature with thermocouples embedded underneath the wall surface. It was measured for the higher wall temperature cases only ($T_{\text{wall}}^{(\text{nom})} \approx 630$ K, see section 3.2). Following the previous measurement of Kosaka et al. [E2], the thermographic phosphor $Gd_3Ga_5O_{12}:Cr^{3+},Ce^{3+}$ (GGG:Cr,Ce) was used with a phosphorescence decay-time approach. A mixture of 1 g GGG:Cr,Ce and 5 ml high-temperature-stable binder (ZYP Coatings Inc., HPC binder) was airbrush-coated to a thin line on the wall, far downstream the quenching event. The post-quenching wall temperature, measured by thermographic phosphors, can be assumed constant, as shown in Kosaka et al. [E2]. Thus, a zero-dimensional TPT measurement, i.e., one single temperature information, suits for control purpose. The thermographic phosphor coating was excited by the $\lambda \approx 283.93$ nm light sheet used for OH-PLIF (see section 5.2.1.3). As the individual emission of both diagnostics is spatially and spectrally clearly separated (OH-PLIF around 305 nm, TPT > 650 nm), no crosstalk was observed. The luminescence signal was collected by an objective lens (Nikon, Nikkor 50 mm, f/1.2) with interference filter (Edmund Optics Inc., long-pass 650 nm, #84-759). Its decay was acquired with a photomultiplier tube (PMT; Hamamatsu Photonics, type H11901-20) and read out by a digital oscilloscope (Tektronix Inc., TDS5034B).

5.2.1.5 Field of Views

Figure 5.3(a) outlines the spatial arrangement of the combined FOVs of the individual laser diagnostics applied as well as the numerical simulation domain used later for comparison. The OH-PLIF FOV extended by $(\Delta y, \Delta z) = (24 \text{ mm}, 32 \text{ mm})$. The zero-dimensional thermochemistry (TC) probe volume, i.e., the spatially superposed DP-CARS and CO-LIF, was scanned point by point to acquire spatial information. For this purpose, the

(a) combined FOVs   **(b)** zoomed near-wall thermochemistry probe volumes
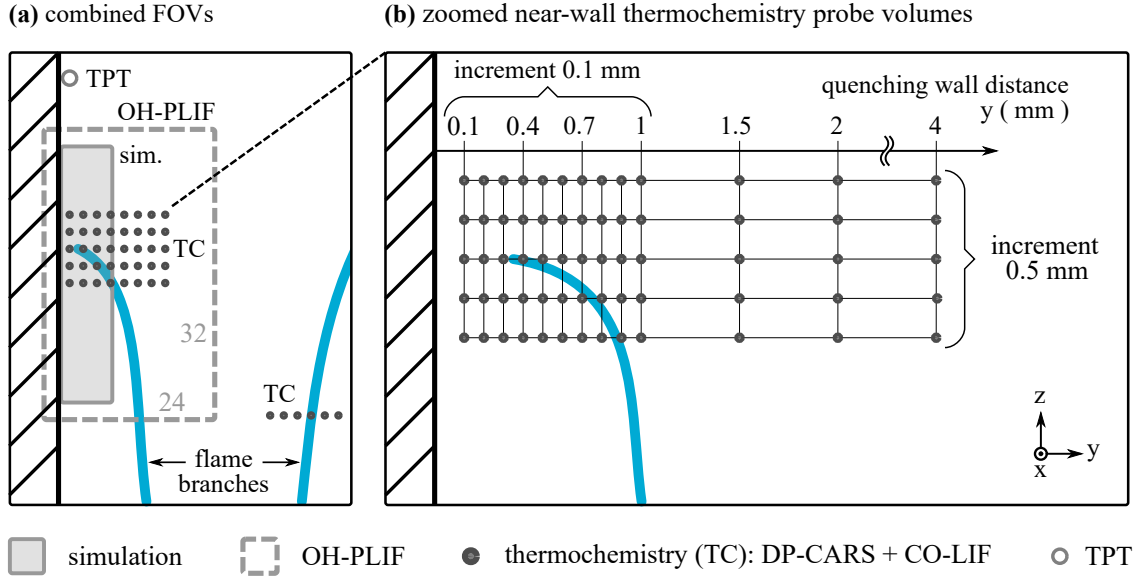
Figure 5.3: Spatial arrangement of the combined OH-PLIF FOV, thermochemistry (TC) and TPT probe volumes along with the simulation domain (a) and detailed view of the scanned TC probe volume locations (b). Numbers indicate dimensions in millimeters. This figure was published in Zentgraf et al. [E11] (parts of Fig. 1) and is reused with permission of Elsevier; reproduced in an adapted version.

entire burner facility was moved on the traversing system, while the laser diagnostics remained fixed. The TC probe volumes were approximately centered with respect to the OH-PLIF. For laminar operation conditions, a two-dimensional field was probed around the near-wall quenching region, as shown in Figure 5.3(b) by a zoomed view. In total, 13 horizontal locations in wall-normal y-direction were assessed (0.1 to 1 mm with $\Delta y = 0.1$ mm; and at 1.5, 2 and 4 mm wall distance), while five different heights in streamwise z-direction were probed (centered around the quenching height; $\Delta z = 0.5$ mm). For turbulent operation, only one z-height (approximately at the mean quenching height) was measured. In this case, variation in z-direction was inherently provided by the turbulent flame front motion from shot-to-shot. In addition, horizontal traces in the unbounded flame branch were measured to capture thermochemistry of an adiabatic flame for reference. The domain of numerical simulation for comparison possessed a range of $(\Delta y, \Delta z) = (6$ mm$, 30$ mm$)$. Please note that the following data analysis used a relative coordinate system with the streamwise coordinate $z = 0$ mm located at the quenching height and $y = 0$ mm at the wall surface. The wall-closest nominal TC position was located at $y = 0.1$ mm.

5.2.1.6 Synchronization and Matching

It is obvious that a correct temporal synchronization and spatial matching of all diagnostics involved is indispensable to reliably measure correlated parameters, as done in this thermochemistry study. With regards to near-wall measurements, a proper definition of the wall position is furthermore crucial. These aspects are covered in the following.

Two synchronized digital pulse generators (Quantum Composers Inc., 9520 Series) controlled the temporal triggering of systems. All lasers were triggered with 10 Hz repetition rate, while the recording systems ran at 20 Hz to capture background intensity without signal in every second image. The schematic for triggering is shown in Figure 5.4(a). To avoid any crosstalk, the laser pulses to capture an instantaneous event were separated by 200 ns for each diagnostic method. First, the CO-LIF was timed, followed by OH-PLIF/TPT and finally the DP-CARS. The total time duration of 400 ns to capture one instantaneous event is not considered critical for correlation of results from individual diagnostics, as this time scale is well-below the process relevant time scales. As evident from the previous section 4.3.2.6 on transient flow phenomena, the quenching point visually moves less than 500 μm downstream between the 250 μs time increments. Thus, near-wall flow motion in the probe volume is less than 1 μm during the 400 ns capturing time, and negligible. Reaction chemistry time scales for formation and oxidation of CO in a flame for example are rather in the order of several milliseconds [E2] (see Fig. 14 in [E2]).

A pinhole-target with 100 μm diameter aided as spatial reference and for matching. It was fit-mounted to the burner's exit nozzle. First, the pinhole-target was moved in the yz-plane by the traversing system to let the DP-CARS probe volume pass. This was done at $x = 0$ mm, i.e., on the wall's centerline position. Second, the CO-LIF UV-beam was guided through the pinhole. This ensured spatial overlap of both diagnostics and correlation of the derived X_{CO_2} and T (DP-CARS) with X_{CO} (CO-LIF). Afterwards, a two-dimensional recording of the pinhole-target determined the thermochemistry probe volume, i.e., DP-CARS/CO-LIF laser position, in the OH-PLIF images. This spatially correlated the thermochemistry results with the instantaneous flame front topology and quenching onset position. In the same manner, a two-dimensional recording of the target rotated towards the CO detection system marked the center of the thermochemistry probe volume on CO-LIF recordings. Both the CO-LIF and OH-PLIF images were spatially scaled using a customized calibration target (line target with square pattern, 1 mm line spacing, equals millimeter paper). This spatial matching procedure of diagnostics was done at the beginning of each measurement day, respectively. However, for a continuous
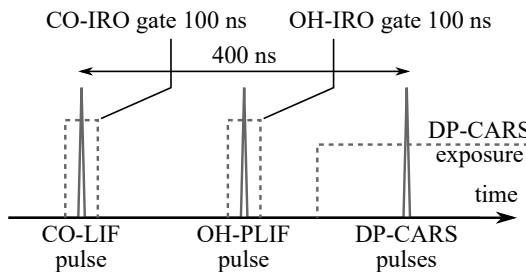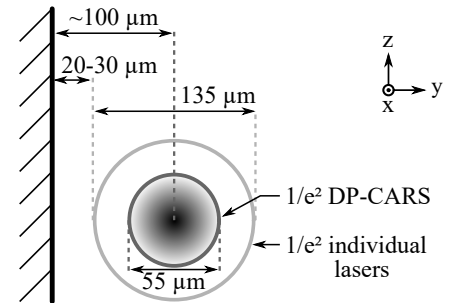
Figure 5.4: Schematic for (a) the temporal synchronization of lasers and detection systems and (b) the estimation of the wall-closest probe volume position. Parts of this figure were published in Zentgraf et al. [E11] (parts of Fig. A.1) and are reused with permission of Elsevier; reproduced in an adapted version.

control of the thermochemistry probe volume matching (i.e., DP-CARS and CO-LIF probe spots) over measurement duration and during combustion operation, an in-situ monitoring was implemented. This was realized by a specially designed beam monitor system shown in Figure 5.5. A flat fused silica glass plate (3 mm thickness, 45° angle-of-incidence, GP in Figure 5.2) was arranged in the path of the combined DP-CARS and CO-LIF beams after their focusing lenses. As the resulting reflections at the glass plate focused in the same manner as the transmitted beams, they were considered to mimic the spatial behavior of the real probe volume. Using the glass plate for deflecting reference beams caused approximately 10% pulse energy loss in the final probe volume. The reflected and focusing beams were guided to a 100 μm pinhole, which served as physically fixed reference for the thermochemistry probe volume. Means, all three DP-CARS beams as well as the CO-LIF beam need to pass the pinhole to express proper matching. The pinhole could be positioned in all spatial dimensions to capture all beams during initial alignment. The transmitted beams were attenuated to level the dynamic of their individual intensity prior to detection using two filters (Schott UG5 1 mm and OD1). Afterwards, the beams impacted a YAG:Tr phosphor screen coated on a fused silica glass plate (5 mm thickness). The phosphor was required to turn the 230 nm UV radiation for CO-LIF into visible light. Resulting radiation from the phosphor screen was then imaged onto a CMOS camera (Thorlabs Inc., DCC1545M) by a combination of spherical lenses mounted in a tubing cage ($f = +35$ mm and $f = +32$ mm). Once initially aligned to the reference pinhole, the imaged spots of the four individual beams (532, 561.7, 607 and 230 nm) were marked (by circles in the recording software) and could be monitored during operation to check for any deterioration, i.e., whether the probe volumes were properly aligned or not. An example recording is shown by the reference image in Figure 5.5. As minor changes in the beam angles did already chance the pinhole transmission significantly, this procedure is considered extremely robust and more sensitive to any mismatching than simply monitoring direct beam reflections. The live monitoring could also be used to re-align the DP-CARS signal over the measurement day, while keeping the combined probe volume at a fixed location, since deterioration of the captured beam spots correlated with a decrease in the DP-CARS signal.
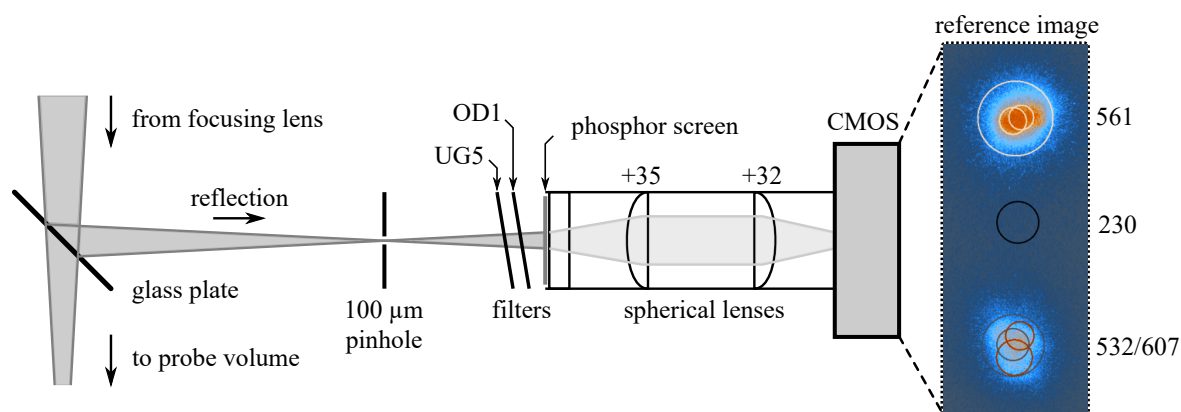
Figure 5.5: Schematic of the probe volume monitoring system with reference image of 532 nm and 561.7 nm beams. This figure was published in Zentgraf et al. [E11] (parts of Fig. A.1) and is reused with permission of Elsevier; reproduced in an adapted version.

Finally, the distance between quenching wall and thermochemistry probe volume is critical for data evaluation. The approach for determining the laser-to-wall distance is depicted by Figure 5.4(b). The procedure combined information from (1) beam monitor recordings of the effective DP-CARS probe volume with (2) the in-situ onset of optical breakdown as the probe volume approaches the wall, means spark formation at the solid surface. Processing the DP-CARS beam monitor recordings yielded that the $1/e^2$ value of the probe volume spanned ≈ 55 μm in wall-normal y-direction. Individual beams featured up to 135 μm $1/e^2$ waist. From an exploratory examination with the SWQ-wall, the first optical breakdown was evident when the wall was approximately intersecting the $1/e^2$ boundary of each individual DP-CARS beam. Following the above values, the derived DP-CARS probe volume center featured a wall distance around 70 μm in those cases. To determine the wall-closest probe volume location for measurement operation, the point of optical breakdown was carefully approached by moving the wall towards the DP-CARS probe volume (with traversing, in 5-10 μm steps) until first sparks were observed. Once first breakdown occurred, the wall was again moved away from the probe volume by 20-30 μm. This was considered a safety distance to (1) protect the IROs and (2) to provide certain tolerance for beam steering-induced laser foci fluctuations during combustion. First, the above procedure was done for the non-reacting case (without flame, wall at 20 °C) to get an initial alignment. Subsequently, it was repeated for the reacting case (with flame, wall at 60 °C or 360 °C). This was required to compensate the thermal expansion of the wall and capture the impact of the above mentioned beam steering. In addition, the determination of the wall-closest position became more accurate through this procedure. The wall-closest position was checked for optical breakdown over a broad range of z-heights afterwards, to ensure safe operation when approaching different z-locations during measurements. This approach finally resulted in ≈ 100 μm nominal wall-closest position. As shown in section 5.3.1.2 later, it appeared capable to determine the wall-closest distance within 20 μm accuracy.

5.2.2 Data Processing

5.2.2.1 DP-CARS

The processing workflow applied to DP-CARS raw data is depicted in Figure 5.6 and outlines graphical results for selected processing steps. At the beginning, recorded DP-CARS raw spectra had to be pre-processed with respect to intensity I and wavenumber $\tilde{\nu}$. For intensity preparation, this involved mean background subtraction, normalization to corresponding mean non-resonant signal (recorded in pure argon gas) and a final square root extraction[9]. Subsequently, the wavenumber-space $\tilde{\nu}$ had to be calibrated for the spectrometer's dispersion, to correctly assign spectral features in $\sqrt{I}$ to $\tilde{\nu}$. For this purpose, experimental data (adiabatic flat-flame burner, premixed CH_4/air, $\Phi = 1$) and a simulated spectrum (by "carsfwsc" algorithm) were compared for identical conditions. A global least square scheme, iteratively optimizing expansion and shift of the wavenumber $\tilde{\nu}$, was

---

[9]These pre-processing steps were performed by MATLAB functions provided by Dr.-Ing. Max Greifenstein from Technical University of Darmstadt (RSM) and were used in this thesis with permission. His kind contribution is acknowledged here.
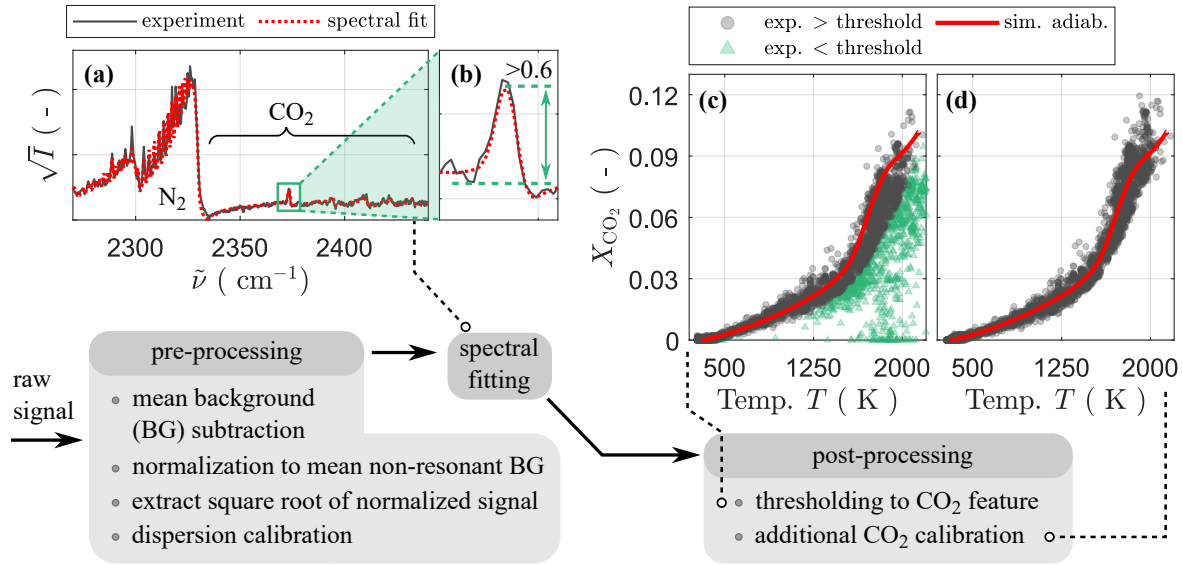
Figure 5.6: DP-CARS data processing workflow with (a)-(d) visualizing selected processing steps. Parts of this figure were published in Zentgraf et al. [E11] (parts of Fig. 3) and are reused with permission of Elsevier; reproduced in an adapted, extended version.

applied to fit the experimental data to simulation and derive the correct $\tilde{\nu}$-vector for further processing.

After pre-processing, the experimental data was evaluated using the spectral fitting algorithm[10] presented by Cutler et al. [40], resulting in a quantitative gas phase temperature T and X_{CO_2} value for each processed single-shot spectrum. During fitting, gas phase temperature T, mole fractions X_{N_2}, X_{CO_2} and wavenumber shift $\Delta\tilde{\nu}$ were allowed to iteratively change for fit optimization, i.e., residuum minimization. An exemplary fit on a single-shot spectrum of experimental data is given in Figure 5.6(a) (near-wall flame branch, $\approx 700\ \mu$m above the wall downstream quenching point, premixed DME/air at $\Phi = 0.83$, values from spectral fitting: $T \approx 1920$ K and $X_{CO_2} \approx 0.09$).

Finally, further post-processing was conducted, related to the derived X_{CO_2} only and necessary to avoid bias from too weak CO_2 DP-CARS signal. It is directly evident from the instantaneous spectrum under reacting conditions in Figure 5.6(a) that the spectral CO_2 features are less pronounced than the N_2 for high temperatures. On the one hand, quantum mechanical characteristics are different in the CO_2 molecule. On the other hand the overall CO_2 concentrations ($X_{CO_2} \leq 0.10$) are much lower compared to N_2 ($X_{N_2} \approx 0.70$) for the combustion environments studied in this thesis, i.e., only combustion formed CO_2 existed. This and further experimental impacts, like signal-drop by beam steering, challenged the evaluation of CO_2 mole fractions under the given reacting conditions. The post-processing of X_{CO_2} comprised two steps: (1) an empirical thresholding criterion to

---

[10]The used fitting algorithm "carsfwsc" was developed and provided by Prof. Dr. Andrew D. Cutler from The George Washington University and was used in this thesis with permission. His kind contribution is acknowledged here. The "carsfwsc" algorithm uses spectroscopic routines from the "carsfitproj" code [41], which is a modified version of the Sandia CARSFIT code [122]. The modifications of "carsfitproj" with respect to CARSFIT are outlined in [41]. All contributions to these codes are acknowledged here.

initially reject too weak CO_2 signal and (2) an additional calibration of non-rejected CO_2 mole fractions to simulation data from section 5.2.3. The thresholding evaluated CO_2 DP-CARS signal quality by means of the most prominent CO_2 feature at $\tilde{\nu} \approx 2373 \text{ cm}^{-1}$, which is the 00^00-10^00 band of CO_2 (see Fig. 3 in [104]). The criterion is visualized in Figure 5.6(b) and based on a comparison of the spectral fit peak (upper green dashed line) to the baseline (lower green dashed line), its difference labeled $\Delta\sqrt{I_{CO_2}}$. The CO_2 DP-CARS signal was considered sufficiently strong for values $\Delta\sqrt{I_{CO_2}} \geq 0.6$ and thus used in further data analysis, while signal with $\Delta\sqrt{I_{CO_2}} < 0.6$ was rejected. To validate the criterion and its threshold, experimental data, measured on the free branch of the laminar V-flame, was compared to numerical simulation for adiabatic reacting conditions in their (CO_2,T) state space. This is depicted in Figure 5.6(c) with black circles $(\Delta\sqrt{I_{CO_2}} \geq 0.6$, $\approx 80\%$ of samples) marking the strong CO_2 signal data, i.e., considered for all further data analysis, while green triangles show rejected data $(\Delta\sqrt{I_{CO_2}} < 0.6$, $\approx 20\%$ of samples). For near-wall measurements (see sections 5.3.2 and 5.3.3), only $\approx 10\%$ of the data were excluded by the thresholding criterion. From Figure 5.6(c), it is clearly evident that the criterion and its threshold are effectively removing unphysical data from the (CO_2,T) scatter. However, it needs to be noted that this threshold value is not universally valid. It depends on the individual experimental conditions and needs to be evaluated for the studied case prior to application, e.g., by a procedure as demonstrated in Figure 5.6(c). While the value of 0.6 well-applied for a lean DME/air operation at $\Phi = 0.83$, a value of 0.3 proved most feasible for CH_4/air combustion at $\Phi = 1.00$. After excluding weak CO_2 data from the ensemble, an additional calibration was applied to the retained X_{CO_2} values to further improve accuracy (average improvement from 9% to 2%, see section 5.3.1.1 for discussion). For this purpose, the known (CO_2,T) state space of the adiabatic reference case is utilized and X_{CO_2} of both the simulation and experiment are curve-fitted with respect to gas phase temperature T. The resulting fitted polynomials defined a temperature-dependent calibration coefficient $C_{CO_2,\text{calib}}(T) = fit_{CO_2,\text{sim}}(T)/fit_{CO_2,\text{exp}}(T)$ that was multiplied to the experimental X_{CO_2} using the corresponding instantaneous temperature T for correction. The finally calibrated results on the adiabatic free flame branch are shown in Figure 5.6(d).

5.2.2.2 CO-LIF

Processing steps applied for CO-LIF are outlined in Figure 5.7. The quantification of CO mole fractions from LIF signal in this thesis based on an established calibration procedure [82, 110, E2] [94, p. 77 ff.] but was advanced and adapted for the studied conditions. The major difference lies in the steps to finally quantify the corrected CO-LIF intensities in terms of concentrations (see outlines on step (IV) below). Basically, the data processing workflow was subdivided into pre-processing and subsequent quantification.

The pre-processing turned signal from individual, two-dimensional LIF raw images $I_{\text{raw}}(x^*,z^*,i)$ into scalar signal values

$$I_{CO}(y,z,i) = \sum_{z^*}\left\{\sum_{x^*} I_{\text{raw}}(x^*,z^*,i) - \bar{I}_{\text{BG}}(x^*,z^*)\right\} - I_{\text{BL}}(z^*,i) \tag{5.1}$$

119
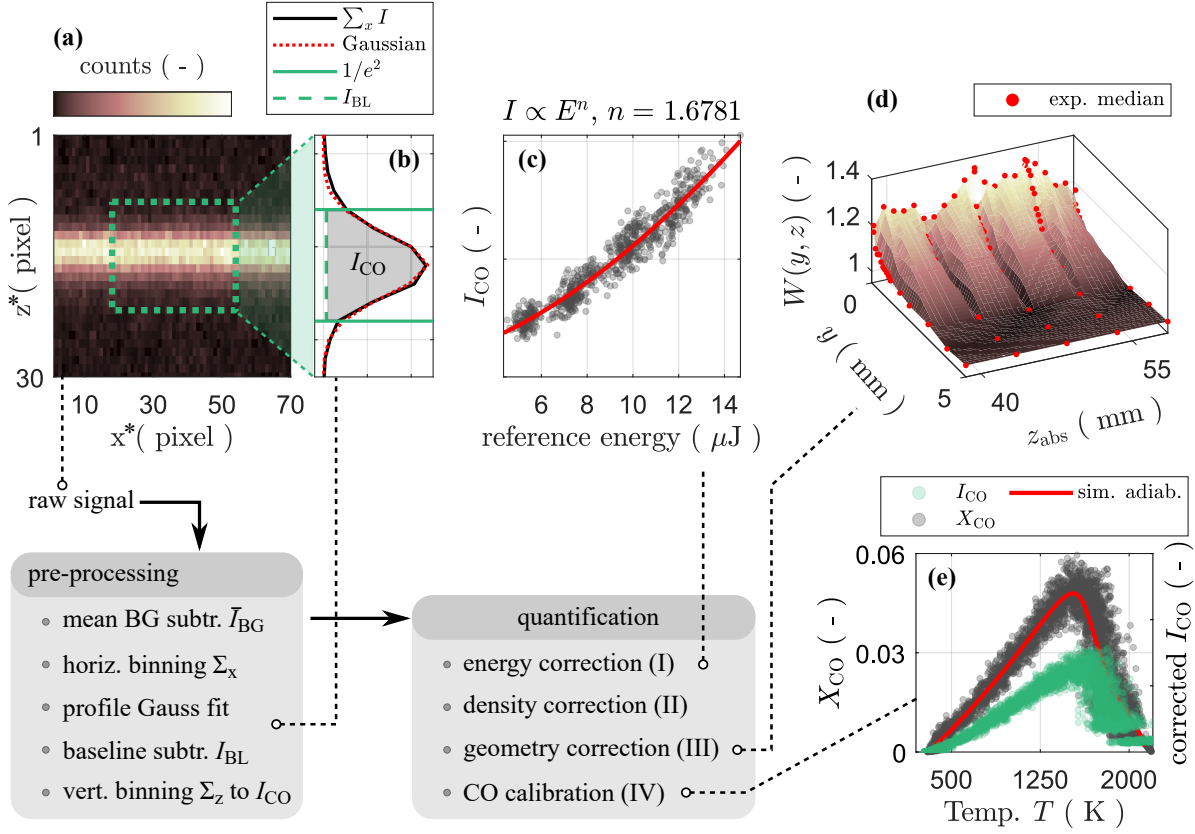
Figure 5.7: CO-LIF data processing workflow with (a)-(e) visualizing selected processing steps. Parts of this figure were published in Zentgraf et al. [E11] (parts of Fig. 3) and are reused with permission of Elsevier; reproduced in an adapted, extended version.

for each instantaneous sample i and spatial (y,z)-location probed by thermochemistry diagnostics, i.e., by scanning the pointwise measurement locations. Please note that the (x^*,z^*)-coordinates in $I_{\text{raw}}(x^*,z^*,i)$ refer to the two dimensions of the raw image, as shown in Figure 5.7(a). First, ensemble-averaged background (BG) intensities $\bar{I}_{\text{BG}}(x^*,z^*)$ were subtracted from the individual raw images $I_{\text{raw}}(x^*,z^*,i)$. This was done pixel-by-pixel in the two-dimensional (x^*,z^*)-space. As outlined in section 5.2.1.6, the BG-ensemble was recorded between consecutive laser pulses in combustion operation mode. Subsequently, the BG-corrected intensity was extracted within a $\Delta x^* \approx 2$ mm region centered at the DP-CARS probe volume (see x^*-bounds of the green, dotted rectangle in Figure 5.7(a)) and summed up in x^*-direction (principal beam direction). The resulting profile is shown in Figure 5.7(b) as black solid line. In a next step, a Gaussian profile was fit to the summed up intensity (see red, dotted line in Figure 5.7(b)), orthogonal to the principal beam direction. The Gaussian profile aided in defining the $1/e^2$-bounds of the LIF-signal. A baseline intensity $I_{\text{BL}}(z^*,i)$ was defined as signal level beyond the $1/e^2$-bounds (see green, dashed line in Figure 5.7(b)) and was subtracted. Finally, intensity values were summed up within the defined $1/e^2$-bounds resulting in a scalar pre-processed, integrated intensity $I_{\text{CO}}(y,z,i)$ for each CO-LIF raw image i, depicted by the gray area in Figure 5.7(b).

After pre-processing, the quantification to CO mole fractions $X_{CO}(y,z,i)$ was done by the relation

$$X_{CO}(y,z,i) = I_{CO}(y,z,i) \cdot \underbrace{\frac{1}{a + b \cdot E^n(i)}}_{(I)} \cdot \underbrace{\frac{T(i)}{T_0}}_{(II)} \cdot \underbrace{\frac{1}{W(y,z)}}_{(III)} \cdot \underbrace{\frac{fit_{CO,sim}(T(i))}{fit_{CO,exp}(T(i))}}_{(IV)} \quad (5.2)$$

with Roman numbers (I) to (IV) summarizing individual correction steps explained in the following. Following Equation (5.2), the pre-processed integrated intensity $I_{CO}(y,z,i)$ was corrected for instantaneous laser energy fluctuations (I), local gas density (II), and geometrical influences from the nearby quenching wall (III), as previously described in Jainski et al. [82]. Finally, corrected intensity values were converted into quantitative CO mole fractions by application of a calibration polynomial (IV) acquired under reacting, adiabatic conditions. In place of step (IV) here, former studies distinguished a *spectroscopic correction* and applied a *global calibration factor* from CO test gas with known concentration [94, p. 79 ff.]. This spectroscopic correction derived relative CO-LIF intensity as function of temperature from diluted, heated CO test gas (for $T \leq 900$ K) and flat flame operation (for adiabatic flame temperature), which resulted in large data gaps > 1000 K in between that had to be closed by manually added support points [94, p. 81 ff.]. For validation and optimization of this procedure, final (CO,T) results on the adiabatic free flame branch had to be checked against simulation [94, p. 82 f.]. In contrast, this thesis condensed those procedures, omitting CO test gas and fitted the corrected data in steps (I)-(III) directly to in situ recorded free flame branch data, as will be described in step (IV) later. The energy correction (I) considered a non-linear dependency $\propto E^n(i)$ to the laser energy E, using an exponent $n = 1.68$. Please note that the value $n = 1.68$ was only valid for the lean DME/air conditions and alters for different operation. The data for energy correction was measured in situ for each operation condition within the exhaust gas of the V-flame by varying the laser energy with the combination of half-wave plate and polarizer in the beam path (see section 5.2.1.2). The dependency of pre-processed LIF signal to reference-energy is depicted in Figure 5.7(c) for the studied conditions. As stated in the laser diagnostics above, an energy dependency with exponent $n \leq 2$ is expected for the studied two-photon LIF. However, values $n \approx 2$ are hardly realizable by application of nanosecond lasers but can be achieved using femtosecond pulses, as demonstrated in Rahman et al. [134] for example. The exponent $n < 2$ indicates photo-ionization of the targeted CO molecules. Using higher laser fluences for two-photon CO-LIF, i.e., lowering n, is accompanied by a trade-off between two important aspects: (1) the photolytic production of CO by dissociation of CO_2 is promoted [117, 134]; (2) results become less dependent on the quenching environment (see discussion at the end of this paragraph). In this thesis, laser energies were decreased and n was chosen higher than in previous studies, like $n = 1.24$ in [82], for a well-balanced compromise between (1) and (2) and to obtain the best possible accuracy. Especially, as the simultaneously applied DP-CARS probes the CO_2 concentration, photolytically generated CO from CO_2 could also bias the DP-CARS quantification and should be avoided. The density correction (II) was done by a ratio of instantaneous gas phase temperature $T(i)$ from simultaneous DP-CARS to a reference temperature $T_0 = 300$ K. The so-called *geometric correction* (III) aimed to compensate for overrated CO-LIF intensity near the quenching wall, biased by signal

back-reflections. As the wall was manufactured from stainless steel, it acted like a mirror and reflected LIF signal to the detection optics. The closer the probe volume was to the wall, the bigger the bias. For correction purpose, a two-dimensional function $W(y,z)$ was composed by operating the burner with a fully homogeneous calibration gas mixture consisting of 1% CO, 99% N_2, as shown in Figure 5.7(d). Correction values are around 1.2-1.3 at wall-closest locations. This is consistent to values slightly above 1.2 in previous SWQ-investigations (see Figure 5.10 in [94, p. 83]). For increasing wall-distances y, values converged unity and are assumed to $W(y,z) = 1$ for $y \geq 5$ mm. While steps (I) to (III) in Equation (5.2) were intensity correction procedures (resulting in the green circles in Figure 5.7(e)), step (IV) comprised the actual quantification to quantitative CO mole fractions. For this purpose, a calibration polynomial was deduced by comparison of measured and intensity-corrected (CO,T) data recorded in the free flame branch to an adiabatic numerical simulation of a freely-propagating flame (see section 5.2.3 for reference) under identical conditions. Both experiment and simulation were fitted on averaged values assessed for $\Delta T = 50$ K increments to derive $fit_{\mathrm{CO,sim}}(T(i))$ and $fit_{\mathrm{CO,exp}}(T(i))$ as function of the instantaneous gas phase temperature T. The ratio of fits was used to derive a calibration coefficient $C_{\mathrm{CO,calib}}(T(i)) = fit_{\mathrm{CO,sim}}(T(i))/fit_{\mathrm{CO,exp}}(T(i))$. Please note that the calibration done for CO is applied in an equal manner than for re-calibrating (CO$_2$,T) in DP-CARS above. Final calibrated X_{CO} is depicted in Figure 5.7(e) by black scatter.

As stated by Mann et al. [110], such a calibration procedure for CO-LIF covers influences from varying Boltzmann fractions, quenching environment and ionization. However, the question arises if this calibration on the adiabatic flame branch is still valid in the near-wall non-adiabatic flame, where chemical environment and thus the quenching rate changes. For the studied combustion conditions, both the quenching rate k_{Q} and the ionization rate (in Equation (2.49): $\sigma_{\mathrm{ion}}\frac{I_{\mathrm{L}}}{h\nu_{\mathrm{L}}}$) are in the same order of magnitude ($\approx 10^9$ s^{-1}), as estimated with an in-house CO-LIF simulation code[11]. From Equation (2.49) it becomes evident that for such conditions a change in k_{Q} has less impact on the fluorescence quantum yield (approximately by a factor of two less, since ionization is an equal loss process). This finally allows transferring the calibration on the adiabatic flame branch to different chemical environments as long as the instantaneous gas phase temperature is measured simultaneously. For higher laser fluences, the CO-LIF signal becomes nearly independent of composition-dependent quenching, as discussed more intensively in Greifenstein et al. [67]. Also Voigt et al. [163] stated this for even higher pressures, where higher quenching rates are present.

5.2.2.3 OH-PLIF

The processing of OH-PLIF images to detect the flame front and quenching point was carried out analogously to the descriptions given in section 4.2.2.3 for the high-speed measurements on flame and flow dynamics. However, as the diagnostics here were implemented low-speed, i.e., low repetition rate laser (better beam profile) and low-speed IRO

---

[11]The simulation was performed and provided by Dr.-Ing. Max Greifenstein from Technical University of Darmstadt (RSM) and was used in this thesis with permission. His kind contribution is acknowledged here. More details on the simulation were given in Zentgraf et al. [E11].

(superior intensifier characteristics), a slightly different processing workflow in terms of filtering and thresholding was applied. The overall procedure equaled the one for high-speed OH-PLIF before. Thus, this outline focuses the differences with respect to the high-speed application only.

The high-speed implementation applied a correction of the instantaneous beam-profile but omitted averaged background subtractions. In turn, a beam-profile correction was not performed on the low-speed data here, as a well-homogeneous intensity region of the laser was selected prior to PLIF excitation (enough laser energy available), but ensemble-averaged background images were subtracted (recorded in situ between consecutive laser pulses during combustion). A 5×5 moving average filter (instead of 21×21 in the high-speed) was sufficient to reduce spatial noise. Finally, the empirical threshold for quenching point detection was set to 0.3 and enabled a robust detection on both laminar and turbulent cases. As previously stated in section 4.2.2.3, the differences in threshold value are mainly appointed to different raw image quality from the changed experimental setup.

5.2.2.4 TPT

The workflow to derive wall surface temperatures from laser-induced phosphorescence decay times is briefly summarized in Figure 5.8. First, decay times had to be assessed from the raw data[12]. This was done iteratively by assuming mono-exponential phosphorescence decay and the application of a non-linear least square fitting scheme, as described in Fuhrmann et al. [60]. Furthermore, an adaptive fitting window and convergence criterion

---

[12]Import of the oscilloscope files (.wfm) was done by the "wfm2readframe" MATLAB function [15].
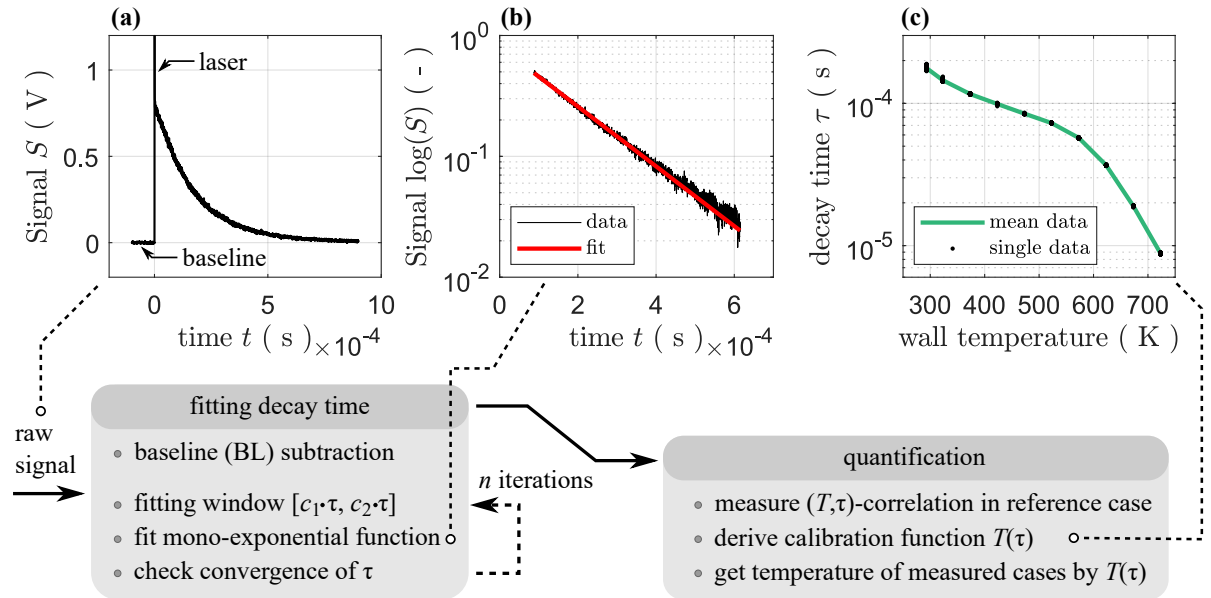
Figure 5.8: TPT data processing workflow with (a)-(c) visualizing selected processing steps.

reported by Pareja et al. [125] was used. Initially, the intensity peak from the laser was detected in the instantaneous voltage output of the oscilloscope (see Figure 5.8(a); prior: signal background; past: luminescence decay). For background correction, the signal from temporal acquisition start to 10 data points prior to laser peak was defined as baseline and its temporal average was subtracted from the instantaneous voltage signal. This principle was also used in Pareja et al. [125]. Subsequently, a mono-exponential fit of the data to the relation $C \cdot e^{-t/\tau}$ was performed by the function "lsqnonlin" implemented in MATLAB (MATLAB R2019b, The MathWorks, Inc.) to assess the scaling C and decay time τ (initial guess: $C_0 = 1$, $\tau_0 = 10^{-4}$ s). Adding an additional offset value to the mono-exponential function for fitting, as done in Fuhrmann et al. [60], was not applied here, as the previous baseline correction sufficiently removed instantaneous background, i.e., signal offset. The fitting was performed iteratively. With respect to the iteration, varying windows on the time axis with range $t \in [c_1 \cdot \tau_n, c_2 \cdot \tau_n]$ were used [125]. The window range was based on the decay time τ_n estimated for the current iteration n and parameters $c_1 = 0.5$, $c_2 = 3.5$ given in Pareja et al. [125] for GGG:Cr and GGG:Cr,Ce phosphors. In total 100 iterations were allowed, i.e., $n \leq 100$. Following the criterion from Pareja et al. [125], the iterative τ_n was considered converged in the case

$$\max(\tau_n)|_{n-2}^{n} - \min(\tau_n)|_{n-2}^{n} < 10^{-3} \cdot \frac{1}{3} \cdot \sum_{n-2}^{n}(\tau_n) \tag{5.3}$$

with respect to the relative difference of the current iteration n to the past two iterations $n - 2$. This procedure was applied to each recorded instantaneous temporal decay curve and proved robust for the applied GGG:Cr,Ce phosphor under the given experimental conditions. An example for a final, converged fit to experimental data is depicted in the semi-logarithmic space in Figure 5.8(b).

Second, assessed decay times τ required quantification in terms of surface temperatures by an in situ calibration. For this purpose, the identical phosphor coating was air-brushed (from identical preparation batch) to both the quenching wall and a small aluminum block equipped with two heating cartridges and two type K thermocouples embedded underneath the surface. The aluminum block was placed in the burner facility and heated to temperature values from 20 °C to 450 °C (50 °C increments starting from 50 °C). The assessed decay time was correlated with the measured temperature $T_{\text{wall}}^{(\text{TC})}$ from the reference thermocouples, finally yielding a calibration curve, as shown in Figure 5.8(c). As thermal equilibrium was assumed in the aluminum block during calibration, a look-up function $T_{\text{wall}}^{(\text{TPT})} = T_{\text{wall}}^{(\text{TC})} = f(\tau)$ was built from $(T_{\text{wall}}^{(\text{TC})}, \tau)$-values of the calibration by piecewise cubic interpolation. Around 480 K, a decay time of $\tau \approx 85$ μs is yielded by Figure 5.8(c), which is well-consistent to the ≈ 90 μs reported in Pareja et al. [125] for GGG:Cr,Ce samples at this temperature (see Fig. 8 in [125]).

This thesis uses TPT only for a zero-dimensional control purpose and thus implements a rather simple application and data processing. Thermometry by laser diagnostics using thermographic phosphors was extensively studies in the past decade, as summarized by the comprehensive reviews of Aldén et al. [4], Brübach et al. [27] and Abram et al. [1]. For a more detailed insight into the TPT topic, the reader is referred to this literature.

5.2.3 Numerical Simulations for Benchmark

Previous experimental studies on thermochemistry in SWQ did mainly compare results to either one-dimensional adiabatic flame simulations [82, E2] or simplified one-dimensional non-adiabatic computations [E2]. Even though, the non-adiabatic one-dimensional calculations performed in Kosaka et al. [E2] were able to reproduce the impact of near-wall enthalpy-losses on the flame, the two-dimensional character of SWQ cannot be completely captured. Evidently, a two-dimensional non-adiabatic simulation appears more promising to compare experimental SWQ results with, as for example presented in the numerical studies of Ganter et al. [62, 63] previously. This thesis used the numerical simulations[13] of two different, laminar flame configurations to complement the experimental insight, provide comparison or serve for orientation in turbulent operation. These simulations were previously presented in Zentgraf et al. [E11] for comparison to the experiment, where the below descriptions refer to. The first numerical configuration consisted of a one-dimensional, adiabatic freely-propagating flame [88] and is called the *adiabatic simulation* in this chapter. The second configuration was a two-dimensional SWQ simulation using fully-resolved chemistry and transport (FCT). It is named the *non-adiabatic simulation* here. The general setup for this SWQ simulation, including solver, grid and numerics, was presented in the work of Steinhausen et al. [E5]. Here, a recently developed mechanism on DME-chemistry by Stagni et al. [153] (31 species and 140 reactions) was applied along with a mixture-averaged approach for species diffusion [38, 39]. In addition to the mixture-averaged transport modeling (abbreviated: MixAvg), a simulation with equal diffusivity model ($Le = 1$ for all species) was provided, to analyze the influence of diffusive transport in FWI. It is emphasized that the simulations were generated independently from the experiment presented in this thesis and not optimized or modified to align with experimental data.

---

[13]All numerical simulations in the FWI context presented in this chapter 5 were performed and provided by M.Sc. M.Sc. Matthias Steinhausen and M.Sc. Yujuan Luo from Technical University of Darmstadt (STFS) and were used in this thesis with permission. Their kind contribution is acknowledged here. Please note that performing detailed numerical combustion simulations is a separate research field and would have been beyond the scope of the work presented.

5.3 Results and Discussion

The results first provide a thorough validation and benchmarking of the applied multi-parameter diagnostics in section 5.3.1. Then, section 5.3.2 discusses laminar near-wall thermochemistry in detail, with focus on the additional information by CO_2 mole fraction. In this context, implications on species diffusion modeling in simulation are discussed. Finally, turbulent FWI thermochemistry is evaluated in section 5.3.3. Here, the influence of individual quenching topology (SWQ- or HOQ-like) is discussed, and potential scenarios for near-wall reaction-transport coupling are proposed. All discussed results are presented for a DME/air mixture at $\Phi = 0.83$, for laminar or turbulent inflow conditions and a wall temperature stabilized at ≈ 60 °C, i.e., OP1 and OP2 in Table 3.1. Parts of the content of section 5.3 were published in Zentgraf et al. [E8, E11] and are reused with permission (see appendix B), in a modified wording and partially extended by further technical and scientific details to fit the structure of this thesis. This concerns parts of sections 5.3.1 (reported in [E11]), 5.3.2 (reported in [E11]) and 5.3.3.1 (reported in [E8]).

5.3.1 Experimental Validation and Benchmarking

The experimental validation and benchmarking of the novel comprehensive (CO_2,CO,T)-diagnostics approach for FWI studies is done for laminar conditions and comprises three important aspects. First, an assessment of accuracy and precision is performed in the state space on the adiabatic free flame branch. Second, the near-wall thermochemistry probe volume location is evaluated with respect to the position of the quenching wall. Third, the near-wall (CO_2,CO,T)-thermochemistry is benchmarked in the physical space. All three steps apply comparison to numerical simulation outlined in section 5.2.3.

5.3.1.1 Accuracy and Precision

Both accuracy and precision of the (CO_2,CO,T)-thermochemistry quantification are assessed using the unbounded branch of the V-flame as adiabatic reference case. The assumption of adiabatic conditions is valid, as the probed locations were $y = 16$ mm to $y = 20.5$ mm far from the wall and radiative heat loss is considered negligible. Thus, a comparison of this experimental data to adiabatic flame simulations is possible. This is first done within state space in Figures 5.9(a)-(c). It is evident that the instantaneous experimental samples after processing and calibration (black circles) well-capture the state-space evolution described by the adiabatic numerical simulation (red line). Green triangles and error bars reflect the experimental mean and $\pm\sigma$ standard deviation on selected temperature increments spanning $\Delta T = 50$ K each (every second increment shown). A small gap in the data exists around $T = 2000$ K and at the fully reacted state (see end of red line), as evident in Figures 5.9(b) and (c). This is due to skipped measurement locations while scanning over the adiabatic branch and does not affect the data quality and further evaluation in any way. As observed in Figure 5.9(c), the instantaneous scatter is highest for the (CO,CO_2)-correlation, as both experimental errors of X_{CO_2} and X_{CO} are superimposed and are higher compared to the lower uncertainties in T.
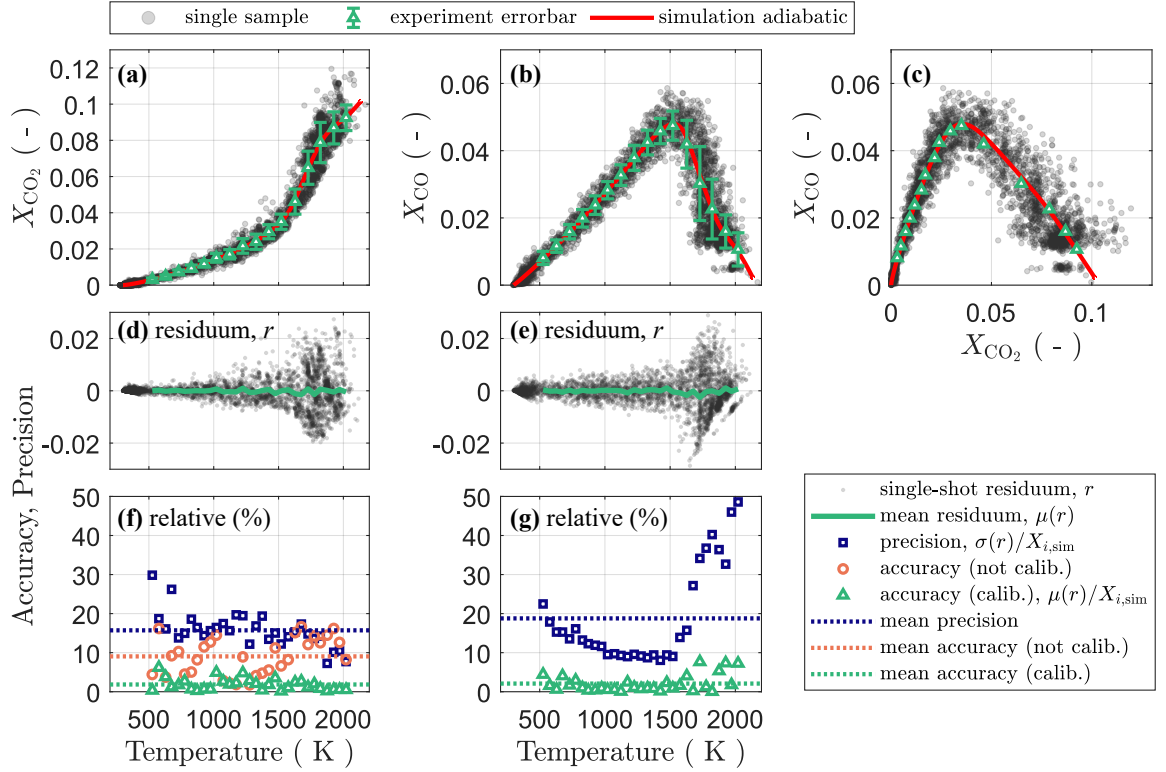
Figure 5.9: Evaluation of accuracy and precision of diagnostics on the adiabatic free flame branch. State spaces in (a)-(c), single-shot residua in (d) and (e), relative accuracy and precision on 50 K temperature increments in (f) and (g). Samples: 4284. This figure was published in Zentgraf et al. [E11] (Fig. 4) and is reused with permission of Elsevier; reproduced in an adapted version.

Within Figures 5.9(d)-(g), accuracy and precision of X_{CO_2} and X_{CO} are discussed in more detail with the statistical evaluation based on $\Delta T = 50$ K increments. Figures 5.9(d) and (e) give absolute values for instantaneous single-shot residua r, i.e., the difference between simulation $X_{i,\text{sim}}$ and experimental mole fraction $X_{i,\text{exp}}$ for species i at given temperature T. Mean residuum traces $\mu(r)$ (green line, based on the $\Delta T = 50$ K increments) present a measure for the accuracy, while the scatter in residuum r depicts the precision and is described by the corresponding standard deviation $\sigma(r)$ here. Average residua $\mu(r)$ are close to zero in both the CO_2 and CO mole fraction, indicating a high accuracy. Between 1700 K and 1800 K, instantaneous residua can peak up to ± 0.02 in both mole fractions, suggesting lower measurement precision. This is a region in the corresponding state spaces, where gradients are steepest with respect to T.

Figures 5.9(f) and (g) evaluate relative accuracy ($\mu(r)/X_{i,\text{sim}}$) and precision ($\sigma(r)/X_{i,\text{sim}}$) by dividing the measures $\mu(r)$ and $\sigma(r)$ by the corresponding simulation mole fraction $X_{i,\text{sim}}$. For CO_2, the average accuracy for the non-calibrated case (orange dotted line, mean over all available temperature increments) is $\approx 9\%$ and improves to $\approx 2\%$ (green dotted line) when applying a calibration as outlined in section 5.2.2.1. It is emphasized that the 9% value, directly originating from the spectral fitting algorithm, is already considered a good accuracy. With respect to temperature, the individual CO_2 accuracy under

non-calibrated conditions (orange circles) is around 5-15% up to 1600 K and increase to nearly 20% above. For the calibrated case (green triangles), individual accuracy values are nearly constant within the entire temperature range. This again confirms an effective application of the applied calibration procedure, as outlined in section 5.2.2.1. The average relative precision of X_{CO_2} (blue dotted line) is around 16% and in its individual values (blue rectangles) observed to decrease with increasing T. In average, the calibrated CO mole fraction X_{CO} features $\approx 2\%$ accuracy (green dotted line) with nearly constant individual values (green triangles) up to 1700 K but deteriorates to $\approx 10\%$ above. This drop in relative values is attributed to the decreasing absolute CO when progressing with its oxidation process to the fully burnt state. As confirmed by Figure 5.9(e), the absolute accuracy expressed by $\mu(r)$ is nearly constant over the entire temperature range. The average precision of X_{CO} is $\approx 10\%$ in the range 750 K $< T <$ 1500 K but increasingly deteriorates for higher temperatures (blue rectangles). Again, this is mainly attributed to the continuously decreasing CO concentrations approaching the fully reacted state but also associated with the steep local gradients over individual temperature bins. Overall, this is not considered critical, as the most important FWI-phenomena are measured at $y \leq 320$ mm wall distance, where the temperature is $T \leq 1500$ K (see Figures 5.13 and 5.14 for reference) and the precision is correspondingly good. Finally, a conservative estimation on accuracy ($\approx 3\%$) and precision ($\approx 4\%$) of the gas phase temperature T is derived for states in the fully burnt, as the nitrogen DP-CARS signal levels are weakest at highest temperatures.

Overall, the presented experimental (CO$_2$,CO,T)-results from the applied simultaneous laser diagnostics appear to well-capture the adiabatic simulation within the unbounded flame branch. Both accuracy and precision are considered good and assumed also valid under non-adiabatic conditions. Thus, the experimental procedure is transferred to the near-wall quenching environment in the following.

5.3.1.2 Benchmarking the Near-Wall Probe Volume Location

It is obvious that precise knowledge of the wall position with respect to the measured locations is indispensable in experimental FWI studies for correct physical interpretation of the results. As near-wall gradients are high, the results are very sensitive to the wall distance. However, due to experimental imperfection, an offset in y-direction may exist between the *nominal* wall distance, where the thermochemistry measurements are believed to have been taken, and the real, physical wall distance. The y-offset results from the superposition of several effects, briefly discussed in the following. First, laser beam steering is present under reacting conditions and believed to feature the major y-offset contribution for thermochemistry results in this thesis. Second, the applied diagnostics cause a spatial filtering of the steep near-wall gradients due to their finite beam waist but it is considered negligible. Third, an inaccuracy in defining the initial wall-closest position at $y = 100\ \mu$m. This aspect is also considered negligible, as the wall closest y-position is determined and set during thermally steady state FWI operation (see section 5.2.1.6) and should thus be sufficiently accurate. Furthermore, errors from inaccuracy of the traversing system are negligible ($\approx 1\ \mu$m with backlash compensation). From the recorded experimental data itself it is hardly possible to quantify the impact of in-
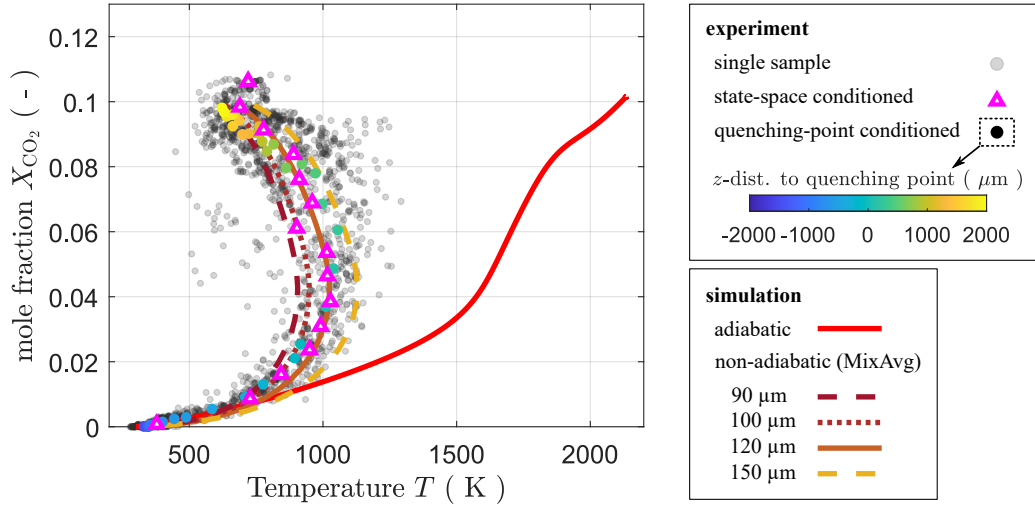
Figure 5.10: Comparison of experimental near-wall data measured at $y = 100 \ \mu$m nominal wall distance to non-adiabatic numerical simulation with mixture-averaged (MixAvg) transport modeling in the state space. Both experiment and simulation comprise data within $z = \pm 2$ mm relative to the instantaneous quenching height. Samples: 1983. This figure was published in Zentgraf et al. [E11] (Fig. 5) and is reused with permission of Elsevier; reproduced in an adapted, extended version.

stantaneous beam steering to the probe volume without taking additional experimental measures (like further monitoring systems). To estimate the likely beam steering-induced y-offset of the *nominal* wall distance, experimental data is benchmarked with corresponding non-adiabatic near-wall simulation. It needs to be noted that these simulations rely on several modeling assumptions, like chemical mechanism or boundary conditions, and consequently feature a certain unknown inaccuracy. Using them as benchmark thus also suffers some imperfection. However, it is expected to yield a first valuable insight into the potential positioning error of the experimental probe volume by beam steering. Performing the comparison in thermochemical state space is likely to mitigate the impact of differing boundary conditions to a certain extent. For example the physical space could suffer deviation in assessing the quenching location. Thus, such an estimation should be performed in the state space only.

The y-offset estimation is presented in Figure 5.10 for experimental data measured at the wall-closest nominal position $y = 100 \ \mu$m in terms of the (CO_2, T) state space. As the experimental data features a certain scatter (due to diagnostic precision and beam steering), averaged values are used for comparison with simulation. Initially, the experimental data is classified into equidistant increments on the CO_2 mole fraction axis, each spanning 0.0025. Subsequently, conditioned averages for X_{CO_2} and T are calculated on each bin (shown as magenta triangles in Figure 5.10). This statistical conditioning in the state space is called *state-space conditioning* in the remainder of this chapter. To further complement this insight, the previously introduced *quenching-point conditioning* is shown (see section 4.2.2.3). Here, each thermochemical probe is classified into 100 μm wide bins with respect to the instantaneous distance Δz to the quenching point (commonly defined at $z = 0$ mm) and averages are calculated on each bin in the physical space. Quenching-

point conditioned averages are shown color-coded in Figure 5.10 with a relative z-measure to the quenching event. It is clearly evident from Figure 5.10 that the averages of experimental data by both conditioning methods are best captured by simulation data at $y = 120$ μm wall distance (solid orange line). This finally yields a y-offset estimation of approximately 20 μm between experiment and simulation, most likely appointed to beam steering bias on the experimental data. This minor offset emphasizes that both experiment and corresponding simulation do match very well. For correction purpose, this offset is added to the nominal wall distance for all thermochemistry considerations in the remainder of this chapter, i.e., the wall-closest thermochemistry probe volume is located at $y = 120$ μm wall distance. A further observation is that most experimental scatter is located within a ± 30 μm y-range, as suggested by the traces of numerical simulation at $y = 90$ μm (red dashed line) and $y = 150$ μm (yellow dashed line) in Figure 5.10. However, the scatter in y-direction superimposes both beam steering as well as diagnostic precision and their impact is not discriminable.
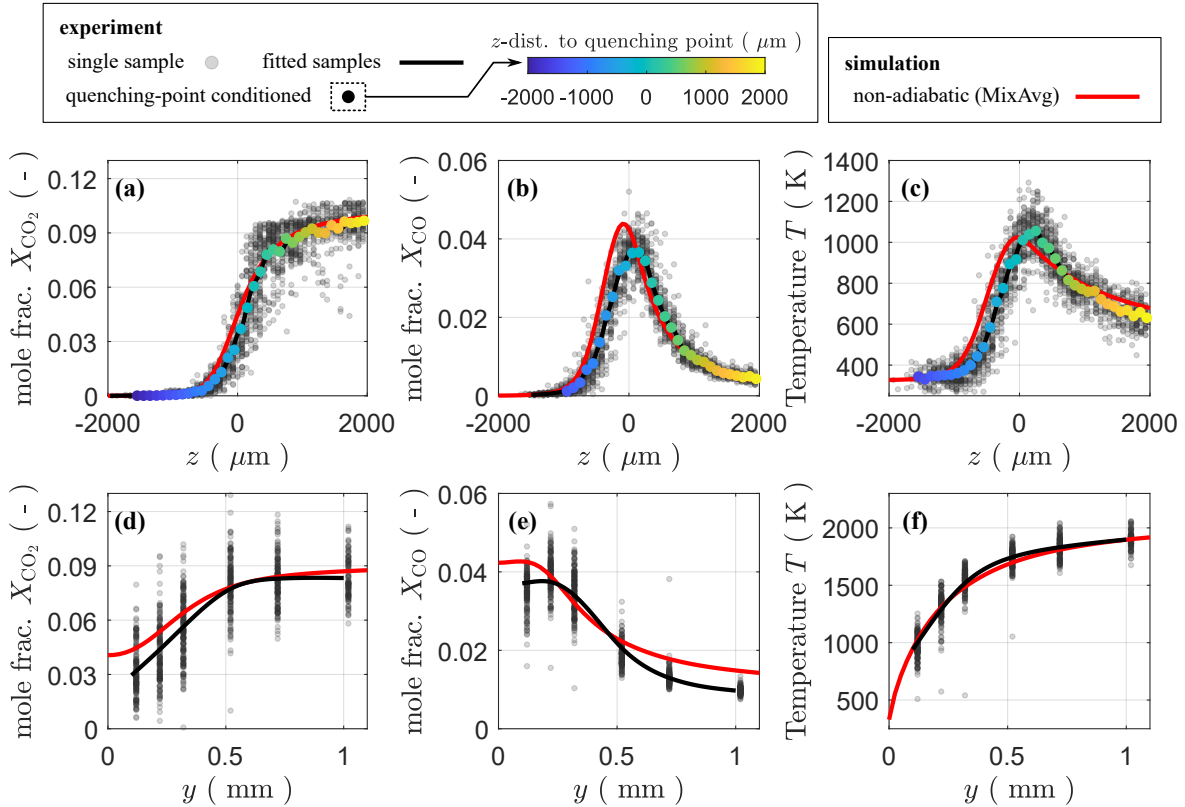
Figure 5.11: Comparison of experimental near-wall data to non-adiabatic numerical simulation with mixture-averaged (MixAvg) transport modeling in the physical space for z-direction at $y = 120$ μm (a)-(c) and y-direction at $z = 0$ mm (d)-(f). Experimental data is described by a smoothing spline fit (black line) and quenching-point conditioned averages calculated for each 100 μm increment on the physical z-axis (color-coded circles). Samples: 1983 (a)-(c) and 928 (d)-(f). Parts of this figure were published in Zentgraf et al. [E11] (Fig. 6) and are reused with permission of Elsevier; reproduced in an adapted, extended version.

5.3.1.3 Benchmarking the Near-Wall Physical Space

An insight into experimental near-wall thermochemistry in its physical space is presented by Figure 5.11 and compared to corresponding non-adiabatic numerical simulation. It discusses both the evolution in streamwise z-direction at the wall-closest position $y = 120$ μm in Figures 5.11(a)-(c) and the wall-normal behavior in y-direction at the quenching point height $z = 0$ mm in Figures 5.11(d)-(f). The latter evolution in y-direction is derived from data measured at 120 μm, 220 μm, 320 μm, 520 μm, 720 μm and 1020 μm wall distance considering samples with $z \in [-100 \ \mu\text{m}, 100 \ \mu\text{m}]$ around the common quenching point height. The evolution of X_{CO_2}, X_{CO} and T is described by a smoothing spline (black line) fitted to the single experimental samples (gray circles). The streamwise evolution in Figures 5.11(a)-(c) is additionally visualized by color-coded quenching-point conditioned averages (calculated for each 100 μm bin in physical z-direction). From Figures 5.11(a)-(c) it is first evident that quenching-point conditioned averages (color-coded circles) and fit (black line) of the experimental data exactly match. This confirms that absolute values of X_{CO_2}, X_{CO} and T are not impacted by binning or filtering the data by 100 μm spatial increments in z-direction, as applied for quenching-point conditioning here. The experimental evolution of CO_2 mole fractions in z-direction at $y = 120$ μm closely matches the non-adiabatic simulation (red line), as shown by Figure 5.11(a). An analogous behavior is observed in the wall-normal y-direction in Figure 5.11(d). Merely close to the quenching wall, the experiment yields lower values compared to the simulation ($\Delta X_{CO_2} \approx 0.013$ at $y = 120$ μm). As shown in Figure 5.11(b), the streamwise z-evolution of CO mole fractions features minor deviation between fitted experiment and simulation in both the peak location (≈ 140 μm) and peak value (≈ 0.007). In the y-profile in Figure 5.11(e), the experimental values are below simulation near the wall ($y = 120$ μm, $\Delta X_{CO} \approx 0.005$) and approaching the burnt bulk gas ($y = 1020$ μm, $\Delta X_{CO} \approx 0.005$). The experimental z-evolution in temperature, as presented in Figure 5.11(c), yields differences in peak z-position (≈ 285 μm) and value (≈ 35 K), while it exactly matches to simulation in the wall-normal evolution shown in Figure 5.11(f).

Overall, deviations in the physical space between experimental results and numerical simulation are only very minor and may occur due to remaining unsteadiness of the experimental V-flame and the boundary conditions assumed in the simulation. All in all, their agreement is considered excellent and the experiment presented in this thesis provides an outstanding validation of the simulation.

5.3.2 Laminar Near-Wall Thermochemistry

A detailed insight into the streamwise z-evolution of the wall-closest laminar SWQ-thermochemistry at $y = 120$ μm over the quenching event is presented in its individual (CO_2,T), (CO,T) and (CO,CO_2) state spaces by Figure 5.12. Each column of Figure 5.12 presents instantaneous thermochemistry probes in individual z-bins with 200 μm width, with the value on top of the column describing the bin center (e.g., bin in left column with $z = -400$ μm ranges from -500 μm to -300 μm). The evolution is presented over the common quenching height at $z = 0$ μm and negative values indicate positions upstream quenching, while positive values give downstream locations. As previously outlined in

section 3.2.2, the laminar flame operation features remaining unsteadiness and causes the quenching location to slightly fluctuate in z-direction. In addition, the quenching flame branch under laminar operation was scanned in the z-direction with 500 μm steps to fully cover the thermochemical progress (see section 5.2.1.5). In order to take these aspects into account, each individual measurement sample is quenching-point conditioned via OH-PLIF recordings, i.e., its instantaneous quenching height is set to $z = 0$ μm, as stated above. As each considered bin in Figure 5.12 spatially extends 200 μm in z-direction, the unsteadiness causes a scatter across this range in the individual state spaces respectively. For comparison of the experimental observation, an adiabatic and non-adiabatic numerical simulation with mixture-averaged transport model is given. The latter depicts a $z = \pm 2$ mm range relative to the quenching height.
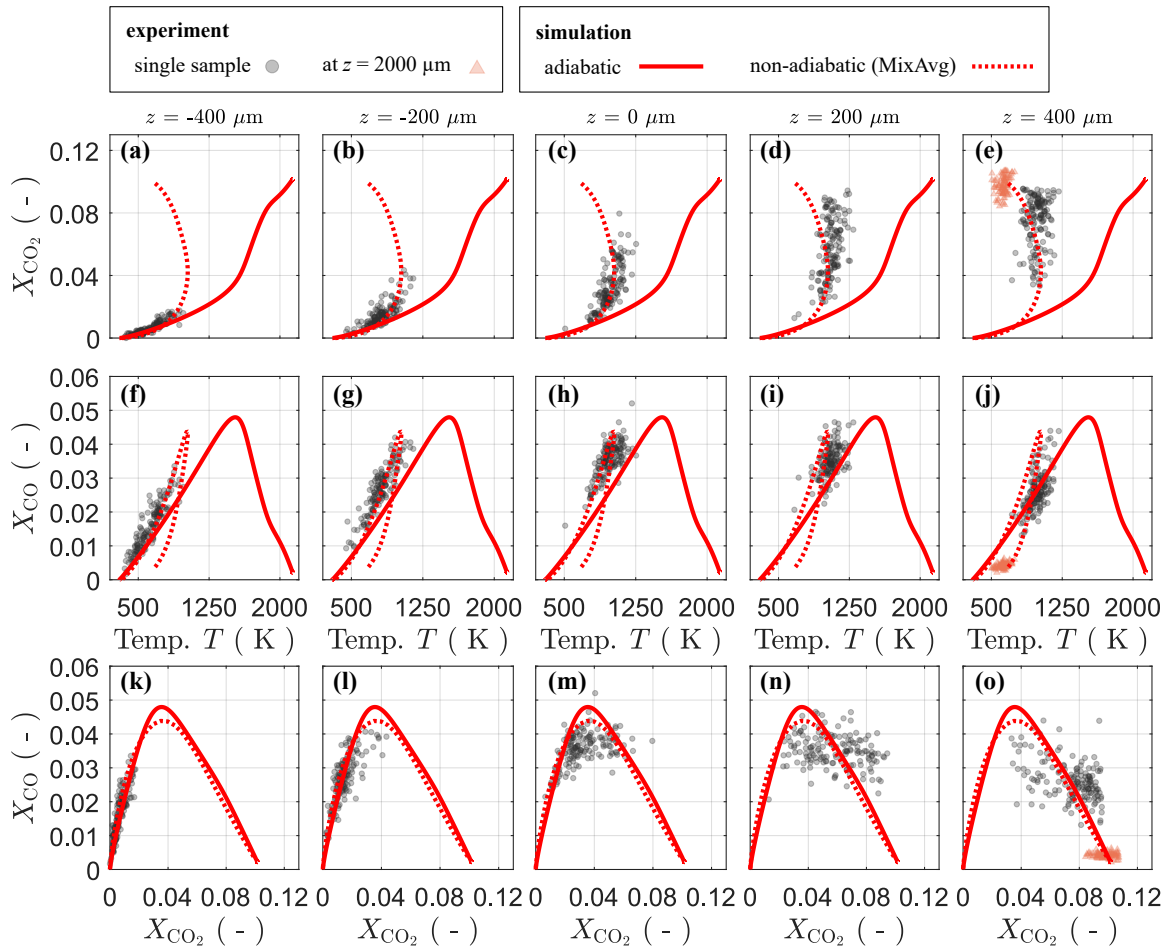
Figure 5.12: Near-wall thermochemistry evolution in z-direction at $y = 120$ μm wall distance in state space with quenching-point conditioning. Adiabatic and non-adiabatic simulations are shown, both with mixture-averaged transport modeling (MixAvg). The non-adiabatic simulation features values at $z = \pm 2$ mm relative to the quenching height. The right column includes additional experimental data at $z = +2$ mm bin location (orange triangle scatter points) capturing the fully reacted state. Samples: 92 to 152 (depending on z-direction bin). This figure was published in Zentgraf et al. [E11] (Fig. 7) and is reused with permission of Elsevier; reproduced in an adapted version.

Starting the discussion in the first column of Figure 5.12, which presents an upstream location centered at $z = -400$ μm, it is first evident that both the (CO_2,T) and (CO,CO_2) scatter in (a) and (k) similarly capture the adiabatic and non-adiabatic simulation trace. As expected, CO_2 is less susceptible to early non-adiabaticity and the difference between adiabatic and non-adiabatic simulation is very small and below experimental uncertainty. In contrast, the early influence of the quenching wall is clearly recognized in the upstream CO mole fraction shown by the (CO,T) state space in Figure 5.12(f). It is more sensitive, as individual states do already follow the non-adiabatic production branch (left branch in (CO,T) state space) of the simulation. Approaching to the next streamwise bin at $z = -200$ μm, shown in the second column of Figure 5.12, the impact of non-adiabaticity further increases and also manifests in the (CO_2,T) scatter in (b). The measured (CO,T) states in (g) fully reproduce the production branch of the non-adiabatic simulation. The (CO,CO_2) scatter in (l) appears unaffected, however, their adiabatic and non-adiabatic evolution are very close to each other, as apparent from both simulation traces. At the quenching location $z = 0$ μm, shown in the third column of Figure 5.12, the (CO_2,T) states in (c) are entirely on the non-adiabatic simulation curve, while the (CO,T) scatter in (h) peaks at the transition between CO-production and CO-oxidation branch. Further downstream thermochemistry evolution in the fourth and last column of Figure 5.12 ($z = 200$ μm and $z = 400$ μm) shows that states follow traces of the non-adiabatic simulation. Finally, at $z = 2000$ μm (shown by orange triangles in last column), fully reacted conditions are reached.

The first major finding from this near-wall thermochemistry evolution is that X_{CO} at locations upstream quenching features a more pronounced impact by diffusive transport towards the wall than CO_2. This can be explained by the fact that CO is formed first during reaction and is subsequently followed by its oxidation to CO_2. As observed at $z = -200$ μm in Figures 5.12(b) and (g), CO_2 thus senses the non-adiabaticity caused by the wall less than CO and both simulation traces of (CO_2,T) coincide up to $T \approx 750$ K. On the one hand, this finding suggests that CO_2 is less affected by the quenching process than CO, as expected for a stable combustion product. On the other hand, CO_2 appears to be a suited component of a progress variable, composed of multiple chemical species, for simulation of premixed near-wall DME/air combustion. The monotonic increase of CO_2 and its small gradients over the reaction zone support the use as progress variable. The second major finding is that the (CO,CO_2) state space, shown in Figures 5.12(k) to (o), is nearly independent from the wall heat loss. This is observed from the very close adiabatic and non-adiabatic behavior in the simulation traces within the entire state space and is experimentally confirmed here within the diagnostics' uncertainty. It is concluded that the (CO,CO_2) states are only influenced marginally by the quenching wall very close to the wall ($y = 120$ μm) and near the quenching event ($z = 0$ μm).

The evolution of thermochemical states in individual correlations is shown in Figure 5.13 for different distances from the quenching wall in y-direction (each column presents one distance indicated as label on top). For detailed discussion, Figure 5.13 covers comprehensive information to describe the experimental data and several simulations for comparison, briefly summarized in the following. Besides the adiabatic (red solid lines) and non-adiabatic simulation using a mixture-averaged transport model (red dotted lines),

an additional non-adiabatic case assuming unity Lewis number transport ($Le = 1$, blue dotted lines) is shown (see section 2.2.1 for Lewis number). Comparison to the latter yields insight into effects that originate from species-dependent diffusion. In Figure 5.13, the single instantaneous experimental data (gray scatter) is described by both state-space (magenta triangles, only every third marker shown) and quenching-point conditioning (color-coded circles, every marker shown), as previously introduced. For state-space conditioning, equidistant increments $\Delta X_{CO_2} = 0.0025$ are applied to condition the statistics in both the (CO_2,T) and (CO,CO_2) correlations. For (CO,T) scatter, $\Delta X_{CO} = 0.00125$ is used with the CO-production and oxidation branches initially split and then conditioned separately. The state-space conditioning performed well in the past when analyzing (CO,T) correlations only, but quenching-point conditioning better captures the evolution
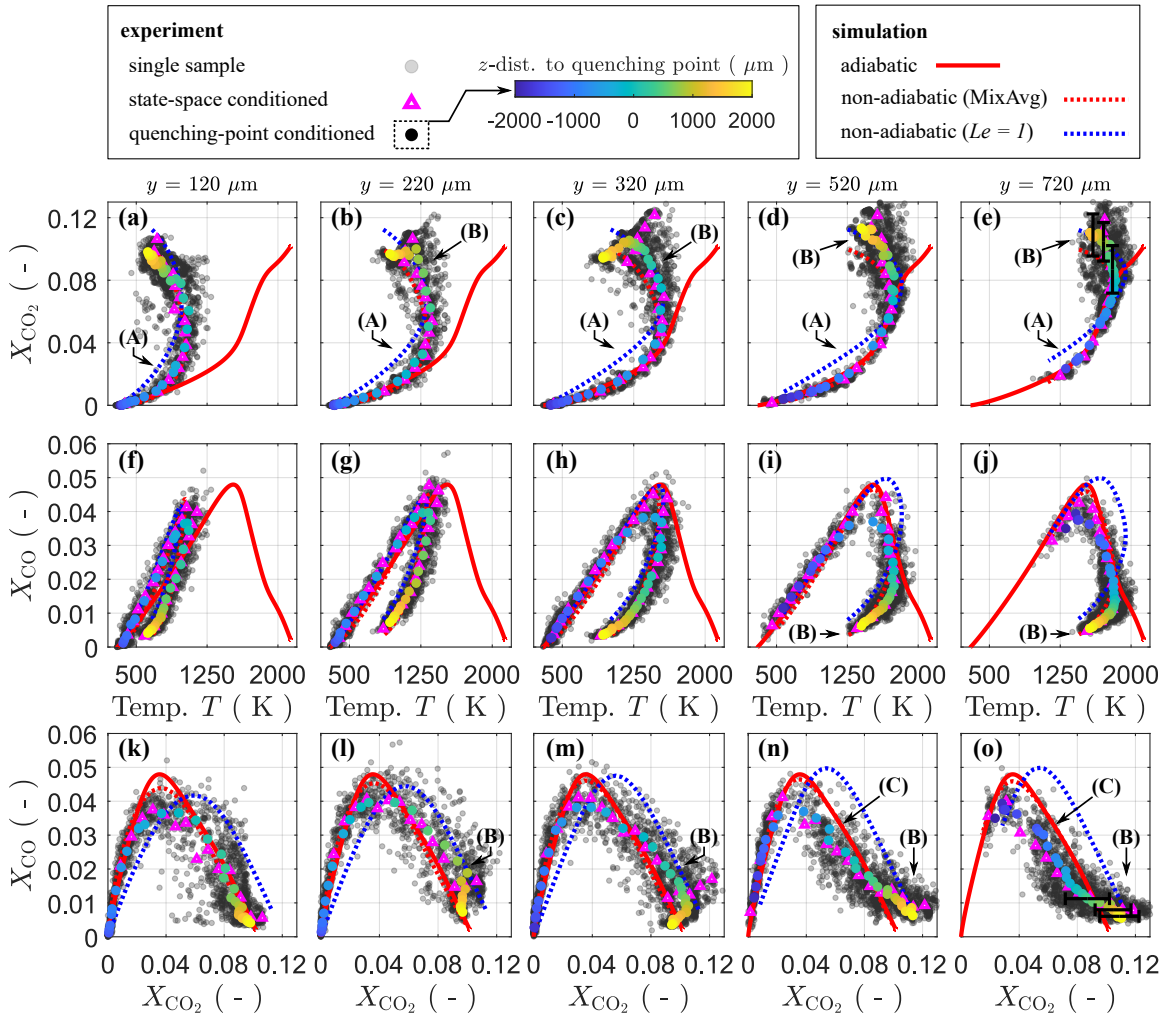
Figure 5.13: Near-wall thermochemistry evolution in z-direction for different wall distances. Adiabatic and non-adiabatic (MixAvg and $Le = 1$) simulations are shown, with non-adiabatic simulations featuring values $z = \pm 2$ mm relative to the quenching height. Labels (A) to (C) highlight features discussed in the text. Samples: 1565 to 2047 (depending on wall distance). This figure was published in Zentgraf et al. [E11] (Fig. 8) and is reused with permission of Elsevier; reproduced in an adapted version.

in (CO_2,T) approaching the reaction's end and is thus applied here in addition. For quenching-point conditioning, the z-space was subdivided into 100 μm wide increments (for each wall distance y) and individual samples are classified into these bins with respect to their instantaneous distance to the common quenching point at $z = 0$ μm, as initially stated in section 5.3.1.2. Averages of X_{CO_2}, X_{CO} and T are calculated for the resulting ensemble statistic classified in each z-bin. For the considered range of $z = \pm 2$ mm in Figure 5.13, this corresponds to 40 bins for evaluation. Since quenching-point conditioning directly relates thermochemistry with streamwise z-evolution over the reaction zone, it is considered to well-capture the chemical reaction progress. From Figure 5.13, it is evident that the state-space and quenching-point conditioning feature some differences in describing the instantaneous scatter of thermochemical states. First, the (CO,T) correlations in Figures 5.13(f)-(j) suggest that experimental data described by quenching-point conditioned averages underestimates CO peaks compared to state-space conditioning and simulation. However, the assessment of physical space in Figure 5.11 confirmed that this is not a conditioning-related issue. It is rather evident that the experimental CO mole fractions overall feature lower values compared to the corresponding simulation. This is not necessarily an experimental shortcoming but could also result from numerical modeling, as referred to in this context in section 5.3.1.3. Conversely, it needs to be questioned why the state-space conditioning apparently increases the experimental peak values in (CO,T) correlations shown in Figure 5.13(f)–(i). Despite state-space conditioned averages appear to better match the simulation, they are evidently biased, since they exceed the average experimental CO trace observed in Figure 5.11(b). State-space conditioned averages are biased near the CO peak due to the split of CO-oxidation and production branch. This separation is required to cope for the non-monotonic behavior of CO mole fractions but finally forces averages to outliers instead of following the physical average. Thus, quenching-point conditioning is considered more robust against such filtering errors and the preferred method to describe the (CO_2,CO,T)-thermochemistry in this thesis. To supplement the discussion in Figure 5.13, the conditioned experimental traces are summarized by Figure 5.14 to outline and compare the trends with increasing wall distance. It focuses on the state-space conditioning in Figures 5.14(a)-(c), while (d)-(f) depict the quenching point-conditioned averages. Please note that for reasons of clarity, only three selected wall distances ($y \in \{120\ \mu m, 320\ \mu m, 720\ \mu m\}$) are shown.

To discuss major findings on thermochemistry in the following, prominent features in Figure 5.13 are labeled (A)-(C). The first feature (A) in Figures 5.13(a)-(e) appoints a shortcoming in modeling the early (CO_2,T) thermochemistry in non-adiabatic simulation with unity Lewis number assumption. Apparently, this assumption is not capable of capturing the correct chemical progress prior to quenching. In contrast, this behavior is not evident in the corresponding early (CO,T) evolution in Figures 5.13(f)–(j). This suggests the following two conclusions. First, the influence of differential diffusion effects needs to be considered, for example by using a mixture-averaged transport model, which evidently captures the thermochemistry evolution better in Figure 5.13. Second, the (CO_2,T) correlation suggests higher sensitivity to differential diffusion effects than the (CO,T) state space. This underlines that additionally measured CO_2 enables further important insights. Here, it significantly aids to disclose the limitation of a unity Lewis number assumption to model FWI for DME/air combustion.

Feature (B) identifies a similar aspect related with differential diffusion, however, in a late stage of reaction progress approaching the fully reacted state. In the (CO_2,T) scatter in Figures 5.13(b)–(e) it is observed that the quenching-point conditioned traces (color-coded circles) develop a trend, departing from the mixture-averaged simulation and towards the simulation with $Le = 1$ assumption. This tendency gets progressively pronounced for increasing wall distances y and is only observed downstream the quenching height, i.e., $z > 0$ μm. For $y = 120$ μm wall distance in Figure 5.13(a), no deviation is apparent and the quenching-point conditioned averages well match the non-adiabatic simulation with mixture-averaged transport model. At $y = 220$ μm, shown in Figure 5.13(b), the trend starts developing and a small bend towards the simulation with $Le = 1$ and back to the simulation with mixture-averaged transport is observed when approaching the fully reacted states. For the next wall distance at $y = 320$ μm the bend is more distinct, as evident from Figure 5.13(c). For further wall distances $y = 520$ μm and $y = 720$ μm in Figures 5.13(d) and (e), the conditioned thermochemistry trace stays on the $Le = 1$ simulation until reaching equilibrium and does not turn back to the simulation considering differential diffusion effects. This effect is equally observed in the (CO,CO_2) thermochemistry, shown by Figures 5.13(l)–(o). Both the experimental (CO_2,T) in Figures 5.13(a)–(c) and (CO,CO_2) in (k)–(m) consistently reveal that thermochemistry approaches the equilibrium state of the non-adiabatic simulation with mixture-averaged transport model for $y \leq 320$ μm. Possibly, this could also be observed for $y \geq 520$ μm, in Figures 5.13(d), (e), (n) and (o), if more data were measured downstream the reaction zone that entirely cover all states towards chemical equilibrium. For further evaluation of this observation, Figures 5.13(e) and (o) include error bars (black) of X_{CO_2} for three selected spatial bins in quenching-point conditioning. Evidently, the CO_2 mole fractions suffer pronounced experimental uncertainty when approaching the fully reacted state. Despite the conditioned averages well-align with the trace of the $Le = 1$ simulation, the lower error bar bounds easily reach the mixture-averaged transport simulation. Consequently, an interpretation of the observed bending of the averaged experimental trace between simulations with mixture-averaged transport model and $Le = 1$ assumption near equilibrium values needs to be considered carefully. Finally, the observations regarding feature (B) do not confirm validity of the $Le = 1$ assumption close to chemical equilibrium of the near-wall reaction at $y \geq 520$ μm. The apparent $Le = 1$ behavior in those areas are rather expected to originate from different, superimposed physical effects. Most likely a local transport effect (maybe three-dimensional) occurs that is not yet captured by modeling. Further investigations are necessary to conclusively clarify these facts and how to model transport in the present configuration best.

In the context of feature (B), it is additionally evident from Figures 5.13(c)–(e) that the scatter of individual experimental X_{CO_2} exceeds the upper equilibrium limits predicted by simulations. This appears to be more pronounced for increasing wall distances. A simulation performed with Cantera 2.4.0 [64] yielded that the equilibrium mole fractions of CO_2 are quite constant around 0.101-0.104 for temperatures from 300 K to 2100 K[14].

---

[14]The simulation was performed and provided by M.Sc. M.Sc. Matthias Steinhausen from Technical University of Darmstadt (STFS) and was used in this thesis with permission. His kind contribution is acknowledged here. The simulation setup was a well-stirred reactor at both constant pressure and temperature using the reaction-mechanism for DME proposed by Stagni et al. [153].

This experimental scatter, which is exceeding the expected equilibrium value, does appear physically inconsistent on a first glance. However, it could be due to local transport effects that were not yet covered in the applied simulation. For example, it could be possible that certain chemical species are diffusively transported from the wall, while CO_2 does not, which would lead to an increase in local CO_2 mole fraction. As pointed out above, these phenomena require further investigation, like advanced diagnostics or three-dimensional numerical simulations with detailed chemistry and transport modeling.

While the state space correlations involving CO_2 mole fractions suggest a tendency towards $Le = 1$ simulation when approaching the equilibrium conditions for increased wall distances, feature (B) manifests differently in the (CO,T) thermochemistry. As observed in Figures 5.13(i) and (j) for $y \geq 520$ μm near the fully reacted values, the quenching-point conditioned experimental data in the CO-oxidation branch better matches the simulation with mixture-averaged transport model than the $Le = 1$ assumption. This is not consistent with the finding from (CO_2,T) and (CO,CO_2) state spaces. For temperatures $T > 1600$ K even an opposite tendency is emerging and (CO,T) states are slightly bending from the simulation with mixture-averaged model in the opposite direction to $Le = 1$, i.e., to higher temperatures as suggested by non-adiabatic simulations. This reveals that capturing the differential diffusion effects in the (CO,T) states also suffers minor imperfection with the applied mixture-averaged modeling.

The impact of different wall distances y on conditioned averages of experimental near-wall thermochemistry is summed up in Figure 5.14 (top row: state-space conditioned, bottom row: quenching-point conditioned). From Figures 5.14(a), (b), (d) and (e) it is directly evident that conditioned averages of the experimental (CO_2,T) and (CO,T) thermochemistry feature clear trends with increasing wall distance y and range within the boundaries of the physically possible state space bounded by adiabatic (solid red line) and non-adiabatic simulation at $y = 120$ μm (dotted blue line). Since this observation is independent from the conditioning approach and true for all wall distances, it suggests further confidence in the accuracy of conditioned averages, including the observations in the (CO,CO_2) state space. Thus, experimental deviations from the simulation trend in (CO,CO_2), as shown by feature (C) in Figures 5.13 (n) and (o), could underline the presence of further relevant transport effects (e.g., three-dimensional), pointed out above. On the one hand, detailed statements from (CO,CO_2) state space are impeded, as adiabatic and non-adiabatic behavior are very close to each other and superimposed by experimental uncertainties. On the other hand, these correlations show least impact on the experimental thermochemistry trend with increasing distance from the wall, shown in Figures 5.14(c) and (f). As further evident from Figure 5.14(c), conditioned averages of (CO,CO_2) overlap within their experimental uncertainty indicated by transparent colored areas (error of X_{CO} with respect to X_{CO_2} increments for $y = 120$ μm and $y = 720$ μm).

Despite the experiments presented in this thesis provide stand-alone thermochemistry results on FWI, it is underlined that the above interpretations of features (A) to (C) were only possible by comparison of the experimental data to the provided simulations (see section 5.2.3). This finally emphasizes the urgent need of detailed, complementary experimental and numerical studies, strongly aiding each other in FWI research.
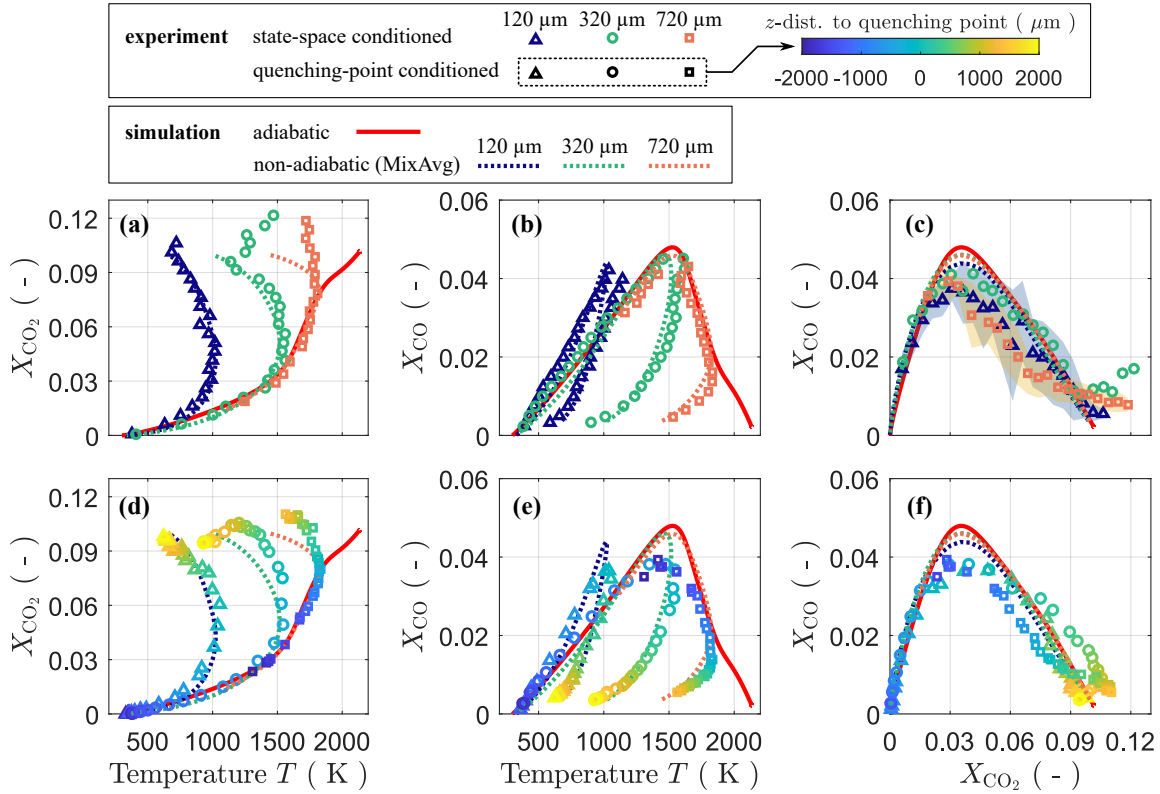
Figure 5.14: Conditioned averages for wall distances $y \in \{120 \, \mu m, 320 \, \mu m, 720 \, \mu m\}$ shown in Figure 5.13. (a)–(c): state-space conditioning on defined CO as well as CO_2 increments; (d)-(f): quenching-point conditioning (symbols equal to top row). This figure was published in Zentgraf et al. [E11] (Fig. 9) and is reused with permission of Elsevier; reproduced in an adapted version.

5.3.3 Turbulent Near-Wall Thermochemistry

The results on turbulent near-wall thermochemistry are presented and discussed in a similar way as the laminar ones above. However, this turbulent consideration puts emphasis on the impact of instantaneous mixing and convective transport, and finally postulates potential scenarios for reaction-transport coupling that could lead to the observed thermochemistry. Hereby, the analysis continues the classification of governing quenching topologies in *SWQ-like* and *HOQ-like* events, as comprehensively discussed in the previous chapter 4 on flame and flow dynamics. Within the about 22000 samples considered, $\approx 50\%$ are SWQ-like and the remaining $\approx 50\%$ are HOQ-like cases (only $\approx 29\%$ from total samples with thermochemistry probe volume inside the approaching wall-parallel reaction) [E8]. As finally concluded in chapter 4, these two topologies feature different characteristics in their flow and transport. This behavior is expected to be reflected in the thermochemistry here and to further yield novel insights into turbulent FWI thermochemistry. The remainder of this section initially presents SWQ-like cases, followed by the HOQ-like events. Finally, both cases are compared by means of a statistical test.

5.3.3.1 SWQ-like Quenching Topologies

State spaces of near-wall thermochemistry for (CO_2,T), (CO,T) and (CO,CO_2) under turbulent inflow conditions and classified as SWQ-like events are presented in Figure 5.15. This is done for three selected wall distances, $y \in \{120\ \mu m, 320\ \mu m, 720\ \mu m\}$ (see top of each column in Figure 5.15). For orientation purpose, adiabatic (red solid line) and non-adiabatic simulations for laminar SWQ conditions with mixture-averaged transport
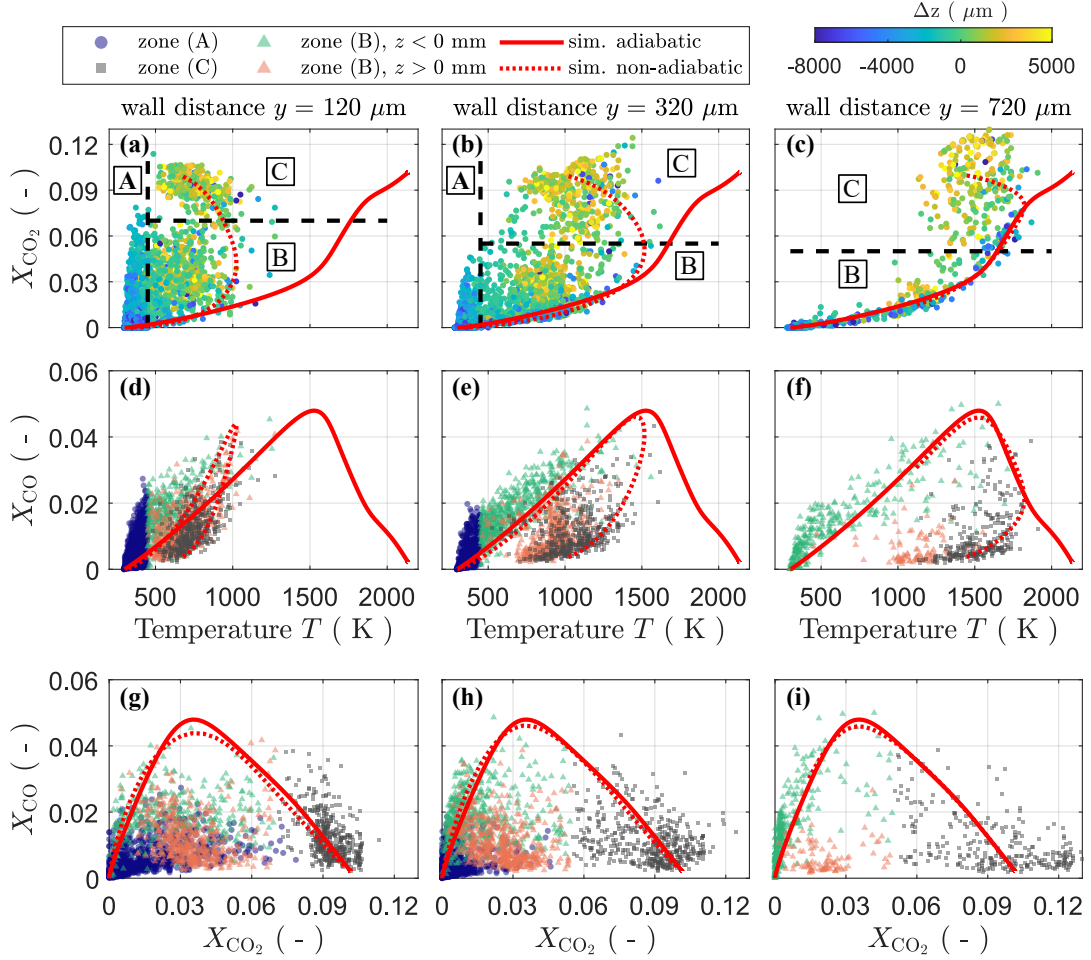
Figure 5.15: Near-wall thermochemical states for SWQ-like quenching topologies at turbulent inflow. Three wall distances $y = 120\ \mu m$ (left column), $y = 320\ \mu m$ (center column) and $y = 720\ \mu m$ (right column) are assessed. Adiabatic and non-adiabatic SWQ simulation for laminar flow conditions with mixture-averaged transport modeling are shown for orientation purpose, within $z = \pm 2$ mm relative to the instantaneous quenching height. Color-coding in (a)-(c) is done relative to the instantaneous quenching height Δz, while data in (d)-(i) feature uniform colors according to their zones A to C that highlight three potential transport scenarios for discussion; boundaries used for classification of thermochemical data in these different zones A to C are shown by black dashed lines in (a)-(c). Samples: 785 to 2805 (depending on wall distance). This figure was published in Zentgraf et al. [E8] (Fig. 5) and is reused with permission of Elsevier; reproduced in an adapted version.

modeling (red dotted line) are shown. Using the previously introduced quenching-point conditioning, a scheme for color-coding the individual scatter points is applied. The top row outlining the (CO_2,T) state space color-codes each scatter by its streamwise distance Δz to the instantaneous quenching event (pre-quenching: blue, $z = -8$ mm; post-quenching: yellow, $z = 5$ mm). This encodes a measure for the streamwise reaction progress over the quenching event. It is first evident that the turbulent SWQ-like thermochemistry evolution significantly differs from the laminar behavior. The scatter in the state space appears broader and is focused to different regimes. From Figure 5.15(a), three prominent zones A, B and C are defined to further discuss the turbulent thermochemistry. These zones were best evident from the (CO_2,T) state space, as states are very close together in the (CO,T) or overlap. This again emphasizes the high potential of additionally measuring CO_2 concentrations to study near-wall FWI thermochemistry. It is thus evident that additional CO_2 provides valuable information that was not accessible in previous studies measuring (CO,T) only. To visualize the zones in the remaining state spaces, i.e., (CO,T) and (CO,CO_2) in Figures 5.15(d)-(i), uniform colors are applied for samples identified in the individual zones A (blue circles), B (green and orange triangles) and C (gray rectangles). Based on the observations in turbulent thermochemical state space and by referring back to the flame and flow dynamics in chapter 4, potential transport mechanisms for the characteristic zones are postulated in Figure 5.16 to explain thermochemistry near the quenching point in SWQ-like topologies. Especially, the existence of vortex structures in the statistical ensemble, as discussed in section 4.3.2.5, is considered relevant for the mechanisms.

Within zone A for $y = 120$ μm wall distance, high CO_2 mole fractions up to $X_{CO_2} \approx 0.08$ are observed at considerably low temperatures $T \leq 450$ K in Figure 5.15(a), along with low CO mole fractions $X_{CO} \leq 0.02$ in Figure 5.15(d). It is particularly striking that all samples in this zone are located upstream the quenching point, i.e., at $z < 0$ mm, and
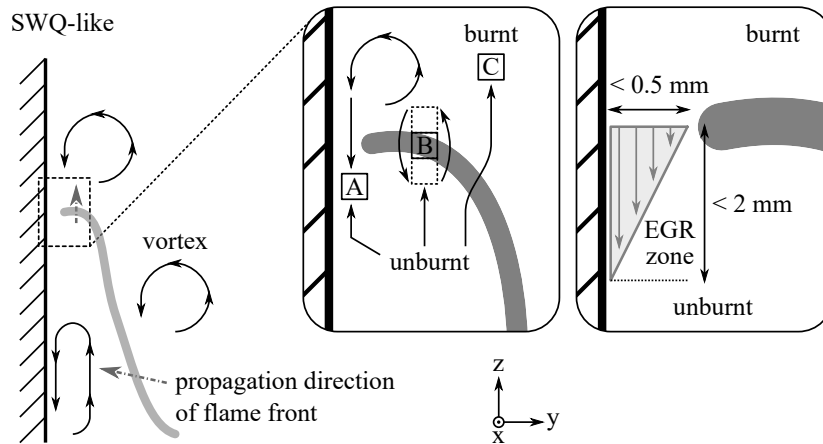
Figure 5.16: Schematic for potential transport scenarios A, B and C in SWQ-like quenching topologies. A zoomed view of scenarios is embedded as well as a view of the EGR-active zone for upstream transport relative to the quenching point. This figure was published in Zentgraf et al. [E8] (Fig. 6) and is reused with permission of Elsevier; reproduced in an adapted, extended version.

thus in the supposed unburnt fresh gas region. Such behavior could not be observed in the corresponding laminar operation in Figure 5.13. It is therefore reasonable that a different transport mechanism is involved. Thus, the question of the origin of these high concentrations of reacted products in the pre-quenching areas arises. As previously discussed in section 4.3.2.3 on turbulent combustion regimes, the studied reaction is predominantly classified in the wrinkled and corrugated flamelet regime. This suggests that the turbulent flow is by no means intense enough to penetrate the flame front or break it up and finally entrain combustion intermediates or products, like expected in the regimes of disturbed reaction zones or well-stirred reactor (see Figure 2.6 for reference). Thus, the high CO_2 mole fractions are not expected to originate from the active flame front nor penetrate trough it, but need to come from somewhere else. The most likely scenario is exhaust gas recirculation (EGR) from the reacted, post-quenching zones. As shown in the zoomed view in Figure 5.16, it is postulated that the momentum of a counterclockwise (CCW) rotating vortex in the vicinity of quenching forces transport of burnt gas upstream the quenching point, through a small gap between flame tip and wall. During this transport, the EGR-fluid is cooled down by enthalpy loss to the wall and is additionally mixed with unburnt fresh gas. This postulated mechanism is strongly supported by the findings presented in the previous chapter 4 on flame and flow dynamics. First, a high probability to observe CCW-vortices right downstream the quenching point is evident from ensemble statistics in Figure 4.31(b). It confirmed that basically a vortex is present in $\approx 25\%$ of the cases, which could aid the postulated transport. Second, instantaneous transients in section 4.3.2.6 affirmed that both a large CCW-vortex right downstream the quenching point can exist simultaneously to a wedge-shaped zone with relative upstream transport to the quenching point, as shown in Figure 4.34. These instantaneous wedge-shaped zones feature typical dimensions of $(\Delta y, \Delta z) \leq (0.5 \text{ mm}, 2 \text{ mm})$ and are assumed an active range for EGR. These dimensions from the flame and flow dynamics measurement do well-match the distances Δz in this thermochemistry study, where high CO_2 concentrations ($X_{CO_2} > 0.05$) are observed pre-quenching. At $y = 120$ μm wall distance, values $X_{CO_2} > 0.05$ do only capture $\approx 1.2\%$ in the respective scatter plot. However, such high mole fractions are consistently detected in the pre-quenching unburnt gas, in average at $\Delta z \approx -1.7$ mm prior to the quenching point. From Figures 5.15(b) and (c) it is observed that zone A is less pronounced at $y = 320$ μm wall distance and entirely vanishes for $y = 720$ μm. This again emphasizes the postulated transport mechanism, as the impact of the wedge-shaped EGR-zone rapidly decreases for increasing wall distances. Overall, there is strong evidence that the postulated EGR-mechanism causes the thermochemistry observed in zone A. Indeed, this was confirmed very recently by numerical simulation [154].

At $y = 120$ μm wall distance, zone B features intermediate CO_2 mole fractions up to $X_{CO_2} \leq 0.07$ (Figure 5.15(a)) and CO concentrations up to $X_{CO} \leq 0.03$ (Figure 5.15(d)) at increased temperature levels between 450 K and 1000 K. Zone B is apparent across the quenching event and covers approximately 60% post-quenching probes, while about 40% are located pre-quenching. This emphasizes the transitional nature of thermochemical states within zone B and also explains the broad variety of observed scattering. However, it is remarkable that despite 60% are in the burnt, CO_2 values are well-below the expected equilibrium value $X_{CO_2} \approx 0.10$. Furthermore, experimental temperatures in both the (CO_2, T) and (CO, T) state space in Figure 5.15 are several hundred Kelvin lower compared

to the corresponding laminar case in Figure 5.13. This is directly observed in Figure 5.15 as difference between individual scattering and the red dotted line for the laminar non-adiabatic simulation. These observations suggest that chemical reaction is progressing within zone B but influenced by heat losses to the quenching wall as well as mixing of burnt products with unburnt fresh gas, as shown in Figure 5.16. The transport mechanism postulated for zone A is less pronounced in the zone B scenarios. For increasing wall distances, the turbulence impact on zone B gradually decreases and states approach the laminar behavior, e.g., like for $y = 720$ μm in Figures 5.15(c) and (f).

The majority of samples in zone C is located in the post-quenching area ($> 85\%$ for all wall distances). Zone C is characterized by the corresponding CO_2 and CO mole fractions in the state space approaching the expected equilibrium value of the non-adiabatic laminar simulation. However, temperatures T are lower than for laminar conditions, which is appointed to a still increased heat flux to the wall by turbulence transport. There is no indication for significant mixing processes between burnt and unburnt gas, like the mechanism proposed for zone A, that affect the thermochemical states within zone C. As already observed for the previously discussed zones A and B, laminar thermochemistry conditions are increasingly approached for increasing wall distances in scenario C, e.g., as observed at $y = 720$ μm. This finally suggests that the major impact of turbulence on thermochemistry in flame quenching is mainly apparent in the near-wall areas, i.e., $y < 720$ μm, and even bigger wall distances could be simplified by the assumption of laminar conditions.

A further interesting point to discuss in this context is on mixing processes observed as signal inhomogeneity in the instantaneous CO-LIF raw images, as exemplary shown in Figure 5.17(a). While processes with OH-PLIF cover the yz-plane only, the small CO-
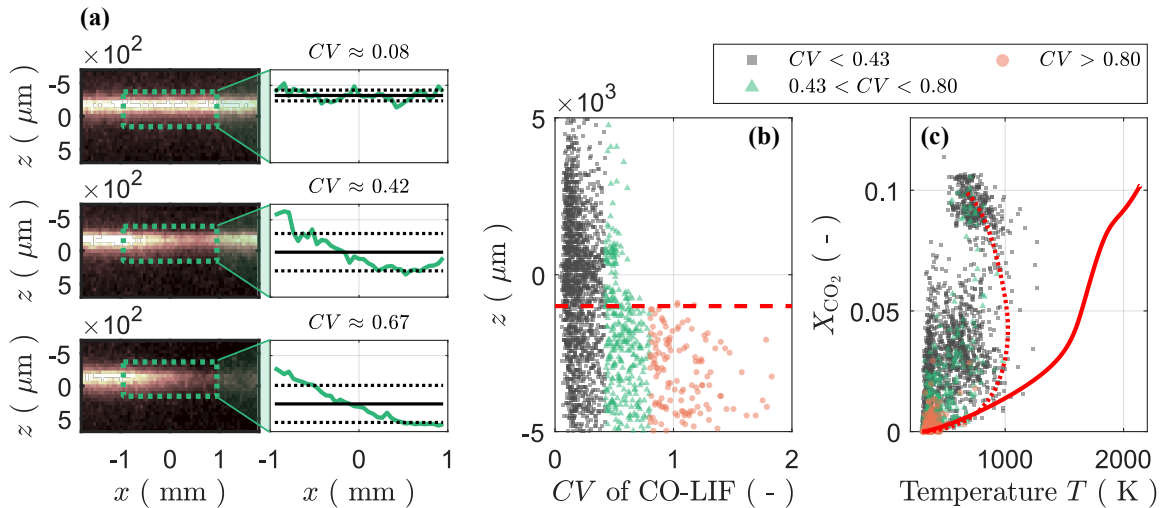
Figure 5.17: Instantaneous mixing impact on spatial CO-LIF signal at turbulent inflow and coefficient of variation CV of signal in principal beam direction x for three examples with different impact (a). All CV values for wall distance $y = 120$ μm with respect to streamwise z-direction (b). (CO_2,T) state space with differently strong mixing from CV color-coded (c). Samples: 2400.

LIF FOV was recorded perpendicular to OH in the xz-plane. This could give a certain insight into out-of-plane transport or mixing with respect to the x-direction. However, interpretation needs to be done very carefully, as the spatial CO-LIF signal is a function of both the local chemical composition and the local gas temperature. Solely from the CO-LIF raw images, no statement is possible if hot or cold gas is mixed to the FOV. Signal inhomogeneity only indicates a certain type of mixing. The left column in Figure 5.17(a) shows background-corrected CO-LIF raw images with increasing degree of signal inhomogeneity from top to bottom. The laser for excitation transits the FOV in x-direction and the green dotted rectangle gives the overlap with the DP-CARS probe volume, used to extract the signal traces in the right column of Figure 5.17(a). First, signal in the extraction rectangle is averaged in beam-normal z-direction, resulting in the green intensity traces $I(x)$. Then, a coefficient of variation (CV) is defined as $CV = \sigma(I(x))/\mu(I(x))$ by rationing the standard deviation (σ, black dotted line) and mean (μ, black solid line) of the signal intensity. This yields a measure for the signals inhomogeneity in x-direction. Higher CV-values describe stronger inhomogeneity and suggest more intense mixing impact in x-direction. For robustness, CV-values were only assigned to cases, where CO signal existed, i.e., where $\mu(I(x))$ in the extraction rectangle exceeded $\mu(I_{\mathrm{BG}}) + 2 \cdot \sigma(I_{\mathrm{BG}})$ of the background intensity I_{BG} (ensures that analyzed signal is only considered beyond the 95% confidence interval of the background).

The derived CV-values can be used for a further, novel conditioning of thermochemistry statistics, as done by Figure 5.17(b) and (c) for SWQ-like samples at a wall distance of $y = 120$ μm. In Figure 5.17(b), CV-values are plotted with respect to their relative distance to the instantaneous quenching point at $z = 0$ mm. This visualization is used to define three prominent CV-classes. First, it needs to be noted that a certain level of CV-values is also observed under laminar operation. From assessing a corresponding set of laminar data, a threshold value of $CV \approx 0.43$ is derived (equals $\mu(CV_{\mathrm{lam}}) + 2 \cdot \sigma(CV_{\mathrm{lam}})$; considered to contain laminar CV-values with a confidence interval of about 95%). These values $CV < 0.43$ can be considered *laminar-like* in their CO-LIF signal homogeneity and are displayed by gray rectangles in Figures 5.17(b) and (c). Furthermore, there appears to be a quite sharp boundary around $z = -1$ mm (see red dashed line in Figure 5.17(b)) below which the CV-values strongly rise. An empirical value of $CV > 0.8$ is selected to define those cases and the corresponding scatter is displayed as orange circles. It is remarkable that this near-wall region at $z < -1$ mm with highest CV-values corresponds well to high vortex activity in the unburnt turbulent boundary layer, as evident from high vortex probabilities in Figure 4.31(b). This could indicate increased mixing tendency with unburnt fresh gas, including the out-of-plane x-direction. Finally, there is a third zone attributed to intermediate mixing impact (green triangles) located between the two previously defined zones.

These three characteristic CV-zones are visualized in the (CO_2, T) space by Figure 5.17(c) using the introduced color-coding. Here, only the (CO_2, T) state space derived from DP-CARS is considered, to better understand the observations in the CO-LIF raw signal from an independent but correlated diagnostic. It is first evident that samples with highest CV-values (orange circles) are all located near ambient temperatures and at negligible CO_2 mole fractions. This supports the above theory that mixing of intermediate reaction

products with fresh gas is very likely. States with intermediate homogeneity from CO-LIF (green triangles) appear to scatter towards zones A and B, previously defined in Figure 5.15. However, most remarkable is that the majority of zones A and B are covered by the lowest CV-value case (gray rectangles), associated with minimum mixing impact in x-direction. This observation is counterintuitive and suggests that the mechanism governing zone A and transporting CO_2 upstream is not apparent in the instantaneous CO-LIF images. This is most likely due to two major aspects: (1) it is not a process in the out-of-plane x-direction but a transport that manifests in the yz-plane, (2) it is a phenomenon driven by macroscopic, energy-containing structures that could extent over the entire x-range captured with CO-LIF (≥ 2 mm of the extraction rectangle for CV) and thus also appears quite homogeneous in the corresponding two-dimensional images.

As already pointed out above, these results need to be interpreted carefully since the raw CO-LIF intensity features multiple dependencies. However, by a combined insight into simultaneous DP-CARS, provided by Figure 5.17(c), and the observations on vortex probabilities from a complementary study in Figure 4.31(b), two interesting findings on species transport in turbulent SWQ-like quenching topologies are derived. First, early reaction intermediates appear to be diluted by mixing with fresh unburnt gas from the turbulent boundary layer at $z < -1$ mm. Second, the transport processes dominating zone A and B do very likely feature no pronounced dependency in x-direction (at least on a scale ≤ 2 mm).

5.3.3.2 HOQ-like Quenching Topologies

While Zentgraf et al. [E8] did only focus the thermochemistry of SWQ-like quenching topologies, this thesis further covers the HOQ-like cases in detail. Their state spaces are shown in Figure 5.18 for three wall distances of the thermochemistry probe volume respectively. They are presented and discussed in an equal manner as SWQ-like cases in the previous section 5.3.3.1. However, color-coding and zone classification is done differently for HOQ-like scenarios. Since the flame front propagates normal to the wall in HOQ events, the distance between instantaneous flame front position and wall Δy is the relevant measure to encode the progress of quenching and is thus used for color-coding the scatter in (CO_2,T) state spaces in Figures 5.18(a)-(c). A difference $\Delta y = -200$ μm (yellow) means that the flame front is approximately 200 μm away from the wall surface, while $\Delta y = -1000$ μm (blue) represents a distance of 1000 μm. In this context, one needs to keep in mind that in such an HOQ-like event the approaching flame extinguishes at a certain distance Δy from the wall, i.e., the quenching distance (see section 2.2.3 for reference). For example, Rißmann et al. [137] evaluated the average quenching distances around 179 μm (CH_4, $\Phi = 1.0$) and 159 μm (C_2H_4, $\Phi = 1.0$) for turbulent transient HOQ. Despite they used different fuels and equivalence ratio, the order of magnitude appears to well-match the upper limit of the color-coding at $\Delta y = -200$ μm applied here. The continuous progression of colors in Figures 5.18(a)-(c) suggests that Δy is the right length scale for conditioning the HOQ-like samples here, which in turn affirms that the considered phenomena are indeed associated with HOQ. Please note that color-coding the scatter with Δz, as previously done for SWQ-like topologies, does not result in any continuous or clear color pattern (not shown here).

With the flame front approaching the wall, i.e., from blue to yellow color, increasing temperatures and a broader variety of CO_2 mole fractions are observed in the state spaces in Figures 5.18(a)-(c). Despite the non-adiabatic simulation (red dotted line) describes a laminar SWQ configuration, the experimental HOQ-like scatter appears to align with the simulation's trace. At a given wall distance, the enthalpy loss of the flame to the nearby wall is expected in the same order, regardless of the instantaneous quenching topology. Therefore, a similar global behavior in the thermochemical state space is to be expected for SWQ- and HOQ-like phenomenons. Two prominent zones D and E are classified in
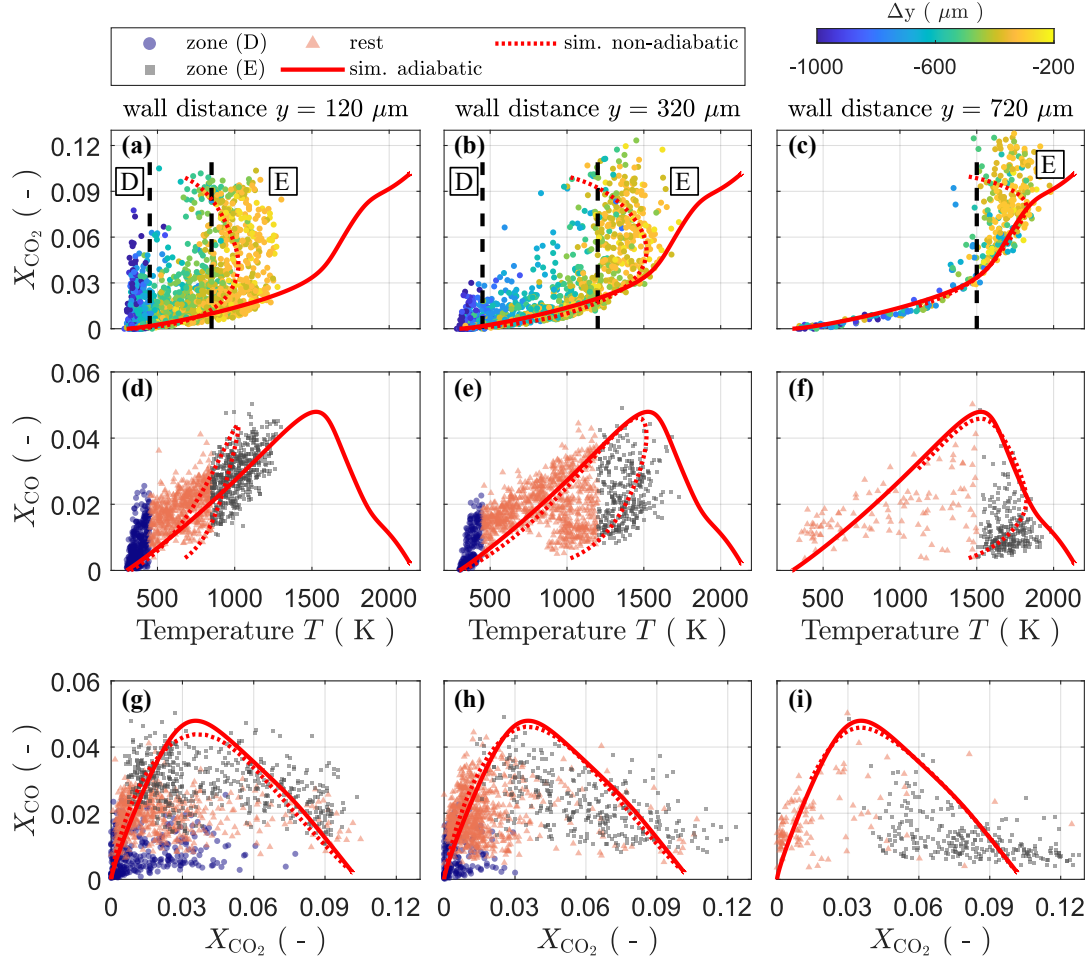
Figure 5.18: Near-wall thermochemical states for HOQ-like quenching topologies at turbulent inflow. Three wall distances $y = 120~\mu$m (left column), $y = 320~\mu$m (center column) and $y = 720~\mu$m (right column) are assessed. Adiabatic and non-adiabatic SWQ simulation for laminar flow conditions with mixture-averaged transport modeling are shown for orientation purpose, within $z = \pm 2$ mm relative to the instantaneous quenching height. Color-coding in (a)-(c) is done relative to the wall-normal distance between flame front and wall Δy, while data in (d)-(i) feature uniform colors according to their zones D and E that highlight two potential transport scenarios for discussion; boundaries used for classification of thermochemical data in these different zones D and E are shown by black dashed lines in (a)-(c). Samples: 386 to 1474 (depending on wall distance).

Figure 5.18 (see dashed black lines) for further discussion. Samples in these zones are colored uniformly in the (CO,T) and (CO,CO_2) state space. Zone D features blue circles, zone E black rectangles and states between D and E are marked by orange triangles and are shown for completeness. Potential transport phenomena that could be involved in the thermochemistry of these zones are given in Figure 5.19 and are discussed in the following.

The behavior of zone D is similar to that in zone A observed previously for SWQ-like cases in Figure 5.15(a), i.e., high CO_2 concentrations at low gas temperatures. At $y = 120\ \mu$m wall distance, values $X_{CO_2} > 0.05$ in zone D do only capture $\approx 0.4\%$ of total samples in the respective scatter plot (about 3 times less compared to the respective SWQ-like events in zone A). Furthermore, this zone is only evident at $y \leq 320\ \mu$m. It features similar characteristics in the (CO,T) and (CO,CO_2) state spaces as zone A. States in zone D are only apparent when the flame is far from the wall (see blue color-coding) and a certain gap in the order of ≈ 1 mm exists between wall and approaching reaction front. The observed thermochemistry is most likely explained by the same mechanism that governs zone A. CO_2 is transported upstream from a previous, spatially close SWQ-like scenario. This can be seen as a kind of leftover from the quenching pre-history. For confirmation, it is referred to Figure 5.20, where three selected SWQ-like scenarios in zone A in (a)-(c) are opposed to three HOQ-like cases from zone D in (d)-(f) by their OH-PLIF signal. All samples feature mole fractions $X_{CO_2} > 0.05$ and a laser probe volume location (red hollow circle) in the pre-quenching region. For a better comparison, the laser probe volume is fixed at the streamwise position $z = 0$ mm in this visualization (red dashed line). It is first evident that the SWQ-like samples in Figures 5.20(a)-(c) feature around 1-2 mm distance between the probe volume, where X_{CO_2} is measured, and the quenching point. In the HOQ-like cases in Figures 5.20(d)-(f), this is observed in a similar manner. Despite the laser position is located within a wall-parallel reaction zone, associated with HOQ, an SWQ-like leftover is evident at $\Delta z \leq 2$ mm downstream. As previously demonstrated in the discussion on flame and flow dynamics in section 4.3.2.6, this is a typical range for relative transport upstream the quenching point. Thus, it is suggested that the processes
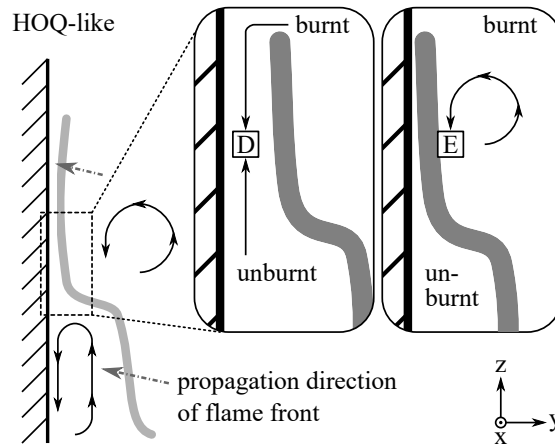
Figure 5.19: Schematic for potential transport scenarios D and E in HOQ-like quenching topologies. A zoomed view for each scenario is embedded.

for zone A and zone D have the same origin and are caused by relative transport of burnt exhaust gas upstream the quenching point, likely forced by a nearby vortex structure.

States in zone E are observed when the detected flame front is very close to the wall, immediately prior to extinction (see yellow color-coding). This is most prominent for wall distances $y \leq 320$ μm. On the one hand, CO_2 mole fractions X_{CO_2} range from 0.01 to equilibrium concentration near 0.10. On the other hand, also CO mole fractions X_{CO} can peak up to 0.05. It is remarkable that the wall-closest CO mole fractions X_{CO} are higher compared to the SWQ-like scenarios, as shown in Figures 5.15(d) and (e). The very high CO concentrations indicate a strong contribution of physical transport (convection and diffusion). This supports the following point of view on transport mechanisms, as shown in Figure 5.19 by the zoomed view. First, the wall-normal propagating flame is expected to suddenly extinguish at the cold wall, leaving a broad variety of instantaneous reaction intermediates, which are cooled down. Second, diffusion processes impact near-wall concentrations, as previously demonstrated for CO in laminar SWQ [62]. Third, fully reacted products are mixed to these intermediates, driven to the wall by strong, energy-containing vortex structures that evidently exist behind the flame front of HOQ-like phenomena, as demonstrated by Figure 4.31(c). Those mechanisms could finally explain the broad range of both CO_2 and CO mole fractions observed in zone E.

Palulli et al. [123], who also classified SWQ- and HOQ-like topology in their numerical study, likewise observed higher near-wall CO concentrations and broader concentration fluctuations in the low temperature region during HOQ-like compared to the SWQ-like. As evident in the above paragraph, this is also indicated here, despite the different operation conditions between the experiment in this thesis and their simulation (methane/air at $\Phi = 1.0$, wall and inlet temperature at 800 K). These findings clearly suggest potential differences in thermochemistry between both instantaneous quenching topologies.
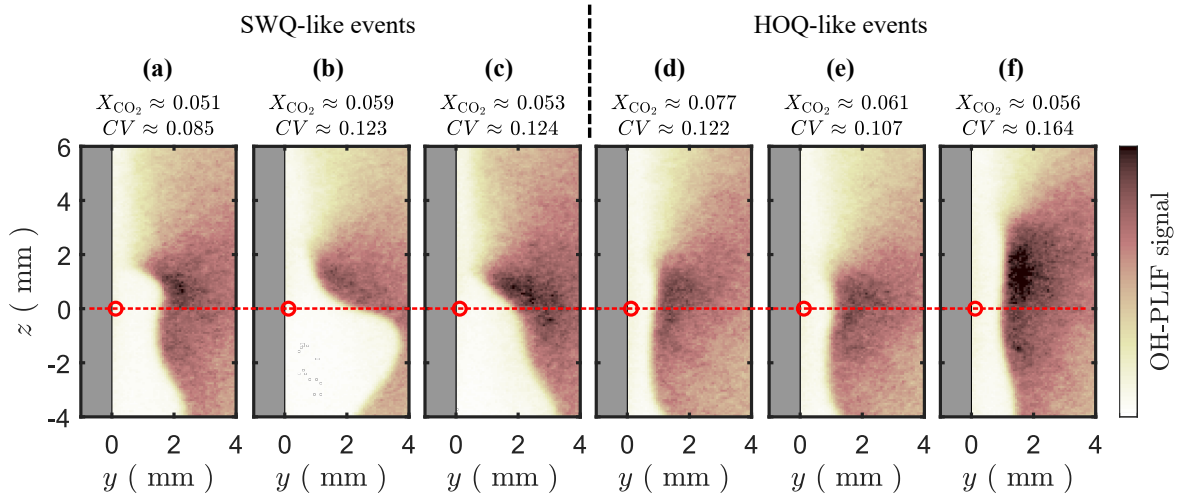
Figure 5.20: Comparison of exemplary SWQ-like (a)-(c) and HOQ-like (d)-(f) instantaneous OH-PLIF scenarios with high CO_2 concentrations ($X_{CO_2} > 0.05$) detected in the pre-quenching. Thermochemistry probe volume as red hollow circle, fixed at common streamwise position $z = 0$ mm shown by red dashed line.

5.3.3.3 Statistical Comparison

After individual discussion of the SWQ- and HOQ-like topologies and their potential governing transport phenomena, a final statistical comparison of both quenching cases is provided. This is done by the means of a categorical chi-squared test, applied to the three-dimensional (CO_2,CO,T)-thermochemistry state space, to derive a statement if SWQ- and HOQ-like thermochemistry is different with *statistical significance* or not. A similar testing was previously done by Greifenstein [66, p. 144 f.] for a two-parameter (CO,OH) state space and motivated the application in this thesis. Following the outlines of Fahrmeier et al. [57, p. 447], chi-squared values are defined by

$$\chi^2 = \sum_{i=1}^{k} \frac{(h_i - n \cdot \pi_i)^2}{n \cdot \pi_i} \tag{5.4}$$

from the actually observed frequency h_i and expected frequency $n \cdot \pi_i$ evaluated on each category $i \in [1, k]$. Here, n gives the total number of independent probes for the considered case (in this experiment: single-shot thermochemistry samples of either SWQ- or HOQ-like topologies), while π_i denotes the probability for a category i [57, p. 446]. The degree of freedom is defined as $k - 1$ [57, p. 447].

To apply this χ^2-test to the presented experimental study, several aspects have to be considered. First, categories i need to be chosen in an appropriate way. It appears most feasible to define three-dimensional bins in the (CO_2,CO,T) state space with consideration of measurement uncertainty in terms of the precision for each variable. This bases on the outlines in section 5.3.1.1. As the following analysis focuses on the wall-closest distance at $y = 120$ μm, corresponding temperatures are below 1200 K. For X_{CO_2} and X_{CO}, an appropriate bin size is estimated from instantaneous residua given by Figures 5.9(d) and (e). In both cases the majority of instantaneous scatter for $T < 1200$ K appears to be well-captured by bins spanning 0.01 on the mole fraction axis (equals ± 0.005). For temperature, 4% precision was derived in section 5.3.1.1. For $T = 1200$ K, this corresponds to a precision of $\approx \pm 50$ K, which finally yields bins with 100 K width to
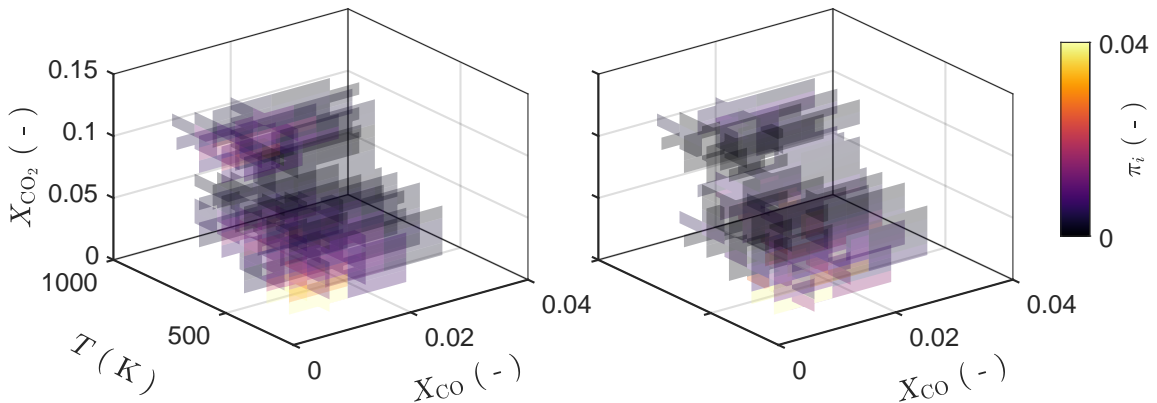
Figure 5.21: Three-dimensional π_i-distributions in the (CO_2,CO,T)-space for SWQ-like (left) and HOQ-like (right) quenching topologies at $y = 120$ μm wall distance, visualized as color-coded slices. Shown binning: $\Delta X_{CO_2} = 0.01$, $\Delta X_{CO} = 0.01$, $\Delta T = 100$ K.

classify the T-dimension. Second, the probability π_i is derived from the overall population of the thermochemical state space, i.e., from combination of both topologies SWQ $\cup$ HOQ. Since individual topology cases originate from the same turbulent operation point, this appears reasonable to calculate a robust basic population state. A combined distribution of cases was also applied in this context by the analysis of Greifenstein [66, p. 144]. Third, the observed frequency of each individual topology h_i (either SWQ-like or HOQ-like) is then compared to the corresponding expected frequency $n \cdot \pi_i$ from the overall population. This is done for each bin i and summed up to χ^2 values according to Equation (5.4). The calculated χ^2 is finally compared to tabulated values of $\chi^2_{1-\alpha}(k-1)$ with a level of significance α and the null hypothesis is rejected for $\chi^2 > \chi^2_{1-\alpha}(k-1)$ [57, p. 447].

As stated by Fahrmeier et al. [57, p. 448], the *approximate* character of this χ^2-test requires sufficient number of statistical probes in the considered categories and thus demands $n \cdot \pi_i \geq 1$ for all and $n \cdot \pi_i \geq 5$ for at least 80% of categories i. To meet this requirement, all bins with $n \cdot \pi_i < 1$ were excluded from the data evaluation here. Overall, only bins are considered that were occupied in the thermochemical state space and were not rejected due to too low sample sizes. The resulting number of occupied bins is defined as k. For the three-parameter thermochemistry at $y = 120~\mu$m, the criterion $n \cdot \pi_i \geq 5$ yielded ratios of $\approx 46\%$ (SWQ-like, $(k-1) = 222$) and $\approx 37\%$ (HOQ-like, $(k-1) = 190$), which suggests that statistics in the selected thermochemistry bins is too weak. By increasing the bin sizes by a factor of 2, these values could be improved to $\approx 78\%$ for both topology cases, but this did not change the statements on statistical significance in the following.

For a first impression, the π_i-distributions in the three-parameter state space are visualized for SWQ- and HOQ-like topologies in Figure 5.21 for a wall distance of $y = 120~\mu$m. Both probability distributions appear to differ visually. An application of Equation (5.4), taking into account the above descriptions, and considering $\alpha \leq 0.05$ finally yields that in both the SWQ- and HOQ-like case at $y = 120~\mu$m the null hypothesis needs to be rejected. Consequently, their individual thermochemistry distributions do not correspond to the one describing the overall thermochemistry population for turbulent FWI. This leads to the conclusion that near-wall three-parameter thermochemistry of the two prominent quenching topologies is evidently different with statistical significance. In turn, this finding motivates to treat such topology phenomena separately in their modeling for numerical simulation, e.g., by different flamelet-based chemistry tabulations.

5.4 Summary

This chapter presented a comprehensive investigation on near-wall thermochemistry during FWI in an SWQ burner. Thermochemical states were quantified simultaneously and spatially correlated by measuring the three parameters X_{CO_2}, X_{CO}, T, along with the qualitative OH distribution for instantaneous flame front position. Latter was assessed to determine the instantaneous quenching position and topology for conditioning purpose of thermochemical states. It was possible to probe the thermochemistry up to 120 μm close to the wall surface. This investigation was achieved by an advanced application of simultaneous dual-pump CARS, CO-LIF and OH-PLIF, which was the first application of these combined diagnostics in an SWQ environment. The results shown in this thesis focused on both laminar and turbulent operation conditions with lean DME/air mixtures at $\Phi = 0.83$ and a wall temperature stabilized to 60 °C. Parts of the content of section 5.4 were published in Zentgraf et al. [E8, E11] and are reused with permission (see appendix B), in a modified wording and partially extended by further technical and scientific details to fit the structure of this thesis.

First, the novel combination of laser diagnostics was validated and benchmarked for the application in SWQ-environments against adiabatic and non-adiabatic laminar flame references from numerical simulation. Detailed validation to adiabatic simulation yielded good accuracy and precision of the quantitative diagnostics. A comparison of the wall-closest experimental data to the corresponding non-adiabatic simulation in state space showed a small offset of only 20 μm, suggesting that they match very well. Comparisons in physical space confirmed the experiment provides outstanding validation data.

Second, near-wall combustion effects under laminar inflow conditions were discussed in detail. Initially, the novel diagnostic approach quantifying (CO_2,CO,T) enabled highly sensitive probing of the near-wall thermochemical states. It was suggested that this approach is clearly superior to the previously applied two-scalar quantification using (CO,T). The conditioning of experimental near-wall thermochemistry data to the instantaneous quenching height from OH-PLIF in $\Delta z = 100$ μm increments in physical space enabled revealing tracing of the reaction evolution across quenching. This *quenching-point conditioning* suggested more robust assessment as the previously applied conditioning in state space and is recommendable for future FWI studies. As it was directly related to the streamwise physical reaction progress, ambiguities on the production and oxidation branches were avoided, e.g., in the (CO,T) correlations. Furthermore, X_{CO_2} proved less affected by the wall than X_{CO} and was thus considered a more robust component to define reaction progress variables in near-wall quenching environments. This especially manifested in the (CO,CO_2) state space that featured minimal impact of non-adiabaticity by the quenching wall. Finally, the impact of differential diffusion effects in near-wall thermochemistry was experimentally proven and confirmed its importance for numerical simulation. This insight was achieved by comparing the experimental data to two-dimensional, non-adiabatic fully-resolved chemistry and transport (FCT) simulations using unity Lewis number assumption and a mixture-averaged transport model. It is emphasized that the latter simulation matches very well to the experimental results. In the early reaction progress, (CO_2,T) states were much more sensitive to the influence of differential diffusion effects than (CO,T) correlations. In turn, the (CO,T) state space yielded such

influences closer to the end of reaction progress at higher temperatures and larger wall distances. In conclusion, additionally measuring X_{CO_2} for thermochemistry evaluation aided significantly to identify the limitations of a unity Lewis number assumption for near-wall combustion in this thesis.

Third, the impact of turbulent inflow conditions was analyzed in a corresponding way, after the experimental approach proved feasible for the laminar case and provided valuable, novel findings. This was done separately for the identified SWQ- ($\approx 50\%$ of samples) and HOQ-like quenching topologies ($\approx 50\%$ of samples). It was initially evident that the near-wall thermochemical states under turbulent inflow conditions were different to laminar ones and populated novel regions in the state spaces. This suggested the presence of specific transport mechanisms for turbulent flow conditions. It was further evident that the near-wall thermochemistry significantly depends on whether an SWQ- or HOQ-like scenario is present. Linking the observations on thermochemistry with the previously presented results on flame and flow dynamics aided significantly in exploring potential transport phenomena. In SWQ-like quenching topologies, three prominent scenarios (A, B and C) were identified from the near-wall (CO_2,T) state space. It is emphasized that these three features were not clearly distinguishable in the other state spaces, which again underlined the great benefit of the additionally measured X_{CO_2}. Zone A is characterized by pronounced mixing of hot exhaust gas with cold unburnt reactants, superimposed with increased wall heat losses. Involving detailed assessment of corresponding flow dynamics in chapter 4 finally suggested that processes observed in zone A are most likely caused by exhaust gas recirculation (EGR) in a wedge-shaped zone forced by momentum of counterclockwise vortices close to the quenching point at the flame tip. Indeed, such EGR processes and the importance of flame-vortex interaction were confirmed very recently by numerical simulation [154]. These EGR processes and the impact of wall heat loss are less pronounced in zone B scenarios. Evidently, the gas phase temperatures are only slightly lower compared to the laminar non-adiabatic reference case. In zone C, EGR influences are no longer apparent. Additional consideration of out-of-plane mixing processes by assessing CO-LIF raw images yielded that early reaction intermediates appear to be diluted by mixing with fresh unburnt gas from the turbulent boundary layer. Furthermore, it suggested that the transport dominating zone A and B does very likely feature no pronounced dependency in x-direction.

For HOQ-like quenching scenarios, two zones D and E were classified from the (CO_2,T) scatter. Influences in zone D were attributed to the same mechanism governing zone A in the SWQ-like scenarios. Zone E in turn was appointed to the sudden extinguishing of reaction intermediates by the instantaneous HOQ-event. This was superimposed by mixing reaction products from the exhaust gas driven to the wall by a big vortex structure and the wall-heat losses that lowered temperature, while maintaining species concentration. Overall, it is strongly suggested that large, energy-containing vortex structures play a major role in the reaction-transport-coupling of turbulent near-wall FWI.

Finally, a statistical evaluation revealed that the three-parameter thermochemistry in the (CO_2,CO,T) state space is different between SWQ- and HOQ-like quenching scenarios with statistical significance. Therefore, these two processes should be considered separately in their reaction chemistry, e.g., for flamelet-generated manifolds (FGM) in

numerical simulation. In this context, it needs to be evaluated if FGM using laminar flamelets only is capable to cover real turbulent FWI operation or if some kind of *flow-scenario dependent FGM* would better suit the physical reality. Especially, with regard to a potential modeling of processes in such tabulations, the presented thesis provides valuable insights. Indeed, this topic was addressed very recently in the numerical study of Steinhausen et al. [154], who included EGR phenomena in their tabulation.

Chapter 6

Partially Premixed FWI

6.1 Aim of the Investigation

This final result chapter provides a first insight into a feasibility study on near-wall thermochemistry during partially premixed flame-wall interaction. It provides an outlook to the previous fully premixed thermochemistry study in chapter 5, as shown in the graphical abstract in Figure 6.1 (framed red). As evident from section 2.2.2.3, partially premixed conditions are mostly applicable in real combustion systems. Despite its practical relevance, such effects have been investigated less thoroughly in fundamental combustion research compared to the operation at fully premixed or non-premixed conditions. So far and to the author's best knowledge, experimental FWI studies on the impact of partial premixing to the detailed near-wall thermochemistry have not yet been reported in literature. Therefore, the major aim of this chapter is to give a first insight into these phenomena and to take a first step into near-wall measurements of partially premixed FWI systems.

In the remainder of this chapter, the impact of partial premixing is first assessed by focusing on the near-wall flame front structure in the vicinity of the quenching event. Subsequently, the resulting near-wall thermochemistry is studied with respect to instantaneous carbon dioxide mole fractions X_{CO_2} and gas phase temperatures T. The acquired OH-PLIF data was very recently used in Steinhausen et al. [E4] for numerical setup validation. Chapter 6 presents an independent study and contents are not reused from [E4].
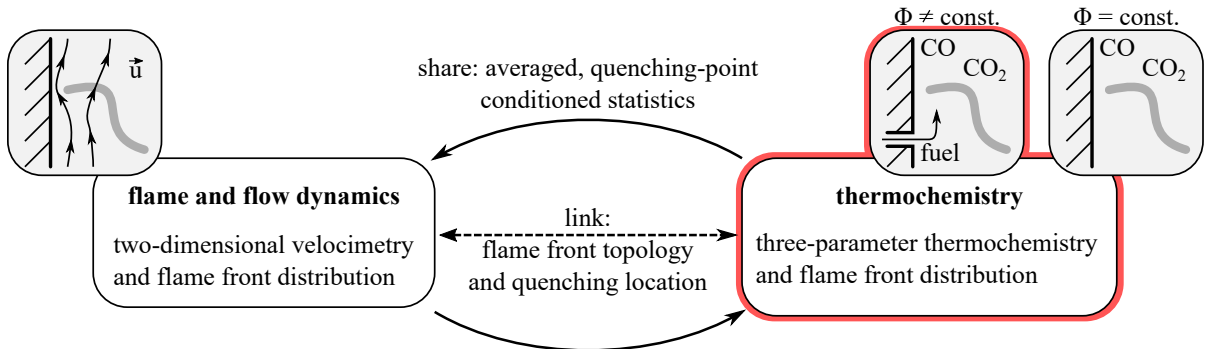
Figure 6.1: Graphical abstract of the applied approach using complementary experimental results to assess transport and reaction phenomena in FWI.

6.2 Methodology

The methods applied to study partially premixed FWI thermochemistry were basically those previously used to assess the fully premixed operation in chapter 5. The only major difference was that the CO-LIF approach has been replaced by an NO-PLIF setup to additionally measure the degree of partially premixing in the vicinity of the wall and upstream the reaction zone. Furthermore, no TPT control system was applied to benchmark the wall temperature. Consequently, the following outline focuses a brief insight into the changes with respect to the previous methods in section 5.2.[15]

To impose partial premixing to the FWI zone in a well-defined way, the quenching wall was modified by a porous sintered structure inlay made of bronze. The inlay featured dimensions $(\Delta x, \Delta z) = (20 \text{ mm}, 5 \text{ mm})$ (active area $\approx 95 \text{ mm}^2$) and was located upstream the quenching event. It covered a region in the wall from $z_{\text{abs}} \approx 30.5 \text{ mm}$ to $z_{\text{abs}} \approx 35.5 \text{ mm}$ above the nozzle exit of the fully premixed main flow, as shown in the

---

[15]The experimental realization of the presented feasibility study was strongly supported by my colleagues Dr.-Ing. Max Greifenstein and M.Sc. Pascal Johe (both: preparation of the PLIF diagnostics and test rig) as well as by my student B.Sc. Jonas Bargon (preparation of the SWQ burner for partially premixed operation). Their kind contribution is acknowledged here.
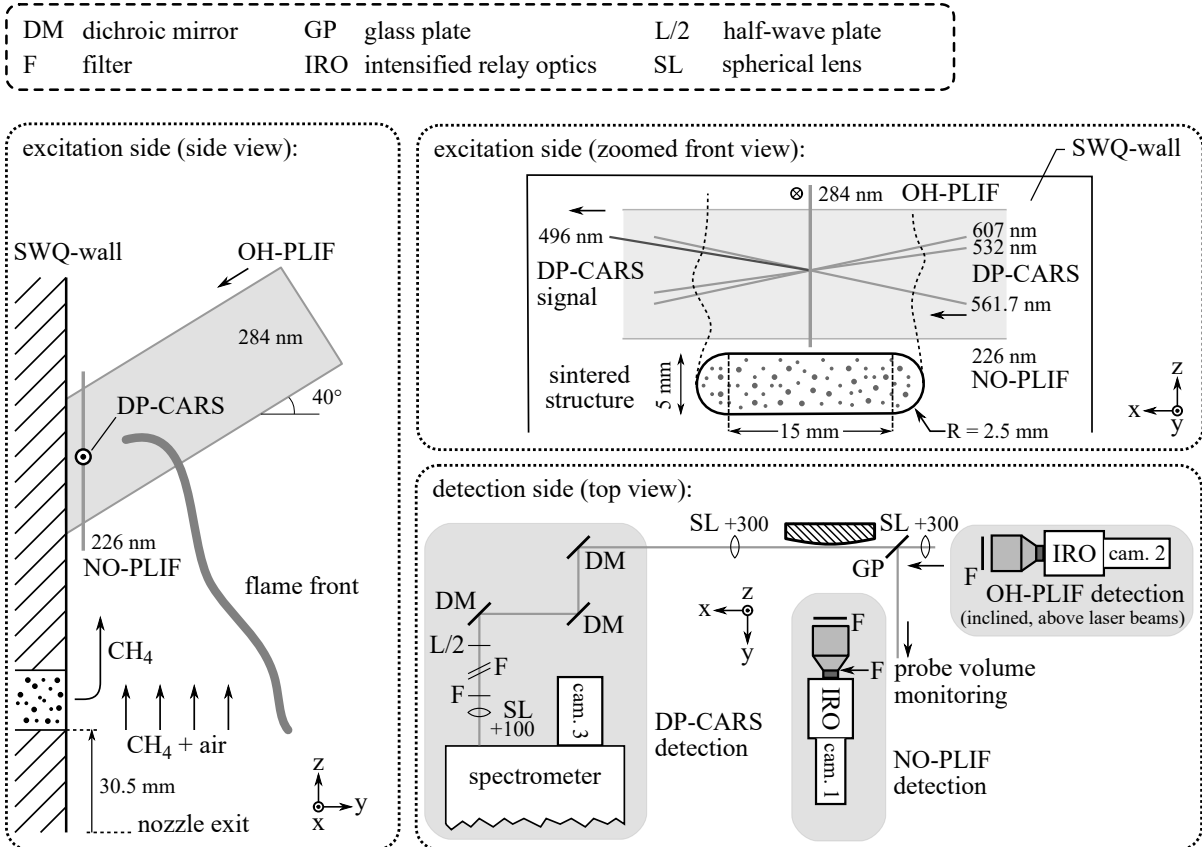
Figure 6.2: Laser diagnostic setup with the excitation and modified quenching wall configuration shown in a side as well as front view and the detection side in a top view. Numbers at spherical lenses denote focal length in millimeters.

side and front view in Figure 6.2. To locate the quenching point closer to the sintered structure, the flame stabilizing rod was placed at $z_{\mathrm{abs}} \approx 7$ mm above the nozzle exit (instead ≈ 16 mm in the usual operation). The surface of the sintered inlay closed flush with the surrounding stainless steel wall. It finally allowed a small amount of CH_4 fuel to seep out of the wall upstream of the quenching point and interact with the fully premixed main flow. This configuration was not meant to provide a *jet-in-crossflow* arrangement but impact the main flow with negligible flow momentum, i.e., no change in the local flow field but local chemistry. As will be evident from the below discussion, this ideal condition of negligible flow momentum however cannot be fulfilled. The setup mimicked for example FWI processes in internal combustion engines where remaining liquid fuel, e.g., originating from spray-wetting of piston or cylinder wall, evaporates to the premixed flow and makes FWI locally richer. As the application presented here was an initial feasibility study, it appeared most reasonable to keep the experimental boundary conditions as simple as possible. Thus, the burner's fully premixed main flow was operated with a stoichiometric CH_4/air mixture ($\Phi = 1.0$) at laminar inflow and the wall temperature stabilized to 60 °C in combustion operation. The secondary, additional CH_4 flow through the sintered structure was set to values of 0 ln/h (for a fully premixed reference), 2 ln/h, 3.5 ln/h and 4.5 ln/h (ln/h: norm liters per hour). Assuming a homogeneous outflow over the area of the sintered structure (≈ 95 mm^2), these flow rates correspond to uniform wall-normal velocities $U_{\mathrm{CH_4,w}}$ of ≈ 0.006 m/s, ≈ 0.011 m/s and ≈ 0.014 m/s, respectively. For the highest secondary CH_4 flow rate, the outflow velocity results to $U_{\mathrm{CH_4,w}} \approx 0.0056 \cdot U_{z,\infty}$, considering a streamwise main flow of $U_{z,\infty} \approx 2.5$ m/s far from the wall (see nozzle exit profiles in Figure 3.3). Despite these wall-normal outflow velocities intuitively appear negligible compared to the main flow, the numerical work of Stroh et al. [157] on drag-reduction control demonstrated that uniformly blowing fluid with $0.005 \cdot U_{\infty}$ out the wall significantly modifies the investigated, non-reacting turbulent boundary layer. They showed that this leads to a thickening of the boundary layer as well as drag reduction. Even though the conditions studied in this thesis are laminar and the flow is reacting, a similar impact is expected. Contrary to the original intention, the influence of the CH_4 trough the wall on the flow field cannot be neglected and could modify the near-wall boundary layer flow in the close downstream region. For diagnostic purpose, the secondary CH_4 flow was seeded with NO calibration gas (10000 ppm), serving as passive tracer for LIF. Furthermore, the fully premixed main flow was added a small amount of 150 ppm NO constant seeding for possible laser sheet correction purpose. Such an additional *background seeding* as reference was demonstrated in the work of Seitz et al. [147] for example. The use of NO tracer gas with LIF is a common procedure to detect mixing in combustion-related environments by laser diagnostics, as previously demonstrated in the works of Sadanandan et al. [141,143] or Johchi et al. [86] for example.

The DP-CARS setup, as described in section 5.2.1.1, was used to simultaneously probe gas phase temperature T and CO_2 mole fraction $X_{\mathrm{CO_2}}$. The data processing of DP-CARS equaled the procedure outlined in section 5.2.2.1, however, omitted the additional post-processing steps (thresholding and calibration) after spectral fitting for a first impression. Usually, these two post-processing aspects become only necessary at higher temperatures (see Figure 5.6 for reference). For assessing only wall-closest positions, as done in the following section, this approach is considered sufficient for a first insight.

For an assessment of the instantaneous flame front distribution and quenching point location, the OH-PLIF setup described in section 5.2.1.3 is applied. However, some minor differences were implemented, as pointed out below for completeness. The $Q_1(9)+Q_2(8)$ line pair of OH was excited around $\tilde{\nu} \approx 35210.42$ cm^{-1} (equals UV radiation at ≈ 284 nm). For detection, a 100 mm UV lens (Sodern, Cerco 2073, $f/2.8$) captured the emission prior to the IRO unit, while the CCD camera (LaVision GmbH, Imager E-Lite 1.4M) for image acquisition applied a 2×2 binning. One bin corresponded to about 80 μm in the physical space, resulting in a total FOV dimension of $(\Delta y, \Delta z) \approx (41$ mm, 57 mm). Detailed data processing was not applied for this feasibility study, as the following section only visualizes ensemble-averaged OH-PLIF raw images with average background subtraction for a first impression of partially premixed quenching topologies. It will get evident from Figure 6.3 in the next section that the near-wall OH signal behaves way different under partially premixed conditions and the actual quenching location is no longer as clear is in fully premixed operation. Thus, refined evaluation routines will be required in future.

For NO-PLIF, the same laser setup was used for excitation as previously applied for CO-LIF in section 5.2.1.2. Only the grating of the dye laser was moved so that instead of 230.1 nm (for CO-LIF), 226.26 nm radiation resulted after the frequency tripling (equals $\tilde{\nu} \approx 44197.55$ cm^{-1}). This wavelength excited the (0,0) vibrational band of NO in its $A^2\Sigma^+ - X^2\Pi$ electronic system (see section 2.3.2.3 for reference). High-reflective mirrors were replaced for this wavelength respectively. The UV-beam was formed to a light sheet by a combination of fused silica cylindrical lenses. It was first expanded and collimated along the vertical z-direction ($f = -50$ mm and $f = +200$ mm) and subsequently, the sheet thickness was focused in horizontal y-dimension ($f = +500$ mm) and deflected to the FOV. The light sheet finally featured ≈ 250 μm width ($1/e^2$-value, measured with beam monitor) and ≈ 8 mm height in the FOV. Pulse energies in the FOV were ≈ 2.5 mJ/pulse. The light sheet for NO-PLIF was overlapped with DP-CARS analogous to the previous CO-LIF (see section 5.2.1.2 for reference), i.e., placed between the incident DP-CARS beams by a small mirror and guided parallel to the quenching-wall along the x-axis. The resulting NO-PLIF signal was captured by a UV-lens (Sodern, Cerco 2073, 100 mm, $f/2.8$) equipped with a UG5 filter (4 mm thickness) in front. An additional high-pass filter around 227 nm was mounted between objective lens and intensified relay optic (IRO) to further reject laser radiation residuals prior to amplification. The signal was recorded by a combination of IRO (LaVision GmbH, low speed IRO, operated in linear regime) gated at ≈ 300 ns and a 2×2 hardware-binned CCD camera (LaVision GmbH, Imager E-Lite 1.4M) with 10 ms exposure time. The recorded FOV featured a physical area of $(\Delta x, \Delta z) \approx (44.4$ mm, 33.0 mm) with each bin on the camera corresponding to ≈ 63 μm in physical space. The following results section only visualizes averaged NO-PLIF raw images after background subtraction for a first impression. A detailed processing to derive mixture fractions or local equivalence ratios from NO-PLIF is yet to be developed in future and an outlook of this thesis.

Temporal synchronization and spatial matching of the individual laser diagnostics was done in an equal manner as in the fully premixed thermochemistry campaign presented previously (see section 5.2.1.6 for reference). The NO-PLIF laser sheet only replaced the laser beam for CO-LIF in the described procedures.

6.3 Results and Discussion

Since this chapter covers a feasibility study, only limited insight into early results is presented in the following and for OP5 in Table 3.1 only (CH_4/air, $\Phi = 1.0$, laminar, $T_{wall}^{(nom)} = 60\ °C$). First, ensemble-averaged signals of both OH- and NO-PLIF are briefly discussed for the four secondary CH_4 flow rates through the sintered structure, as introduced above. Subsequently, the corresponding near-wall (CO_2,T)-thermochemistry at $y = 100\ \mu$m and $y = 300\ \mu$m nominal wall distance is evaluated.

Figure 6.3 outlines ensemble-averaged raw signals of OH-PLIF (top row) and NO-PLIF (bottom row). Each column presents one secondary CH_4 flow rate through the sintered structure embedded in the quenching wall, indicated at the column's top. To facilitate relative comparison between the shown cases, images are presented with respect to absolute streamwise coordinate z_{abs} from the nozzle exit. The thermochemistry probe volume (i.e., DP-CARS) is shown as red hollow circle, while the dimension of the NO-PLIF laser sheet is indicated by a dotted red line. Please note that both diagnostic locations are shown for orientation purpose only, at the specific configuration demonstrated in Figure 6.3. As
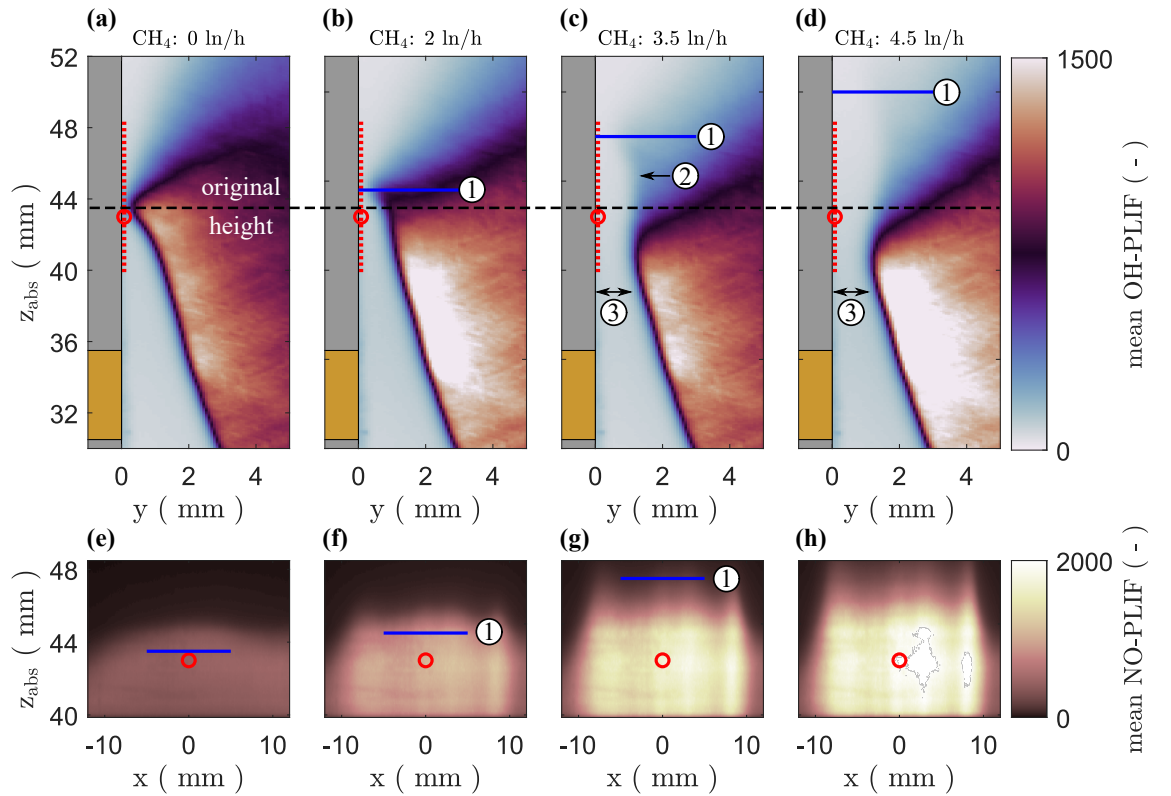
Figure 6.3: Ensemble-averaged raw signals of OH-PLIF (top row) and NO-PLIF (bottom row) for local partial premixing at the quenching event. Each column presents one secondary CH_4 flow rate, indicated at the column's top. Red hollow circles: thermochemistry probe volume; dotted red line: NO-PLIF laser sheet; blue solid line: estimated quenching height; bronze-colored rectangle: sinter structure; gray rectangle: quenching wall. Samples: 400.

previously presented for the fully premixed thermochemistry in section 5.2.1.5, the burner was traversed in a comparable manner to scan thermochemical states at different wall-distances y and streamwise z-positions. The OH-PLIF images depict the position of the sintered structure that seeds additional CH_4 to the main flow as bronze-colored rectangle in the quenching wall (gray). Figure 6.3(a) first presents the fully premixed reference case without secondary CH_4 seeding that develops a typical SWQ quenching topology, e.g., as previously shown for lean DME/air combustion in Figure 4.12. The *original quenching height* of this fully premixed topology is indicated as horizontal black dashed line and serves for relative comparison in the further partially-premixed cases. In the corresponding Figure 6.3(e) a weak NO-PLIF signal is observed that reflects the 150 ppm constant NO-seeding of the main flow. For a secondary CH_4 flow of 2 ln/h, shown in Figure 6.3(b), the *novel* quenching point is evidently shifted downstream by ≈ 1 mm (see feature ①) and slightly pushed from the wall. No major change in the flame structure is apparent but the region surrounding the quenching point appears slightly stretched in an S-shape. The corresponding NO-PLIF signal in Figure 6.3(f) increases. Further increasing the secondary flow to 3.5 ln/h leads to an intensification of the effects, as shown by Figure 6.3(c). The flame structure near the quenching point evidently changes and features a more pronounced S-shape (see feature ②). The original reaction zone is shifted from the quenching wall by approximately 1 mm (see feature ③), while the apparent quenching location moves far downstream (by ≈ 4 mm compared to the fully premixed reference case, see feature ①). At this operation condition, the local lifting of the flame was visually observable by eye with its local chemiluminescence becoming a turquoise color while performing the experiment. As shown in the work of Kojima et al. [93], C_2^* bands become pronounced in the chemiluminescence of a premixed laminar CH_4/air flame at atmospheric pressure when increasing the equivalence ratio beyond stoichiometry, like the $C_2^*(0,0)$ transition around 515 nm, which is in the visible green. This could explain the observed locally turquoise color during experiments and emphasizes that the local equivalence ratio in the quenching zone was apparently getting richer. Finally, for 4.5 ln/h secondary CH_4 in Figure 6.3(d), a gap of ≈ 1 mm remains between the original reaction zone and wall (see feature ③), while a clear quenching point is no longer observed but could be assumed further downstream (see feature ①). Possibly, the local mixture near the quenching point is too rich to ignite under these partially premixed conditions. This could be further assessed in future by quantification of the NO-LIF in terms of local equivalence ratio.

The major finding from these ensemble-averaged OH-PLIF images is that the near-wall reaction zone is increasingly pushed from the quenching wall when increasing the local fuel quantity (i.e., equivalence ratio), while the local flame structure changes in an S-shape with the quenching point shifted downstream. As the near-wall flame structure derived from OH signal evidently changes during partially premixed operation, refined processing is required in future to reliably detect the *novel quenching point*, which is depicted by ① in Figure 6.3. In this context, it has to be evaluated, if a novel definition of the quenching point is needed. Very recently, a complementary simulation of Steinhausen et al. [E4] confirmed the observed behavior in flame structure when increasing the CH_4 flow rate through the wall. They further pointed out that the classical definition of the quenching point on gradients from OH-PLIF signal is no longer feasible, while a definition using the maximum heat flux at the quenching wall appeared more reliable. From the NO-PLIF

recordings in Figures 6.3(e)-(h), it can only be seen that the amount of secondary fuel, marked by NO-tracer gas, apparently increases. Furthermore, the impact of the quenching flame is evident at top of the individual FOVs, where NO-PLIF signal drops due to the rise in temperature by nearby reaction. The estimated *novel* quenching height, where the flame is expected closest to the wall, is shown as blue horizontal line for reference (see feature ①). Further interpretation would require a processing to derive local equivalence ratios, to be done in the future.

Figure 6.4 provides a corresponding insight into the near-wall thermochemistry for the four different secondary fuel flow rates by showing the instantaneous scatter over a broad range in streamwise z-direction (individual ranges span between $z_{abs} \in [41\,\text{mm}, 45\,\text{mm}]$ for 0 ln/h and $z_{abs} \in [39\,\text{mm}, 50\,\text{mm}]$ for 4.5 ln/h; scanned with 0.5 mm increments in z-direction). The shown thermochemistry results were not yet coupled with the instantaneous OH-PLIF recordings, e.g., to perform a quenching-point conditioning like demonstrated previously. This is due to the new challenges posed to detect the quenching point under partially premixed operation, as described above. Nevertheless, to show some insights into the z-dependent evolution, instantaneous samples are color-coded on the absolute heights of the original quenching point (green scatter, one measurement height at $z_{abs} = 43.5$ mm, see black dashed line in Figure 6.3) as well as their suggested novel quenching height (orange
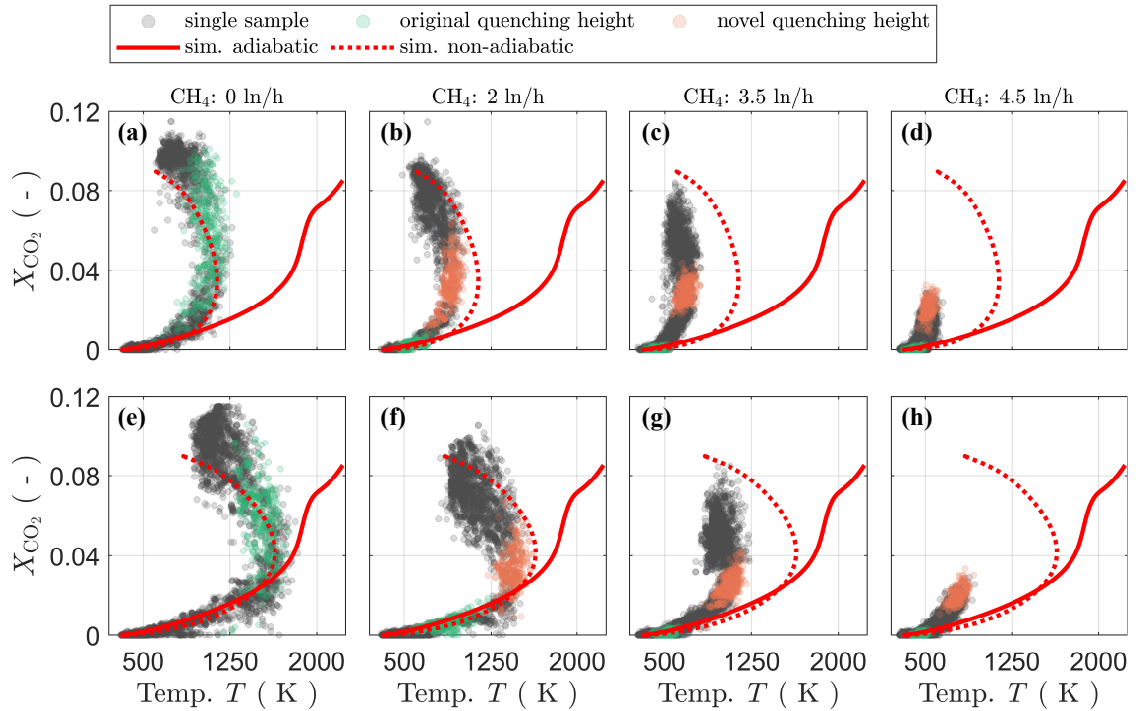
Figure 6.4: Instantaneous scatter of (CO_2,T) thermochemistry for $y = 150\,\mu$m (top row) and $y = 350\,\mu$m wall distance (bottom row) for local partial premixing at the quenching event. Each column presents one secondary CH_4 flow rate, indicated at the column's top. Colored scatter: sampled at one measurement height representing the original quenching height (green, at black dashed line in Figure 6.3) and novel quenching height (orange, at blue solid line in Figure 6.3). Samples: 4268 to 9372 (depending on case).

159

scatter, one measurement height for each flow rate respectively, 2 ln/h: $z_{abs} = 44.5$ mm, 3.5 ln/h: $z_{abs} = 47.5$ mm, 4.5 ln/h: $z_{abs} = 50.0$ mm; see blue solid lines in Figure 6.3). All other probes are shown as gray scatter. In Figure 6.4 corresponding adiabatic and non-adiabatic numerical simulation[16] for fully premixed, laminar CH_4/air combustion is provided for comparison. As previously done in section 5.3.1.2, the wall-closest, fully premixed (CO_2,T) scatter in Figure 6.4(a) is evaluated against the corresponding near-wall, non-adiabatic numerical simulation, yielding that the simulation trace at $y = 150$ μm best fits the experiment (procedure not shown here). The nominal wall distances from the performed measurements are thus expected to feature an offset of ≈ 50 μm, which is added to the values in the following. From the reference case without secondary CH_4 seeding in Figure 6.4(a) it is first evident that the (CO_2,T) state space possesses a clear trend and well-follows the numerical simulation. Only near the equilibrium, experimental values of X_{CO_2} are slightly higher than the numerical ones. Potentially, an additional calibration of CO_2 mole fractions could resolve this issue. Samples at the original quenching height (green scatter) cover a broad range of thermochemical states along the non-adiabatic simulation trace, as expected for a quenching event. When imposing a secondary CH_4 flow rate of 2 ln/h, shown in Figure 6.4(b), three major observations are apparent compared to the fully premixed reference case. First, overall gas phase temperatures T decrease by a few hundred Kelvin. Second, measured peak values of X_{CO_2} drop. Third, samples on the original quenching height (green scatter) reflect the fully premixed adiabatic behavior of an early reaction stage, while the suggested novel quenching height (orange scatter) deviates towards higher CO_2 concentrations. At this point it is emphasized that the fully premixed computations do only serve for orientation here and cannot be compared to the partially premixed experimental data, as the local equivalence ratio impact is missing. The observed trends continue for a secondary flow rate increased to 3.5 ln/h in Figure 6.4(c). For 4.5 ln/h in Figure 6.4(d) the expected reaction progress is strongly inhibited and mole fractions do not exceed $X_{CO_2} = 0.03$. This fits to the above finding from OH-PLIF recordings at this flow rate, where no clear quenching point was apparent, most likely due to a near-wall mixture that is too rich. The observed trends made in Figures 6.4(a)-(d) for $y = 150$ μm are equally reproduced in Figures 6.4(e)-(h) for the wall distance $y = 350$ μm and are not discussed in more detail for this reason. The above observations appear physical and may be explained by the following aspects. Near-wall temperatures are decreased for increased CH_4 secondary seeding as (1) the flame is pushed from the quenching wall and (2) unburnt, cold CH_4 remains in the near-wall area that dilutes reaction intermediates and products. The latter point could also be the reason for the decreased peak mole fraction values of CO_2. The findings suggest that near-wall partially premixing minimizes the wall heat flux, as temperatures close to the wall drop significantly.

---

[16]All numerical simulations in the FWI context presented in this chapter 6 were performed and provided by M.Sc. M.Sc. Matthias Steinhausen and M.Sc. Yujuan Luo from Technical University of Darmstadt (STFS) and were used in this thesis with permission. Their kind contribution is acknowledged here. Please note that performing detailed numerical combustion simulations is a separate research field and would have been beyond the scope of the work presented. Information on the general setup for this SWQ simulation (solver, grid and numerics) can be found elsewhere [E5].

Overall, this first feasibility study on partially-premixed FWI provided some very interesting and valuable insights on the one hand. On the other hand, it yielded many open issues to be addressed in future FWI research. Initially, a quantification of the NO-PLIF signal in terms of local equivalence ratios is to be aimed for, which is possible in the unburnt region with the recorded data where no temperature impact on the LIF-signal exists. This would enable the correlation of local near-wall mixture pre-history with instantaneous thermochemistry. Furthermore, a novel classification of the partially premixed quenching topologies from OH-PLIF recordings is conceivable. Under these partially premixed conditions, a re-evaluation of the impact of non-adiabaticity on near-wall thermochemistry appears necessary. As the reaction zone is pushed from the quenching wall, there is possibly no real near-wall reaction in a classical SWQ-sense but maybe novel thermochemistry evolution around 1 mm from the wall. In this context, it should be evaluated whether the decreasing wall heat flux by local near-wall fuel enrichment could be employed for some technical applications.

Chapter 7

Conclusion and Outlook

Finally, the scientific contents achieved in this thesis are summarized in a conclusion. An outlook of potential future experimental studies following this work is given subsequently.

7.1 Conclusion

Three comprehensive experimental campaigns on atmospheric side-wall quenching (SWQ) were presented in this thesis. The SWQ phenomenon was studied by means of various advanced laser diagnostics, which were applied simultaneously within each campaign. Initially, the flame and flow dynamics during SWQ were evaluated in detail (chapter 4), followed by a thorough analysis of the near-wall thermochemistry (chapter 5). These two campaigns considered fully premixed laminar and turbulent dimethyl ether (DME)/air flames at $\Phi = 0.83$ and $T_{\mathrm{wall}}^{(\mathrm{nom})} = 60$ °C. A final feasibility study on partially premixed SWQ was then demonstrated for laminar, stoichiometric CH_4 fuel (chapter 6). With regard to the open scientific questions in FWI research, outlined in section 1.1, this work provides a valuable contribution with novel findings on FWI that extended beyond the state of research. Furthermore, the acquired measurement results provide outstanding validation data for numerical FWI simulation. Concrete results and conclusions from the three measurement campaigns are summarized below.

Flame and Flow Dynamics In the first campaign on near-wall flame and flow dynamics, two-dimensional fields of flow velocity (by particle image velocimetry (PIV), two-components) and flame front distribution (by laser-induced fluorescence (LIF) of OH) were simultaneously measured. Initially, it became evident that turbulent operation of the SWQ burner leads to alternating SWQ- ($\approx 43.4\%$ of samples) and head-on quenching (HOQ)-like topologies ($\approx 56.6\%$) with approximately the same probability of occurrence. From that point, all data was conditioned on the instantaneous quenching onset and classified with respect to the quenching topology (SWQ-like or HOQ-like). This was done thoroughly throughout the thesis and enabled robust statistical analysis, preserving spatial features relative to quenching, as well as a statistical linking to the thermochemistry campaign. Accordingly, various flow metrics were assessed to further investigate the near-wall transport behavior governing these two distinguished turbulent quenching topologies.

First, turbulent boundary layers were accessed down to their viscous sublayer to at least $y^+ = 1.5$ by the highly-resolved PIV. During reaction, the inner structure of turbulent boundary layers remained nearly unaffected by combustion in the pre-quenching area, but thickened with evolution in streamwise z-direction over the quenching onset. This was appointed to the changing near-wall viscosity. Up to $y^+ = 5$, the viscous sublayer remained unaffected by the quenching events. For $y^+ > 5$ the normalized streamwise velocity profiles (u_z^+) underrated the log law values. This tendency increased when approaching the quenching onset in streamwise direction and partially recovered downstream. It was attributed to a complex interplay between thermal expansion, change of viscosity and wall-normal velocity gradient. The local gas temperature, driven by the heat release of reaction, was identified as the key parameter. Overall, it is concluded that the common scaling laws of turbulent boundary layers for non-reacting conditions are no longer valid during flame quenching. This investigation partially aided the unresolved issue to explore the structure of fluid boundary layers during FWI, as stated by Dreizler and Böhm [49] as open scientific question (see section 1.1).

An analysis of integral length scales revealed that wall-normal scales (L_{yy}) rise faster in HOQ- than SWQ-like cases with increasing wall distance. This suggested bigger, energy containing near-wall structures in the HOQ-like topology, which could imply increased instantaneous mixing and more intense wall-normal convective transport than in SWQ-like cases. Within the quenching area, combustion regimes of SWQ-like events are in the wrinkled flamelets regime, while HOQ-like cases are predominantly located in the corrugated flamelets. Despite both cases were very close to each other, this suggested that HOQ-like events are associated with higher level of turbulence interacting with the local quenching reaction, again implying potentially higher transport and reaction rates.

A simplified, two-dimensional projection of turbulence anisotropy yielded that the SWQ-like case is rather anisotropic with respect to the projection in the post-quenching zone, while HOQ-like topologies featured isotropic behavior in the projection directly behind the flame front (along with more intense velocity fluctuations). This could suggest elongated eddies in the HOQ-like case.

Near-wall vortex structures were assessed by using a simplified two-dimensional Q-criterion. Evidently, rather elongated structures in z-direction prevailed at high probability within the undisturbed boundary layer in the pre-quenching areas. The SWQ-like case featured high vortex probability directly downstream the quenching point that could promote near-wall exhaust gas recirculation (EGR). In the HOQ-like topology high probability was observed close to the wall-parallel reaction zone in the burnt gas, presumably pushing the reaction to the wall. During reaction, nearly all vortices turned counterclockwise ($> 99\%$). It is concluded that the significantly different local presence of vortices is crucial for the actual quenching topology.

A final consideration of a transient evolving from an HOQ- to SWQ-like event confirmed the view on major vortex structures proposed from vortex probabilities. An evaluation of instantaneous relative fluid movement suggested relative near-wall transport of fluid upstream the quenching event, possibly causing near-wall EGR.

Thermochemistry The second campaign on near-wall thermochemistry quantified the gas phase temperature T and CO_2 mole fractions X_{CO_2} (both by dual-pump coherent anti-Stokes Raman spectroscopy (DP-CARS)) as well as CO mole fractions X_{CO} (by CO-LIF) at a time. This was done along with the instantaneous flame front position (by OH-PLIF). All diagnostics were applied simultaneously and spatially correlated. The comprehensive application of DP-CARS, CO- and OH-LIF was the first application of these combined diagnostics in an SWQ environment.

An initial validation of the novel combination of laser diagnostics against results from adiabatic and non-adiabatic numerical simulation yielded good accuracy and precision of the quantitative three-parameter thermochemistry diagnostics for SWQ application. A comparison of the wall-closest experimental data to the corresponding non-adiabatic simulation in state space showed a small offset of only 20 μm, suggesting that they match very well. The wall-closest experimental thermochemistry probe volume thus resulted 120 μm above the wall surface. Comparisons in physical space confirmed the experimental results as outstanding validation data.

Subsequently, the near-wall (CO_2,CO,T) three-parameter thermochemistry was discussed for laminar inflow conditions. The novel approach enabled highly sensitive probing of the near-wall thermochemical states and appeared superior to the previously applied two-scalar quantification using (CO,T). Conditioning of experimental near-wall thermochemistry data to the instantaneous quenching height from OH-PLIF in $\Delta z = 100$ μm increments in physical space enabled revealing tracing of the reaction evolution across quenching. This *quenching-point conditioning* suggested more robust insights as conditioning in state space and is recommendable for future FWI studies. X_{CO_2} proved less affected by the wall than X_{CO} and was thus considered a more robust component to define reaction progress variables in near-wall quenching environments. Especially, the (CO,CO_2) state space featured minimal impact of non-adiabaticity. The importance of differential diffusion effects in near-wall DME/air combustion for numerical FWI simulation was experimentally proven. This was achieved by comparing the experiment to provided two-dimensional, non-adiabatic simulations using unity Lewis number assumption and a mixture-averaged transport model. The latter simulation matched very well to the experimental results. In the early reaction progress, (CO_2,T) states were much more sensitive to the influence of differential diffusion effects than (CO,T) correlations. In turn, the (CO,T) states yielded such influences closer to the reaction end at higher temperatures and increased wall distances. These experiments contributed to the major task on specific multi-parameter thermochemistry measurements in future FWI studies formulated by Dreizler and Böhm [49] (see section 1.1).

Finally, the impact of turbulent inflow conditions was analyzed in a corresponding way, separately for the SWQ- ($\approx$ 50% of samples) and HOQ-like quenching topology cases ($\approx$ 50%). Evidently, near-wall thermochemical states under turbulent conditions were different to laminar ones and populated novel regions in the state spaces, suggesting the presence of novel transport mechanisms. State spaces furthermore significantly depended on whether an SWQ- or HOQ-like scenario was present. In SWQ-like cases, three prominent thermochemistry scenarios were identified from the near-wall (CO_2,T) correlations. As these zones were not clearly distinguishable in the other state spaces, it emphasized the

importance of additionally measured X_{CO_2}. The most prominent scenario was characterized by pronounced mixing of hot exhaust gas with cold unburnt reactants, superimposed with increased wall heat losses. Linking these findings with the previously presented results on flame and flow dynamics suggested that the observed processes are most likely caused by EGR forced by the momentum of counterclockwise vortices close to the quenching point. Similarly, two scenarios were identified for HOQ-like cases. One scenario was equally appointed to EGR as above, the other was attributed to the sudden extinguishing of reaction intermediates by the instantaneous HOQ-event, superimposed by mixing products from the exhaust driven to the wall by a big vortex structure. Overall, the findings strongly suggested that large, energy-containing vortex structures play a major role in the reaction-transport-coupling of turbulent near-wall FWI. Finally, a statistical evaluation revealed that the three-parameter thermochemistry in the (CO_2, CO, T) state space is different between SWQ- and HOQ-like quenching scenarios with statistical significance. In conclusion, near-wall thermochemistry is significantly different for turbulent conditions than for laminar ones. This should be considered for modeling in numerical simulation. This investigation partially aided the unresolved issue to clarify if chemistry-turbulence interaction claims for refined combustion models, as stated by Dreizler and Böhm [49] as open scientific question (see section 1.1).

Overall, it can be concluded that additionally measuring CO_2 mole fractions for near-wall thermochemistry evaluation aids significantly to identify and discuss FWI-related phenomena. An evaluation of near-wall CO_2 mole fractions is recommended for future FWI studies.

Partial Premixing   The third feasibility campaign on partially premixed SWQ simultaneously quantified the (CO_2, T) thermochemistry (by DP-CARS), along with flame front position (by OH-PLIF) and mixing field of additional CH_4 fuel seeded out the quenching wall (by NO-PLIF). For increasing the local near-wall CH_4 quantity (i.e., equivalence ratio) the reaction zone was increasingly pushed from the quenching wall, while the local flame structure changed in an S-shape and the quenching point shifted downstream. In the near-wall thermochemistry, temperatures as well as mole fraction values of CO_2 were significantly decreased for increased CH_4 secondary fuel seeding. The findings suggested that near-wall partially premixing minimizes the wall heat flux. The NO-PLIF was not yet quantified in terms of local equivalence ratios. It is concluded that both the near-wall flame structure and thermochemistry significantly change under partially premixed conditions.

7.2 Outlook

Even though there have already been intensive research efforts in the field of experimental FWI, there are still many open issues that should be addresses in future. Mainly the following points are considered relevant: (1) further refined simultaneous multi-parameter measurements; (2) further assessment of the three-dimensional nature of turbulent FWI.

This section draws a brief outlook on possible future research projects that could be carried out following the presented dissertation.

As evident from the presented thesis, the extension of the previously used (CO,T) state space by CO_2 mole fractions as additional parameter yielded fruitful and novel insights. It is therefore obvious to measure even more chemical species quantitatively and simultaneously in future FWI studies. One promising way to realize this is via the DP-CARS approach implemented here. It has been demonstrated in the past that DP-CARS is capable to simultaneously probe three species in combustion processes, like for example N_2/O_2/CO [18], N_2/O_2/H_2 [119] or N_2/H_2/CO [166], by well-chosen adjustment of the used wavelength. Furthermore, DP-CARS can be emerged to a so-called WIDECARS approach that has been reported capable to simultaneously measure gas temperature and most major species concentrations in combustion environments (N_2, O_2, H_2, CO, CO_2, C_2H_4) [159]. Such a WIDECARS implementation would require a broadband Stokes laser with increased spectral width of $\approx$ 18 nm FWHM [159]. As given in section 5.2.1.1, the Stokes laser used here featured around 8 nm FWHM. With respect to the DP-CARS approach used in this thesis, which probes N_2 and CO_2, it appears further beneficial to access O_2 as third species, as potential Raman-active transitions exist only $\approx$ 180 cm^{-1} from the ones probed in CO_2 (see outlines on DP-CARS in section 2.3.2.2 for reference). To evaluate the reaction progress, this is considered extremely beneficial, as it would cover both a reactant (O_2) and product (CO_2).

Another possibility to further enhance simultaneous chemical species detection is by application of a spontaneous Raman scattering setup, like presented for one-dimensional measurements across the reaction zone in counterflow-stabilized flames by Trabold et al. [161] for example. Barlow et al. [13] tested a spontaneous Raman scattering setup close to heated surfaces (foil samples) exposed to combustion products ($\approx$ 150 μm resolution in wall-normal direction). However, spontaneous Raman scattering measurements were impeded in their investigation by too strong black-body radiation of the surface at higher heating temperatures. A feasibility study on qualitative Raman imaging of gaseous H_2O
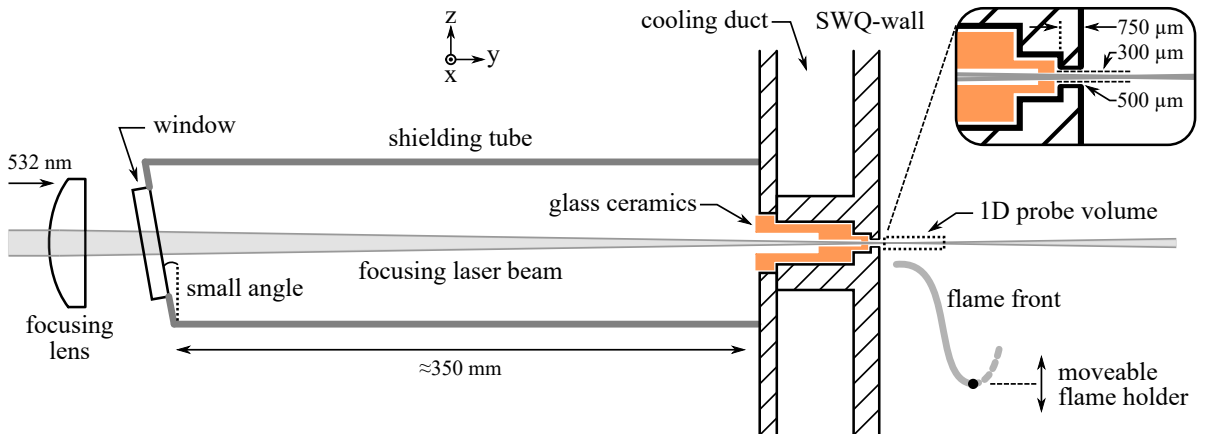

Figure 7.1: Schematic of a possible experimental arrangement to realize one-dimensional near-wall measurements by spontaneous Raman scattering.

during SWQ was demonstrated previously in the thesis of Kosaka [94, p. 129 ff.]. In his study, the wall-closest probe volume location was estimated to $120 - 240$ μm, but had to be increased by another 50 μm safety distance to avoid laser-wall interaction. In both studies [13, 94], the exciting laser beam passed wall-tangential (corresponds the x-axis in this thesis). Such orientation of the Raman probe volume would yield scalar values with respect to the yz-plane, like in the DP-CARS or CO-LIF measurements presented here. However, it would be desirable to acquire one-dimensional surface-normal information, as for example recently shown by Barlow and Harmon [12] in the gas phase above a liquid surface (≈ 28 μm surface-normal data spacing). A prototype for a refined approach that would facilitate one-dimensional, wall-normal multiple-species measurements above the solid wall surface is shown in Figure 7.1[17]. The laser beam to excite spontaneous Raman scattering is guided from the backside of the wall and focuses on a small passage in the wall (≈ 500 μm diameter), through the cooling duct. The passage is lined with an axially symmetric customized glass ceramics (Macor® machinable glass ceramics, manufactured from rod with 10 mm diameter, orange area in Figure 7.1, inner diameter step-wise tapered down to ≈ 300 μm at the exit). The ceramics is meant to act as a beam dump, which absorbs impacting radiation in its volume. This causes diffuse scattering, which appears monochromatic and can most likely be suppressed by suited filters, but avoids direct contact of the high energy laser pulses to the stainless steel wall leading to optical breakdown, i.e., bright visible spark formation (spectrally broadband emission). A closed hollow body (shielding tube Figure 7.1) is mounted at the laser entrance at the backside of the wall to prevent mass transport out/into the wall through the small passage. The laser is first focused and enters the hollow body by an inclined window (small angle to avoid parallel reflections). This concept is based on the beam guiding through the opposed jet burner configuration shown in Trabold et al. [161] for spontaneous Raman scattering measurements. The focused beam finally exits the quenching wall and enters the FOV in a wall-normal, one-dimensional probe volume that can be imaged by a customized Raman spectrometer, like the one presented by Trabold et al. [161]. As the wall must not move in this approach, the burner cannot be traversed anymore and its position is inherently fixed to the laser diagnostics. To compensate this, the flame holder rod was designed movable to access different streamwise z-positions of the FWI phenomenon using a piezo-electric driven linear stage (Thorlabs Inc., PD1/M) as actuator. A prototype, as shown by Figure 7.1, has been designed and manufactured during this thesis. However, it has not yet been applied for one-dimensional spontaneous Raman scattering measurements during FWI due to limited experimental capacity in the laboratory. As it appears very promising, this prototype should be tested in future.

To further assess the three-dimensional nature of turbulent FWI experimentally, an application of *cross-sheet* diagnostics appears promising. Besides the typically accessed yz-plane, it became evident that further transport processes in the out-of-plane x-direction could be present but are not captured. Thus, simultaneously assessing the yz-plane along with either the xy- or xz-plane could lead to further novel insights. This would be most applicable for OH-PLIF, but could be realized for PIV as well.

---

[17]The idea to use glass ceramics for the wall passage of the laser beam for spontaneous Raman scattering originates from Dr. Robert Barlow. The fruitful discussions, advice and support is acknowledged here.

The potential near-wall transport scenarios proposed in the turbulent three-parameter thermochemistry in chapter 5 could be utilized to derive new insights for modeling in numerical simulation, e.g., adapted chemistry tabulation to cover the impact of near-wall EGR-phenomena. Indeed, this was addressed very recently in the numerical study of Steinhausen et al. [154].

As the focus of this thesis was on DME fuel and turbulent operation, it would be desirable to evaluate the additionally measured data on parameter variation (fuel, equivalence ratio and wall temperature) in the three-parameter thermochemistry campaign (see Table 3.1). This could eventually yield further novel insights by the additionally available CO_2 mole fraction.

Furthermore, the recorded data on partially premixed thermochemistry, as presented in terms of a feasibility study in chapter 6, should be evaluated in more detail. Especially, the NO-PLIF should be quantified in terms of mixture fraction or local equivalence ratios and then correlated with the instantaneous thermochemical state. Studies on partially premixed operation could also be expanded to a turbulent case in future.

Appendix A

Technical Supplement

This appendix chapter provides a technical supplement summarizing some good-practice engineering solutions that were realized within this thesis and significantly aided in reaching the scientific aims. This information is beyond the scientific scope of the presented work, but considered quite helpful for experimental researchers within the community of laser diagnostics in combustion, dealing with similar topics.

A.1 Vibrational Bed Seeder

To perform velocity measurements by PIV in this thesis, a special *vibrational bed seeder* was designed and built to disperse the required solid particle seeding to the studied flow. A schematic of the device is shown in Figure A.1. It consisted of a cylindrical stainless steel vessel (150 mm inner diameter, 275 mm height) that could be closed by flange-

Figure A.1: Sketch of the vibrational bed seeder.

mounting lids on top and bottom. The top lid contained the outflow, while the bottom lid consisted of a 0.5 mm thick stainless steel membrane (i.e., thin sheet) that was flange-mounted to the vessel. The membrane could be forced to oscillations by a pneumatic vibrator (Netter Vibrator, NTS 180 NF; driven with ≈ 2 bar system pressure) that was mounted freely suspended to the membrane (not shown in Figure A.1). All corresponding passages were provided with flat seals. The inflow was reduced to a cross-section with 4 mm diameter and side-fed to the vessel (≈ 20 mm above the membrane; recommended above the seeding bulk). Dry air was used as inflow medium. The seeder device provided suitable, homogeneous seeding conditions in the flow range $0.2 - 11$ m^3/h (probably also higher rates possible) for both Al$_2$O$_3$ (MSE Supplies LLC, nominal diameter 300 nm) and tungsten carbide particles (A.L.M.T. Corp., tungsten carbide powder WC02N, ≈ 100 nm grain size). The ground plate was mounted to a rack, which in turn was placed on a rubber mat for damping on the floor of the lab (not shown in Figure A.1). Prior to operation, approximately 100 g of seeding bulk material was placed on the membrane. It was filled to the seeder from top, after it was vacuum-dried for at least 24 h to reduce humidity in the powder and thus avoid particle agglomeration. During operation, the vibration caused seeding to disperse from the bulk powder to the above gas phase, where it was entrained by the entering flow. The vibrator was only run for a short time duration of $10-20$ s prior to each data acquisition and switched off several seconds before recording, to avoid bias of the membrane oscillation to the flow during measurements (e.g., additional intermittency). In case seeding was not required but the flows were needed to maintain during steady state operation, the device could be circumvent by a bypass line from in- to outflow (not shown in Figure A.1, but similar to Fig. 2.14 in [133, p. 27]). It is recommended to bypass the seeder most of the operation time and only switch the inflow to the seeder vessel for the short data acquisition period (directly after vibration was turned off until the end of data recording). This saves seeding powder, minimizes potential hazard and furthermore showed to yield best seeding results in the recorded data. Several potential incidents can occur in this device during operation, like leakage or a bursting membrane due to excessive pressure. Besides handling with care, a user who wants to replicate and operate such a device needs to take additional dust hazard prevention in any case, like wearing suited respiratory protection.

A.2 Movable DP-CARS Unit

For dual-pump CARS (DP-CARS) measurements in this thesis, all required lasers and optics for excitation were arranged on a movable, two-level lab-table unit. This was done to (1) optimize the use of space and (2) easily facilitate the use of this DP-CARS system on other test rigs at RSM institute. A sketch of the designed and built device is shown in Figure A.2. The entire unit featured a dimension of ≈ 2 m length, ≈ 1.1 m width and ≈ 1 m height. As shown in Figure A.2(a), the lower level was provided with heavy-duty rollers (for moving to other test rigs) and screwable feet (for fixing it in place at a certain test rig). The lower level contained the Nd:YAG pump lasers (one Spectra-Physics PIV 400, custom-modified: PIV-overlap removed and individual Nd:YAG cavities split with independent second harmonic generation stages; resulting in two independent
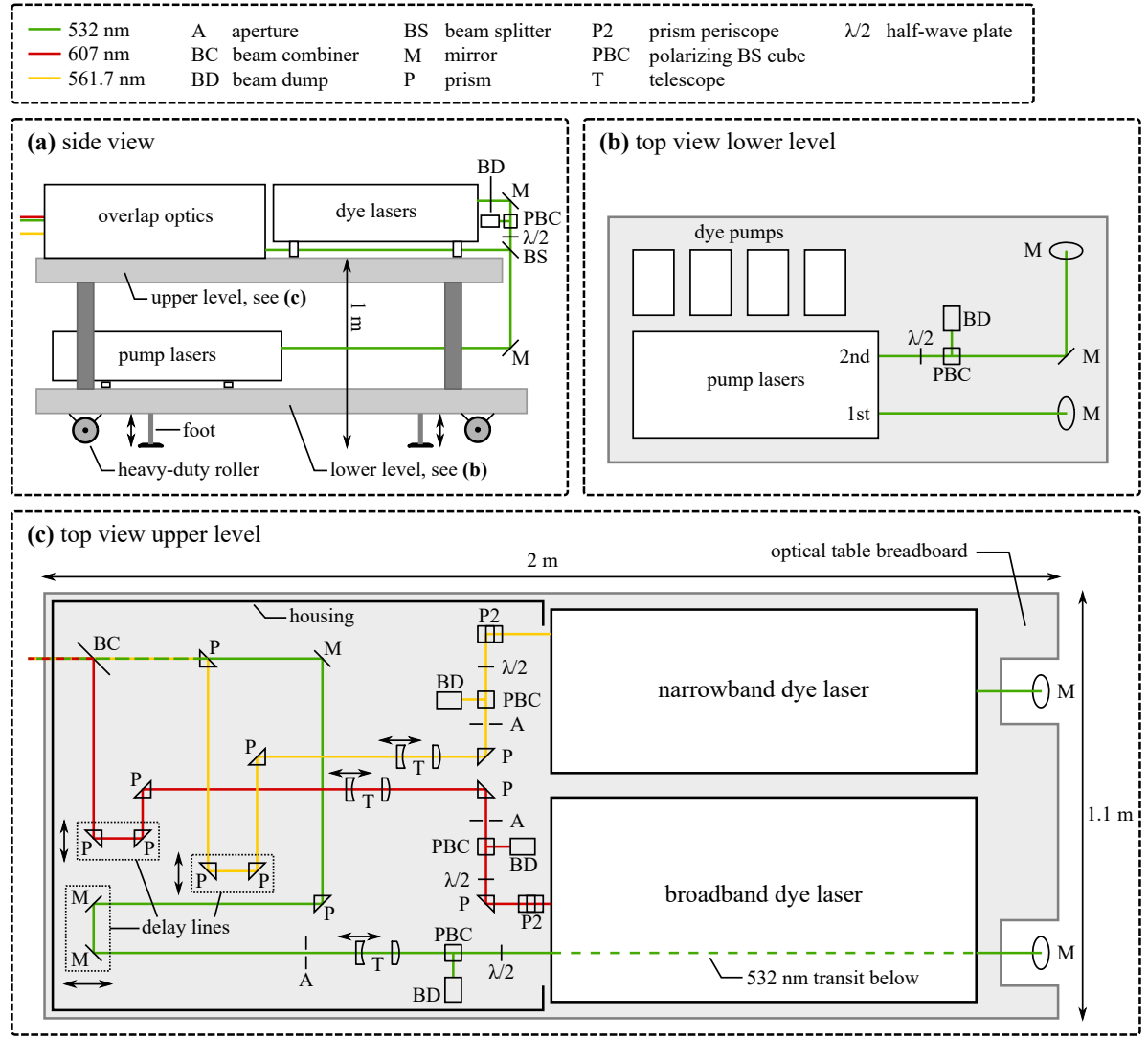
Figure A.2: Sketch of the movable DP-CARS unit: (a) side view, (b) top view of lower level and (c) top view of upper level.

532 nm lasers) as well as the dye pumps (in total four; two for each dye laser). This is depicted in Figures A.2(a) and (b). The two individual pump laser beams at 532 nm were energy-controlled by combinations of half-wave plates and polarizing beam splitter cubes and guided to the upper level by periscopes of high reflective mirrors. As shown in detail by Figure A.2(c), the upper level contained the two dye lasers and further optics for beam conditioning and overlap. The first 532 nm beam was split when reaching the upper level, as depicted in Figure A.2(a). The reflected beam was directly guided to the overlap optics and served as 532 nm pump radiation for the DP-CARS process. The transmitted beam optically pumped the broadband Stokes laser (centered around 607 nm). The second 532 nm beam optically pumped the narrowband dye laser (around 561.7 nm). More details on the dye laser's specifications can be found in section 5.2.1.1. After generation of the three required laser wavelengths, the beams were conditioned and overlapped. This is shown in detail in Figure A.2(c). In the box for overlap optics, each

path of the three individual lasers (532 nm, 561.7 nm, 607 nm) contained (1) an energy control unit consisting of half-wave plate and polarizing beam splitter cube, (2) a telescope to slightly modify beam divergence and optimize individual beam foci in the DP-CARS probe volume, (3) a delay line to adjust temporal delay of the laser pulse (see movable optics in Figure A.2(c) surrounded by dotted rectangles). In the beam paths of both dye lasers only broadband anti-reflection coated prisms were arranged to provide flexibility to use other wavelengths. Finally, all three laser beams were overlapped and left the housing to the test rig, i.e., DP-CARS probe volume. The beam combiner (BC) shown in Figure A.2(c) did only overlap the 532 nm and 607 nm pulse, while the 561.7 nm beam passed right below the optic.

Appendix B

Publication Declarations and Permissions

This appendix chapter contains declarations on the author's contributions to scientific publications and permissions to reuse contents of the author's journal publications.

As this thesis reuses contents of the author's publications [E8], [E9] and [E11], declarations on the author's contribution for these three publications are given in section B.1. Contents from other publications with a scientific contribution of the author (either as first author [E7, E10, E12] or as coauthor [E1–E6]) are given as conventional literature references in the text, in case it is referred to them in this dissertation. Accordingly, no declarations are appended in section B.1 for these works [E1–E7, E10, E12], as contents are not reused but solely referred to.

In section B.2, the permission of the publisher Elsevier to reuse contents of the two *Combustion and Flame* publications [E11] and [E8] in this dissertation is given.

Since publication [E9] is a conference paper and no copyright has passed to a publisher upon publication, permission for reusing it in this dissertation is not required.

B.1 Declarations on the Contribution to the Scientific Publication

Declaration on the contribution to the scientific publication
Erklärung zum Eigenanteil der wissenschaftlichen Veröffentlichung
Ph.D. candidate, Florian Zentgraf, M.Sc.

<u>Paper:</u> **Florian Zentgraf**, Pascal Johe, Matthias Steinhausen, Christian Hasse, Max Greifenstein, Andrew D. Cutler, Robert S. Barlow, Andreas Dreizler, Detailed assessment of the thermochemistry in a side-wall quenching burner by simultaneous quantitative measurement of CO_2, CO and temperature using laser diagnostics. *Combustion and Flame* 235, 111707 (2022). https://doi.org/10.1016/j.combustflame.2021.111707

Co-Authors:	Pascal Johe, M.Sc. Matthias Steinhausen, M.Sc. M.Sc. Christian Hasse, Prof. Dr. Max Greifenstein, Dr. Andrew D. Cutler, Prof. Dr. Robert S. Barlow, Dr. Andreas Dreizler, Prof. Dr. habil.

Scientific contribution of the Ph.D. candidate Florian Zentgraf:

Implemented a dual-pump coherent anti-Stokes Raman spectroscopy (DP-CARS) approach to the studied side-wall quenching (SWQ) burner for simultaneous probing of N_2 (for temperature) and CO_2. Combined it with laser-induced fluorescence of CO and OH as well as phosphor thermometry for simultaneous multi-parameter investigations.

Performed comprehensive near-wall measurements on premixed SWQ with lean dimethyl ether/air mixtures under laminar conditions. The final execution of the measurement was supported by Pascal Johe.

Developed evaluation code, processed the experimental data and conducted detailed analysis of the near-wall three-parameter (CO_2, CO, temperature)-thermochemistry. The spectral fitting code for DP-CARS data was provided by Andrew D. Cutler. Numerical simulation data for comparison with experiment was provided by Matthias Steinhausen.

Visualized data, wrote the initial paper manuscript, acted as corresponding author, took responsibility of further drafting iterations and corrections in the journals review process with the support of the other co-authors.

Entire contribution:

Took a leading role in planning, designing and conducting the experiments, data processing, analysis as well as interpretation and writing of the manuscript.

The publication is not the subject of any further ongoing or completed dissertation.

Florian Zentgraf	Pascal Johe	Matthias Steinhausen
Christian Hasse	Max Greifenstein	Andrew D. Cutler
Robert S. Barlow	Andreas Dreizler	

Declaration on the contribution to the scientific publication
Erklärung zum Eigenanteil der wissenschaftlichen Veröffentlichung
Ph.D. candidate, Florian Zentgraf, M.Sc.

Paper: **Florian Zentgraf**, Pascal Johe, Andrew D. Cutler, Robert S. Barlow, Benjamin Böhm, Andreas Dreizler, Classification of flame prehistory and quenching topology in a side-wall quenching burner at low-intensity turbulence by correlating transport effects with CO_2, CO and temperature. *Combustion and Flame*, 111681 (2021).
https://doi.org/10.1016/j.combustflame.2021.111681

Co-Authors:	Pascal Johe, M.Sc.
	Andrew D. Cutler, Prof. Dr.
	Robert S. Barlow, Dr.
	Benjamin Böhm, Dr.
	Andreas Dreizler, Prof. Dr. habil.

Scientific contribution of the Ph.D. candidate Florian Zentgraf:

Performed comprehensive near-wall measurements on premixed side-wall quenching (SWQ) with lean dimethyl ether/air mixtures under turbulent conditions. The final execution of the measurement was supported by Pascal Johe.

Developed evaluation code, processed the experimental data and conducted detailed analysis of the near-wall three-parameter (CO_2, CO, temperature)-thermochemistry, specially classified by the turbulent quenching topology (associated with either SWQ or head-on quenching). The spectral fitting code for dual pump coherent anti-Stokes Raman spectroscopy data was provided by Andrew D. Cutler.

Visualized data, wrote the initial paper manuscript, acted as corresponding author, took responsibility of further drafting iterations and corrections in the journals review process with the support of the other co-authors.
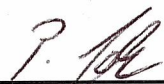
Entire contribution:

Took a leading role in planning, designing and conducting the experiments, data processing, analysis as well as interpretation and writing of the manuscript.

The used methodology to measure three-parameter (CO_2, CO, temperature)-thermochemistry in this study based on the previous laminar paper (https://doi.org/10.1016/j.combustflame.2021.111707). The publication is not the subject of any further ongoing or completed dissertation.

Andrew Cutler

Digitally signed by Andrew Cutler
DN: cn=Andrew Cutler, o=GWU, ou=MAE, email=adcutler@gwu.edu, c=US
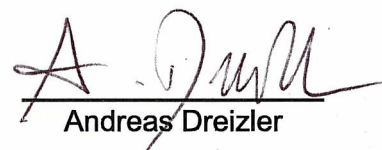Date: 2021.12.15 16:32:47 -05'00'

_____
Florian Zentgraf

_____
Pascal Johe

_____
Andrew D. Cutler

_____
Robert S. Barlow

_____
Benjamin Böhm

_____
Andreas Dreizler

Declaration on the contribution to the scientific publication
Erklärung zum Eigenanteil der wissenschaftlichen Veröffentlichung
Ph.D. candidate, Florian Zentgraf, M.Sc.

<u>Paper:</u> **Florian Zentgraf**, Pascal Johe, David Escofet-Martin, Robert S. Barlow, Benjamin Böhm, Brian Peterson, Andreas Dreizler, On the evolution of turbulent boundary layers during sidewall quenching. *30. Deutscher Flammentag - für nachhaltige Verbrennung*, Hannover-Garbsen 28.-29.09.2021, Online-Tagungsband S. 1100-1105 (2021).

Co-Authors:	Pascal Johe, M.Sc. David Escofet-Martin, Dr. Robert S. Barlow, Dr. Benjamin Böhm, Dr. Brian Peterson, Dr. Andreas Dreizler, Prof. Dr. habil.
Scientific contribution of the Ph.D. candidate Florian Zentgraf:	Implemented a high-speed, highly resolved particle image velocimetry (PIV) approach to the studied side-wall quenching (SWQ) burner for near-wall turbulent boundary layer measurements. Combined it with planar laser-induced fluorescence (PLIF) of OH for simultaneous investigations of flow field and flame front distribution.
	Performed comprehensive near-wall measurements on premixed side-wall quenching (SWQ) with lean dimethyl ether/air mixtures under turbulent conditions. The final execution of the measurement was supported by Pascal Johe.
	Developed evaluation code, processed the experimental data and conducted detailed analysis of the acquired near-wall PIV and OH-PLIF data to assess turbulent boundary layers, specially classified by the instantaneous turbulent quenching topology (associated with either SWQ or head-on quenching).
	Visualized data, wrote the initial paper manuscript, acted as corresponding author, took responsibility of further drafting iterations and corrections with the support of the other co-authors.
Entire contribution:	Took a leading role in planning, designing and conducting the experiments, data processing, analysis as well as interpretation and writing of the manuscript.

The paper is a conference contribution. The publication is not the subject of any further ongoing or completed dissertation.

_____	_____	_____
Florian Zentgraf	Pascal Johe	David Escofet-Martin
_____	_____	_____
Robert S. Barlow	Benjamin Böhm	Brian Peterson
_____		
Andreas Dreizler		

B.2 Permission by Elsevier

According to the homepage of the publisher Elsevier (https://www.elsevier.com/about/policies/copyright#Author-rights, accessed on 16 January 2022) the following author rights apply for publications in Elsevier's proprietary journals (the below statements are valid for manuscripts published either open access or on subscription; the below author rights are only an excerpt of the ones relevant for this dissertation):

- The authors "[...] retain the rights to use their research data freely without any restriction [...]".

- The authors have the right to "[...] re-use their own material in new works without permission or payment (with full acknowledgement of the original article) [...]". This right includes "[...] 1. Extend an article to book length, 2. Include an article in a subsequent compilation of their own work, 3. Re-use portions, excerpts, and their own figures or tables in other works. [...]".

- The authors have the right to "[...] use and share their works for scholarly purposes (with full acknowledgement of the original article) [...]". This right includes "[...] 5. Include in a thesis or dissertation (provided this is not published commercially) [...]".

Consequently, reusing contents of the publications [E11] and [E8] as well as the underlying research data in this dissertation is the right of the author and thus permitted. Corresponding statements from the Copyright Clearance Center on these two publications can be found below.
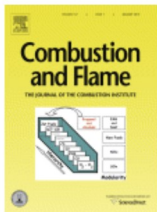
Detailed assessment of the thermochemistry in a side-wall quenching burner by simultaneous quantitative measurement of CO 2 , CO and temperature using laser diagnostics

Author:
Florian Zentgraf,Pascal Johe,Matthias Steinhausen,Christian Hasse,Max Greifenstein,Andrew D. Cutler,Robert S. Barlow,Andreas Dreizler

Publication: Combustion and Flame

Publisher: Elsevier

Date: January 2022

Journal Author Rights

BACK   CLOSE WINDOW
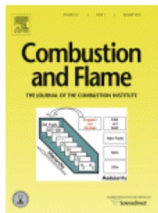
Classification of flame prehistory and quenching topology in a side-wall quenching burner at low-intensity turbulence by correlating transport effects with CO 2 , CO and temperature

Author:
Florian Zentgraf,Pascal Johe,Andrew D. Cutler,Robert S. Barlow,Benjamin Böhm,Andreas Dreizler

Publication: Combustion and Flame

Publisher: Elsevier

Date: Available online 30 August 2021

Journal Author Rights

BACK   CLOSE WINDOW

References

[1] C. Abram, B. Fond, and F. Beyrau. Temperature measurement techniques for gas and liquid flows using thermographic phosphor tracer particles. *Progress in Energy and Combustion Science*, 64:93–156, 2018.

[2] U. Ahmed, N. Chakraborty, and M. Klein. Scalar Gradient and Strain Rate Statistics in Oblique Premixed Flame–Wall Interaction Within Turbulent Channel Flows. *Flow, Turbulence and Combustion*, 106(2):701–732, 2021.

[3] M. Aldén, H. Edner, G. Holmstedt, S. Svanberg, and T. Högberg. Single-pulse laser-induced OH fluorescence in an atmospheric flame, spatially resolved with a diode array detector. *Applied Optics*, 21(7):1236–1240, 1982.

[4] M. Aldén, A. Omrane, M. Richter, and G. Särner. Thermographic phosphors for thermometry: A survey of combustion applications. *Progress in Energy and Combustion Science*, 37(4):422–461, 2011.

[5] M. Aldén, S. Wallin, and W. Wendt. Applications of Two-Photon Absorption for Detection of CO in Combustion Gases. *Applied Physics B Photophysics and Laser Chemistry*, 33(4):205–208, 1984.

[6] A. C. Alkidas. Combustion-chamber crevices: the major source of engine-out hydrocarbon emissions under fully warmed conditions. *Progress in Energy and Combustion Science*, 25(3):253–273, 1999.

[7] T. Alshaalan and C. J. Rutland. Wall heat flux in turbulent premixed reacting flow. *Combustion Science and Technology*, 174(1):135–165, 2002.

[8] T. M. Alshaalan and C. J. Rutland. Turbulence, scalar transport, and reaction rates in flame-wall interaction. *Symposium (International) on Combustion*, 27(1):793–799, 1998.

[9] B. Atakan, J. Heinze, and U. E. Meier. OH laser-induced fluorescence at high pressures: spectroscopic and two-dimensional measurements exciting the A-X (1,0) transition. *Applied Physics B: Lasers and Optics*, 64(5):585–591, 1997.

[10] P. W. Atkins, J. de Paula, and J. J. Keeler. *Physikalische Chemie*. Wiley-VCH, Weinheim, Germany, 6th edition, 2022.

[11] J. H. Bae, J. Y. Yoo, H. Choi, and D. M. McEligot. Effects of large density variation on strongly heated internal air flows. *Physics of Fluids*, 18(7):075102, 2006.

[12] R. Barlow and R. Harmon. High-Resolution Raman Measurements of Gradients at Interfaces, Report No. SAND2018-10769R, Sandia National Laboratories, 2018.

[13] R. S. Barlow, R. P. Lucht, D. M. Jassowski, and S. D. Rosenberg. Gas-phase measurements of combustion interaction with materials for radiation-cooled chambers. In *27th Joint Propulsion Conference*, Reston, Virigina, 1991. American Institute of Aeronautics and Astronautics.

[14] M. Bellenoue, T. Kageyama, S. A. Labuda, and J. Sotton. Direct measurement of laminar flame quenching distance in a closed vessel. *Experimental Thermal and Fluid Science*, 27(3):323–331, 2003.

[15] E. Benkler. wfm2read.m (https://www.mathworks.com/matlabcentral/fileexchange/6764-wfm2read-m), MATLAB Central File Exchange. Retrieved October 28, 2019.

[16] W. G. Bessler, C. Schulz, T. Lee, J. B. Jeffries, and R. K. Hanson. Strategies for laser-induced fluorescence detection of nitric oxide in high-pressure flames. I. A-X(0,0) excitation. *Applied Optics*, 41(18):3547–3557, 2002.

[17] W. G. Bessler, C. Schulz, T. Lee, J. B. Jeffries, and R. K. Hanson. Strategies for laser-induced fluorescence detection of nitric oxide in high-pressure flames. III. Comparison of A-X excitation schemes. *Applied Optics*, 42(24):4922–4936, 2003.

[18] F. Beyrau, A. Datta, T. Seeger, and A. Leipertz. Dual-pump CARS for the simultaneous detection of N_2, O_2 and CO in CH_4 flames. *Journal of Raman Spectroscopy*, 33(11-12):919–924, 2002.

[19] R. W. Bilger, S. B. Pope, K. N. C. Bray, and J. F. Driscoll. Paradigms in turbulent combustion research. *Proceedings of the Combustion Institute*, 30(1):21–42, 2005.

[20] A. Bohlin, C. Jainski, B. D. Patterson, A. Dreizler, and C. J. Kliewer. Multiparameter spatio-thermochemical probing of flame–wall interactions advanced with coherent Raman imaging. *Proceedings of the Combustion Institute*, 36(3):4557–4564, 2017.

[21] A. Bohlin and C. J. Kliewer. Diagnostic Imaging in Flames with Instantaneous Planar Coherent Raman Spectroscopy. *The Journal of Physical Chemistry Letters*, 5(7):1243–1248, 2014.

[22] A. Bohlin, M. Mann, B. D. Patterson, A. Dreizler, and C. J. Kliewer. Development of two-beam femtosecond/picosecond one-dimensional rotational coherent anti-Stokes Raman spectroscopy: Time-resolved probing of flame wall interactions. *Proceedings of the Combustion Institute*, 35(3):3723–3730, 2015.

[23] A. Bohlin, B. D. Patterson, and C. J. Kliewer. Communication: Simplified two-beam rotational CARS signal generation demonstrated in 1D. *The Journal of Chemical Physics*, 138(8):081102, 2013.

[24] R. Borghi. On the Structure and Morphology of Turbulent Premixed Flames. In C. Casci and C. Bruno, editors, *Recent Advances in the Aerospace Sciences*, pages 117–138. Plenum Press, New York, 1985.

[25] G. Borman and K. Nishiwaki. Internal-combustion engine heat transfer. *Progress in Energy and Combustion Science*, 13(1):1–46, 1987.

[26] B. Boust, J. Sotton, S. A. Labuda, and M. Bellenoue. A thermal formulation for single-wall quenching of transient laminar flames. *Combustion and Flame*, 149(3):286–294, 2007.

[27] J. Brübach, C. Pflitsch, A. Dreizler, and B. Atakan. On surface temperature measurements with thermographic phosphors: A review. *Progress in Energy and Combustion Science*, 39(1):37–60, 2013.

[28] D. Brüggemann, B. Wies, X. X. Zhang, T. Heinze, and K.-F. Knoche. CARS Spectroscopy for Temperature and Concentration Measurements in a Spark Ignition Engine. In D. F. G. Durão, M. V. Heitor, J. H. Whitelaw, and P. O. Witze, editors, *Combusting Flow Diagnostics*, NATO ASI Series, Series E, pages 495–511. Springer, Dordrecht, 1992.

[29] G. Bruneaux, K. Akselvoll, T. Poinsot, and J. H. Ferziger. Flame-Wall Interaction Simulation in a Turbulent Channel Flow. *Combustion and Flame*, 107(1):27–44, 1996.

[30] O. Carrivain, M. Orain, N. Dorval, C. Morin, and G. Legros. Experimental Spectroscopic Studies of Carbon Monoxide (CO) Fluorescence at High Temperatures and Pressures. *Applied Spectroscopy*, 71(10):2353–2366, 2017.

[31] Y. A. Çengel and J. M. Cimbala. *Fluid Mechanics: Fundamentals and Applications*. McGraw-Hill, New York, NY, 3rd edition, 2014.

[32] P. Chakraborty, S. Balachandar, and R. J. Adrian. On the relationships between local vortex identification schemes. *Journal of Fluid Mechanics*, 535:189–214, 2005.

[33] F. Chen and H. Liu. Particle image velocimetry for combustion measurements: Applications and developments. *Chinese Journal of Aeronautics*, 31(7):1407–1427, 2018.

[34] R. K. Cheng, R. G. Bill Jr., and F. Robben. Experimental study of combustion in a turbulent boundary layer. *Symposium (International) on Combustion*, 18(1):1021–1029, 1981.

[35] K.-S. Choi and J. L. Lumley. The return to isotropy of homogeneous turbulence. *Journal of Fluid Mechanics*, 436:59–84, 2001.

[36] C. W. Clendening Jr., W. Shackleford, and R. Hilyard. Raman scattering measurements in a side-wall quench layer. *Symposium (International) on Combustion*, 18(1):1583–1590, 1981.

[37] S. Cobeldick. MatPlotLib Perceptually Uniform Colormaps (https://www.mathworks.com/matlabcentral/fileexchange/62729-matplotlib-perceptually-uniform-colormaps), MATLAB Central File Exchange. Retrieved August 6, 2021.

[38] T. P. Coffee and J. M. Heimerl. Transport algorithms for premixed, laminar steady-state flames. *Combustion and Flame*, 43:273–289, 1981.

[39] C. F. Curtiss and J. O. Hirschfelder. Transport Properties of Multicomponent Gas Mixtures. *The Journal of Chemical Physics*, 17(6):550–555, 1949.

[40] A. D. Cutler, E. C. A. Gallo, and L. M. L. Cantu. WIDECARS spectra fitting in a premixed ethylene-air flame. *Journal of Raman Spectroscopy*, 47(4):416–424, 2016.

[41] A. D. Cutler, E. C. A. Gallo, L. M. L. Cantu, R. D. Rockwell, and C. P. Goyne. Coherent anti-Stokes Raman spectroscopy of a premixed ethylene–air flame in a dual-mode scramjet. *Combustion and Flame*, 189(1):92–105, 2018.

[42] J. W. Daily and E. W. Rothe. Effect of laser intensity and of lower-state rotational energy transfer upon temperature measurements made with laser-induced fluorescence. *Applied Physics B Lasers and Optics*, 68(1):131–140, 1999.

[43] W. Demtröder. *Experimentalphysik 3: Atome, Moleküle und Festkörper*. Springer, Berlin, Heidelberg, 4th edition, 2010.

[44] W. Demtröder. *Laser Spectroscopy 2: Experimental Techniques*. Springer, Berlin, Heidelberg, 5th edition, 2015.

[45] M. D. Di Rosa and R. L. Farrow. Cross sections of photoionization and ac Stark shift measured from Doppler-free B ← X(0, 0) excitation spectra of CO. *Journal of the Optical Society of America B*, 16(5):861–870, 1999.

[46] G. H. Dieke and H. M. Crosswhite. The ultraviolet bands of OH Fundamental data. *Journal of Quantitative Spectroscopy and Radiative Transfer*, 2(2):97–199, 1962.

[47] C.-P. Ding, B. Peterson, M. Schmidt, A. Dreizler, and B. Böhm. Flame/flow dynamics at the piston surface of an IC engine measured by high-speed PLIF and PTV. *Proceedings of the Combustion Institute*, 37(4):4973–4981, 2019.

[48] T. Dreier, A. Dreizler, and J. Wolfrum. The Application of a Raman-Shifted Tunable KrF Excimer Laser for Laser-Induced Fluorescence Combustion Diagnostics. *Applied Physics B Photophysics and Laser Chemistry*, 55(4):381–387, 1992.

[49] A. Dreizler and B. Böhm. Advanced laser diagnostics for an improved understanding of premixed flame-wall interactions. *Proceedings of the Combustion Institute*, 35(1):37–64, 2015.

[50] S. A. J. Druet and J.-P. E. Taran. CARS Spectroscopy. *Progress in Quantum Electronics*, 7(1):1–72, 1981.

[51] A. C. Eckbreth, T. J. Anderson, and G. M. Dobbs. Multi-Color CARS for Hydrogen-Fueled Scramjet Applications. *Applied Physics B Photophysics and Laser Chemistry*, 45(4):215–223, 1988.

[52] D. V. Efimov, P. de Goey, and J. A. van Oijen. QFM: quenching flamelet-generated manifold for modelling of flame–wall interactions. *Combustion Theory and Modelling*, 24(1):72–104, 2020.

[53] F. El-Diasty. Coherent anti-Stokes Raman scattering: Spectroscopy and microscopy. *Vibrational Spectroscopy*, 55(1):1–37, 2011.

[54] M. Elstner. *Physikalische Chemie II: Quantenmechanik und Spektroskopie.* Springer Spektrum, Berlin, Heidelberg, 1st edition, 2021.

[55] D. Escofet-Martin, A. O. Ojo, N. T. Mecker, M. A. Linne, and B. Peterson. Simultaneous 1D hybrid fs/ps rotational CARS, phosphor thermometry, and CH* imaging to study transient near-wall heat transfer processes. *Proceedings of the Combustion Institute*, 38(1):1579–1587, 2021.

[56] P. Ewart. A modeless, variable bandwidth, tunable laser. *Optics Communications*, 55(2):124–126, 1985.

[57] L. Fahrmeir, R. Künstler, I. Pigeot, and G. Tutz. *Statistik: Der Weg zur Datenanalyse.* Springer, Berlin, Heidelberg, 6th edition, 2007.

[58] U. Fey, M. König, and H. Eckelmann. A new Strouhal–Reynolds-number relationship for the circular cylinder in the range $47 < \text{Re} < 2 \times 10^5$. *Physics of Fluids*, 10(7):1547–1549, 1998.

[59] F. Foucher, S. Burnel, C. Mounaïm-Rousselle, M. Boukhalfa, B. Renou, and M. Trinité. Flame wall interaction: effect of stretch. *Experimental Thermal and Fluid Science*, 27(4):431–437, 2003.

[60] N. Fuhrmann, J. Brübach, and A. Dreizler. On the mono-exponential fitting of phosphorescence decays. *Applied Physics B Lasers and Optics*, 116(2):359–369, 2014.

[61] T. Fuyuto, H. Kronemayer, B. Lewerich, J. Brübach, T. Fujikawa, K. Akihama, T. Dreier, and C. Schulz. Temperature and species measurement in a quenching boundary layer on a flat-flame burner. *Experiments in Fluids*, 49(4):783–795, 2010.

[62] S. Ganter, A. Heinrich, T. Meier, G. Kuenne, C. Jainski, M. C. Rißmann, A. Dreizler, and J. Janicka. Numerical analysis of laminar methane–air side-wall-quenching. *Combustion and Flame*, 186(1):299–310, 2017.

[63] S. Ganter, C. Straßacker, G. Kuenne, T. Meier, A. Heinrich, U. Maas, and J. Janicka. Laminar near-wall combustion: Analysis of tabulated chemistry simulations by means of detailed kinetics. *International Journal of Heat and Fluid Flow*, 70(1):259–270, 2018.

[64] D. G. Goodwin, R. L. Speth, H. K. Moffat, and B. W. Weber. Cantera: An Object-oriented Software Toolkit for Chemical Kinetics, Thermodynamics, and Transport Processes, version 2.4.0, 10.5281/ZENODO.4527812, 2021.

[65] M. A. Gregor and A. Dreizler. A quasi-adiabatic laminar flat flame burner for high temperature calibration. *Measurement Science and Technology*, 20(6):065402, 2009.

[66] M. Greifenstein. *Experimental investigations of flame-cooling air interaction in an effusion cooled pressurized single sector model gas turbine combustor.* Dissertation, Technical University of Darmstadt, Darmstadt, 2021.

[67] M. Greifenstein and A. Dreizler. Influence of effusion cooling air on the thermochemical state of combustion in a pressurized model single sector gas turbine combustor. *Combustion and Flame*, 226(1):455–466, 2021.

[68] M. Greifenstein and A. Dreizler. MARSFT: Efficient fitting of CARS spectra using a library–based genetic algorithm. *Journal of Raman Spectroscopy*, 52(3):655–663, 2021.

[69] A. Gruber, R. Sankaran, E. R. Hawkes, and J. H. Chen. Turbulent flame–wall interaction: a direct numerical simulation study. *Journal of Fluid Mechanics*, 658:5–32, 2010.

[70] D. Han, A. Satija, J. Kim, Y. Weng, J. P. Gore, and R. P. Lucht. Dual-pump vibrational CARS measurements of temperature and species concentrations in turbulent premixed flames with CO_2 addition. *Combustion and Flame*, 181:239–250, 2017.

[71] R. K. Hanson, R. M. Spearrin, and C. S. Goldenstein. *Spectroscopy and Optical Diagnostics for Gases*. Springer eBook Collection Engineering. Springer, Cham, 1st edition, 2016.

[72] M. Härtl, K. Gaukel, D. Pélerin, and G. Wachtmeister. Oxymethylene Ether as Potentially CO_2-neutral Fuel for Clean Diesel Engines Part 1: Engine Testing. *MTZ worldwide*, 78(2):52–59, 2017.

[73] C. Hasse, M. Bollig, N. Peters, and H. A. Dwyer. Quenching of Laminar Iso-Octane Flames at Cold Walls. *Combustion and Flame*, 122(1-2):117–129, 2000.

[74] E. P. Hassel and S. Linow. Laser diagnostics for studies of turbulent combustion. *Measurement Science and Technology*, 11(2):R37–R57, 2000.

[75] A. Heinrich, S. Ganter, G. Kuenne, C. Jainski, A. Dreizler, and J. Janicka. 3D Numerical Simulation of a Laminar Experimental SWQ Burner with Tabulated Chemistry. *Flow, Turbulence and Combustion*, 100(2):535–559, 2018.

[76] A. Heinrich, F. Ries, G. Kuenne, S. Ganter, C. Hasse, A. Sadiki, and J. Janicka. Large Eddy Simulation with tabulated chemistry of an experimental sidewall quenching burner. *International Journal of Heat and Fluid Flow*, 71:95–110, 2018.

[77] J. C. R. Hunt, A. A. Wray, and P. Moin. Eddies, Stream, and Convergence Zones in Turbulent Flows, Center for Turbulence Research, Proceedings of the Summer Program 1988: 193–208, 1988.

[78] IEA. World Energy Outlook 2021, IEA, Paris https://www.iea.org/reports/world-energy-outlook-2021.

[79] C. Jainski. *Experimentelle Untersuchung der turbulenten Flamme-Wand-Interaktion*. Dissertation, Technical University of Darmstadt, Darmstadt, 2016. Publisher: Optimus Verlag, Göttingen.

[80] C. Jainski, L. Lu, A. Dreizler, and V. Sick. High-speed micro particle image velocimetry studies of boundary-layer flows in a direct-injection engine. *International Journal of Engine Research*, 14(3):247–259, 2013.

[81] C. Jainski, M. Rißmann, B. Böhm, and A. Dreizler. Experimental investigation of flame surface density and mean reaction rate during flame–wall interaction. *Proceedings of the Combustion Institute*, 36(2):1827–1834, 2017.

[82] C. Jainski, M. Rißmann, B. Böhm, J. Janicka, and A. Dreizler. Sidewall quenching of atmospheric laminar premixed flames studied by laser-based diagnostics. *Combustion and Flame*, 183:271–282, 2017.

[83] C. Jainski, M. Rißmann, S. Jakirlic, B. Böhm, and A. Dreizler. Quenching of Premixed Flames at Cold Walls: Effects on the Local Flow Field. *Flow, Turbulence and Combustion*, 100(1):177–196, 2018.

[84] S. Jakirlić, K. Hanjalić, and C. Tropea. Anisotropy Evolution in Relaminarizing Turbulent Boundary Layers: a DNS-aided Second-Moment Closure Analysis. In H.-J. Rath, C. Holze, H.-J. Heinemann, R. Henke, and H. Hönlinger, editors, *New Results in Numerical and Experimental Fluid Mechanics V*, volume 92 of *Notes on Numerical Fluid Mechanics and Multidisciplinary Design (NNFM)*, pages 496–503. Springer, Berlin, Heidelberg, 2006.

[85] J. Jeong and F. Hussain. On the identification of a vortex. *Journal of Fluid Mechanics*, 285:69–94, 1995.

[86] A. Johchi, J. Pareja, B. Böhm, and A. Dreizler. Quantitative mixture fraction imaging of a synthetic biogas turbulent jet propagating into a NO-vitiated air co-flow using planar laser-induced fluorescence (PLIF). *Experiments in Fluids*, 60(5):82, 2019.

[87] K. Kajihara, Y. Ikuta, M. Oto, M. Hirano, L. Skuja, and H. Hosono. UV–VUV laser induced phenomena in SiO₂ glass. *Nuclear Instruments and Methods in Physics Research Section B: Beam Interactions with Materials and Atoms*, 218:323–331, 2004.

[88] R. J. Kee, J. F. Grcar, M. D. Smooke, and J. A. Miller. A Fortran program for modeling steady laminar one-dimensional premixed flames, Report No. SAND85-8240, Sandia National Laboratories, 1985.

[89] W. Ketterle, M. Schäfer, A. Arnold, and J. Wolfrum. 2D Single-Shot Imaging of OH Radicals Using Tunable Excimer Lasers. *Applied Physics B Photophysics and Laser Chemistry*, 54(2):109–112, 1992.

[90] T. M. Kiehne, R. D. Matthews, and D. E. Wilson. The significance of intermediate hydrocarbons during wall quench of propane flames. *Symposium (International) on Combustion*, 21(1):481–489, 1988.

[91] B. J. Kirby and R. K. Hanson. Planar laser-induced fluorescence imaging of carbon monoxide using vibrational (infrared) transitions. *Applied Physics B Lasers and Optics*, 69(5-6):505–507, 1999.

[92] T. Kissel. *Spektroskopische Methoden zur Charakterisierung wandnaher Verbrennungsprozesse*. Dissertation, Technical University of Darmstadt, Darmstadt, 2011.

[93] J. Kojima, Y. Ikeda, and T. Nakajima. Spatially resolved measurement of OH*, CH*, and C₂* chemiluminescence in the reaction zone of laminar methane/air premixed flames. *Proceedings of the Combustion Institute*, 28(2):1757–1764, 2000.

[94] H. Kosaka. *Experimental Investigation of Flame-Wall Interaction by Laser-based Diagnostics*. Dissertation, Technical University of Darmstadt, Darmstadt, 2019.

[95] J. R. Lakowicz. *Principles of Fluorescence Spectroscopy*. Springer, New York, 3rd edition, 2006.

[96] A. Lawitzki, I. Plath, W. Stricker, J. Bittner, U. Meier, and K. Kohse-Höinghaus. Laser-Induced Fluorescence Determination of Flame Temperatures in Comparison with CARS Measurements. *Applied Physics B Photophysics and Laser Chemistry*, 50(6):513–518, 1990.

[97] J.-H. Lee and H. J. Sung. Effects of an adverse pressure gradient on a turbulent boundary layer. *International Journal of Heat and Fluid Flow*, 29(3):568–578, 2008.

[98] M. Lee, Y. Fan, C. B. Reuter, Y. Ju, and Y. Suzuki. DME/Oxygen wall-stabilized premixed cool flame. *Proceedings of the Combustion Institute*, 37(2):1749–1756, 2019.

[99] T. Lee, W. G. Bessler, H. Kronemayer, C. Schulz, and J. B. Jeffries. Quantitative temperature measurements in high-pressure flames with multiline NO-LIF thermometry. *Applied Optics*, 44(31):6718–6728, 2005.

[100] T. Li, J. Pareja, F. Fuest, M. Schütte, Y. Zhou, A. Dreizler, and B. Böhm. Tomographic imaging of OH laser-induced fluorescence in laminar and turbulent jet flames. *Measurement Science and Technology*, 29(1):015206, 2018.

[101] T. Li, M. Schiemann, J. Köser, A. Dreizler, and B. Böhm. Experimental investigations of single particle and particle group combustion in a laminar flow reactor using simultaneous volumetric OH-LIF imaging and diffuse backlight-illumination. *Renewable and Sustainable Energy Reviews*, 136(3):110377, 2021.

[102] S. Linow, A. Dreizler, J. Janicka, and E. P. Hassel. Comparison of two-photon excitation schemes for CO detection in flames. *Applied Physics B Lasers and Optics*, 71(5):689–696, 2000.

[103] R. P. Lucht. Three-laser coherent anti-Stokes Raman scattering measurements of two species. *Optics Letters*, 12(2):78–80, 1987.

[104] R. P. Lucht, V. Velur-Natarajan, C. D. Carter, K. D. Grinstead Jr., J. R. Gord, P. M. Danehy, G. J. Fiechtner, and R. L. Farrow. Dual-Pump Coherent Anti-Stokes Raman Scattering Temperature and CO_2 Concentration Measurements. *AIAA Journal*, 41(4):679–686, 2003.

[105] B. Lumpp, D. Rothe, C. Pastötter, R. Lämmermann, and E. Jacob. Oxymethylene Ethers as Diesel Fuel Additives of the Future. *MTZ worldwide*, 72(3):34–38, 2011.

[106] M. Luo and D. Liu. Effects of dimethyl ether addition on soot formation, evolution and characteristics in flame-wall interactions. *Energy*, 164(1–2):642–654, 2018.

[107] M. Luo and D. Liu. Pollutants Emissions of CO and Soot from Flame-wall Interactions in Fundamental and Practical Energy Conversion Systems: A Review. *ES Energy & Environment*, 3:4–24, 2019.

[108] B. Luong. N-dimensional histogram (https://www.mathworks.com/matlabcentral/fileexchange/23897-n-dimensional-histogram), MATLAB Central File Exchange. Retrieved September 14, 2021.

[109] T. H. Maiman. Stimulated Optical Radiation in Ruby. *Nature*, 187(4736):493–494, 1960.

[110] M. Mann, C. Jainski, M. Euler, B. Böhm, and A. Dreizler. Transient flame–wall interactions: Experimental analysis using spectroscopic temperature and CO concentration measurements. *Combustion and Flame*, 161(9):2371–2386, 2014.

[111] A. R. Masri. Partial premixing and stratification in turbulent flames. *Proceedings of the Combustion Institute*, 35(2):1115–1136, 2015.

[112] V. Masson-Delmotte, P. Zhai, A. Pirani, S. L. Connors, C. Péan, S. Berger, N. Caud, Y. Chen, L. Goldfarb, M. I. Gomis, M. Huang, K. Leitzell, E. Lonnoy, J. B. R. Matthews, T. K. Maycock, T. Waterfield, O. Yelekçi, R. Yu, and B. Zhou. IPCC, 2021: Summary for Policymakers. In: Climate Change 2021: The Physical Science Basis. Contribution of Working Group I to the Sixth Assessment Report of the Intergovernmental Panel on Climate Change. Cambridge University Press, Cambridge, United Kingdom and New York, NY, USA, pages 3-32.

[113] A. Melling. Tracer particles and seeding for particle image velocimetry. *Measurement Science and Technology*, 8(12):1406–1416, 1997.

[114] G. Merziger, G. Mühlbach, D. Wille, and T. Wirth. *Formeln + Hilfen höhere Mathematik*. Binomi Verlag, Barsinghausen, 6th edition, 2010.

[115] A. V. Mokhov, A. P. Nefedov, B. V. Rogov, V. A. Sinel'shchikov, A. D. Usachev, A. V. Zobnin, and H. B. Levinsky. CO Behavior in Laminar Boundary Layer of Combustion Product Flow. *Combustion and Flame*, 119(1-2):161–173, 1999.

[116] Y. Nagano, T. Tsuji, and T. Houra. Structure of turbulent boundary layer subjected to adverse pressure gradient. *International Journal of Heat and Fluid Flow*, 19(5):563–572, 1998.

[117] A. P. Nefedov, V. A. Sinel'shchikov, A. D. Usachev, and A. V. Zobnin. Photochemical effect in two-photon laser-induced fluorescence detection of carbon monoxide in hydrocarbon flames. *Applied Optics*, 37(33):7729–7736, 1998.

[118] T. T. Ng, R. K. Cheng, F. Robben, and L. Talbot. Combustion-turbulence interaction in the turbulent boundary layer over a hot surface. *Symposium (International) on Combustion*, 19(1):359–366, 1982.

[119] S. O'Byrne, P. M. Danehy, and A. D. Cutler. $N_2/O_2/H_2$ dual-pump CARS: Validation experiments. In *20th International Congress on Instrumentation in Aerospace Simulation Facilities, 2003. ICIASF '03*, pages 287–295. IEEE, 25-29 Aug. 2003.

[120] A. O. Ojo, D. Escofet-Martin, J. Collins, G. Falconetti, and B. Peterson. Experimental investigation of thermal boundary layers and associated heat loss for transient engine-relevant processes using HRCARS and phosphor thermometry. *Combustion and Flame*, 233:111567, 2021.

[121] M. Orain, P. Baranger, B. Rossow, and F. Grisch. Fluorescence spectroscopy of 1,2,4-trimethylbenzene at high temperatures and pressures: application to temperature measurements. *Applied Physics B Lasers and Optics*, 100(4):945–952, 2010.

[122] R. E. Palmer. The CARSFT Computer Code for Calculating Coherent Anti-Stokes Raman Spectra: User and Programmer Information, Report No. SAND89-8206, Sandia National Laboratories, 1989.

[123] R. Palulli, M. Talei, and R. L. Gordon. Unsteady flame–wall interaction: Impact on CO emission and wall heat flux. *Combustion and Flame*, 207(2):406–416, 2019.

[124] J. Pareja, A. Johchi, T. Li, A. Dreizler, and B. Böhm. A study of the spatial and temporal evolution of auto-ignition kernels using time-resolved tomographic OH-LIF. *Proceedings of the Combustion Institute*, 37(2):1321–1328, 2019.

[125] J. Pareja, C. Litterscheid, A. Molina, B. Albert, B. Kaiser, and A. Dreizler. Effects of doping concentration and co-doping with cerium on the luminescence properties of $Gd_3Ga_5O_{12}:Cr^{3+}$ for thermometry applications. *Optical Materials*, 47(1):338–344, 2015.

[126] N. Peters. Laminar flamelet concepts in turbulent combustion. *Symposium (International) on Combustion*, 21(1):1231–1250, 1988.

[127] N. Peters. *Turbulent Combustion*. Cambridge monographs on mechanics. Cambridge University Press, Cambridge, 2000.

[128] T. Poinsot and D. Veynante. *Theoretical and Numerical Combustion*. R.T. Edwards, Inc., Philadelphia, Pa., 1st edition, 2001.

[129] T. J. Poinsot, D. C. Haworth, and G. Bruneaux. Direct Simulation and Modeling of Flame-Wall Interaction for Premixed Turbulent Combustion. *Combustion and Flame*, 95(1-2):118–132, 1993.

[130] S. B. Pope. *Turbulent Flows*. Cambridge University Press, Cambridge, 2000. 6th printing 2009.

[131] P. Popp, M. Smooke, and M. Baum. Heterogeneous/homogeneous reaction and transport coupling during flame-wall interaction. *Symposium (International) on Combustion*, 26(2):2693–2700, 1996.

[132] X. Qin and Y. Ju. Measurements of burning velocities of dimethyl ether and air premixed flames at elevated pressures. *Proceedings of the Combustion Institute*, 30(1):233–240, 2005.

[133] M. Raffel, C. E. Willert, S. T. Wereley, and J. Kompenhans. *Particle Image Velocimetry: A Practical Guide*. Springer, Berlin, Heidelberg, 2nd edition, 2007.

[134] K. A. Rahman, K. S. Patel, M. N. Slipchenko, T. R. Meyer, Z. Zhang, Y. Wu, J. R. Gord, and S. Roy. Femtosecond, two-photon, laser-induced fluorescence (TP-LIF) measurement of CO in high-pressure flames. *Applied Optics*, 57(20):5666–5671, 2018.

[135] A. Renaud, C.-P. Ding, S. Jakirlic, A. Dreizler, and B. Böhm. Experimental characterization of the velocity boundary layer in a motored IC engine. *International Journal of Heat and Fluid Flow*, 71(4):366–377, 2018.

[136] K. F. Renk. *Basics of Laser Physics*. Springer, Berlin, Heidelberg, 1st edition, 2012.

[137] M. Rißmann, C. Jainski, M. Mann, and A. Dreizler. Flame-Flow Interaction in Premixed Turbulent Flames During Transient Head-On Quenching. *Flow, Turbulence and Combustion*, 98(4):1025–1038, 2017.

[138] J. Rosell, J. Sjöholm, M. Richter, and M. Aldén. Comparison of Three Schemes of Two-Photon Laser-Induced Fluorescence for CO Detection in Flames. *Applied Spectroscopy*, 67(3):314–320, 2013.

[139] S. Roy, J. R. Gord, and A. K. Patnaik. Recent advances in coherent anti-Stokes Raman scattering spectroscopy: Fundamental developments and applications in reacting flows. *Progress in Energy and Combustion Science*, 36(2):280–306, 2010.

[140] S. Roy, T. R. Meyer, R. P. Lucht, V. M. Belovich, E. Corporan, and J. R. Gord. Temperature and CO_2 concentration measurements in the exhaust stream of a liquid-fueled combustor using dual-pump coherent anti-Stokes Raman scattering (CARS) spectroscopy. *Combustion and Flame*, 138(3):273–284, 2004.

[141] R. Sadanandan, J. Fleck, W. Meier, P. Griebel, and C. Naumann. 2D mixture fraction measurements in a high pressure and high temperature combustion system using NO tracer-LIF. *Applied Physics B Lasers and Optics*, 106(1):185–196, 2012.

[142] R. Sadanandan, W. Meier, and J. Heinze. Experimental study of signal trapping of OH laser induced fluorescence and chemiluminescence in flames. *Applied Physics B Lasers and Optics*, 106(3):717–724, 2012.

[143] R. Sadanandan, R. A. Schießl, D. Markus, and U. Maas. 2D Mixture Fraction Studies in a Hot-Jet Ignition Configuration Using NO-LIF and Correlation Analysis. *Flow, Turbulence and Combustion*, 86(1):45–62, 2011.

[144] M. Saffman. Parametric Studies of a Side Wall Quench Layer. *Combustion and Flame*, 55(2):141–159, 1984.

[145] H. Schlichting and K. Gersten. *Grenzschicht-Theorie*. Springer, Berlin, Heidelberg, 10th edition, 2006.

[146] C. Schulz and V. Sick. Tracer-LIF diagnostics: quantitative measurement of fuel concentration, temperature and fuel/air ratio in practical combustion systems. *Progress in Energy and Combustion Science*, 31(1):75–121, 2005.

[147] F. Seitz, R. Schießl, and D. Markus. Evaluation strategies for LIF-based measurements of the mixing field in a transient free jet: Proceedings of the European Combustion Meeting – 2015, Paper P4-06, March 30–April 2, 2015, Budapest, Hungary.

[148] J. M. Seitzman, J. Haumann, and R. K. Hanson. Quantitative two-photon LIF imaging of carbon monoxide in combustion gases. *Applied Optics*, 26(14):2892–2899, 1987.

[149] T. A. Semelsberger, R. L. Borup, and H. L. Greene. Dimethyl ether (DME) as an alternative fuel. *Journal of Power Sources*, 156(2):497–511, 2006.

[150] P. B. Sergeev, A. P. Sergeev, and V. D. Zvorykin. Radiation resistance of optical materials for windows of UV and VUV excimer lasers. *Quantum Electronics*, 37(8):706–710, 2007.

[151] A. Singh, M. Mann, T. Kissel, J. Brübach, and A. Dreizler. Simultaneous Measurements of Temperature and CO Concentration in Stagnation Stabilized Flames. *Flow, Turbulence and Combustion*, 90(4):723–739, 2013.

[152] J. Spurk and N. Aksel. *Strömungslehre: Einführung in die Theorie der Strömungen*. Springer, Berlin, Heidelberg, 9th edition, 2019.

[153] A. Stagni, Y. Luo, M. Steinhausen, A. Dreizler, and C. Hasse. Chemistry effects in the wall quenching of laminar premixed DME flames. *Combustion and Flame*, 232:111529, 2021.

[154] M. Steinhausen, T. Zirwes, F. Ferraro, A. Scholtissek, H. Bockhorn, and C. Hasse. Flame-vortex interaction during turbulent side-wall quenching and its implications for flamelet manifolds, accepted for presentation at the *39th International Symposium on Combustion* and under revision for publication in *Proceedings of the Combustion Institute*, January 2022.

[155] C. Strassacker, V. Bykov, and U. Maas. REDIM reduced modeling of quenching at a cold wall including heterogeneous wall reactions. *International Journal of Heat and Fluid Flow*, 69(2):185–193, 2018.

[156] C. Strassacker, V. Bykov, and U. Maas. Reduced modeling of Flame-Wall-Interactions of premixed isooctane-air systems including detailed transport and surface reactions. *Proceedings of the Combustion Institute*, 38(1):1063–1070, 2021.

[157] A. Stroh, Y. Hasegawa, P. Schlatter, and B. Frohnapfel. Global effect of local skin friction drag reduction in spatially developing turbulent boundary layer. *Journal of Fluid Mechanics*, 805:303–321, 2016.

[158] R. Suntz, H. Becker, P. Monkhouse, and J. Wolfrum. Two-Dimensional Visualization of the Flame Front in an Internal Combustion Engine by Laser-Induced Fluorescence of OH Radicals. *Applied Physics B Photophysics and Laser Chemistry*, 47(4):287–293, 1988.

[159] S. A. Tedder, J. L. Wheeler, A. D. Cutler, and P. M. Danehy. Width-increased dual-pump enhanced coherent anti-Stokes Raman spectroscopy. *Applied Optics*, 49(8):1305–1313, 2010.

[160] M. P. Thariyan, V. Ananthanarayanan, A. H. Bhuiyan, S. V. Naik, J. P. Gore, and R. P. Lucht. Dual-pump CARS temperature and major species concentration measurements in counter-flow methane flames using narrowband pump and broadband Stokes lasers. *Combustion and Flame*, 157(7):1390–1399, 2010.

[161] J. Trabold, D. Butz, S. Schneider, K. Dieter, R. Barlow, A. Dreizler, and D. Geyer. Fast shutter line-imaging system for dual-dispersion Raman spectroscopy in ethanol and OME flames. *Combustion and Flame*, 111864, 2022.

[162] K. H. Tran, C. Morin, M. Kühni, and P. Guibert. Fluorescence spectroscopy of anisole at elevated temperatures and pressures. *Applied Physics B Lasers and Optics*, 115(4):461–470, 2014.

[163] L. Voigt, J. Heinze, M. Korkmaz, K. P. Geigle, and C. Willert. Planar measurements of CO concentrations in flames at atmospheric and elevated pressure by laser-induced fluorescence. *Applied Physics B Lasers and Optics*, 125(5):71, 2019.

[164] S. Wan, Y. Fan, K. Maruta, and Y. Suzuki. Wall chemical effect of metal surfaces on DME/air cool flame in a micro flow reactor. *Proceedings of the Combustion Institute*, 37(4):5655–5662, 2019.

[165] J. Warnatz, U. Maas, and R. W. Dibble. *Combustion: Physical and Chemical Fundamentals, Modeling and Simulation, Experiments, Pollutant Formation*. Springer, Berlin, Heidelberg, 4th edition, 2006.

[166] M. C. Weikl, T. Seeger, R. Hierold, and A. Leipertz. Dual-pump CARS measurements of N_2, H_2 and CO in a partially premixed flame. *Journal of Raman Spectroscopy*, 38(8):983–988, 2007.

[167] N. Zettervall, C. Fureby, and E. J. K. Nilsson. Reduced Chemical Kinetic Reaction Mechanism for Dimethyl Ether-Air Combustion. *Fuels*, 2(3):323–344, 2021.

[168] T. Zirwes, T. Häber, F. Zhang, H. Kosaka, A. Dreizler, M. Steinhausen, C. Hasse, A. Stagni, D. Trimis, R. Suntz, and H. Bockhorn. Numerical Study of Quenching Distances for Side-Wall Quenching Using Detailed Diffusion and Chemistry. *Flow, Turbulence and Combustion*, 106(2):649–679, 2021.

List of Publications

[E1] P. Johe, F. Zentgraf, M. Greifenstein, M. Steinhausen, C. Hasse, and A. Dreizler. Characterization of flow field and combustion dynamics in a novel pressurized side-wall quenching burner using high-speed PIV/OH-PLIF measurements. *International Journal of Heat and Fluid Flow*, 94(3):108921, 2022.

[E2] H. Kosaka, F. Zentgraf, A. Scholtissek, L. Bischoff, T. Häber, R. Suntz, B. Albert, C. Hasse, and A. Dreizler. Wall heat fluxes and CO formation/oxidation during laminar and turbulent side-wall quenching of methane and DME flames. *International Journal of Heat and Fluid Flow*, 70:181–192, 2018.

[E3] H. Kosaka, F. Zentgraf, A. Scholtissek, C. Hasse, and A. Dreizler. Effect of Flame-Wall Interaction on Local Heat Release of Methane and DME Combustion in a Side-Wall Quenching Geometry. *Flow, Turbulence and Combustion*, 104(4):1029–1046, 2020.

[E4] M. Steinhausen, F. Ferraro, M. Schneider, F. Zentgraf, M. Greifenstein, A. Dreizler, C. Hasse, and A. Scholtissek. Effect of flame retardants on side-wall quenching of partially premixed laminar flames, accepted for publication in *Proceedings of the Combustion Institute*, July 2022.

[E5] M. Steinhausen, Y. Luo, S. Popp, C. Strassacker, T. Zirwes, H. Kosaka, F. Zentgraf, U. Maas, A. Sadiki, A. Dreizler, and C. Hasse. Numerical Investigation of Local Heat-Release Rates and Thermo-Chemical States in Side-Wall Quenching of Laminar Methane and Dimethyl Ether Flames. *Flow, Turbulence and Combustion*, 106(2):681–700, 2021.

[E6] M. Stephan, F. Zentgraf, E. Berrocal, B. Albert, B. Böhm, and A. Dreizler. Multiple scattering reduction in instantaneous gas phase phosphor thermometry: applications with dispersed seeding. *Measurement Science and Technology*, 30(5):054003, 2019.

[E7] F. Zentgraf, E. Baum, B. Böhm, A. Dreizler, and B. Peterson. On the turbulent flow in piston engines: Coupling of statistical theory quantities and instantaneous turbulence. *Physics of Fluids*, 28(4):045108, 2016.

[E8] F. Zentgraf, P. Johe, A. D. Cutler, R. S. Barlow, B. Böhm, and A. Dreizler. Classification of flame prehistory and quenching topology in a side-wall quenching burner at low-intensity turbulence by correlating transport effects with CO_2, CO and temperature. *Combustion and Flame*, 239:111681, 2022.

[E9] F. Zentgraf, P. Johe, D. Escofet-Martin, R. S. Barlow, B. Böhm, B. Peterson, and A. Dreizler. On the evolution of turbulent boundary layers during sidewall quenching. 30. Deutscher Flammentag - für nachhaltige Verbrennung, Hannover-Garbsen 28.-29.09.2021, Online-Tagungsband pages 1100-1105, 2021.

[E10] F. Zentgraf, P. Johe, H. Hoche, B. Göckel, S. Becker, M. Oechsner, and A. Dreizler. Assessment of the impact of multiple mild-steam decontaminations on the protection performance of disposable KN95 filtering facepiece respirators. *Infection Prevention in Practice*, 3(2):100136, 2021.

[E11] F. Zentgraf, P. Johe, M. Steinhausen, C. Hasse, M. Greifenstein, A. D. Cutler, R. S. Barlow, and A. Dreizler. Detailed assessment of the thermochemistry in a side-wall quenching burner by simultaneous quantitative measurement of CO_2, CO and temperature using laser diagnostics. *Combustion and Flame*, 235:111707, 2022.

[E12] F. Zentgraf, M. Stephan, E. Berrocal, B. Albert, B. Böhm, and A. Dreizler. Application of structured illumination to gas phase thermometry using thermographic phosphor particles: a study for averaged imaging. *Experiments in Fluids*, 58(7):82, 2017.